TESIS DE LA UNIVERSIDAD
DE ZARAGOZA

2026

6

Fabian Uwe Sigloch

Fabrication of Tungsten-based Nano-SQUIDs on Cantilever by means of Focused Ion Beam Induced Deposition

Director/es

De Teresa Nogueras, José María
Sangiao Barral, Soraya

http://zaguan.unizar.es/collection/Tesis

ISSN 2254-7606

Prensas de la Universidad
Universidad Zaragoza

Universidad de Zaragoza
Servicio de Publicaciones

ISSN 2254-7606

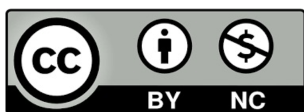

Universidad Zaragoza

Tesis Doctoral

FABRICATION OF TUNGSTEN-BASED NANO-SQUIDS ON CANTILEVER BY MEANS OF FOCUSED ION BEAM INDUCED DEPOSITION

Autor

Fabian Uwe Sigloch

Director/es

De Teresa Nogueras, José María
Sangiao Barral, Soraya

UNIVERSIDAD DE ZARAGOZA
Escuela de Doctorado

2025

Repositorio de la Universidad de Zaragoza – Zaguan http://zaguan.unizar.es

Universidad Zaragoza
1542

Tesis Doctoral

Fabrication of Tungsten-based Nano-SQUIDs on Cantilever by means of Focused Ion Beam Induced Deposition

Autor

Fabian Uwe Sigloch

Director/es

José María de Teresa Nogueras
Soraya Sangiao Barral

Facultad de Ciencias
2025

Repositorio de la Universidad de Zaragoza – Zaguan
http://zaguan.unizar.es

CSIC
CONSEJO SUPERIOR DE INVESTIGACIONES CIENTÍFICAS

Universidad Zaragoza
1542

DOCTORAL THESIS

Fabrication of Tungsten-based Nano-SQUIDs on Cantilever by means of Focused Ion Beam Induced Deposition

Fabian Uwe Sigloch

June 26, 2025

Supervised by

Prof. José María de Teresa Nogueras
Dr. Soraya Sangiao Barral

Instituto de Nanociencia y Materiales de Aragón (INMA)
CSIC – Universidad de Zaragoza

INMA FIBsuperProbes

Abstract

Fabrication of Tungsten-based NanoSQUIDs on Cantilever by means of Focused Ion Beam Induced Deposition
by Fabian Uwe Sigloch

Scanning Probe Microscopy (SPM) has long become an indispensable tool in solid state physics for the characterization and manipulation of a plethora of surface-properties on the nanoscale. In Scanning SQUID Microscopy (SSM), the spatial resolution of SPM methods is combined with the unpreceded flux sensitivity of a Superconducting Quantum Interference Device (SQUID).
The SQUID-on-Lever (SoL) is an emerging implementation of SSM where the SQUID is placed on the tip of an SPM cantilever, combining the SQUID's sensitivity with the topographic contrast and the tip-sample-distance control of Atomic Force Microscopy (AFM). Novel, innovative fabrication techniques are required to overcome the high aspect ratio of the protruding tip, posing a significant challenge to conventional, resist-based nanofabrication methods.
The work presented in this doctoral thesis forms a contribution to the FIBSuper-Probes initiative, investigating the use of Focused Ion Beam (FIB) processing for the functionalization of SPM cantilevers with superconducting structures for the fabrication of SoL probes, among others. With FIB milling and Focused Ion Beam Induced Deposition (FIBID) deposition available in the same instrument, in-situ switching between subtractive and additive methods offers a high degree of flexibility for the fabrication of complex devices on the nanoscale.
The efforts are centered around the tungstenhexacarbonyl ($W(CO)_6$) precursor, which upon irradiation with a Ga^+-FIB, forms a deposit composed of mostly W and C. The resulting deposit forms a type-II superconductor with a critical temperature of approximately 4.5 K and can be patterned with a resolution of approximately 50 nm.
This work marks the first step on a path towards the bottom-up fabrication of SoL devices in a single-step procedure. We present prototypes of tungsten-based nanoSQUIDs patterned on both, conventional silicon chips and the top side of SPM cantilevers, prepatterned with gold contacts, and their respective magnetotransport characteristics.

Resumen

Fabrication of Tungsten-based NanoSQUIDs on Cantilever by means of Focused Ion Beam Induced Deposition

by Fabian Uwe Sigloch

La microscopía de sonda de barrido (Scanning Probe Microscopy, SPM) se ha convertido desde hace tiempo en una herramienta indispensable en la física del estado sólido para la caracterización y manipulación de una gran variedad de propiedades superficiales a escala nanométrica. En la microscopía de barrido SQUID (Scanning SQUID Microscopy, SSM), la resolución espacial de los métodos SPM se combina con la sensibilidad al flujo sin precedentes de un dispositivo de interferencia cuántica superconductora (Superconducting Quantum Interference Device, SQUID).

El SQUID-on-Lever (SoL) es una implementación emergente de SSM en la que el SQUID se coloca en la punta de una micropalanca SPM, combinando la sensibilidad del SQUID con el contraste topográfico y el control de la distancia punta-muestra de la microscopía de fuerza atómica (Atomic Force Microscopy, AFM). Para superar la alta relación de aspecto de la punta sobresaliente, se requieren técnicas de fabricación novedosas e innovadoras, lo que supone un desafío significativo para los métodos convencionales de nanofabricación basados en resinas.

El trabajo presentado en esta tesis doctoral contribuye a la iniciativa FIBSuperProbes, investigando el uso del procesamiento mediante un haz de iones focalizado (Focused Ion Beam, FIB) para la funcionalización de micropalancas SPM con estructuras superconductoras para la fabricación, entre otros, de sondas SoL. Con la posibilidad de realizar tanto fresado FIB como deposición inducida por haz de iones focalizado (Focused Ion Beam Induced Deposition, FIBID) en el mismo instrumento, la conmutación in situ entre métodos sustractivos y aditivos ofrece un alto grado de flexibilidad en la fabricación de dispositivos complejos a escala nanométrica.

Los esfuerzos se centran en el precursor hexacarbonilo de tungsteno ($W(CO)_6$), que, tras la irradiación con un FIB de Ga^+, forma un depósito compuesto principalmente de W y C. El depósito resultante forma un superconductor de

tipo II con una temperatura crítica de aproximadamente 4.5 K y puede ser modelado con una resolución de aproximadamente 50 nm.
Este trabajo marca el primer paso hacia la fabricación ascendente (bottom-up) de dispositivos SoL en un procedimiento de un solo paso. Presentamos prototipos de nanoSQUIDs basados en tungsteno, modelados tanto en chips de silicio convencionales como en la cara superior de micropalancas SPM, prepatronados con contactos de oro, junto con sus respectivas características de magnetotransporte.

Acknowledgements

It took thirty years to reach the point of submitting this doctoral thesis. Over the course of these years, many extraordinary people have crossed my path, each of them shaping the person I have become and playing a vital role in this achievement. To all of them, I extend my heartfelt thanks.

First and foremost, I thank my parents. Through highs and lows, they have always stood by me, offering unwavering emotional and financial support, and providing guidance when needed—always allowing me the freedom to make my own decisions and follow my own path.

I am deeply grateful to Jose Maria and Soraya for their early guidance, their teaching, and for introducing me to the scientific world. Their support was also essential during my initial arrival in Spain. Pablo was not only instrumental in helping me find my way around the lab but also a key source of ongoing technical discussions and support during my first days here.

Ruben and Alba, thank you for the stimulating exchange of ideas and for fostering such a warm and engaging office environment. Amaia, it was a pleasure to work closely with you—your insights into fabrication and characterization were invaluable.

My thanks go to the staff of the Laboratorio de Microscopias Avanzadas (LMA)—Isabel, Laura, Ruben, Lucía, and Mariano—for their help with microscopy and sample fabrication. I am also grateful to Ana and Eva for their assistance with low-temperature measurements in the PPMS system.

Special thanks to our collaborators in the FIBSuperProbes project, especially Julian and Dieter from the Eberhard Karls University of Tübingen. Your support in SQUID characterization, theoretical insights, and discussions were indispensable, not only for measurements carried out in your facilities but also for the interpretation of my own results.

To Christina, our department's secretary, thank you for all your help with bureaucracy, especially during the challenging first months after my arrival.

I also wish to thank Houssem and Panos for being close friends throughout the years—your company and support have meant a lot. Andrea and her wonderful circle of friends made me feel welcome in Zaragoza and shared with me the beauty of the surrounding mountains through many memorable hikes.

Finally, I am especially grateful to all my close friends back home for their enduring friendship and support across the distance. Yannik and Matthias deserve particular mention for always having my back. A special thank you to Yannik, as well, for his patience and understanding during the writing phase of this thesis while we worked together.
To all of you—thank you for being part of this journey.

Contents

List of Figures xi

List of Tables xv

1. Introduction 1
- 1.1. Nanoscience 3
  - 1.1.1. Motivation 3
  - 1.1.2. Optical Resolution 4
  - 1.1.3. Imaging with Charged Particles 5
  - 1.1.4. Scanning Probe Microscopy 10
- 1.2. Nanofabrication 15
  - 1.2.1. Resist-Based Techniques 15
  - 1.2.2. Direct-Write Techniques 18
  - 1.2.3. Comparison of Lithographic Techniques 27
- 1.3. Superconducting Quantum Interference Device 30
  - 1.3.1. Superconductivity 30
  - 1.3.2. Josephson Effect 34
  - 1.3.3. Superconducting Quantum Interference Device 39
- 1.4. The FIBSuperProbes Project 45
  - 1.4.1. Functionalization of Probes for Scanning Probe Microscopy 45
  - 1.4.2. Scanning SQUID Microscopy 46
- 1.5. Objective and Structure of this Thesis 48

2. Experimental Methods 51
- 2.1. Substrates 53
  - 2.1.1. Optical Lithography 53
  - 2.1.2. Electron Beam Lithography 54
  - 2.1.3. Standard Silicon Wafer 55
  - 2.1.4. Cantilevers 57
- 2.2. Nanofabrication with Focused Ion- and Electron Beams 59
  - 2.2.1. The Dual Beam System 59
  - 2.2.2. The $W(CO)_6$ Precursor 61
  - 2.2.3. Process Parameters 63

2.2.4. Transmission Electron Microscopy 64
2.3. Magnetotransport at Low Temperatures 67
2.3.1. Physical Properties Measurement System 67
2.3.2. Cryogen-Free Measurement System 69
2.3.3. Systems at the University of Tübingen 70

3. Cryogen Free Magnet Setup 73
3.1. The Cryostat 75
3.1.1. The Primary Circuit 75
3.1.2. The Variable Temperature Insert 76
3.2. Electronics 79
3.3. Operation 81
3.3.1. Preinstalled Interface 81
3.3.2. Development of a Custom Interface 81
3.3.3. User Guide 84
3.4. Testing the System 86
3.4.1. Cooldown 86
3.4.2. Electric Characterization 87
3.4.3. Magnetic Field 89
3.5. Summary 91

4. Ga^+-FIB for SQUID Fabrication 93
4.1. Deposition of Tungsten-based Nanostructures 95
4.1.1. Conditions on Cantilevers 95
4.1.2. Beam Current 97
4.1.3. Dwell Time 99
4.1.4. Deposition Rate 101
4.2. SQUID-Design Approaches 104
4.2.1. Long Nano-Bridges 104
4.2.2. Short Constrictions 108
4.2.3. SNS-Junctions 110
4.2.4. Deposition on Cantilevers 112
4.2.5. Incorporation of a Modulation line 113
4.3. Summary 116

5. SQUID Characterization 117
5.1. Long Nano-Bridge SQUIDs 119
5.1.1. Fabrication 119
5.1.2. Electrical Properties 120
5.1.3. Magnetic Properties 121

5.2. Short Constriction Junctions 126
5.2.1. First Generation 126
5.2.2. Second Generation 131
5.3. SNS Contacts 138
5.3.1. Fabrication 138
5.3.2. Electrical Properties 138
5.4. SQUID on Lever 141
5.4.1. Long-bridge SoL 141
5.4.2. Short-Constriction SoL 148
5.5. Summary 154

6. Conclusions and Outlook **157**
6.1. Cryogen Free Magnet System 159
6.2. Ga^+-FIBID for SQUID Nanofabrication 160
6.3. SQUID Characterization 162

7. Conclusiones y Perspectivas **165**
7.1. Sistema Criogénico Libre de Helio 167
7.2. FIBID con Ga^+ para Nanofabricación de SQUIDs 168
7.3. Caracterización de SQUIDs 170

Acronyms **173**

Symbols **177**

Bibliography **185**

Appendices **i**

A. Ga^+ FIBID for SQUID Fabrication **iii**
A.1. Thermal Diffusion iii
A.2. Dwell Time v
A.3. Deposition Rate vi
A.4. SQUID viii

B. SQUID Characterization **xi**
B.1. Long Nano-Bridge SQUIDs xi
B.1.1. The Cooldown Curve xi
B.2. Short-Constriction SQUIDs xiv
B.2.1. The Influence of the Reading Count xiv
B.2.2. Modulation of I_c xvi

B.3. SQUID on Lever xvii
B.3.1. Long-Bridge SoL xvii
B.3.2. Short-Constriction SoL xvii

List of Figures

1.1. Overview of the nanoscale. 3
1.2. Schematic representation of the Rayleigh criterion for resolution. 5
1.3. SEM Schematic and Beam Profile 7
1.4. Electron-Matter Interaction. 8
1.5. Ion-Matter Interaction 9
1.6. Lennard Jones Force and Operation Mode of an SPM 11
1.7. MFM Operation Mode 12
1.8. Approaches to SSM 13
1.9. Resist-based Lithography 16
1.10. Schematic illustration of the FIBID/FEBID process 20
1.11. Distinction of Deposition Regimes. 22
1.12. The dynamic of the deposition process. 25
1.13. Mechanisms of the generation of halo. 27
1.14. Comparison of the main lithography techniques. 28
1.15. Phase diagram of superconductivity 31
1.16. The characteristic lengths of a superconductor. 34
1.17. RCSJ model of a Josephson junction and the tilted washboard potential 36
1.18. Effect of noise in a Josophson junction. 39
1.19. Schematic illustration of a SQUID 40
1.20. Modulation of the critical current in a SQUID. 42
1.21. SQUID on Lever 46

2.1. First-generation chip design. 56
2.2. Second-generation chip design. 56
2.3. SEM micrograph of a cantilever from the side. 57
2.4. Layout of the apex of cantilevers. 58
2.5. The Helios Nanolab 600 Dual Beam system from Thermo Fischer 59
2.6. Schematic representation of a LMIS used for ion extraction. . . . 60
2.7. Schematic representation of different milling strategies. 65
2.8. The Physical Properties Measurement System. 68
2.9. Oscilloscope recordings of the current output of the Physical Properties Measurement System (PPMS). 69

2.10. Probe used in the liquid helium dewars. *Photography:* Julian Linek. 70
2.11. Image of the probe for the cryostat. *Photography:* Julian Linek. . 72

3.1. Main components of the CFMS 76
3.2. The Variable Temperature Insert. 77
3.3. The CFMS rack equipped with the measurement electronics. . . 80
3.4. The delivered and custom made breakout boxes. 80
3.5. The VTI control interface. 82
3.6. Main window of the custom user interface. 83
3.7. Experiment configuration in the custom interface. 84
3.8. Wiki of the CFMS. 85
3.9. Cooldown of the CFMS. 86
3.10. Temperature stability of the CFMS. 87
3.11. Electronic noise at too high helium pressure in the sample space. 88
3.12. Transport characterization of a SQUID in the CFMS after optimization. 89
3.13. Magnetic field stability and persistent mode of the CFMS. 90

4.1. Schematic representation of the diffusion conditions on large chips and cantilevers. 96
4.2. Ion Beam induced heating of substrates. 97
4.3. Evolution of the substrate temperature. 98
4.4. Impact of the contact material on the IV characteristics in a Superconducting Quantum Interference Device (SQUID) 99
4.5. TEM micrographs of a deposition series at various dwell times on a cantilever. 100
4.6. Deposition rate as a function of dwell time. 101
4.7. Influence of the dwell time on the critical temperature. 102
4.8. Comparison of the deposition rate on a large chip and an Scanning Probe Microscopy (SPM) cantilever. 103
4.9. Quantitative analysis of the deposition rate on a chip and a cantilever. 103
4.10. Schematic of the fabrication process of a long-bridge SQUID of 1st generation. 105
4.11. SEM micrographs of the fabrication process of a long-bridge SQUID. 106
4.12. Decreasing the inner loop area of a long-bridge SQUID of first generation. 106
4.13. Fabrication process of a long-bridge SQUID of second generation. 107

4.14. Fabrication process of a short-constriction SQUID of first generation. 109
4.15. Fabrication process of a short-constriction SQUID of second generation. 110
4.16. Schematic of the fabrication process of an Superconducting-Normal-Superconducting (SNS) SQUID. 111
4.17. SEM micrographs of SNS-SQUIDs. 112
4.18. Positioning of SQUIDs on cantilevers. 113
4.19. Design approaches for SQUIDs with a modulation line. 114

5.1. Scanning Electron Microscopy (SEM) micrographs of long-bridge SQUIDs. 119
5.2. Electric properties of long-bridge SQUIDs. 121
5.3. Magnetic properties of long-bridge SQUIDs. 122
5.4. SEM micrographs of long-bridge SQUIDs indicating the effective area. 122
5.5. Meta analysis of the $V(B)$ curves at constant I_{b}. 124
5.6. SEM micrographs of short-constriction SQUIDs with modulation lines. 126
5.7. IV characteristics of short-constriction SQUIDs with modulation lines. 128
5.8. Crtitical current modulation of a short constriction SQUID. 129
5.9. IV characteristics of SQUIDs in the facilities of Tübingen 130
5.10. SEM micrograph of a short-constriction SQUID of first generation. 131
5.11. Cooldown curve of a short-constriction SQUID of second generation. 133
5.12. IV characteristics of a short-constriction SQUID on a large substrate. 134
5.13. Voltage modulation of a first generation short constriction SQUID 135
5.14. Meta analysis of the voltage modulation of a first-generation short-constriction SQUID 136
5.15. Effective area of a short-constriction SQUID of second generation 137
5.16. SEM micrographs of an SNS SQUID. 138
5.17. Electric properties of an SNS SQUID. 139
5.18. SEM Micrographs of a long-bridge SQUID on a cantilever. 142
5.19. Superconducting properties of a long-bridge SQUID on a cantilever. 143
5.20. IV-characteristics of a long-bridge SQUID on a cantilever at 50 mT. 144
5.21. Voltage modulation of a long-bridge SQUID on a cantilever. . . . 145
5.22. Performance analysis of a long-bridge SQUID on a cantilever. . . 146
5.23. Effective area of a long-bridge SQUID on a cantilever. 147

5.24. SEM Micrographs of a short-constriction SQUID on a cantilever. 148
5.25. Superconducting properties of a short-constriction SQUID on a cantilever. 149
5.26. IV-characteristics of a short-constriction SQUID on a cantilever at 50 mT. 150
5.27. Voltage modulation of a short-constriction SQUID on a cantilever. 151
5.28. Performance analysis of a short-constriction SQUID on a cantilever. 152
5.29. Effective area of a short-constriction SQUID on a cantilever. . . . 153

A.1. Failed deposition process of an SQUID on Lever (SoL). v
A.2. SEM micrographs of a deposition rate experiment on a chip and a cantilever, analyzed in a SEM. vi
A.3. Comparison of the deposition rate on a chip and a cantilever. . . vii
A.4. SEM micrograph of a long-bridge SQUID of first generation on an SPM cantilever. viii
A.5. SEM micrographs of the constrictions of a short-constriction SQUID of second generation. viii
A.6. SEM micrograph of an SNS-SQUID before deposition of the metallic W-C ix

B.1. In-depth analysis of the cooldown curves of long-bridge SQUIDs. xi
B.2. IV characteristics of long-bridge SQUIDs analyzed with various filters. xii
B.3. IV of a short-constriction SQUID of second generation at 1, 10, 25 readings xiv
B.4. Field dependence of I_c for a short-constriction SQUID. xvi
B.5. Field dependence of I_c for a long-bridge SoL. xvii
B.6. Field dependence of I_c for a long-bridge SQUID on a cantilever. . xvii

List of Tables

1.1. Yield of various electron-/ion-sample-interaction mechanisms. . . 19
1.2. Overview of SQUID development. 44

2.1. Reported properties of W-C fabricated by means of Ga^+ Focused Ion Beam Deposition (FIBID). 62

4.1. Nominal and measured distances in SQUIDs structures with low inner loop areas. 107

5.1. Analysis of the modulation depth of a short-constriction SQUID. 129

Chapter 1

Introduction

Contents

1.1. Nanoscience 3
1.1.1. Motivation 3
1.1.2. Optical Resolution 4
1.1.3. Imaging with Charged Particles 5
1.1.4. Scanning Probe Microscopy 10
1.2. Nanofabrication 15
1.2.1. Resist-Based Techniques 15
1.2.2. Direct-Write Techniques 18
1.2.3. Comparison of Lithographic Techniques 27
1.3. Superconducting Quantum Interference Device 30
1.3.1. Superconductivity 30
1.3.2. Josephson Effect 34
1.3.3. Superconducting Quantum Interference Device 39
1.4. The FIBSuperProbes Project 45
1.4.1. Functionalization of Probes for Scanning Probe Microscopy 45
1.4.2. Scanning SQUID Microscopy 46
1.5. Objective and Structure of this Thesis 48

1.1. Nanoscience

1.1.1. Motivation

On a daily basis, we are used to thinking in the *macroscopic scale*, that is objects of size and distance that are visible to the naked eye, down to a size of 100 µm[1] [1]. With the invention of magnifying instruments in the late 16th century [2], these limits were pushed in both, astronomy via telescopes [3] and biology via the first compound microscopes [2].
Obtaining accessibility to the *microscopic scale* and later the *nanoscale* revealed the extent to which our lives are governed by objects, organisms, and effects that are too small for direct observation without technical assistance. Ever since, the pursuit to push the resolution limit has been ongoing, culminating in Richard Feynman's famous talk "There's Plenty of Room at the Bottom" in 1959 [4] where he envisioned the manipulation of matter on the atomic scale. The field of *nanotechnology* emerged with the invention of the Scanning Tunneling Microscope (STM) in 1981, realizing Feynman's vision in 1989 by manipulating individual atoms [5]. Figure 1.1 provides a schematic overview of objects and organisms at the nanoscale.
Although not directly accessible, nanotechnology is governing modern day life. The quantum mechanical effects dominating on the *nanoscale* are at the base.

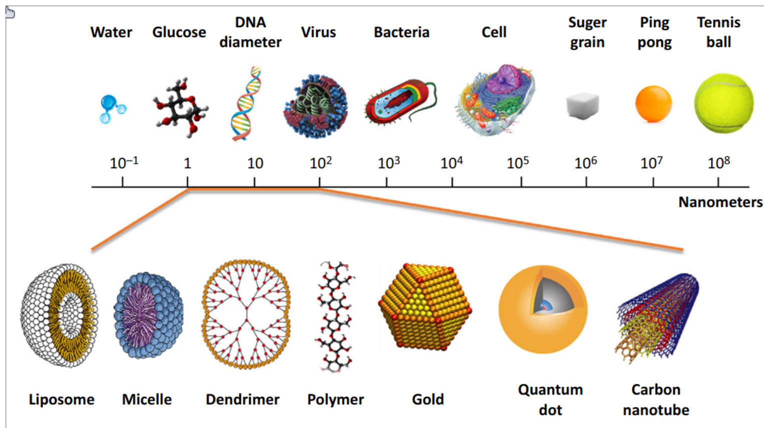

Figure 1.1.: Schematic illustration of the plethora of wondrous phenomena impacting daily life ranging from human perception down to the sub-nanometer regime. Reprinted from [6].

[1]The resolution limit of the naked eye is approximately one arcminute [1], corresponding to 100 µm at 25 cm distance.

1.1.2. Optical Resolution

The observation of effects on a small scale has long surpassed the use of visible light as the primary method to investigate the rich physics at these dimensions. Any optical system consists of lenses with finite apertures, resulting in diffraction of the incoming light, described by the Point Spread Function (PSF). The PSF for an ideal diffraction-limited optical system produces an image described as the *Airy pattern* [7], from which the *Rayleigh criterion* [8] is derived. The Rayleigh criterion states that two point-like emitters can just be resolved if the center of the Airy disk of one image coincides with the first minimum of the other (fig. 1.2). For optical microscopes, this results in a resolution limit of

$$\delta_r = \frac{0.61\lambda}{\mathrm{NA}} \approx \frac{\lambda}{2\mathrm{NA}} \; , \tag{1.1}$$

where δ_r is the minimum resolvable distance, λ is the wavelength of light, and NA is the numerical aperture of the optical system.
With violet light at $\lambda = 400\,\mathrm{nm}$, the shortest visible wavelength, the resolution limit for *classical* optical microscopy is approximately 200 nm. Highly sophisticated methods, such as super-resolution microscopy, report values down to 20 nm. [9]
To improve the spatial resolution of optical microscopy, other technologies emerged. In 1939, the first enlarged image generated by X-rays was captured [10]. X-ray microscopy became a practical tool for material scientists in the 1970s, enabled by the development of synchrotrons to generate highly coherent X-ray radiation [11]. X-ray microscopy achieves higher resolution due to the shorter wavelengths, typically in the range of 0.1 nm to 10 nm. Challenges in this approach arise from the interaction of X-rays with matter, which necessitates novel focusing methods and imaging techniques. Unlike optical systems, the resolution of X-ray microscopy is predominantly limited by *aberrations*, rather than the Rayleigh criterion for the diffraction. [12]
The development of electron optics began in the early 20th century, culminating in the construction of the first Transmission Electron Microscopy (TEM) in 1931 by M. Knoll and E. Ruska [13], followed in 1937 by the first SEM developed by M. v. Ardenne [14]. For electrons, the wavelength is determined by the acceleration voltage of the beam, reaching down to 7 pm at 30 kV in SEM and 2 pm at 300 kV in TEM. Similar to X-ray microscopy, the resolution is limited by aberrations of the optical system rather than by diffraction [15]. The field of electron and ion optics is discussed in detail in section 1.1.3.

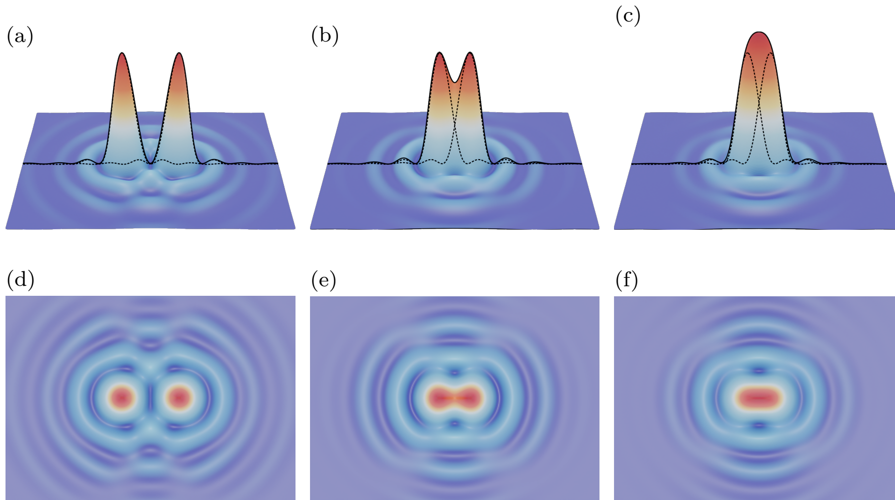

Figure 1.2.: Schematic representation of the Rayleigh criterion $\delta_r \approx \lambda/2\mathrm{NA}$. (a, d) The center of the PSF of two distinct point emitters are in a distance $d > \delta_r$ and are clearly resolved. (b, e) depict the limit of resolution $d = \delta_r$ according to the Rayleigh criterion where the minimum of one of the PSFs disks coincides with the maximum of the other and vice versa. (c, f) The objects are in a distance $d < \delta_r$ and cannot be resolved.

In the late 20th century, the field of microscopy was augmented by SPM. The availability of piezoelectric actuators and powerful computers enabled the precise controlling of the vertical and lateral position of a sharp probe on a given surface with subatomic precision. Pioneered by STM in 1981 at IBM [16], other probes soon emerged to exploit a large range of physical effects, generating false-color images of the *mode* measured by the respective probe [17]. Techniques in SPM relevant to this thesis are introduced in section 1.1.4.

1.1.3. Imaging with Charged Particles

In contrast to electromagnetic waves, charged particles such as electrons and ions cannot be focused by simple glass lenses. Instead, the path of a beam of charged particles is influenced by electric and magnetic fields, described within the framework of *electron optics*. The principles of electron optics are directly applicable to ions, differing only in polarity of the charge and the charge-to-mass ratio [18].

Beam Formation

At the beginning of the beam formation process in electron- and ion optics, charged particles are extracted from a *source* and accelerated to a given velocity by the *extraction electrodes*. Figure 1.3a illustrates the schematic composition of a basic scanning electron or ion microscope.
To source electrons, a V-shaped filament, or *cathode*, made of a durable material such as tungsten (W) or lanthanum hexaboride (LaB_6), is set at a high negative potential. To overcome the work function, they can be thermally excited via *thermionic emission*. Applying an electric field reduces the work function through the *Schottky effect*, enabling *Schottky emission* at lower temperatures. If the strength of the electric field at the apex of the tip is sufficiently strong, thermal excitation is no longer required, and electrons can overcome the reduced work function via tunneling. The process is referred to as *field emission*. [19]
Sourcing ions is typically achieved by either Liquid Metal Ion Sources (LMISs) or Gas Field Ion Source (GFIS). In LMIS, a reservoir holding the source material is heated to liquefy the metal. Below the reservoir, a sharp needle is wetted by the liquefied metal, which forms a *Taylor cone*, acting as an effective source with a diameter of approximately 2 nm. At the apex of the cone, the electric field generated by the *extraction electrodes* reaches magnitudes of 10 V/nm, leading to Field Evaporation (FEV) [20]. For ionizing gaseous atoms such as helium (He), neon (Ne), etc., the Taylor cone mechanism used for liquefied metals cannot be exploited to form a small effective source. Instead, the apex of a tungsten tip is shaped into either a single atom or a trimer, which acts as the source. While a single atom is favorable for achieving high resolution, it is unstable, and the trimer is preferred for practical applications. The emission occurs from gaseous atoms injected near the positively charged tip, where they ionize at the apex [21].
Both electrons and ions are electrostatically accelerated to the desired velocity and focused into a small spot by one or more *condenser lenses*. An array of apertures with varying diameter is used to cut off parts of the beam, thereby controlling the beam current.
In Focused Ion Beam (FIB) and SEM *Scanning coils* deflect the focused beam in plane to raster the beam — focused to a small spot by the *objective lens* — across the surface of a bulk sample. In TEM, a broad beam passes through an electron-transparent specimen and is subsequently focused by the objective lens. Scanning Transmission Electron Microscopy (STEM) combines both techniques, using a focused beam scanned across an electron-transparent sample, with the

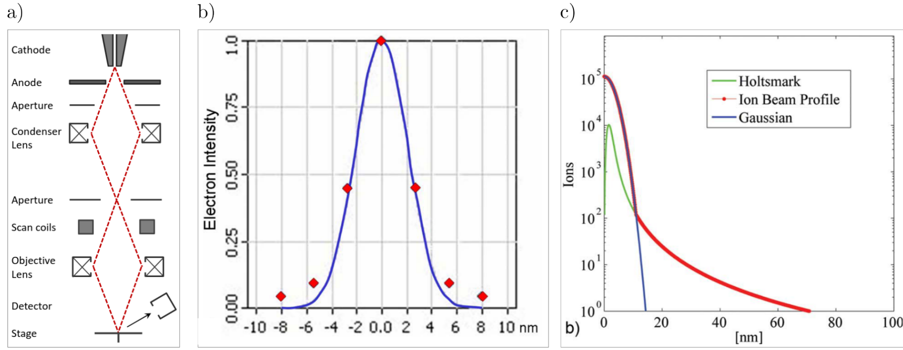

Figure 1.3.: (a) Schematic representation of the column of an electron or ion microscope. The red line denotes the outer contour of the cone of the charged particles that are generated in the Cathode and focused to a tiny spot on the specimen. Reprinted from [25]. (b) Radial distribution of the intensity in an electron beam representing, modeled by a Gaussian distribution [22]. (c) Radial intensity distribution of an ion beam. In addition to the Gaussian profile, a tail modelled by a Holtsmark function extends reaches further from the center. Reprinted from [23].

signal collected beneath. Additional elements such as a beam blanker and aberration correctors, can also be included in the column. [19]
In SEM and FIB systems, the purpose of the objective lens is to focus the beam to a finite spot that is as small as possible. The electron distribution per unit area around the center of the beam is given by [22]

$$f\left(r\right)=\underbrace{\frac{I_{\mathrm{B}}/\mathrm{e}_0}{2\pi\sigma_{\mathrm{N}}}}_{f_0}\exp\left(-\frac{r^2}{2{\sigma_{\mathrm{N}}}^2}\right) \quad , \tag{1.2}$$

where I_{B} denotes the electron beam current, e_0 is the elementary charge and σ_{N} is the standard deviation of the normal distribution. Several definitions of the beam diameter exist, with the Full Width Half Maximum (FWHM) and the width at $1/\mathrm{e}^2$ being the most common. For ion beams, Coulomb repulsion within the beam plays a more significant role, leading to an additional low-intensity tail [23]. The tail can be modelled as a Holtsmark distribution [24]. The beam distribution functions of electron and ion beams are shown in fig. 1.3.

Image Formation

The processes underlying image formation in bulk and transparent samples are fundamentally different. Here, we focus on the interaction of charged particles

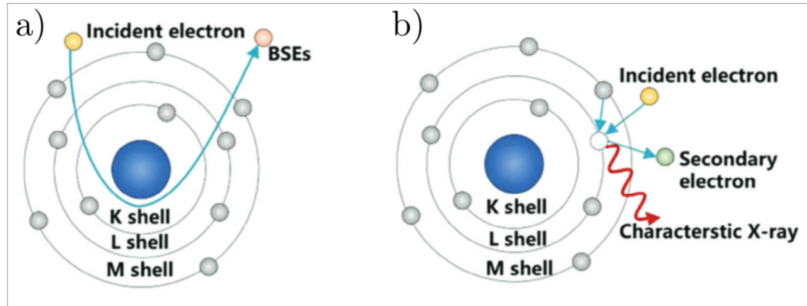

Figure 1.4.: Different interaction mechanisms of electrons with matter. (a) Elastic scattering of an incident electron with the positive potential of the nucleus results in a Back Scattered Electron (BSE). (b) Inelastic scattering of an incident electron with the electron shell results in a Secondary Electron (SE). Upon relaxation of an electron in a higher shell a characteristic X-ray is emitted. Reprinted from [27].

with bulk samples. For an introduction to the image formation in TEM and STEM, see, for example, Reimer and Kohl[15].
When the highly energetic, charged particles in FIB and SEM systems strike the surface of a bulk sample, they transfer their energy to the sample via random scattering events within a teardrop-shaped *interaction volume*. For electrons, elastic scattering due to the interaction of Primary Electrons (PEs) with the positively charged nuclei results in the emission of highly energetic Back Scattered Electrons (BSEs). Inelastic scattering with the electron shell of the target atoms produces low-energy ($E_{\mathrm{kin}} \leq 50\,\mathrm{eV}$) Secondary Electrons (SEs), leaving an unoccupied electronic state in the atom. When a higher-level electron relaxes to fill the vacant state, a characteristic X-ray is emitted. [26]
All these signals can be used to generate a false-color image by correlating the signal intensity with the lateral position of the beam. For imaging, SEs are commonly collected, as they originate near the surface, providing high topographic contrast. X-rays, on the other hand, are rarely used for imaging but contain valuable information about the chemical composition of the specimen. The energy of each photon corresponds to the energy difference between the vacant state and the state from which an electron relaxes. In Energy Dispersive X-Ray Spectroscopy (EDXS), this characteristic energy is attributed to the element from which the transition arises. [26]
In the case of ions, most of the energy is transferred via elastic scattering with nuclei. The impinging ion transfers parts of its momentum to a stationary atom in the sample, potentially displacing it. The displaced atom, as well as the impinging ion, can subsequently displace further atoms, leading to a *collision*

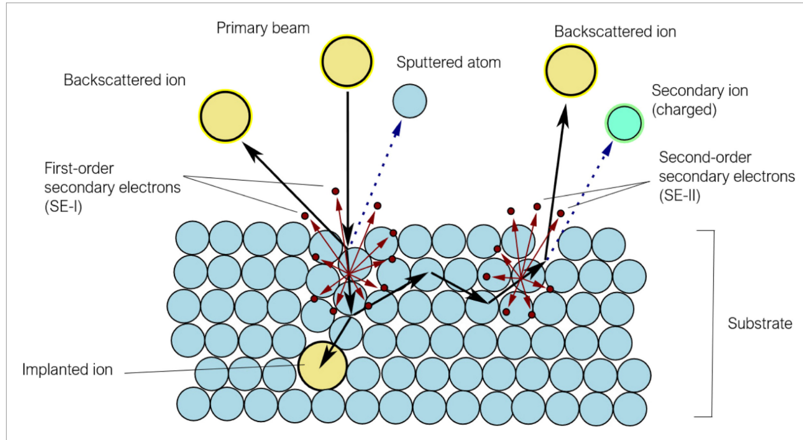

Figure 1.5.: Schematic representation of different types of ion-matter interaction. The heavy ions result in dislocation and emission of target atoms and ions in addition to the electronic interactions in electron-ion-interaction. Reprinted from [28].

cascade and resulting in *amorphization* of the target. An impinging ion that comes to rest within the substrate results in *ion implantation*.
If, after a scattering event, the momentum is directed towards the surface and the energy is sufficiently high to overcome the surface binding energy, the primary ion leaves the substrate as a *backscattered ion*. The same applies to displaced substrate atoms, which can result in *sputtered atoms* or Secondary Ions (SIs). Both processes contribute to *ion milling*, while SIs can also be used for imaging or spectroscopy. [29]
Inelastic scattering events result in the production of phonons, plasmons, and SE. SEs are categorized in *first order* (SE_{I}) and *second order* (SE_{II}) SEs. First order SEs are generated within the area of primary irradiation, while second order SEs are produced by displaced substrate atoms or primary ions scattered into a region outside primary irradiation area. While SIs can be used for imaging, the yield of SEs is $10\times$ to $1000\times$ higher, making this the primary method of imaging in FIB. [29]
The detection of SEs is primarily achieved with an Everhart-Thornley-Detector (ETD) [30]. The detector is positioned inside the process chamber above the specimen. It consists of a scintillator held at high positive voltage to accelerate incident electrons, converting them into photons. These photons are guided outside the chamber and amplified using a photomultiplier. Discrimination between low energy SEs and highly energetic BSEs or massive SIs is accomplished with a Faraday cage surrounding the scintillator. The cage is maintained at a

low positive voltage, attracting SEs while largely ignoring by highly energetic particles. [26]

1.1.4. Scanning Probe Microscopy

Since the invention of STM in 1981 [16], a plethora of scanning probe techniques have emerged. These methods share a common principle: they use piezoelectric actuators to raster scan a sharp probe across a surface. Operation is done in either *constant height* or *constant interaction mode*.
In constant height mode, the vertical position d_z is kept fixed, and the signal of the investigated mode is collected directly. This approach requires sufficiently flat surfaces and a sample inclination of 0°, conditions that are often not met. In constant interaction mode, a feedback loop continuously adjusts the vertical position of the probe to maintain a constant interaction signal. This minimizes the risk of crashing the sensitive tip into the sample and compensates for surface inclination.
The spatial resolution of all SPM methods is primarily determined by the size of the apex of the probe tip. The signal obtained is a convolution of the shape of the tip and the substrate. [17]

Atomic Force Microscopy

Atomic Force Microscopy (AFM) is, alongside STM, one of the flagship of methods in the family of SPM techniques. Introduced in 1986 [31], AFM uses a non-magnetic, insulating tip to raster scan a surface and measure its topography. Probes terminating in a single atom at the apex are capable of achieving atomic resolution [32].
The tip-sample interaction is ideally modelled by the Lennard-Jones force:

$$F_{\mathrm{LJ}}(d_z) = -\frac{6A}{{d_z}^7} + \frac{12B}{{d_z}^{13}} \ . \tag{1.3}$$

The term $6A/{d_z}^7$ models the attractive *van der Vaals* force at distances $d_z \lesssim 10\,\mathrm{nm}$, while $12B/{d_z}^{13}$ accounts for the strong repulsive force due to the overlap of electronic orbitals between the sample and the tip atoms (Pauli exclusion principle) at distances $d_z \lesssim 1\,\mathrm{Å}$.
The setup of an AFM is illustrated in fig. 1.6b. A stiff cantilever with a protruding tip is positioned above the surface to be investigated. The back of the cantilever is irradiated by a laser beam, with its reflection captured by a horizontally split photo diode. Forces exerted by the surface on the tip cause the cantilever to bend, altering the intensity measured by the two halves of the detector. [17]

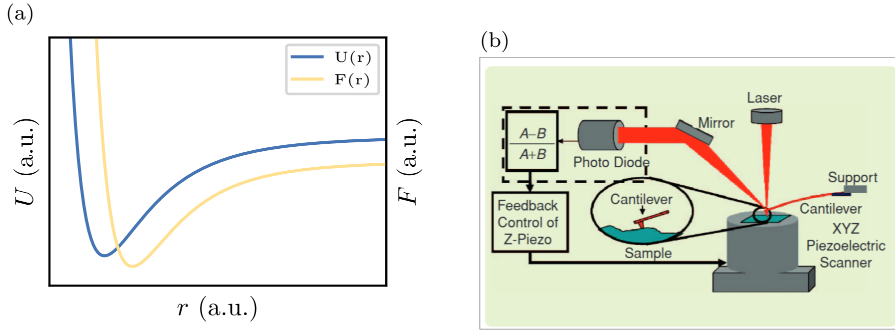

Figure 1.6.: (a) Schematic illustration of the force and potential of a surface. When approaching, an attractive van der Waals force acts. At close proximity, the Pauli exclusion principle gives rise to a strong repulsive force. (b) Schematic illustration of an AFM setup. As the cantilever scans the surface, the forces acting on the cantilever result in its bending. As a consequence, the reflection of the laser is shifted and the intensity distribution in the split photodiode changes. Reprinted from [17]

Magnetic Force Microscopy

One year after the development of the first AFM, the first Magnetic Force Microscopy was built [33]. An AFM probe was modified with a ferromagnetic coating to raster scan a magnetic sample. The magnetic stray field of the sample surface exerts a long-range magnetic force [34, 35]

$$\boldsymbol{F} = \mu_0 \left(q + \boldsymbol{m} \cdot \nabla \right) \boldsymbol{H} \propto \frac{1}{{d_z}^2} \,, \tag{1.4}$$

superimposing the atomic Lennard Jones force. The measured signal corresponds to a shift in frequency of the cantilever oscillation, which does not distinguish between magnetic and atomic forces. Since the atomic force decays more rapidly, measurements at larger tip-sample distance are straight forward to analyze. However, for high spatial resolution and magnetic field sensitivity, the tip-sample distance must be minimized, making signal interpretation reliant on prior knowledge of the topography.
Figure 1.7 illustrates the most common mode of operation in Magnetic Force Microscopy (MFM) for obtaining both magnetic and topographic signals. More sophisticated operation modes and interaction models are reviewed in [35].
Another crucial factor for the resolution in MFM is the probe itself. Conventional probes are simply AFM probes magnetized with a ferromagnetic thin-film coating. A variety of approaches have been pursued to enhance the spatial and field resolution of MFM by fabricating more sophisticated probes. The current highest reported resolution is 10 nm, achieved with a commercial AFM probe

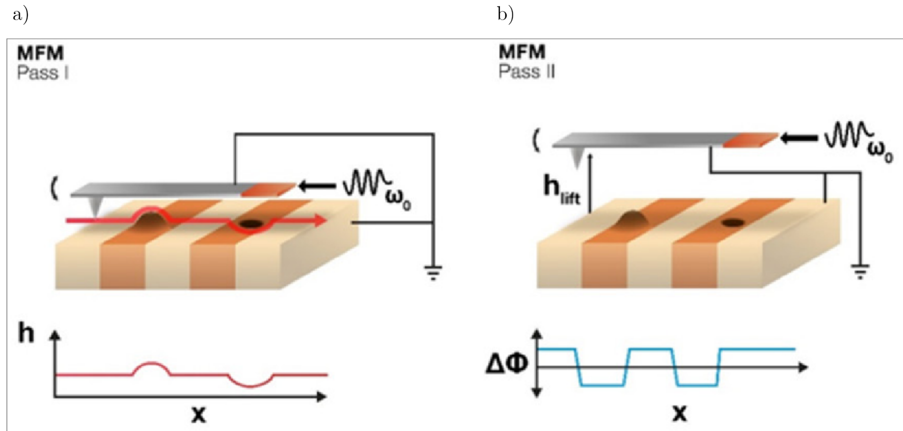

Figure 1.7.: Schematic illustration of the common operation mode of a MFM. (a) In a first scan in close proximity to the surface, the short-range forces dominated by the topographic mode is measured. (b) In a second scan in bigger height, the long-range magnetic mode is measured. Reprinted from [35].

magnetized by a magnetic nanopillar grown on the apex via Focused Electron Beam Deposition (FEBID) [36, 37]. The functionalization of AFM probes via FEBID is reviewed in [38].
The magnetic force, and thus the signal measured in MFM, is a convolution of the magnetic stray field of the sample and the magnetic properties of the tip superimposed with the convolution of the topography and the shape of the tip. Quantitative analysis of the signal is therefore complex and requires sophisticated modeling, making it challenging to provide a unified *field sensitivity*. Additionally, the magnetic field of the probe itself can influence or even alter the magnetization of the sample and vice versa [35].

Scanning SQUID Microscopy

A different approach to characterizing the magnetic stray field of a given surface is Scanning SQUID Microscopy (SSM). A SQUID is a magnetic field sensor with unprecedented magnetic field sensitivity. Its fundamental design is a superconducting loop interrupted by two Josephson Junctions (JJs), acting as a flux-to-voltage transducer. A comprehensive introduction to SQUIDs will be given in section 1.3.3.
In Scanning SQUID Microscopy (SSM), the SQUID or an attached pickup loop is scanned across the surface to map the magnetic stray field (fig. 1.8). To maintain superconductivity, the microscope or just the SQUID must be cooled below the critical temperature of the superconducting structure.

The lateral resolution of SSM is primarily determined by the size of the pickup loop and its distance to the surface. With ongoing advancements in lithographic methods (section 1.2.1), the size of the SQUID could be reduced down to $(200 \times 200)\,\text{nm}^2$ [40]. However, in conventional SSM, the SQUID is placed on a large, planar substrate, leading to lateral resolutions typically in the range of 1 µm [41].
The state-of-the-art is the SQUID on Tip (SoT) method, developed in 2010 [42]. In this technique, the superconducting material is deposited onto the tip of a pulled quartz tube via a multistep evaporation process. SQUIDs with loop sizes of down to 40 nm in diameter have been used to scan a surface at distances as close as 10 nm, controlled using a quartz tuning fork [43]. Although the authors do not directly report spatial resolution, it is presumably below 200 nm, based on 200 nm reported for a SoT probe with a SQUID diameter of 245 nm [44].
The magnetic field sensitivity is solely determined by the SQUID properties and will be discussed in section 1.3.3. The magnetic field is measured as an electric voltage arising purely from the magnetic stray field, making signal interpretation straightforward. However, the lack of sensitivity to surface topography complicates probe-to-sample distance control and increases the risk of crashing the tip into the sample.

Other SPM Methods

In addition to the SPM methods introduced here, a plethora of other probes have been developed, each specialized on measuring specific sample properties. STM probes the local density of states by measuring the tunneling current between a surface and a tip at a given voltage [16]. In Kelvin Probe Force Microscopy (KPFM), the work function of a sample is measured [45]. Near-field

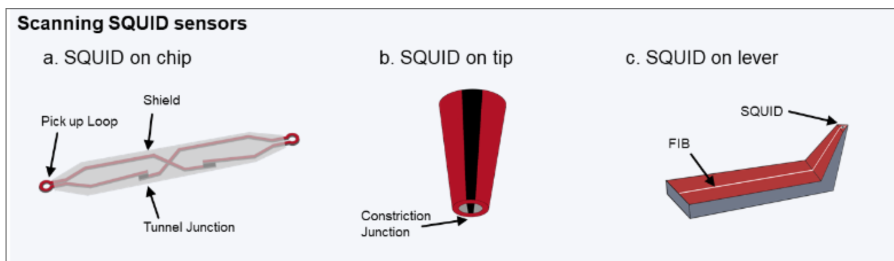

Figure 1.8.: Schematic illustration of different approaches to SSM. (a) In classic SSM, the SQUID is placed on a planar chip. (b) In SQUID on Tip (SoT), the SQUID is located at the apex of a pulled quartz tube. (c) In SQUID on Lever (SoL), an SPM cantilever is functionalized by addition of a SQUID sensor. Reprinted from [39].

Scanning Optical Microscopy (NSOM) overcomes the resolution limit associated to the *far field* of light by exploiting *evanescent waves* in the *near field*. A lateral resolution of 6 nm has been reported [46].
In correlative microscopy, optical, electron and scanning probe techniques are combined to measure several modes simultaneously, providing deeper insight into the properties of a sample [47]. For instance, the simultaneous measurement of SEM and AFM images has been demonstrated [48].
Beyond imaging, SPM techniques have also been used to manipulate matter on the atomic scale, fulfilling Feynman's vision [49]. Notable demonstrations include the visualization of the eigenstates of a quantum corral constructed of 48 Fe atoms on a Cu(111) surface [50], and the stop-motion movie "A Boy And His Atom"[2], made by manipulating individual CO molecules on a Cu substrate [51]. Both examples utilized STM.

[2] Online access to the video: https://www.youtube.com/watch?v=oSCX78-8-q0

1.2. Nanofabrication

At the core of any nanotechnology project lies the nanofabrication process — the foundation upon which innovative devices and materials are built. Nanofabrication enables the creation of structures with tailored electric, magnetic, optical and mechanical properties on the nanoscale. In this section, we focus on the nanofabrication techniques most relevant to this thesis and assess their specific use cases.

In section 1.2.1 we will briefly introduce resist-based lithographic techniques such as Optical Lithography (OL) and Electron Beam Lithography (EBL), which remain the gold standard for large-scale patterning. These methods excel in creating high-precision, reproducible structures over extensive areas. However, they rely on masks (Optical Lithography (OL)) and resists (both, OL and Electron Beam Lithography (EBL)), which increase process complexity, and they are generally limited to large, flat substrates limiting their adaptability for unique and irregular geometries.

In section 1.2.2, we turn towards direct-write techniques, namely Focused Electron/Ion Beam Induced Deposition (FEBID/FIBID) and Focused Ion Beam (FIB) Milling. These approaches stand out for their ability to directly write nanostructures — both additive and subtractive — without requiring masks or resists. This flexibility enables the integration of multiple functionalities into a single fabrication step, and the creation of structures on non-planar or unconventional substrates.

1.2.1. Resist-Based Techniques

Resist-based lithographic techniques represent one of the most common approaches in nanofabrication. These methods employ a Photo Resist (PR) — a polymeric material whose solubility in a developer changes upon irradiation with photons or electrons.

The process begins with the deposition of the target layer on a substrate, which is then coated with a PR via *spin coating*. In a first step, localized *exposure* of the resist alters its solubility according to the desired pattern. In the second step, the resist is partially *developed*, meaning the exposed (or unexposed) portions are removed with a suitable solvent. This leaves certain areas of the target layer exposed while others remain protected by the polymeric film, forming a mask of the desired pattern. In a third step, *etching* is used to remove the target layer in the exposed regions down to the substrate. Once the residual resist is removed, the target layer with the desired pattern remains. An overview of the lithographic process using etching is shown in fig. 1.9a.

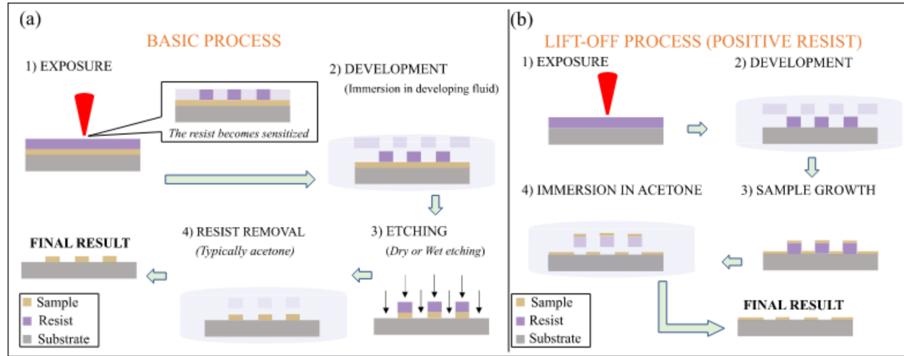

Figure 1.9.: Schematic illustration of resist-based lithography. (a) In the basic process, the target layer is directly applied to the substrate and covered by the photoresist. (1) The photoresist is locally exposed to phonons or electrons, altering its solubility. (2) A solvent is used to develop the structure, removing the exposed (*positive resist*) or unexposed (*negative resist*) parts. (3) The exposed parts of the target layer are removed via etching. (4) The resist is removed and the final structure remains. (b) In the lift-off process the photoresist is directly applied to the substrate and step (1) and (2) are performed the same way as in the basic process. (3) The target layer is deposited on top of the resist and the exposed substrate. (4) During lift-off, the target layer in direct contact with the substrate remains. Reprinted from [28].

Alternatively, rather than depositing the target layer before lithography the PR can be applied directly to the substrate, and the desired structure is deposited after development. In this variation, removing the PR mask with a solvent will *lift-off* the material on top of the resist, leaving only the material directly adhering to the substrate. A schematic overview of the lift-off process is shown in fig. 1.9b.

Optical Lithography

In OL, exposure is performed using UltraViolet (UV) light, with the resolution largely dependent on the wavelength of the light. The light passes through a prefabricated photomask, designed according to the desired pattern. A full wafer is exposed simultaneously, processing hundreds of identical structures in parallel. The high throughput makes OL the preferred technology for industrial applications [52].
The mask aligners commonly available in scientific laboratories use Hg lamps and LEDs that achieve resolutions in the range of 1 µm. In contrast, the steppers used in industrial applications target a resolution in the 10 nm range [28]. The

latest Extreme UltraViolet (EUV) equipment by the company ASML, with wavelength of 13.5 nm, has allowed to fabricate microchips with 8 nm resolution for the most advanced nodes [53].

Electron Beam Lithography

For scientific applications, throughput is often less important than achieving high resolution and flexibility. In EBL, the resist is patterned using electrons in a SEM. Resolutions of 100 nm are routinely achieved, and sub-10 nm fabrication has been reported [54].
Unlike OL, where entire wafers are exposed simultaneously, EBL is a serial process in which the electron beam raster scans the electron-sensitive resist to write the desired pattern. This inherently slower process limits scalability for industrial applications. For scientific applications, however, the elimination of photomasks combined with the high resolution provides the flexibility needed to fabricate low quantities of high-quality samples [28]. Furthermore, the ongoing development of multibeam systems aim to improve the throughput [55].

Nanoimprint Lithography

In NanoImprint Lithography (NIL) the pattern transfer is achieved through the pressure applied by a mold containing the desired design onto a thin resist layer coated on a substrate. The resist is deformed by the mold, and by applying heat or UV light, the resist is solidified, following etching and resist removal, the sample retains a pattern complementary to that of the mold.

Characteristics of Nanoimprint Lithography:

- **Resolution:** The technique's resolution depends heavily on the quality and fabrication of the mold. As nanolithography methods are used to create the mold, its features can reach dimensions as small as a few nanometers.
- **High Throughput:** With the appropriate mechanical systems, NIL enables the simultaneous imprinting of large areas, making it a highly efficient process.
- **Additional Processing:** Extra steps, such as residual resist removal, may be necessary to achieve a clean transfer.

Despite its ability to achieve both high resolution and high throughput, NIL is primarily utilized in niche applications, such as creating smart surfaces for biotechnology, due to its specialized requirements. [56]

1.2.2. Direct-Write Techniques

Direct-write lithographic techniques obliterate the need for a resist. The most significant approaches in this field are Focused Ion Beam milling for material removal and Focused Electron / Ion Beam Induced Deposition (FEBID / FIBID) for material deposition. The interaction mechanisms of electrons and ions, introduced in section 1.1.3 for imaging purposes, are similarly exploited for nanofabrication.

Focused Ion Beam Milling

In FIB, the sputtering effect of ions is harnessed for *ion milling*, subtractive lithography process with a resolution in the 10 nm range [57]. During ion milling, the ion beam is scanned across the surface according to a predefined pattern. The sputter yield (γ_S) scales with the mass of the ions used, while resolution generally improves with decreasing mass [28]. Due to the stability and ease of use of Ga^+ LMIS, Ga^+ ions to this day dominate the field. Nevertheless, developments in recent years have broadened the range of available ions. GFIS systems now enable the use of noble gases such as He^+, Ne^+, and Xe^+ [58], while Liquid Metal Alloy Ion Sources (LMAISs) facilitate *in situ* switching between a wide range of ions, from Li^+ and Bi^+ [59].
The vertical sputter rate for a beam at normal incidence can be calculated as

$$R_S\left(r\right) = \gamma_S \frac{M_{mol}}{\rho_{mol} N_A e_0} \;, \tag{1.5}$$

where M_{mol} and ρ_{mol} are the molecular mass and density of the target material, and N_A is the Avogadro constant. The sputter yield (γ_S) depends on the type of ions, their acceleration voltage, and the target material. Many common systems are thoroughly investigated experimentally [22], and new systems can be simulated using the Stopping and Range of Ions in Matter (SRIM) simulation tool [60].

Focused Ion / Electron Beam Induced Deposition

Additive direct-write nanolithography can be achieved using FIBID or FEBID. The chamber of the FIB or SEM is equipped with a Gas Injection System (GIS) to deliver a gaseous *precursor* to the sample. The precursor gas consists of molecules containing the targeted element and organic components. These molecules physically adsorb onto the substrate, forming a monolayer. Once adsorbed, the molecules exist in a dynamic equilibrium of adsorption and desorption on the surface [28].

Table 1.1.: Yield of Secondary Electrons (SEs), Excited Surface Atoms (ESAs) and Sputtered Atoms (SAs) for Ga^+ and e^- ions at 30 kV and 5 kV acceleration on a Si substrate.

	V_{el}, V_{Ion} (kV)	γ_{SE} [61]	γ_{ESA} [22]	γ_{S} [22]
Ga^+	30	3.3	5.5	2.6
e^-	30	0.15		
Ga^+	5	2.5	4.3	1.7
e^-	5	≈ 0.5		

Precursor Dissociation: Upon local irradiation with a focused electron or ion beam, the molecules dissociate into a non-volatile part and volatile by-products. While the volatile constituents are removed by the instrument's vacuum system, the non-volatile components, often metallic, remain on the surface as a deposit. The process is schematically illustrated in fig. 1.10. To form a deposit in the desired pattern, the beam is traced across the surface following the given pattern while fresh precursor gas is constantly supplied by the GIS.
The dissociation of precursor molecules is a complex process that has yet to be quantitatively modeled. In FEBID, the decomposition is mainly driven by the low energy SEs and the highly energetic PEs [62]. In FIBID, SEs and Excited Surface Atom (ESA) are identified as primary contributors to the deposition process [22]. Table 1.1 lists the yield of SE and ESA for electrons and gallium ions at commonly used beam energies. The higher yield of SEs and the additional generation of ESA in FIBID makes it the faster process, allowing one to run it at lower beam currents. However, the simultaneous sputtering of the substrate material and the fresh deposit in FIBID must be taken into account. For a simplified model, the decomposition of the Tungsten Hexacarbonyl ($W(CO)_6$) precursor can be described as:

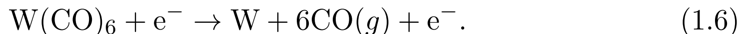

$$W(CO)_6 + e^- \rightarrow W + 6CO(g) + e^-. \tag{1.6}$$

However, the dissociation process is rarely ideal. Incomplete dissociation results in a deposit comprising the target material embedded in an organic matrix. For $W(CO)_6$, the deposit contains W, C and O due to residual organic components. The chemical composition depends on the process parameters used during deposition.

Deposition Rate: The vertical deposition or growth rate in a rotationally symmetric system for a stationary beam, is given by

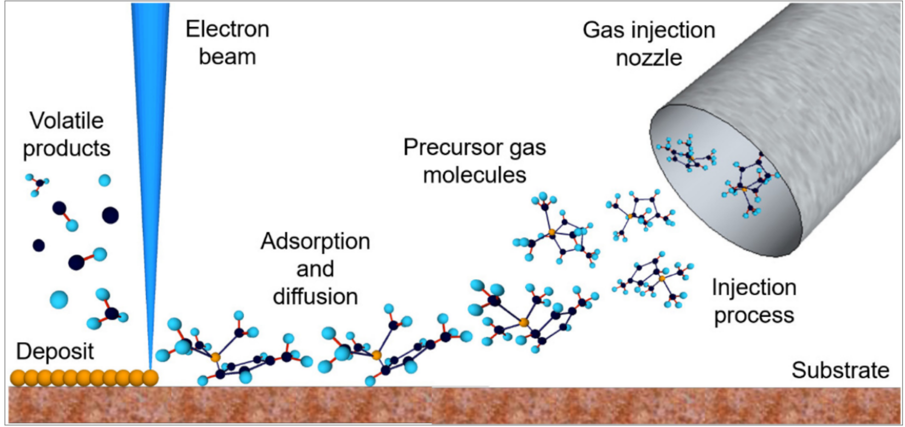

Figure 1.10.: Schematic illustration of the FIBID/FEBID process. The gaseous precursor is injected into the vacuum chamber and adsorbs to the substrate. An electron or ion beam is traced across the substrate following a predefined pattern. Upon irradiation, the precursor molecules dissociate into a deposit remaining on the substrate and volatile products that are removed from the vacuum system of the instrument. Reprinted from [28].

$$R_{\mathrm{D}}\left(r\right) = V_{\mathrm{p}} n_{\mathrm{p}}\left(r\right) \int_{0}^{E_0} \sigma\left(E\right) f\left(r, E\right) \mathrm{d}E \ , \tag{1.7}$$

where:

- V_{p} is the volume of a dissociated precursor molecule,
- $n_{\mathrm{p}}(r)$ is the number of adsorbed precursor molecules per surface unit and
- $\sigma(E)$ is the energy-dependent interaction crosssection of SEs with precursor molecules resulting in dissociation,
- $f(r, E)$ is the spatial and energy distribution of emitted electrons, obtained as a convolution of the incident beam and the emitted electron spectrum.

Since the exact energy dependence of the interaction cross-section and the electron distribution are generally unknown, the cross-section is typically replaced by an experimentally determined effective cross-section σ integrated over the energy spectrum and the electron distribution is approximated by eq. (1.2) [22], resulting in the simplified deposition rate

$$R_{\mathrm{D}}\left(r\right) = V_{\mathrm{p}} n_{\mathrm{p}}\left(r\right) \sigma f\left(r\right) = \gamma_{\mathrm{D}} V_{\mathrm{p}} f\left(r\right) \frac{n_{\mathrm{p}}\left(r\right)}{n_{\mathrm{p}_0}} \ , \tag{1.8}$$

where γ_{D} denotes the deposition yield and n_{p_0} the density of available adsorption sites.

Precursor Dynamics: The dynamic equilibrium of adsorbed precursor molecules per unit area, $n_\mathrm{p}(r,t)$, is given by the differential equation:

$$\frac{\partial n_\mathrm{p}}{\partial t} = \underbrace{sJ\left(1-\frac{n_\mathrm{p}}{n_{\mathrm{p}0}}\right)}_{\text{Adsorption}} + \underbrace{D\left(\frac{\partial^2 n_\mathrm{p}}{\partial r^2}+\frac{1}{r}\frac{\partial n_\mathrm{p}}{\partial r}\right)}_{\text{Diffusion}} - \underbrace{\frac{n_\mathrm{p}}{\tau_\mathrm{r}}}_{\text{Desorption}} - \underbrace{\sigma f n_\mathrm{p}}_{\text{Dissociation}} , \tag{1.9}$$

where:

- s is the sticking probability of a precursor molecule on the substrate,
- J is the precursor gas flux and
- D is the diffusion coefficient,
- τ_r is the residence time of precursor molecules.

The adsorption and desorption terms resemble *non-dissociative Langmuir adsorption*, where the surface coverage is given as

$$\frac{n_\mathrm{p}}{n_{\mathrm{p}0}} = \frac{sJ\tau_\mathrm{r}/n_{\mathrm{p}0}}{1+sJ\tau_\mathrm{r}/n_{\mathrm{p}0}} \tag{1.10}$$

The model holds for simple molecules that are purely physisorbed to the surface in a monolayer.
Neglecting the diffusion term, the effective residence time is:

$$\tau_\mathrm{eff}\left(r\right) = \frac{1}{sJ/n_{\mathrm{p}0} + 1/\tau_\mathrm{r} + \sigma f\left(r\right)} , \tag{1.11}$$

and the deposition rate (eq. (1.8)) becomes

$$R_\mathrm{D}\left(r\right) = sJ\tau_\mathrm{eff}\left(r\right)\sigma f\left(r\right) . \tag{1.12}$$

We introduce the dimensionless residence time ratio

$$\widetilde{\tau} = \frac{\tau_\mathrm{eff}\left(r\to\infty\right)}{\tau_\mathrm{eff}\left(r=0\right)} , \tag{1.13}$$

where $f(r)$ has its maximum at the center of the beam ($r=0$) and approaches 0 far away from the beam spot.
The ratio reflects the balance between precursor replenishment and dissociation:

- In the *electron-limited* regime ($\widetilde{\tau} \gtrsim 1$), replenishment is fast compared to the dissociation rate.
- In the *precursor-limited* regime ($\widetilde{\tau} \gg 1$), replenishment is slower than the dissociation rate and the irradiated spot depletes of precursor molecules.

Figure 1.11a displays the radial distribution of the deposition rate for various values of $\widetilde{\tau}$, neglecting diffusion.

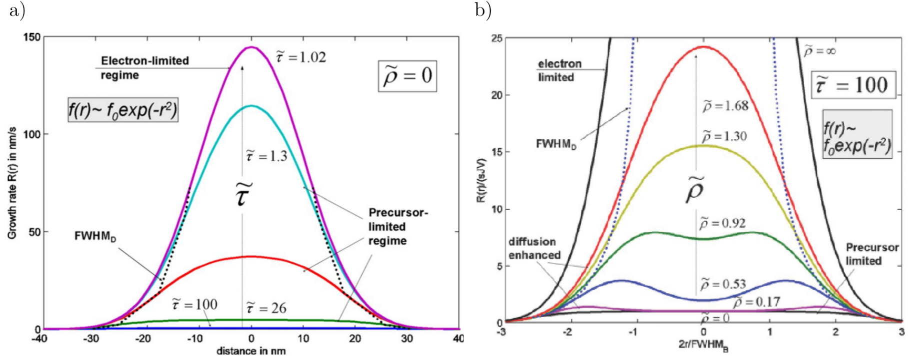

Figure 1.11.: (a) Deposition rate without diffusion for different normalized residence time ($\widetilde{\tau}$). At low $\widetilde{\tau}$, precursor supply is high enough to maintain a high surface coverage and the deposition rate follows the Gaussian beam profile (electron limited regime). For higher $\widetilde{\tau}$ replenishment is insufficient and the deposition rate decreases (precursor limited regime). (b) Deposition rate at $\widetilde{\tau} = 100$ under consideration of diffusion with increasing normalized diffusion length ($\widetilde{\rho}$). At low $\widetilde{\rho}$, the process is in the precursor limited regime. At moderate $\widetilde{\rho}$, diffusion partially replenishes the irradiated region (diffusion enhanced regime). At high $\widetilde{\rho}$, the process is in the electron limited regime. Reprinted from [22].

Influence of Diffusion: When considering diffusion, the rapid dissociation at high $\widetilde{\tau}$ can be partially mitigated if the diffusion length:

$$\rho_{\text{diff}}\,(r=0) = D \cdot \tau_{\text{r}}\,(r=0) \tag{1.14}$$

is significant compared to the spot size. In the *diffusion-enhanced* regime, precursor molecules from outside the beam spot replenish the spot via diffusive movement across the surface. Figure 1.11b shows the deposition rate at $\widetilde{\tau} = 100$ for various values of the diffusion length normalized by the FWHM of the beam

$$\widetilde{\rho} = \frac{2\rho_{\text{diff}}}{FWHM_{\text{B}}}\ . \tag{1.15}$$

For high $\widetilde{\rho}$, the Gaussian deposition profile typical of the electron limited regime is recovered. At moderate $\widetilde{\rho}$, precursor molecules are primarily dissociated in the outer regions of the beam spot, resulting in faster growth at the walls and resulting in a characteristic cowboy-hat-shaped deposit.
Both deposition rate and resolution are highest in the electron-limited regime, where precursor replenishment outpaces dissociation. For FIBID, where milling and deposition occur simultaneously, maintaining a higher deposition rate than sputtering is essential to achieve net deposition.

Temperature Dependence: In addition to precursor dissociation due to SEs and ESAs, the electron or ion beam also acts as a localized heat source $H_\mathrm{S}(r, z)$ within the substrate. The heat diffusion in the substrate can be described by the differential heat diffusion equation in cylindrical coordinates:

$$\frac{\partial T}{\partial t} = \kappa \nabla^2 T + H_\mathrm{S}\left(\boldsymbol{r}, t\right) \tag{1.16}$$

$$= \kappa \left(\frac{\partial^2 T}{\partial r^2} + \frac{1}{r}\frac{\partial T}{\partial r} + \frac{\partial^2 T}{\partial z^2} \right) + H_\mathrm{S}\left(r, z, t\right) \ , \tag{1.17}$$

where κ is the thermal diffusivity of the substrate.
Approximating the heat as being homogeneously dissipated in a hemisphere of radius $R_\mathrm{I}/2$, where R_I denotes the radius of the interaction volume, and considering heat diffusion into the semi-infinite substrate, the temperature increase at the center of a stationary beam [22] is given by:

$$\Delta T\left(r = 0\right) = \frac{V_\mathrm{a} I_\mathrm{B}(1-\eta)}{2\pi\kappa R_\mathrm{I}/2} \ , \tag{1.18}$$

where η denotes the total yield of particles and radiation leaving the substrate, i.e., BSEs, SIs, x-rays, etc..
For FIBID, the energy loss to the vacuum is negligible [63]. High electron beam currents, in the microampere range, can result in temperature increases in the order of 100 K at the beam center, depending on the substrate properties. This heating can cause thermal dissociation of the precursor [22]. For beams of heavy ions, substrate heating is more pronounced at the same current due to smaller interaction volumes.
Even moderate beam currents, which increase the substrate temperature by only a few Kelvin, can significantly impact the deposition process. Both, the diffusion coefficient (D), and the residence time (τ_r), are temperature dependent [22]:

$$D = D_0 \exp\left(-\frac{E_\mathrm{diff}}{k_\mathrm{B}T}\right) \ , \tag{1.19}$$

$$\tau_\mathrm{r} = \tau_{\mathrm{r},0} \exp\left(\frac{E_\mathrm{des}}{k_\mathrm{B}T}\right) \ , \tag{1.20}$$

where E_diff and E_des are the diffusion activation energy and the desorption energy, respectively. The ratio of diffusion activation energy and desorption energy is highly dependent on the precursor and the substrate and typically falls within the range of $E_\mathrm{des}/E_\mathrm{diff} = 3 - 10$ [22].

Dynamic Conditions: In the preceding discussion, we examined the deposition rate for a stationary beam in the steady-state condition $\frac{\partial n}{\partial t} = 0$. Without electron or ion beam irradiation, the dynamic equilibrium of the non-dissociative Langmuir adsorption (eq. (1.10)) is uniformly established across the surface. When the beam is activated, precursor dissociation begins, depleting n_p within the beam spot. Over time, a new equilibrium is achieved.
If the equilibrium under irradiation does not fall within the electron limited-regime, the beam can be turned off before equilibrium is reached while coverage is still sufficiently high. Without irradiation, the system replenishes precursor molecules in the irradiated area and the beam can be turned on again. Figure 1.12a illustrates the dynamics of depletion and replenishment for $\widetilde{\tau} = 1000$, comparing continuous and intermittent irradiation.
For most practically relevant structures, which are larger than the beam spot, the beam is raster-scanned along a predefined pattern. The *dwell time* (τ_d) refers to the time the beam remains on a single pixel of the pattern before moving to the next, allowing for precursor replenishment previous spots.
The pattern generator slices the target structure into a list of beam positions during a single *pass*. The number of pixels depends on the lateral dimensions of the structure and the desired spacing between adjacent spots, referred to as the *pitch* (Δx, Δy). The pitch is typically less than or equal to the beam diameter to ensure a continuous deposit. Figure 1.12b schematically illustrates the position list of an exemplary structure.
The *refresh time* is determined by the dwell time and the number of pixels per pass. For small structures, where the refresh time is insufficient for adequate precursor replenishment, an additional delay can be introduced between two consecutive passes.
The *volume per dose*, defined as the volume of material deposited or removed per unit charge, is calculated from the deposition rate integrated over the spot size and divided by the beam current. To achieve the desired thickness (t) at a given beam current, the pattern generator calculates the required *dose*, i.e., the total charge, and determines the number of passes needed to meet this requirement.

Deposition Parameters: The deposition conditions depend on numerous interdependent parameters that vary significantly for each material system. Additionally, sputtering and deposition of material lead to dynamic changes in the target's topography, chemical composition and temperature, introducing a time-dependent complexity for which, to our knowledge, no comprehensive, an-

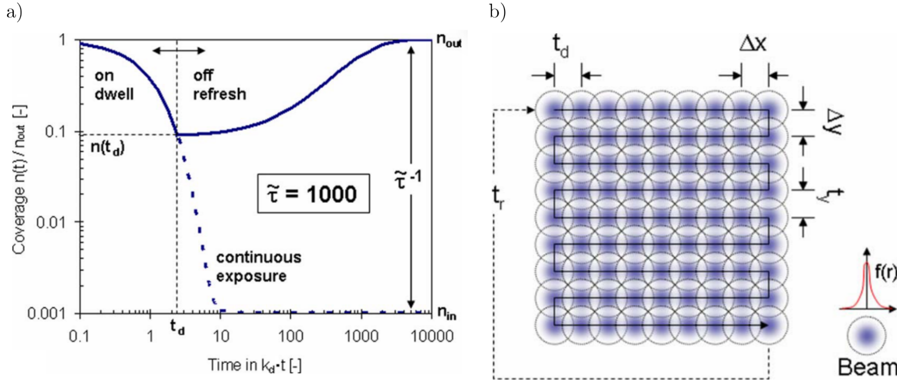

Figure 1.12.: (a) The time-evolution of the surface coverage after initializing irradiation with ions or electrons at $\widetilde{\tau} = 1000$. The coverage decreases towards an equilibrium on a low level, indicated by the dashed line. The solid line shows the replenishment after turning the beam off while coverage is still high. (b) Schematic illustration of the deposition process of a large pattern. The structure is sliced into pixels, distanced by a defined pitch. The beam rests on each pixel for a defined dwell time before moving to the next. Reprinted from [22].

alytical model exists to date. In recent years, numerical methods have emerged for ab initio simulation of the molecular dynamics [64–67], but these methods remain computationally expensive and published data remains limited at the time of writing.
As a result, successful high-resolution deposition still heavily relies on the expertise of operators of the FIB or SEM systems. Typically, the volume per dose for a desired system is calibrated and passed to the pattern generator. However, minor changes in the conditions can introduce deviations that significantly impact deposition quality, particularly when operating near the resolution limits of the instrument. To address these variations, operators iteratively optimize the following key parameters for the target structure:

- **Acceleration voltage:** Higher primary particle energy increases resolution but reduces the deposition rate. Depending on the instrument, the acceleration voltage can range from 0.2 kV to 60 kV, with 30 kV being the most common.
- **Beam current:** The electron or ion beam current is usually set in the pA to nA range. Higher currents result in faster deposition rates but at the expense of resolution. Furthermore, excessive currents can lead to precursor depletion.

- **Dwell time:** Longer dwell times increase the risk of precursor depletion, particularly at high beam currents. Typical dwell times fall within the ns to µs range.
- **Pitch:** The pitch is the distance between adjacent pixels in the pattern, usually set to be less than or equal to the beam diameter. This *overlap* ensures a continuous deposit. However, a too low pitch can result in precursor depletion.
- **Refresh time:** Refresh time is the total time between two consecutive passes, allowing for precursor molecule replenishment. It depends on the dwell time, pitch, and lateral dimensions of the deposit. If required, an additional delay can be introduced to facilitate sufficient replenishment.

Halo: The considerations above are focused on the area directly irradiated by the primary beam, where the deposition rate is highest. However, the deposit is not confined to the beam spot, but several mechanisms contribute to the growth of a *halo* around the target area.
In FEBID, the *inner halo* in the range of a few tens of nanometers is primarily caused by first-order SEs generated directly by PEs. The *outer halo*, which can extend up to several hundreds of nanometers, is predominantly due to second-order SEs, i.e., SEs produced by BSEs. For thicker deposits, additional SEs may be generated within the deposit itself and exit through the walls, resulting in edge broadening.
In FIBID, in addition to SEs and ESAs generated outside the beam spot, the Holtsmann tail of the beam (fig. 1.3c) contributes to the growth of halo.

Scanning Probe Lithography

In Scanning Probe Lithography (SPL), the nanometric tips of SPM as introduced in section 1.1.4, are utilized to interact with surfaces down to the atomic level, enabling nanolithography with exceptionally high resolution. For example, STM was used to create the “quantum corral”, where Fe atoms were precisely positioned on a Cu surface [50][3]. While STM-based SPL manipulates individual atoms, AFM-based SPL modifies surface properties locally, offering greater flexibility and a variety of approaches depending on the mechanism and property altered. A review of the various methods is given, among others, in [68].

[3] Another impressive example is the stop-motion clip “A Boy And His Atom”, available on YouTube [51]. While not scientifically published, it is a fun-to-watch demonstration of individual CO molecules manipulated by STM.

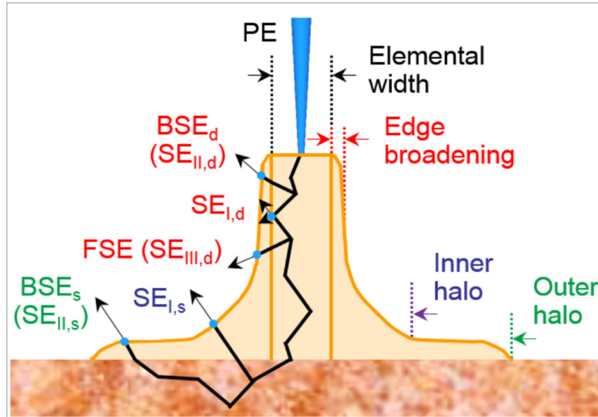

Figure 1.13.: Schematic illustration of the mechanisms resulting in the generation halo. The inner halo is mainly caused by secondary electrons of first order, generated by primary electrons. The outer halo is mainly caused by secondary electrons of second order, generated by backscattered electrons. For high deposits, secondary electrons generated within the deposit itself result in edge broadening. Reprinted from [28].

AFM-based SPL can alter surface composition, height, or physical/chemical properties through thermal, mechanical, or chemical effects, or by deposition. A notable example is oxidation SPL, where a voltage applied across a tip in a humid environment triggers a highly localized oxidation reaction via a water meniscus. This enables the creation of features with nanometric precision, such as dielectric barriers.
While SPL achieves unmatched resolution—atomic scale with STM and sub-20 nm with AFM—it is inherently slow and challenging to scale for industrial applications, limiting its use to niche applications, often in combination with large-area lithography techniques.

1.2.3. Comparison of Lithographic Techniques

In this section, the previously described lithographic techniques are compared based on four critical parameters: resolution, throughput, cost, and complexity, A summary is provided in fig. 1.14.

Resolution: SPL techniques excel in resolution, achieving atomic resolution with STM and sub-20 nm with AFM. Optical lithography, typically achieves 500 nm resolution with standard setups but can reach sub-10 nm in specialized,

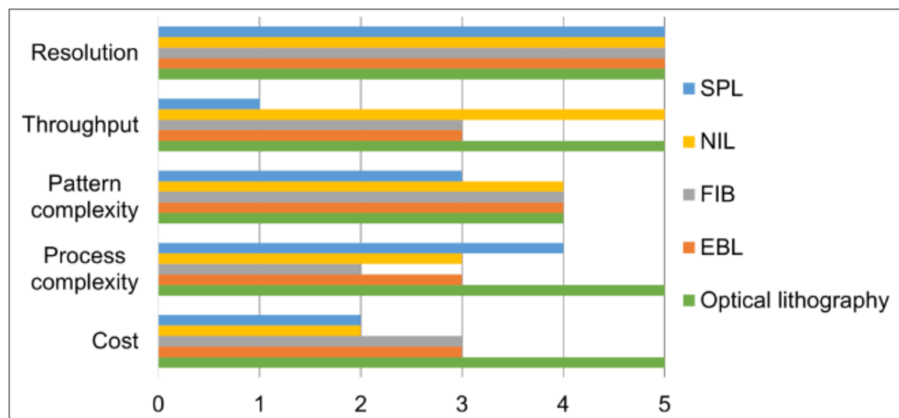

Figure 1.14.: Comparison of the main lithography techniques in terms of resolution (5=high), throughput (5=high), pattern complexity (5=good), process complexity (5=high), and equipment cost (5=expensive). Reproduced from [69].

industrial setups. Similarly, EBL, FIB, and NIL can achieve sub-10 nm resolution with suitable equipment, resists, or molds.

Throughput: High throughput varies by context. In industry, where mass production is critical, only highly optimized optical lithography meets the requirement of processing hundreds of wafers per hour. For research or niche applications, standard OL setups or NIL offer the parallel processing of hundreds of structures on a single wafer. On the other hand, EBL, FIB, and SPL are inherently slower due to their sequential nature, even with multi-beam or multi-tip enhancements.

Pattern Complexity: FIBID and FEBID stand out as the most versatile techniques, enabling both 2D and 3D patterning with ease. In contrast, most other lithographic techniques are primarily suited for 2D patterning.

Process Complexity: Process complexity varies widely across techniques. Optical lithography in industrial applications involves highly sophisticated equipment and processes to achieve high throughput and precision. Research setups, however, often use simpler tools such as mask aligners, reducing complexity. Techniques like EBL, FIB, and SPL can achieve resolutions comparable to industrial optical lithography but with less complex processes.

Cost: Steppers for optical lithography are the most expensive, reflecting their industrial-scale throughput and resolution capabilities. Other techniques, while less costly, trade-off speed and throughput for flexibility and accessibility.

The considerations above highlight the importance of selecting the appropriate technique based on the requirements of the given application. While sophisticated OL instruments are indispensable for industrial applications requiring high throughput, research and prototyping typically require versatility at comparable resolution, which is more effectively achieved using techniques such as FIB, EBL, and SPL. OL systems typically available in research facilities typically offer good throughput at the cost of resolution. In the scope of this project, we combine OL, EBL and FIB to make use of their individual strengths (see sections 2.1 and 2.2).

1.3. Superconducting Quantum Interference Device

A Superconducting Quantum Interference Device (SQUID), exploits the fundamental principles of superconductivity, specifically the *Josephson effect* and *flux quantization* to achieve magnetic flux sensitivity far beyond that of any conventional sensor. SQUIDs are capable of detecting changes in magnetic flux as small as fractions of a magnetic flux quantum, making them indispensable tools in disciplines ranging from medical imaging and quantum computing to geology and material science.
In section 1.3.1 we introduce the fundamental phenomenology and theory of superconductivity, a fascinating phenomenon exhibited by certain materials below a certain critical temperature. These materials demonstrate zero electrical resistance and perfect diamagnetism.
Section 1.3.2 delves into the Josephson effect and the concept of *Josephson junctions*, which consist of two superconductors separated by an insulating or metallic layer. These junctions can carry a non-resistive but highly phase-sensitive *Josephson current*.
Finally, in section 1.3.3, we explore how the extraordinary magnetic field sensitivity arises from the interplay of flux quantization within a superconducting loop and the properties of Josephson junctions.

1.3.1. Superconductivity

Phenomenology

Superconductivity is a remarkable state of matter emerging in certain materials at low temperatures. When cooled below a *critical temperature* (T_c), they exhibit zero electric Direct Current (DC) resistance, making them *ideal conductors*, and *ideal diamagnetism*, allowing them to completely expel magnetic fields. These properties were first discovered in 1911 by Heike Kamerlingh Onnes [70], shortly after helium was first liquefied in 1908 [71], marking the birth of the broad field of superconductivity. For a detailed overview of the field, refer to [72–75].
Besides the temperature, it was later found that superconductivity also breaks down beyond a *critical magnetic field* B_c, and a *critical current density* J_c. These parameters are interdependent, forming a three-dimensional phase diagram, as illustrated in fig. 1.15. The critical points refer to the intersections of these parameters with their respective axes when the other two parameters

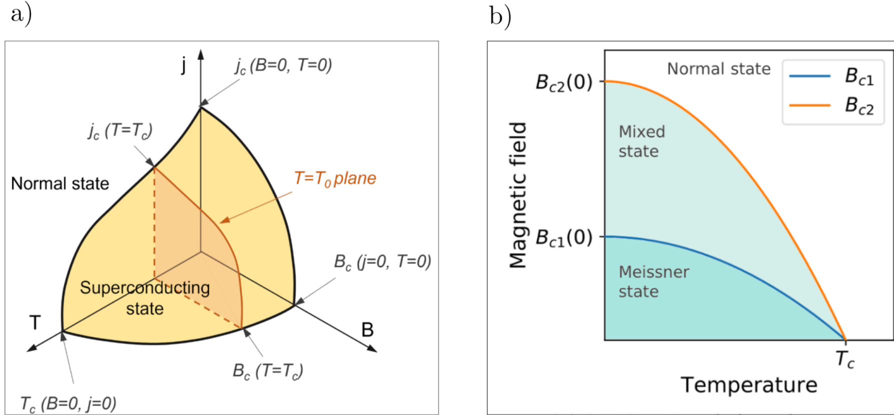

Figure 1.15.: (a) 3 dimensional phase diagram of a superconductor. The critical field, temperature and current density are interdependent. Reprinted from [69]. (b) critical field in dependence of the critical temperature. The Meißner phase below B_{c1} is common for type-I and type-II superconductors. Above B_{c1} the superconducting order collapses in a type-I superconductor. A type-II superconductor enters the mixed state (Shubiknov phase) where magnetic flux threads the superconductor in vortices, until the normal state is reached at B_{c2}. Reprinted from [78].

are set to zero. The expulsion of magnetic fields, described by the *Meißner-Ochsenfeld* effect [76], occurs only inside the bulk material. Any penetration of an external magnetic field into a superconductor decays exponentially according to:

$$B(x) = B_0 \cdot \exp(-x/\lambda_\mathrm{L}) \tag{1.21}$$

where λ_L is the London penetration depth [77]. This shielding effect is caused by surface currents that oppose the applied field.
Superconductors are classified into two types based on their response to external magnetic fields. Type-I superconductors exhibit a single critical field (B_c) beyond which they completely revert to the normal state. Type-II superconductors display two critical fields. Below a lower critical field ($B_{\mathrm{c}1}$), they are in the *Meißner phase*, acting as ideal diamagnets. Between $B_{\mathrm{c}1}$ and an upper critical field ($B_{\mathrm{c}2}$), they enter the *Shubiknov phase*, where magnetic flux partially penetrates the superconductor in form of quantized *vortices*. These vortices consist of normal-conducting cores surrounded by circulating supercurrents. As the field strength increases, the vortex density rises until the superconducting order collapses at $B_{\mathrm{c}2}$.

Ginzburg-Landau Theory

On an electronic level, type-I superconductivity can be understood by the Bardeen-Cooper-Schrieffer (BCS) theory as the condensation of two fermionic electrons into bosonic *Cooper pairs* via phonon-mediated interactions [79]. However, Bardeen-Cooper-Schrieffer (BCS) theory does not fully explain type-II superconductivity or high temperature superconductors, and a complete microscopic explanation of these materials remains an open question [80].
In contrast, the Ginzburg-Landau (GL) theory provides a phenomenological framework to describe the emergence of superconductivity as a phase transition in a macroscopic electronic state. For type-I superconductors, Ginzburg-Landau (GL) can be derived from BCS theory [80], and it also holds for type-II superconductors on a phenomenological level [81].
In GL theory, the superconducting state is described by an order parameter, formulated within the framework of Landau's theory of phase transitions. The order parameter takes the form of a pseudo wave function:

$$\psi_\mathrm{s}\left(\boldsymbol{r}\right) = \left|\psi_\mathrm{s}\left(\boldsymbol{r}\right)\right| \exp\left(\mathrm{i}\varphi\right), \tag{1.22}$$

where $\left|\psi_\mathrm{s}\left(\boldsymbol{r}\right)\right|^2 = n_\mathrm{s}\left(\boldsymbol{r}\right)$ represents the local density of superconducting electrons. φ is the phase of the wave function.
ψ_s satisfies the Schrödinger equation for a free particle with a non-linear term:

$$\frac{1}{2m^*}\left(\frac{\hbar}{\mathrm{i}}\nabla - \frac{q}{\mathrm{c}}\boldsymbol{A}\right)^2 \psi_\mathrm{s} + \beta\left|\psi_\mathrm{s}\right|^2 \psi_\mathrm{s} = -\alpha\left(T\right)\psi_\mathrm{s}\;, \tag{1.23}$$

where α and β are phenomenological expansion coefficients. This equation incorporates the effects of temperature and the magnetic vector potential ($\boldsymbol{A}$). From this framework, the expression for the supercurrent can be retrieved:

$$\boldsymbol{J}_\mathrm{s} = \frac{\hbar}{m^*}\left(\nabla\varphi - \frac{q}{\hbar}\boldsymbol{A}\right)\left|\psi_\mathrm{s}\right|^2\;. \tag{1.24}$$

which resembles the quantum mechanical expression for the current of a charged particle with effective mass m^* and charge q. For conventional resistive currents, $q = \mathrm{e}_0$, whereas for supercurrents $q = 2\mathrm{e}_0$, corresponding to the charge of a Cooper pair.

Flux Quantization

According to the Meißner effect, the magnetic field inside a superconductor is expelled, resulting in zero magnetic flux within the bulk. Consequently, supercurrents are localized near the surface of the superconductor, decaying

exponentially with a characteristic length scale of λ_L. Inside the bulk of a superconductor, the density of a supercurrent vanishes. Using eq. (1.24) and setting $q = 2e_0$ for Cooper pairs, we find:

$$\nabla\varphi = \frac{2e_0}{\hbar}\boldsymbol{A} \ . \tag{1.25}$$

For a superconducting loop, the order parameter must remain single valued throughout the superconductor. This implies that the phase difference after travelling around a closed path $\mathcal{C}$ must be an integer multiple of 2π:

$$\oint_{\mathcal{C}} \nabla\varphi \, \mathrm{d}\boldsymbol{s} = 2\pi n \ , \tag{1.26}$$

where n is an integer. The magnetic flux enclosed by the same path $\mathcal{C}$ is given by:

$$\Phi = \oint_{\mathcal{C}} \boldsymbol{A} \, \mathrm{d}\boldsymbol{s} \ . \tag{1.27}$$

Combining these two conditions with eq. (1.25), we obtain:

$$\oint_{\mathcal{C}} \nabla\varphi \, \mathrm{d}\boldsymbol{s} = \frac{2e_0}{\hbar} \oint_{\mathcal{C}} \boldsymbol{A} \, \mathrm{d}\boldsymbol{s} \tag{1.28}$$

$$2\pi n = \frac{2e_0}{\hbar}\Phi \ . \tag{1.29}$$

Finally, this leads to *flux quantization*:

$$\Phi = n\frac{h}{2e_0} \equiv n\Phi_0 \ , \tag{1.30}$$

where $\Phi_0 = h/2e_0$ is the magnetic flux quantum. The flux quantization is upheld by a circular current I_{loop} in the superconducting loop. This current either compensates or enhances an externally applied magnetic field, ensuring that the total flux within the loop satisfies the quantization condition.

The Proximity Effect

For temperatures $T < T_c$, the superconducting order parameter acquires a non-trivial solution within the GL framework:

$$|\psi_s|^2 = -\frac{\alpha}{\beta} = -\frac{\alpha_0\,(T - T_c)}{\beta_0} = n_s \ , \tag{1.31}$$

introducing a temperature dependence to the density of superconducting electrons.

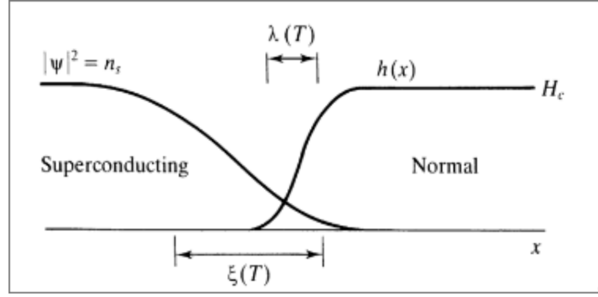

Figure 1.16.: The characteristic lengths of a superconductor at an interface. The London penetration depth λ_L is the scale over which a magnetic field decays into the bulk of a superconductor. The coherence length ξ is the length scale over which the density of superconducting electrons decays, spilling into the normal conductor. Reprinted from [72].

The London penetration depth can thus be expressed as:

$$\lambda_\mathrm{L} = \sqrt{\frac{m\beta_0}{\mu_0 q^2 \alpha_0 \left(T - T_\mathrm{c}\right)}}\ , \tag{1.32}$$

valid for temperatures $T \ll T_\mathrm{c}$. Additionally, the coherence length, ξ, is introduced:

$$\xi = \frac{\hbar}{\sqrt{2m\alpha_0 \left(T - T_\mathrm{c}\right)}}\ . \tag{1.33}$$

The coherence length describes the length scale over which the density of superconducting electrons can vary. At the surface of a superconductor, n_s does not abruptly drop to zero but smoothly decays over the distance ξ. When a normal metal is in direct contact with a superconductor, the superconducting state can partially extend into the normal metal, resulting in a finite density of superconducting electrons within the normal conductor. The extent of this penetration depends on the coherence length of the normal conductor (ξ_N), known as the *proximity effect*.

1.3.2. Josephson Effect

Phenomenology

The *Josephson effect* emerges in heterostructures where two superconducting regions (S) are separated by a thin insulating (I) barrier. In 1962, Brian Josephson

predicted that for a sufficiently thin insulating layer, a zero-resistance current, known as the *Josephson current*, can flow through the junction [82]. This effect arises when the order parameters of the superconducting regions, extending into the normal metal due to the proximity effect, overlap. The Josephson current obeys the first Josephson equation:

$$I_{\mathrm{J}} = I_0 \sin(\delta) \ , \tag{1.34}$$

where I_0 is the maximum critical current of the junction. $\delta = \varphi_1 - \varphi_2$ expresses the phase difference of the superconducting order parameter in either of the two banks. When a finite voltage drops across the junction, the phase difference evolves over time according to the second Josephson equation:

$$\frac{\mathrm{d}\delta}{\mathrm{d}t} = \frac{2\mathrm{e}_0 V}{\hbar} = \frac{2\pi}{\Phi_0} V \ . \tag{1.35}$$

This temporal evolution of the phase difference causes the Josephson current to oscillate at the *Josephson frequency*:

$$\omega_{\mathrm{J}} = \frac{2\pi V}{\Phi_0} \ . \tag{1.36}$$

Resistively Capacitively Shunted Junction Model

The Resistively Capacitively Shunted Junction (RCSJ) model provides a framework to describe real Josephson junctions by representing them as an ideal Josephson junction connected in parallel with a resistor and a capacitor (fig. 1.17a). This circuit captures the dynamics of a biased junction, where the total current is distributed among the three paths:

$$I_{\mathrm{b}} = I_0 \sin(\delta) + \frac{V}{R_{\mathrm{N}}} + C\frac{\mathrm{d}V}{\mathrm{d}t} \ , \tag{1.37}$$

where

- I_{b} is the bias current,
- $I_0 \sin(\delta)$ is the current of the ideal Josephson junction,
- V/R_{N} is the current in the resistive path in the normal state,
- $C\mathrm{d}V/\mathrm{d}t$ is the displacement current due to the junction's capacitance.

Using the second Josephson equation (eq. (1.35)), the time evolution of the phase difference δ can be described as:

$$\frac{\Phi_0}{2\pi} C \frac{\mathrm{d}^2\delta}{\mathrm{d}t^2} + \frac{\Phi_0}{2\pi} \frac{1}{R_{\mathrm{N}}} \frac{\mathrm{d}\delta}{\mathrm{d}t} = I_{\mathrm{b}} - I_0 \sin(\delta) = -\frac{2\pi}{\Phi_0} \frac{\partial U_{\mathrm{J}}}{\partial \delta} \ . \tag{1.38}$$

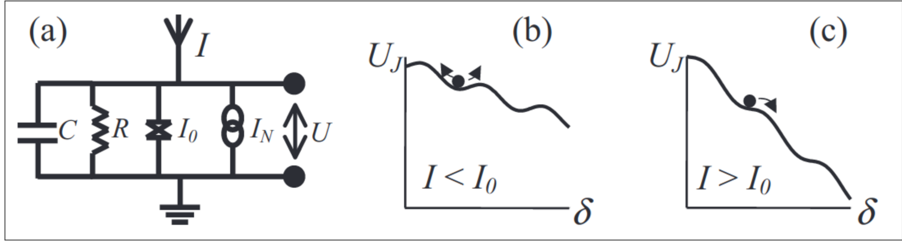

Figure 1.17.: (a) Circuit of a Josephson junction in the RCSJ model. An ideal Josephson junction is connected in parallel with a resistor and a capacitor. (b) The tilted washboard potential in the superconducting state ($I_b < I_c$) where the phase is trapped in a potential minimum. (c) In the normal state near the critical current ($I_b > I_c$) the potential is tilted and the phase escapes, continuously developing and resulting in a finite voltage. Reprinted from [83].

This equation, a *Langevin equation*, is analogous to the motion of a point-like particle in a *tilted washboard potential*[4], given by:

$$U_{\mathrm{J}} = \frac{\Phi_0}{2\pi}\left(I_0\left(1 - \cos\left(\delta\right)\right) - I_{\mathrm{b}}\delta\right) \tag{1.39}$$

For bias current $I_{\mathrm{b}} < I_0$, the phase is trapped in a potential minimum, and the junctions operates in the zero-voltage state (fig. 1.17b). For currents $I_{\mathrm{b}} > I_0$, the potential tilts sufficiently for the phase to escape, advancing continuously and resulting in a finite voltage.
The behavior of the RCSJ model is governed by the *characteristic frequency* (ω_{c}) and the *Stewart-McCumber parameter* (β_{c}). The characteristic frequency is:

$$\omega_{\mathrm{c}} = \frac{2\pi I_0 R_{\mathrm{N}}}{\Phi_0} , \tag{1.40}$$

which corresponds to the Josephson frequency at the characteristic voltage $V_{\mathrm{c}} = I_0 R_{\mathrm{N}}$.
The Stewart-McCumber parameter is given by:

$$\beta_{\mathrm{c}} = \frac{2\pi}{\Phi_0} I_0 {R_{\mathrm{N}}}^2 C , \tag{1.41}$$

[4] A point-like particle of mass m driven by a force F moves in a potential U as

$$m\frac{\mathrm{d}^2x}{\mathrm{d}t^2} + \mu\frac{\mathrm{d}x}{\mathrm{d}t} = F - \frac{\partial U}{\partial x} - \frac{\partial U - Fx}{\partial x}$$

with the friction coefficient μ. The driving force F, corresponding to the bias current I_{b}, results in a tilt of the potential. The velocity $\mathrm{d}x/\mathrm{d}t$ corresponds to the voltage $U \sim \mathrm{d}\delta/\mathrm{d}t$ and the friction to the conductance $1/R_{\mathrm{N}}$.

describing the damping of the system.
Rewriting the phase equation eq. (1.38) in terms of these parameters:

$$\frac{\beta_\mathrm{c}}{{\omega_\mathrm{c}}^2}\frac{\mathrm{d}^2\delta}{\mathrm{d}t^2}+\frac{1}{\omega_\mathrm{c}}\frac{\mathrm{d}\delta}{\mathrm{d}t}=\frac{I_\mathrm{b}}{I_0}-\sin\left(\delta\right)\ . \tag{1.42}$$

For high capacitance ($\beta_\mathrm{c} \gg 1$), the junction exhibits hysteresis in its IV characteristics. The critical current when increasing the bias current differs from the return current (I_r).
Superconducting-Insulating-Superconducting (SIS) junctions generally exhibit high capacitance and large β_c, resulting in hysteretic behavior.

Weak Links

Classical Josephson contacts of the SIS type rely on a tunneling current through a very thin insulating layer, requiring the length of the junction to allow for a significant overlap of the order parameters of either side. This is governed by the superconducting coherence length ξ, generally a few nm [75]. Lengths on this scale are challenging to achieve in in-plane heterostructures and are commonly achieved by multi-step lithography processes. In *weak links*, on the other hand, the insulating layer is replaced by a region of weaker superconducting properties, allowing for a current to flow.
In Constriction-type Josephson Junction (c-JJ), the superconducting path is locally confined to a narrow cross-section. This reduction in dimensionality creates a region with concentrated current density, resulting in a lower critical current compared to the surrounding superconductors.
In SNS-junctions, the insulating layer is replaced by a metallic conductor. In SNS junctions, Cooper pairs penetrate into the normal conductor due to the proximity effect, where superconducting properties are induced in the normal metal over the characteristic length scale ξ_N.
The microscopic mechanism underlying the proximity effect is Andreev reflection. When an electron in the normal conductor with an energy below the superconducting gap approaches the interface, it cannot enter the superconductor due to the lack of available states. However, the electron can pair with another electron from the superconductor, forming a Cooper pair. This process leaves behind a hole in the normal conductor, with the same momentum and spin as the incoming electron, effectively retro-reflecting the electron as a hole at the interface.
In an SNS junction, this reflected hole can undergo a similar process at the opposite superconductor interface, creating another Cooper pair while injecting an

electron back into the normal conductor. The repeated Andreev reflections between the superconducting interfaces give rise to Andreev Bound States (ABS) within the superconducting energy gap. These states are localized in the normal region and arise from the coherent superposition of electron and hole-like excitations. The ABS spectrum depends on the phase difference between the superconductors and governs the flow of the supercurrent through the junction, forming the microscopic basis of the Josephson effect in SNS systems.
The maximum length of junctions formed by weak links is extended up to [83]

$$l \lesssim 3 \cdot \xi_{\mathrm{N}} \; . \tag{1.43}$$

Furthermore, weak links generally obtain a low capacitance, resulting in low β_{c} and, in turn minimizing the hysteresis associated with capacitance. However, weak links carry a resistive current, resulting in a locally increased temperature. If the cooling power of the bath can not fully compensate for the heating, the effective temperature inside the junction does not correspond to the externally controlled temperature, resulting in a thermal hysteresis [84].
For a more in-depth discussion on weak links, refer to textbooks like [75].

Susceptibility to Noise

The behaviour of Josephson junctions is very susceptible to noise. As an example, we describe here some noise sources in the current.
To account for random fluctuations of the bias current, the bias is modelled as $I_{\mathrm{b}} \rightarrow I_{\mathrm{b}} + I_{\mathrm{N}}\,(t)$, where I_{N} represents the noise current. While I_{N} averages to zero over time, on short timescales, fluctuations can temporarily alter the effective bias current. These fluctuations influence the tilt of the washboard potential:

$$U_{\mathrm{J}} = \frac{\Phi_0}{2\pi}\left(I_0\,(1-\cos(\delta)) - (I_{\mathrm{b}} + I_{\mathrm{N}}\,(t))\right) \; . \tag{1.44}$$

Even when the junction operates in the superconducting state $(I_{\mathrm{b}} < I_0)$, random noise currents can temporarily raise the total current above the critical current $(I_{\mathrm{b}} + I_{\mathrm{N}} > I_0)$. This allows the phase to escape to another pontential minimum, resulting in a finite voltage.
The influence of thermal noise on the Josephson contact is described by the noise parameter:

$$\Gamma = \frac{2\pi k_{\mathrm{B}} T}{I_0\,\Phi_0} \; . \tag{1.45}$$

As Γ increases, the sharp transition in the IV characteristic becomes rounded, as illustrated in fig. 1.18 for a junction with negligible β_{c}, hence a weak link.

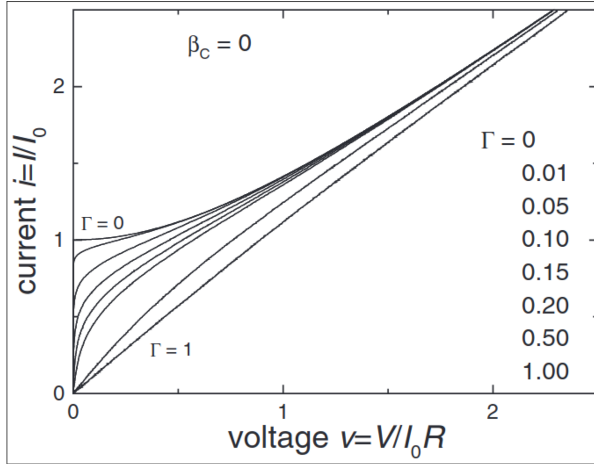

Figure 1.18.: The effect of noise on the IV characteristic of a Josephson junction. With increasing noise parameter (Γ) the abrupt transition is more and more rounded. Reprinted from [83].

One primary source of noise is thermal fluctuations. Thermal noise is frequency independent (*white noise*) with Gaussian distributed amplitudes. Rewriting the noise parameter as $\Gamma = I_{\mathrm{th}}/I_0$, a thermal noise current can be introduced as

$$I_{\mathrm{th}} = \Gamma I_0 = \frac{2\pi}{\Phi_0} k_{\mathrm{B}} T \ , \tag{1.46}$$

providing a measure for the maximal amplitude of the thermal current fluctuations. For SQUID operation, the maximum Josephson current must be greater than the thermal noise current $I_0 \gtrsim I_{\mathrm{th}}$. At 4.2 K, the thermal noise current is approximately 176 nA, decreasing to 83 nA at 2 K.
Another fundamental source of noise is the frequency dependent $1/f$ noise arising from defects inside the junction. Furthermore, imperfections in experimental setups, such as inadequate filtering of 50 Hz power grid noise or coupling to environmental electromagnetic radiation, can introduce fluctuations.
A comprehensive introduction to noise in Josephson contacts can be found in [83].

1.3.3. Superconducting Quantum Interference Device

A Superconducting Quantum Interference Device (SQUID) exploits the fundamental principles of superconductivity, specifically flux quantization (section 1.3.1) and the phase sensitivity of a Josephson Junction (JJ) (section 1.3.2),

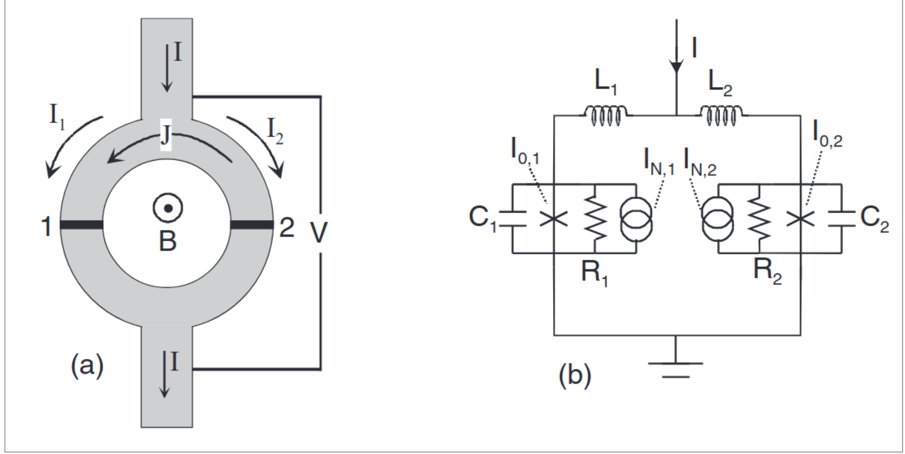

Figure 1.19.: (a) Schematic illustration of a SQUID and (b) the circuit of a SQUID in the RCSJ model. Reprinted from [83].

to form a magnetic flux sensor with unprecedented sensitivity. The *RF-SQUID* consists of a superconducting loop interrupted by one Josephson Junction (JJ), while the *DC-SQUID* employs two JJs connected in parallel. This section focuses on the DC-SQUID, comprehensive literature on both types of SQUIDs can be found in [83, 85] and others. The schematic configuration of a DC-SQUID is depicted in fig. 1.19.

Current Modulation The current through each of the two contacts $k = 1,\ 2$ is given by half the bias current plus the directional loop current ensuring flux quantization:

$$I_{\mathrm{J},k} = \frac{I_{\mathrm{b}}}{2} \pm I_{\mathrm{loop}} = I_{0,k} \sin\left(\delta_k\right) + \frac{\Phi_0}{2\pi R_{\mathrm{N},k}} \frac{\mathrm{d}\delta_k}{\mathrm{d}t} + \frac{\Phi_0}{2\pi} C_k \frac{\mathrm{d}^2\delta_k}{\mathrm{d}t^2} + I_{\mathrm{N},k} \tag{1.47}$$

The phase difference between the junctions is given by:

$$\delta_2 - \delta_1 = \frac{2\pi}{\Phi_0}\left(\Phi + LI_{\mathrm{loop}}\right) = \frac{2\pi}{\Phi_0}\Phi_{\mathrm{T}} \tag{1.48}$$

where the term LI_{loop} accounts for the flux generated by the circulating loop current. The total flux Φ_{T} threading the loop obeys flux quantization. The applied flux is related to the magnetic flux density B via the effective area A_{eff} :

$$\Phi = B \cdot A_{\mathrm{eff}} \tag{1.49}$$

Due to flux focusing, the effective area is generally larger than the geometric area A_{geom} of the hole of the SQUID.
The inductance (L) of a SQUID includes both a geometric and a kinetic contribution. The kinetic inductance becomes significant when the film thickness and the linewidth of the loop are comparable to or smaller than the London penetration depth λ_{L}. The performance of the SQUID is characterized by the screening parameter:

$$\beta_{\text{L}} = \frac{2LI_0}{\Phi_0} \; . \tag{1.50}$$

In the case of symmetric junctions and in the limit of $\beta_{\text{L}} \ll 1$, the solution of $I_{\text{b}} = I_{\text{J},1} + I_{\text{J},2}$ from eq. (1.47) yields a flux-dependent critical current of

$$I_{\text{c}}(\Phi) = 2I_0 \left| \cos\left(\pi \frac{\Phi}{\Phi_0}\right) \right| \; . \tag{1.51}$$

In the limit of small β_{L}, the critical current modulates periodically with integer multiples of Φ_0 reaching a maximum of $2I_0$ at $n\Phi_0$ and a minimum of 0 at $(n+1/2)\Phi_0$. As β_{L} increases, *modulation depth* decreases [86]:

$$\frac{I_{\text{c}}^{\max} - I_{\text{c}}^{\min}}{I_{\text{c}}^{\max}} = \frac{1}{\beta_{\text{L}}} \; . \tag{1.52}$$

For large β_{L}, the modulation of I_{c} becomes sawtooth-shaped:

$$I_{\text{c}}(\Phi) = 2I_0 - 2\frac{|\Phi - n\Phi_0|}{L} \text{ where } n - \frac{1}{2} \leq \frac{\Phi}{\Phi_0} \leq n + \frac{1}{2} \; . \tag{1.53}$$

The critical current modulation and the dependence of the modulation depth on β_{L} is illustrated in fig. 1.20.

Voltage Modulation In the limit of $\beta_{\text{c}} \ll 1$, a flux dependent, sinusoidal voltage modulation is observed for bias currents $I_{\text{b}} \gtrsim I_{\text{c}}$:

$$V(\Phi) = \frac{R_{\text{N}}}{2}\sqrt{{I_{\text{b}}}^2 - {I_{\text{c}}}^2(\Phi)} \tag{1.54}$$

As a *flux-voltage-transducer*, SQUIDs are biased slightly above I_{c}, and the voltage is measured. For small enough flux changes $\delta\Phi$, the corresponding voltage change is linear

$$\delta V = \frac{\partial V}{\partial \Phi}\delta\Phi \; . \tag{1.55}$$

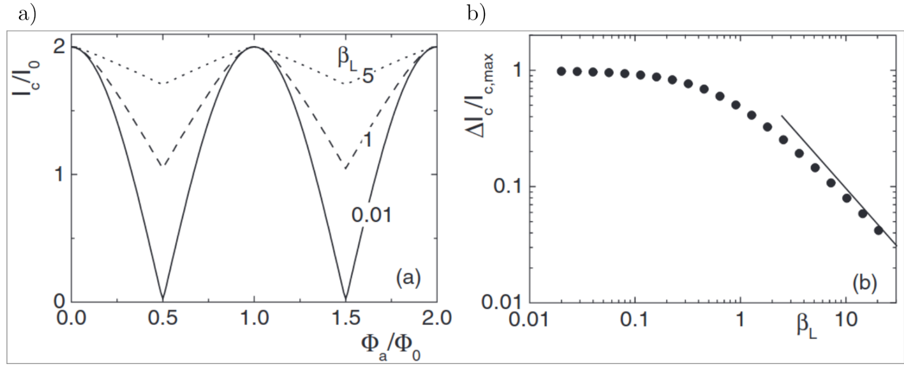

Figure 1.20.: (a) Flux-dependent I_c modulation in a SQUID in units of the magnetic flux quantum (Φ_0) for various screening parameters (β_L). (b) Modulation depth of I_c in dependence of β_L. With increasing β_L the modulation decays. Reprinted from [83].

The bias current and a well defined external flux is usually chosen to maximize the slope of the $V(\Phi)$ curve. A key characteristic is the *transfer coefficient*, marking the *working point* of the SQUID:

$$V_\Phi = \max \left| \frac{\partial V}{\partial \Phi} \right| \tag{1.56}$$

Flux Sensitivity The sensitivity in the voltage state is limited by random fluctuations of the voltage. This is commonly expressed by the spectral density of voltage noise power S_V. The spectral density of flux noise power is given by the relation

$$S_\Phi = \frac{S_V}{{V_\Phi}^2} \; , \tag{1.57}$$

and the rms flux noise $\sqrt{S_\Phi}$ in units of $\Phi_0/\sqrt{\mathrm{Hz}}$ is a key parameter for the comparison of SQUID sensitivity.
Thermal fluctuations, as treated before for individual Josephson contacts, enter via Nyquist-Johnson noise with

$$S_V = 4k_\mathrm{B}TR \; . \tag{1.58}$$

In the case of SQUIDs, the thermal fluctuations in the circulating current in turn result in fluctuations of the total flux $\Phi_\mathrm{T} = \Phi + LI_\mathrm{loop}$ proportional to its inductance. Numerical solutions to the Langevin equation (eq. (1.44)) yield data approximated by

$$S_\Phi \approx 4\,(1 + \beta_\mathrm{L})\,\frac{\Phi_0 k_\mathrm{B} T L}{I_0\,R_\mathrm{N}} \tag{1.59}$$

in the limit of low thermal noise ($\beta_L \Gamma < 0.1$). The lowest flux noise is obtained for $\beta_L = 2LI_0/\Phi_0 \approx 1$, an important target for practical SQUID design. A detailed description of this numerical approach can be found in [83].
More broadly speaking, an additional criterion for the low noise regime for SQUID operation can be defined by introducing the fluctuation-threshold inductance

$$L_F = \frac{(\Phi_0/2\pi)^2}{k_B T} \ . \tag{1.60}$$

The fluctuation-threshold inductance is 1.87 nH at 4.2 K and 3.99 nH at 2 K. The two criteria for low noise SQUID operation hence are

$$L < L_F = (\Phi_0/2\pi)^2/k_B T \tag{1.61}$$

$$1 \gg \Gamma = 2\pi k_B T/\Phi_0 I_0 \tag{1.62}$$

State of the Art From eq. (1.59) it can be inferred that reducing the dimension of SQUIDs could significantly enhance their sensitivity by reducing the geometric inductance in a smaller loop. The downsizing from the micro- to the nanoscale, enabled by progress in nanofabrication techniques, has allowed to reduce the flux noise from the $\mu\Phi_0/\sqrt{\text{Hz}}$ to tens of $\text{n}\Phi_0/\sqrt{\text{Hz}}$.
The low flux noise, in combination with the low size of the sensor, enabled the detection and analysis of individual magnetic nanoparticles. In recent years, the focus shifted novel fabrication techniques and SQUID designs to fabricate three-axis vector sensors, high temperature SQUIDs operating in liquid nitrogen at 78 K, based on Grain Boundary (GB) junctions in $YBa_2Cu_3O_7{-}x$ (YBCO). Furthermore, the toolbox of SSM is augmented by SoT and SoL, highly sensitive SQUIDs on sharp tips, i.e. pulled quartz tubes and the tip of AFM cantilevers. This topic is further discussed in section 1.4.2.
In table 1.2 we provide an overview over the development of SQUIDs in recent years.

Table 1.2.: Overview of the development of SQUID fabrication, design approaches and sensitivities in recent years.

Type	Fabrication	Material	A_{loop} (µm^2)	T (K)	$\sqrt{S_\Phi}$ (µ$\Phi_0/\sqrt{\mathrm{Hz}}$)	Publication	Note
SIS	Lithography	Nb/NbO$_x$/Pb	$2 \cdot 17.5 \times 17.5$	4.2	0.84	1984 [87]	No details on fabrication
SIS	HYPRES	Nb/Al-AlO$_x$/Nb	8×8	<0.5, 4	0.25, 0.8	2001 [88]	Commercial manufacturer [89]
SIS	OL, FIB	Nb/Al-AlO$_x$/Nb	$\pi \cdot 225^2$	4.2	0.2	2014 [90]	Ga$^+$-FIB milling used to edit existing SQUID
SIS	OL	Nb/AlO$_x$/Nb	0.8×0.8	4.2	0.066	2015 [91]	Cross-type junctions [92]
SNS	EBL	Nb/HfTi/Nb	0.2×0.2	4.2	0.25	2013 [93]	
SNS	EBL	Nb/HfTi/Nb	0.6×0.09 (x, y) 0.5×0.5 (z)	4.2	0.17 (x), 0.16 (y) 0.24 (z)	2016 [94]	Three-axis vector SQUID
c-JJ	EBL	Nb, Al	$\pi \cdot 0.5^2$	4.2	100, 40	2000 [95]	
c-JJ	FIB	Nb	$\pi \cdot 0.075^2$	4.2	1.5	2007 [96]	
c-JJ	FIB	Nb / W-C	$\pi \cdot 0.18^2$	6.8	0.2	2008 [97]	Nb / W-C bilayer
c-JJ	FIBID	W-C	0.7×0.3	2	—	2022 [98]	
SoT	Evaporation	Al	$\pi \cdot 0.029^2$	0.3	1.8	2010 [42]	Directional evaporation on on a pulled quartz tube
SoT	Evaporation	In, Sn	$\pi \cdot 18^2$	0.3	0.042	2020 [43]	Directional evaporation on on a pulled quartz tube
SoL	FIB	Nb	$\pi \cdot 0.18^2$	4.2	0.48	2022 [99]	FIB milling on Nb covered tip of AFM cantilever
GB	PLD	YBCO	3×6	78	2.6	2020 [100]	GB fabricated by Ion Milling

1.4. The FIBSuperProbes Project

This work is carried out in the framework of the FIBSuperProbes initiative[5]. Bringing together researchers from the CSIC-University of Zaragoza, the Eberhard Karls University of Tübingen, and the University of Basel in a joint project with *IBM Zürich*, we join our efforts to augment the capabilities of SPM probes by functionalizing them with superconducting structures, forming SQUID on Lever (SoL). The project seeks to develop cutting-edge tools for nanoscale imaging and sensing.

1.4.1. Functionalization of Probes for Scanning Probe Microscopy

In section 1.1, we have discussed the spectacular advances in the field of nanoscience, particularly by the outstanding capabilities of SPM (section 1.1.4). However, to this day, the technique is carried out with rather simple probes consisting of a conducting, insulating or magnetic sharp tip. These designs are generally sensitive to a single mode, and overlapping modes must be separated through cumbersome methods. For instance, in MFM, magnetic and topographic forces overlap, complicating analysis.
In the past, numerous approaches to functionalize SPM cantilevers with superconducting sensors on the nanoscale have been carried out, to no avail. The high aspect ratio of the protruding tip prohibits the use of conventional, resist based techniques of nanofabrication (section 1.2.1).
The FIBSuperProbes project overcomes these challenges by employing FIB processing, a versatile direct-write technique (section 1.2.2). FIB processing is not limited to flat structures, which is impressively demonstrated by the fabrication of freestanding 3D structures on the nanoscale making it the ideal technique for dealing with the protruding tip of the SPM probe. Key advantages of FIB include:

- **Substrate versatility:** FIB can fabricate features on non- planar substrates, including freestanding 3D nanoscale structures.
- **In-situ switching between patterning strategies:** In FIB, the operator is able to switch *in situ* between additive and subtractive, i.e., deposition and milling, with a resolution of down to 10 nm.

[5]This project has received funding from the European Union's Horizon 2020 research and innovation programme under grant agreement No 892427. More information can be found on the official website at `https://www.fibsuperprobes.com` [101].

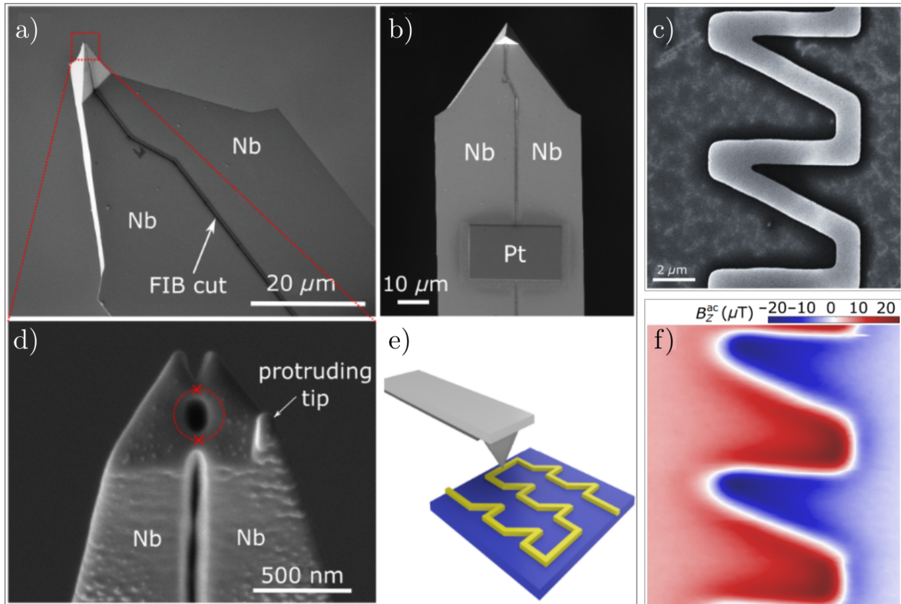

Figure 1.21.: (a, b, d) SEM micrographs of an SoL. (e) Schematic representation of the scanning process of an exemplary sample. (c) SEM micrograph of an exemplary sample and (f) magnetic field contrst of the sample with an AC current flowing through the wire.

- **Imaging:** The fabrication process can be observed in real-time, especially in combined FIB/SEM systems.

With respect to the numerous advantages of FIB processing, the project follows various approaches to utilize a combination of milling, deposition and material modification on different systems to functionalize SPM cantilevers with various sensors. At the core of these efforts, *IBM Zürich* provides the scientific groups with device-ready, custom designed cantilevers, building on the expertise arising from the *Millipede* data storage project.

1.4.2. Scanning SQUID Microscopy

Traditionally, magnetic field imaging on the nanoscale has been conducted by MFM. However, this technique is limited by the simultaneous measurement of the topographic and magnetic contrast via the force they exert. Furthermore, the magnetic tip-sample-interaction can potentially change the magnetic state of either.

Scanning SQUID Microscopy (SSM), on the other hand, senses the magnetic field transduced into an electric signal. To the point of writing, the field of SSM in terms of both sensitivity and lateral resolution is lead by SoT devices fabricated via directional evaporation of superconducting materials on a pulled quartz tube [43, 102], as introduced in section 1.1.4.
Albeit the impressive results obtained by these SoT sensors, the insensitivity to the topography leads to surface defects and sample inhomogeneities significantly perturbing the signal. Also, tip crashing into the surface is frequent. We strive to overcome these limitations by our functionalized cantilevers that are capable of picking up the force exerted from the surface like in traditional AFM, while at the same time measuring the magnetic field as a purely electric signal.
To achieve this goal, various approaches are followed in the project, including

- **Milling on coated cantilevers:** SPM cantilevers are coated by a thin film of a superconducting material such as Nb. A c-JJ SQUID is patterned by He^{+}, Ne^{+}, or Ga^{+} FIB milling.
- **YBCO modification:** High-temperature superconductors operating at $\sim 80\,\mathrm{K}$ such as YBCO are modified via localized He^{+} irradiation, creating GB junctions [103].
- **Deposition:** Superconducting nanowires [104] and SNS contacts [105] fabricated bottom-up by FIBID and FEBID are utilized to create SQUIDs.

These advancements promise to deliver a new generation of tools for non-invasive magnetic imaging with a spatial resolution down to 10 nm with high magnetic field sensitivity while simultaneously sensing topographic contrast. An exemplary SoL fabricated by FIB milling on a thin-film covered SPM cantilever is shown in fig. 1.21.

1.5. Objective and Structure of this Thesis

Among the various approaches pursued in the framework of the FIBSuper-Probes initiative, our group is dedicated to the *deposition* approach. In this thesis, we present the first steps on a path to the fabrication of functional SoL in a single-step, bottom-up deposition process. The challenges along the path were manifold. In order to shed light on the various aspects to consider, we laid out the relevant physical background in this chapter (chapter 1).
In chapter 2 we describe the experimental setup. Section 2.1 introduces the preparation of the substrates, i.e., conventional, large Si/SiO_2 chips and cantilevers provided by *IBM Zürich*. Section 2.2 provides an overview of the Ion- and Electron-Microscopes used for imaging and sample fabrication and the relevant parameters chosen for the experiments carried out in this thesis. Lastly, section 2.3 introduces the available systems for the characterization of the magnetotransport properties of our SQUIDs.
In chapter 3, we explore a new experimental setup installed in our laboratories in the early stages of this project, the CFMS (Cryogen Free Magnet Setup). The setup includes a self-contained cryogenic circuit, a superconducting magnet and the electronics required for characterization of magnetotransport properties of a given sample. We introduce the cryogenic (section 3.1.2) and electronic components (section 3.2), the in-house solutions in soft- and hardware to augment functionality and improve the quality of the system (section 3.3). We then assess the capabilities of the system and evaluate the advantages and disadvantes for SQUID characterization in the scope of this project (section 3.4) and summarize the findings in section 3.5.
Chapter 4 is dedicated to the path towards the fabrication of SQUIDs on Levers (SoL). We explore the difference in the deposition process between large Si/SiO_2 chips and cantilevers and the implications on the fabrication parameters for W-C deposits in section 4.1. In section 4.2 we explore various SQUID designs and fabrication recipes developed throughout the course of the project. Section 4.3 provides an overview of the chapter.
The efforts described in the chapters before culminate in chapter 5 where we present the characterization of the magnetotransport properties of the various SQUID-design approaches. We present results obtained on SQUIDs with Josephson Junctions consisting of long nanobridges (section 5.1), short constrictions (section 5.2) and SNS-contacts (section 5.3) on large substrates. In section 5.4 we present the transfer of the long-bridge and short-constriction approaches to the cantilevers. The chapter is briefly summarized in section 5.5.

Finally, chapter 6 and chapter 7 wrap up the efforts taken in this thesis in English and in Spanish, respectively. We present the overcome and remaining challenges on the path towards the fabrication of the first functional SQUID-device on an SPM cantilever fabricated by a single-step deposition process using Ga^+-FIBID. Furthermore, we propose suggestions for future experiments to further advance the technique.

Chapter 2

Experimental Methods

Contents

2.1. Substrates 53
- 2.1.1. Optical Lithography 53
- 2.1.2. Electron Beam Lithography 54
- 2.1.3. Standard Silicon Wafer 55
- 2.1.4. Cantilevers 57

2.2. Nanofabrication with Focused Ion- and Electron Beams 59
- 2.2.1. The Dual Beam System 59
- 2.2.2. The $W(CO)_6$ Precursor 61
- 2.2.3. Process Parameters 63
- 2.2.4. Transmission Electron Microscopy 64

2.3. Magnetotransport at Low Temperatures 67
- 2.3.1. Physical Properties Measurement System 67
- 2.3.2. Cryogen-Free Measurement System 69
- 2.3.3. Systems at the University of Tübingen 70

2.1. Substrates

Initial investigations into the properties of FIBID-grown W-C- SQUIDs were conducted on commercially available Si/SiO_2 wafers. These studies served as a foundation for transferring the fabrication process to the cantilevers provided by *IBM Zürich*. In this section we provide an overview of the practical aspects of Optical Lithography (OL) (section 2.1.1) and Electron Beam Lithography (EBL) (section 2.1.2), which were employed to pre-pattern suitable chips (section 2.1.3) and cantilevers (section 2.1.4) with Au contacts.

2.1.1. Optical Lithography

The chips for preliminary experiments were fabricated via OL. A custom photomask was designed in *KLayout* [106] the mask manufacturer, *DeltaMask* [107], transfered the desired pattern onto a fused quartz plate as a chromium (Cr) motif. Quartz is transparent to the UV light used in subsequent steps, while chromium blocks the radiation. Once fabricated, the mask can be reused to produce chips with the same pattern at the wafer scale.

The physical principles of OL have been outlined in section 1.2.1. Here, we detail the specific steps of the lift-off process carried out in our laboratory. The OL process was conducted in a Class 100 clean room, where the particle count exceeding 0.5 µm in size is maintained below 3520 particles per cubic meter. The clean room is illuminated with filtered light to prevent unintentional exposure of the photoresist to UV radiation.

In a first step, a uniform thin layer of photoresist is applied to the wafer using a *SÜSS MicroTec* spin coater. During *spin coating*, a drop of resist is placed at the center of the wafer and uniformly spread over the entire surface. The thickness of the resist layer is controlled by the rotation speed and the resist's viscosity.

The pattern from the mask was transferred onto the resist using a *SÜSS MicroTec MA6* mask-aligner system. This system provides precise control of the mask's position relative to the wafer via a motorized stage with micrometric precision. It allows translational and rotational adjustments in the X–Y plane and controls the mask-sample distance. For our experiments, lithography was performed in contact mode, where the photomask is in physical contact with the sample.

The aligner's mercury (Hg) lamp emits UV light with selectable wavelengths (436 nm, 405 nm and 365 nm) via optical filters. For this work, the 405 nm wavelength was used to sensitize the resist. Light intensity was measured during each experiment with a photodetector, and exposure time is calibrated based

on the resist's thickness and properties to ensure the correct UV dose. The system's resolution limit is in the micrometer range. To ensure successful lift-off process, all features were designed to have a minimum size and distance of 5 µm.
Metallic pads were deposited using a *BOC Edwards Auto500* e-beam evaporator. In this system, a heated filament emits electrons via thermionic emission. These electrons, accelerated by a potential difference, are directed towards the target material using a magnetic field. The impact causes the target material to sublimate, and the resulting atoms deposit onto the wafer. A quartz crystal microbalance monitors the thickness of the deposited layer in real time to ensure precision.
The full process is as following:

1. **Resist Deposition:** A 2.5 µm thick film of reversal resist (TI35 ESX) is spin-coated onto the wafer.
2. **Soft bake:** The resist-covered wafer is baked for 1 min at 100 °C to evaporate the solvent of the resist.
3. **Exposure:** The wafer and mask are aligned in the mask aligner, and the resist is selectively exposed to UV light at a dose of 175 mJ/cm^2.
4. **Reversal bake:** The wafer is baked for 2 min at 130 °C, reversing the resist behavior from positive to negative.
5. **Flood exposure:** The entire wafer is exposed to UV light without the mask, sensitizing the previously unexposed areas.
6. **Development:** The exposed areas are dissolved in the developer (AZ developer, Microchemicals), partially exposing the wafer surface.
7. **Metallization:** A 5 nm thick buffer layer of Cr is evaporated onto the wafer to improve adhesion, followed by the deposition of 50 nm thick Au contacts.
8. **Lift-off:** The wafer is submerged in acetone, dissolving the remaining resist and removing the metal film not in direct contact with the substrate.

2.1.2. Electron Beam Lithography

In the first generation of standard silicon chips (see section 2.1.3), we employed Electron Beam Lithography (EBL) to pattern Au contacts at a higher resolution than that possible using OL. While the EBL process does not allow for high throughput— processing single chips at a time instead of full wafers—it offers high flexibility in contact design with a resolution in the 100 nm range.
EBL was performed using an *ELPHY* by *RAITH*, connected to a *Helios Nanolab 600 Dual Beam* instrument, as shown in fig. 2.5, and described in more detail in section 2.2.1.

Due to its low throughput, EBL was employed to single chips pre-patterned by OL, with Au contacts and alignment markers. The smallest available write field on our chips is $(50 \times 50)\,\mu m^2$, offering a beam pitch of 12.2 nm, which is limited by the SEM's resolution at the corresponding magnification.

1. **MMA Deposition:** A 400 nm thick film of a more sensitive resist (MMA 8.5 MAA EL 10) is spread over the surface of the chip via spin-coating at 4000 rpm.
2. **PMMA Deposition:** A 240 nm thick film of PMMA 950k is spread over the surface of the chip via spin-coating at 4000 rpm.
3. **EBL:**
    a) **Calibration:** The SEM is calibrated to the chip by focusing three corners to account for inclination of the chip.
    b) **Alignment:** The write field is aligned to either existing markers or the edges of the chip.
    c) **Exposure:** The resist is exposed according to the desired pattern.
    d) **Repeat:** The alignment and exposure steps are repeated for the next write field, going from largest to smallest. If the current is changed in between, calibration has to be repeated as well.
4. **Development:** The exposed areas are dissolved in the developer (MIBK:IPA), partially exposing the wafer surface.
5. **Metallization:** A 5 nm thick buffer layer of Cr is evaporated onto the wafer, improving adherence of the 50 nm thick Au contacts.
6. **Lift-off:** The wafer is submerged in acetone, dissolving the remaining resist and hence the metal film not in direct contact with the substrate.

2.1.3. Standard Silicon Wafer

Chips fabricated from a commercial Si wafer covered by a 300 nm thick layer of thermally grown SiO_2 serve as the standard platform for experiments in our laboratory. These chips have the advantage that the FIBID (section 2.2) conditions are well known. The chips were pre-patterned with Au contacts according to the process described in section 2.1.1.

Two different chip layouts were used during the experiments. For initial studies, a wafer was pre-patterned with Au contacts and diced into chips of $(10 \times 10)\,mm^2$. Each chip featured four $(400 \times 400)\,\mu m^2$ contact pads deposited at the outer edges, extending towards the inner $(400 \times 400)\,\mu m^2$ write field. The contacts terminate in 30 μm wide fingers, spaced 30 μm apart.

To bring the contacts closer to the deposition area, EBL was employed to pattern leads terminating in 300 nm wide contacts. This technique allowed for high flexibility in the final contact design. By this approach, deposition area for

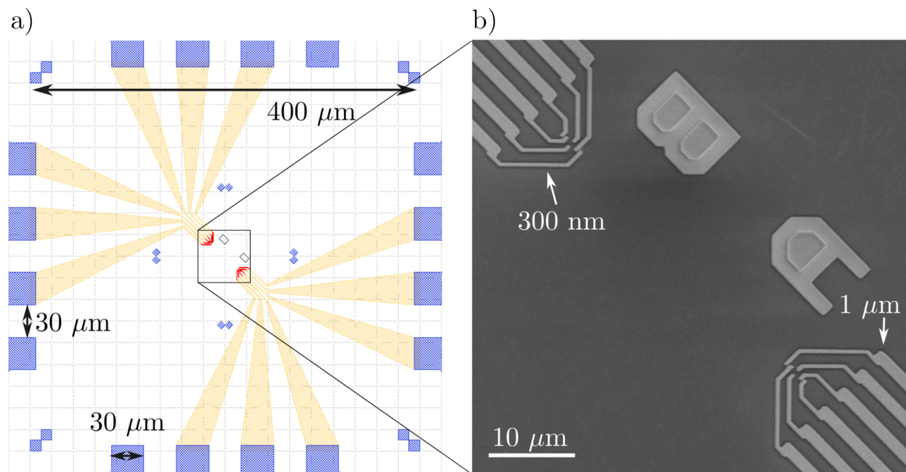

Figure 2.1.: (a) KLayout design of the inner part of a chip of first generation. The blue parts is fabricated by OL. The yellow and red parts are fabricated by EBL in two consecutive steps. (b) A SEM micrograph of the innermost part of the chip. The sample is deposited between the leads via FIBID, only requiring to conduct deposition in an area of $(1 \times 5)\,\mu\text{m}^2$.

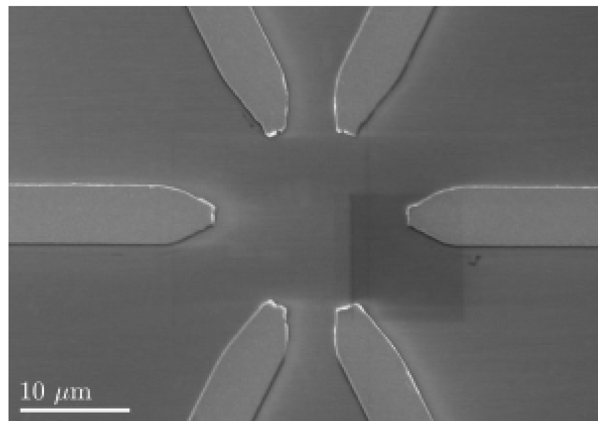

Figure 2.2.: SEM micrograph of a chip of second generation. The contacts are directly patterned by OL. FIBID is conducted in an area of $(15 \times 17)\,\mu\text{m}^2$.

FIBID was reduced to $(1 \times 5)\,\mu m^2$, minimizing the time required for the FIBID process. Furthermore, this layout was designed with advanced experiments in mind, such as individually tuning the I_c of either of the Josephson junctions via electrostatic gating [108]. The layout of the first-generation chips is shown in fig. 2.1.
However, the additional EBL process proved cumbersome for initial SQUID characterization, which is the main focus of this work. As a result, a second-generation chip design was adopted, where the contacts were directly patterned via OL in a circular arrangement around the deposition area. The area utilized for FIBID was expanded to $(15 \times 17)\,\mu m^2$, representing a reasonable balance between deposition time and process complexity. The layout of a chip of second generation is shown in fig. 2.2.

2.1.4. Cantilevers

The focus of this work is the functionalization of SPM cantilevers. Pre-patterned cantilevers were fabricated in collaboration with *IBM Zürich* [109]. As part of the *Millipede* [110] project, the company developed a process to batch-fabricate SPM cantilevers with Au contacts on the upper surface.
The cantilevers are composed of a 1.3 mm wide silicon body coated with a 50 nm layer of thermally grown SiO_2. At the apex, a thin, narrow extrusion, 44 µm wide, extends towards the tip. Figure 2.3 shows the SEM micrograph of a cantilever from the side.

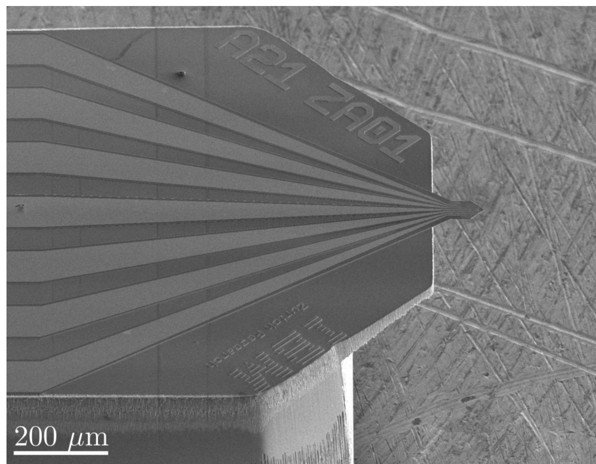

Figure 2.3.: SEM micrograph of a cantilever from the side.

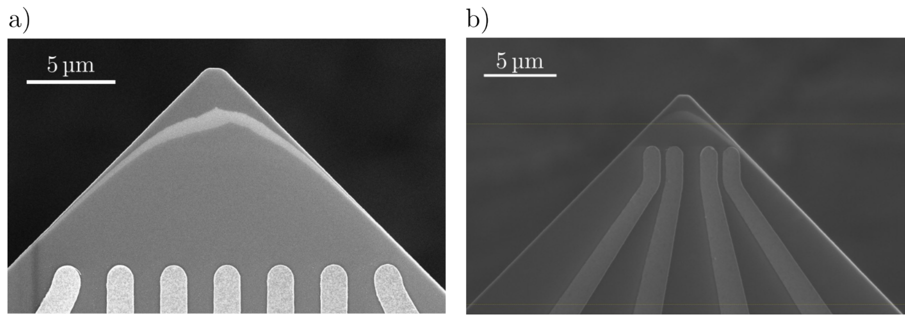

Figure 2.4.: SEM micrographs of the layout of two generations of cantilevers. The contacts run up to 12.5 µm (a) and 4 µm (b) from the apex.

In a first cantilever layout, the Au contacts end in 1 µm wide fingers, stopping 12.5 µm from the apex of the tip (fig. 2.4a). In a second generation, in order to minimize the SQUID-to-surface distance, the Au contacts were extended to end just 4 µm from the apex (fig. 2.4b).

2.2. Nanofabrication with Focused Ion- and Electron Beams

2.2.1. The Dual Beam System

The fabrication of nano-SQUIDs is performed using a *Helios Nanolab 600 Dual Beam* system by *Thermo Fischer* as depicted in fig. 2.5. The dual beam system combines a Ga^+ FIB and a SEM column in a single instrument, enabling *in situ* switching between electron- and ion-beam induced imaging and processing. The fundamentals of electron- and ion beam focusing and image formation have been introduced in section 1.1.3. Here, we focus on the Helios 600 instrument available in our lab.
At the core of the system is the process chamber in which the sample is placed. For imaging and processing, a SEM column is mounted vertically above the sample. Additionally, a Ga^+ FIB column is mounted at an angle of 52° with respect to the electron column. The chamber furthermore has several slots to integrate a variety of detectors and additional instruments for sample processing or *in situ* characterization.

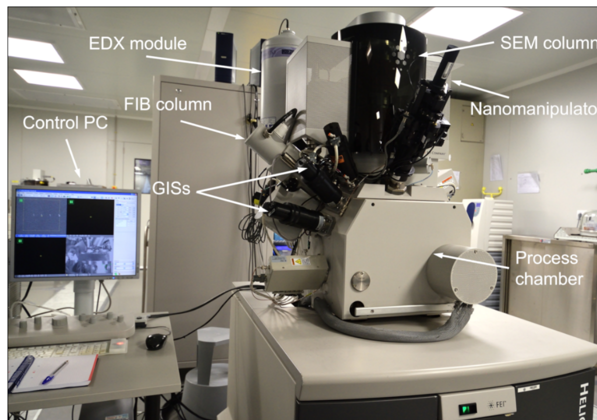

Figure 2.5.: The Helios Nanolab 600 Dual Beam system from Thermo Fischer. Reprinted from [69]

The Ion Source

The system is equipped with a Liquid Metal Ion Source (LMIS) to extract Ga^+ ions from a bath of liquefied Ga. Ga is a wide-spread material for FIB due to

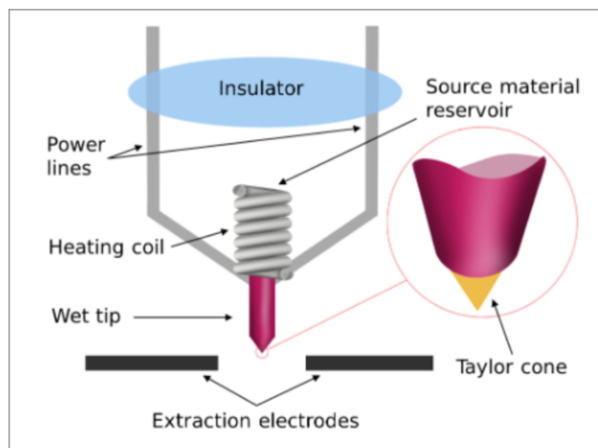

Figure 2.6.: Schematic representation of a Liquid Metal Ion Source (LMIS) used for ion extraction. Reprinted from [69].

its excellent properties. It has a low melting point of $\sim 29.8\,°C$ and a low vapor pressure of $\sim 10^{-18}$ mbar [111], allowing for ion extraction at low effort and a long lifetime of ~ 1500 h of the source.
For the extraction of ions, the Ga reservoir is heated up and liquefied by a coil surrounding the reservoir. The liquid Ga wets a sharp tungsten needle of typically 1 µm to 5 µm in diameter. The extraction electrodes are used to apply a voltage of 10 kV between themselves and the tip. In the electric field, a Taylor cone of 2 nm to 5 nm forms, resulting in a strong electric field at the apex, resulting in ionization and extraction of the Ga ions.

The Ion Column

In addition to the condenser and objective lenses and the scanning coils used to focus and raster the beam (see section 1.1.3), the column is equipped with an array of apertures. The apertures are essentially orifices with differing diameter, only allowing parts of the beam to pass through and thus controlling the beam current. The desired aperture is mechanically moved to the center of the optical axis. Furthermore, the system has stigmator lenses to correct astigmatism, that is elliptical distortion of the beam. A beam blanker blocks the entire beam, which is especially important in FIB to avoid damaging the sample by ion milling.

The Process Chamber

The process chamber houses the sample and all instruments to process and investigate the sample. It is kept at vacuum of $\sim 10^{-6}$ mbar under normal operation. A low pressure inside the chamber is important in imaging as colissions of the beams with gas molecules reduce the image resolution. It becomes crucial in FIBID/FEBID to guarantee a high quality deposit.
Samples are mounted on a movable stage that allows precise adjustments in three spatial directions, as well as rotation around the vertical axis and tilting up to approximately 60°. Vertical movement is used to align the sample to the *eucentric height* at which the optical axes of the focused electron- and ion-beams intersect.
The process chamber also houses in situ processing components essential for FIBID. Of particular importance are the nozzles that deliver gaseous precursor materials, with their reservoirs located outside the chamber. The entire assembly of reservoirs, valves, and nozzles responsible for storing and delivering precursor gases is referred to as the Gas Injection System (GIS). Precursor materials, often stored as solids, are sublimated by integrated heaters and delivered through the nozzles.
Imaging is mostly done by an Everhart-Thornley-Detector (ETD) mounted at an angle of 30° (see section 1.1.3). The system is furthermore equipped with a Through-the-Lens Detector (TLD) located inside the column and a detector for Energy Dispersive X-Ray Spectroscopy (EDXS).
Other instruments available are micromanipulators used to extract lamellae required for TEM and microprobes enabling *in situ* electric characterization.

2.2.2. The $W(CO)_6$ Precursor

At the center of this work stands the $W(CO)_6$ precursor. Upon dissociation during the deposition process, a composite of tungsten and carbon (W-C) remains as deposit. The most striking feature of W-C nanodeposits is their superconductivity, first reported by Sadki et al. in 2004 for Ga^+ FIBID with $T_c = 5.2$ K [112], and extensively studied ever since. By contrast, superconductivity in single-crystal tungsten occurs at much lower temperatures around 11 mK [113]. Studies on amorphous W systems, stabilized by Si or Ge and prepared by Low Pressure Chemical Vapor Deposition (LPCVD), show a similar increase of T_c, suggesting it being related to the amorphous structure of the material system [114]. However, hollow nanopillars grown by He^+ FIBID exhibit a crystalline structure, reopening the debate on the origin of superconductivity in W-C [104].

Ga^+-FIBID

The material properties of Ga^+ FIBID grown W-C have been extensively studied ever since. The structure of the deposit is reported to be amorphous to nanocrystalline, with an atomic content of W in the range of 40 % to 50 % and C of 30 % to 40 % [115–119]. By virtue of the technique, the W-C matrix additionally exhibits implantation of Ga atoms (10 % to 20 %) and traces of O (0 % to 5 %) [115–119]. Li et al. show a strong dependence of the chemical composition on the ion beam current used [120]. A comprehensive overview of the reported values is provided in table 2.1.

Table 2.1.: Reported properties of W-C fabricated by means of Ga^+ FIBID.

	T_c (K)	W:C:Ga:O (%)	Microstructure
Sadki et al. [115]	5.2 ± 0.5	40:40:20:0	Amorphous
Luxmore et al. [116]	5.5 ± 1.0	51:37:12:0	Nanocrystalline
Spoddig et al. [117]	5.2 ± 0.5	17:35:13:4	Nanocrystallites
Li et al. [118]	5.0 to 5.5	53:34:11:2	Nanocrystallites
Córdoba et al. [119]	4.3 ± 0.3	40:43:10:7	Nanocrystallites

The variations in microstructure and chemical composition have implications on the electric and superconducting properties of the deposit. The critical temperature is reported in the range of 4.3 K to 5.5 K [112, 116–119]. In 2021, Blom et al. showed that also FEBID-grown W-C turns superconducting with $T_c \sim 5\,\mathrm{K}$ when deposited at unconventionally large currents [105]. In W-C nanopillars grown by He^+ FIBID, critical temperatures of up to 7.1 K are reported [104].
For SQUID-applications, especially the superconducting and magnetic properties are relevant. W-C forms a second order superconductor with an upper critical field of $B_{c,2} = (7 - 8.5)\,\mathrm{T}$ at 2 K [121–123]. Extrapolation of the critical field to 0 K yields a value of $B_{c,2}(0) = 9.5\,\mathrm{T}$ [112].
The London penetration depth is reported as $\lambda_L = 850\,\mathrm{nm}$ [124], a significant challenge for the fabrication of SQUIDs as fully repelling the magnetic field won't be possible in thin films. Furthermore, the coherence length at zero temperature is calculated to $\xi(0) = 6\,\mathrm{nm}$ [112, 119]. Hence, fulfilling the requirement for phase coherence, and thus a single-valued Current Phase Relation (CPR), requires junction lengths of (eq. (1.43))

$$l \leq 3.5 \cdot \xi_N = 18\,\mathrm{nm}\ . \tag{2.1}$$

FEBID

The decomposition of the $W(CO)_6$ precursor under irradiation with a focused electron beam results in deposits with a wide spectrum of applications. At moderate electron beam currents of $I_{el} = (3.3 - 3.9)$ nA and $V_{el} = 5$ kV, the atomic content of W increases proportionally to the current from 22 % to 37 %, resulting in insulating to metallic behavior [125]. At a higher current of 5 nA and $V_{el} = 10$ kV, the atomic content of W increases to 50 % and a transition to the superconducting regime is observed at $T_c = 2.0$ K [126].
The tunability of the material's properties via the beam parameters was, e.g., exploited by Lahabi et al. to fabricate SNS-JJs in a single-step, direct-write process [105]. Recently, three-dimensional superconducting nanocircuits with $T_c = 5$ K have been grown by FEBID using high currents [127].

2.2.3. Process Parameters

All samples presented in this thesis were fabricated using a *Thermo Fisher Helios 600 DualBeam* system, which integrates both an SEM and a FIB column. This system enables simultaneous imaging and processing capabilities, essential for high-resolution nanofabrication.
The process chamber is maintained at a base pressure of approximately 10^{-6} mbar, which rises to 10^{-5} mbar during deposition due to the introduction of precursor gases. For optimal precursor supply without introducing electrostatic disturbances, the gas injection system (GIS) needle is positioned 100 µm above the sample surface and 50 µm laterally from the beam spot.

Deposition with Ga^+ Ions: For deposition using Ga^+ ions, the ion beam is accelerated at $V_{Ion} = 30$ kV. A volume per dose of 8.3×10^{-2} µm^3/nC is maintained. Unless otherwise stated, the beam current is set to $I_{Ion} = 9.7$ pA at a dwell time of $\tau_d = 200$ ns, though earlier experiments utilized $I_{Ion} = 1.5$ pA at $\tau_d = 500$ µs. In section 4.1.3 the choice of these parameters is discussed in detail. In either case, the overlap is set to zero, meaning the pitch equals the beam diameter. The deposition process is highly sensitive to factors such as beam diameter, which depends on the ion beam current and focusing quality, and the chamber vacuum conditions, which affect beam scattering.

Deposition with Electrons: For deposition with electrons, the beam is accelerated at $V_{el} = 5$ kV, with a volume per dose of 8.0×10^{-3} µm^3/nC. The electron beam current is set to 1.4 nA, and the dwell time is 1.4 ms. An overlap of 60 % is typically applied to ensure continuous deposition.

Imaging: For imaging, an electron beam accelerated at $V_{el} = 5\,\mathrm{kV}$ is used. The beam current is adapted dynamically to optimize contrast and resolution.

Factors Influencing Resolution: Achieving the highest possible resolution requires careful control of several factors. The beam diameter serves as a fundamental physical limit, influenced by the ion beam current and focus quality. Additionally, residual air molecules and high precursor gas pressures can scatter the beam, resulting in broadening. Variations in small-scale features, such as nanowire widths or trench depths, are attributed to differences in focus, vacuum conditions, and precise knowledge of the deposition rate.

2.2.4. Transmission Electron Microscopy

Transmission Electron Microscopy (TEM) is a powerful characterization technique that utilizes the interaction of a high-energy electron beam (typically 300 keV) transmitted through a thin specimen ($< 100\,\mathrm{nm}$) to generate high-resolution images. The system used in the scope of this thesis is the *Scientific Titan Low Base* from *Thermo Fisher* operated in Scanning Transmission Electron Microscopy (STEM) mode. While in conventional TEM a broad beam with a plane wave front is used to generate the image STEM uses a focused beam similar to SEM to scan the sample.

Lamella Preparation

In TEM and STEM an electron-transparent sample is required as the beam passes through the sample and the detector is placed on the other side. To achieve electron-transparency a lamella is cut from the sample, perpendicular to the surface. To achieve this, FIB milling replaced the cumbersome grinding from past days in most cases. In our case, the Helios 600 presented before was employed for this purpose.
At first, a rectangular Pt deposit of $\sim$ 100 nm thickness is deposited on the region to be extracted, followed by a $\sim$ 1-µm- thick layer of Pt to protect the sample. Thereafter, the lamella is cut via FIB milling from two sides of the deposit.
To achieve FIB milling, the instrument can be operated in different modes, as illustrated in fig. 2.7. In standard operation mode, the generally rectangular pattern is sliced as described in section 1.2.2 and the full pattern is scanned until the desired depth is reached. This results in a box-shaped hole in the sample (fig. 2.7 a).

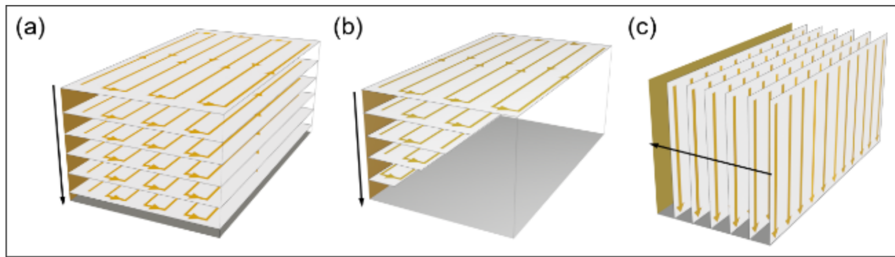

Figure 2.7.: Schematic representation of different milling strategies. (a) In standard mode, a box schaped hole is milled layer-by-layer. (b) In Regular Cross Section (RCS) a wedge shaped hole is milled. (c) In CCS the hole is milled line-by-line. Reprinted from [69].

The process time can be reduced significantly with the Regular Cross Section (RCS) mode of the instrument. In this mode, used for cutting lamellae, the pattern is traced in a staircase manner cutting a wedge-shaped hole. Near the desired lamella the full depth is reached, decreasing over distance (fig. 2.7 b). To optimize the process time, this step is conducted at high ion beam current. The high current employed in RCS leaves the wall of the hole damaged by ion implantation and amorphization. Therefore, a Cleaning Cross Section (CCS) step is employed. In this mode, the pattern is trace line by line always milling to the desired depth before moving to the next line in direction of the desired sample (fig. 2.7 c). This step is performed at a lower beam current to minimize ion damage.
The two processes are performed on both sides of the lamella to cut a slab from the material. The lamella is thereafter picked up by the micro manipulator housed in the process chamber and attached to a grid. While on the grid, the lamella is further thinned with the ion beam at a low beam current to the desired thickness of 50 nm to 100 nm.

Imaging

The Titan Low Base TEM instrument employed in the scope of this thesis is equipped with a high-brightness Schottky field emission gun (X-FEG). The electron beam used in our experiments was accelerated at 300 kV towards the sample and scanned across the surface. The electrons are passing through the sample. In the center of the optical axis a high intensity spot of unscattered electrons passes through the sample. Some electrons, however, are scattered to outer regions.

These scattered electrons are collected by annular detectors. An Annular Bright Field (ABF) detector collects electrons scattered at low angles, a High-Angle Annular Dark Field (HAADF) detector detects strongly scattered electrons. Strong scattering occurs mostly at heavy elements. Therefore, HAADF detectors obtain a strong material contrast. Experiments in the scope of this thesis were conducted using the HAADF detector.

2.3. Magnetotransport at Low Temperatures

Magnetotransport refers to the study of electrical properties, specifically the transport of electrons, in the presence of a magnetic field. Dealing with superconductors, any experiment must be conducted below the critical temperature. In the facilities of the University of Zaragoza, two systems were at our disposal. The Physical Properties Measurement System (PPMS) is available through the *Servicio de Apoyo a la Investigación* (SAI) of the University of Zaragoza. The Cryogenic-Free Measurement System (CFMS) is a system purchased by our group recently and delivered and set up at the beginning of this project. Furthermore, through the collaboration with our project partners at the Eberhard Karls University of Tübingen, some experiments could be run in systems optimized for noise suppression, a crucial aspect in SQUID characterization.

2.3.1. Physical Properties Measurement System

The Physical Properties Measurement System (PPMS) by *Quantum Design* is a versatile and modular instrument designed for the comprehensive characterization of materials under a wide range of conditions. Its primary components include a cryostat supplied with liquid helium and a superconducting magnet coil integrated into a helium dewar. This setup enables precise control over temperature and magnetic fields, making it a highly versatile tool for the characterization of superconducting structures under a wide range of conditions. The 9 T version of the PPMS is shown in fig. 2.8a.
The cryogenic system of the PPMS allows for stable temperatures down to 1.9 K, which are critical for studies involving low-temperature phenomena. The cooling is achieved by evaporation of liquid 4 He. The helium is collected after evaporation and liquefied in a central liquefacation facility at the CSIC-University of Zaragoza.
Two similar instruments are available, differing in the magnet coil incorporated. In the standard system, out-of-plane magnetic fields of up to 9 T are available. The second system can achieve 14 T. Both systems allow the setting of the magnetic field with a resolution of 0.1 mT. In *persistent mode*, the current input and output of the magnet are shorted by a superconducting strip, allowing to disconnect the external current supply. The magnetic field is upheld by a circular supercurrent, ensuring a highly stable magnetic field.
The PPMS features an evacuated sample chamber located within the helium dewar, which is equipped with a 12-pin connector at its base to establish electrical

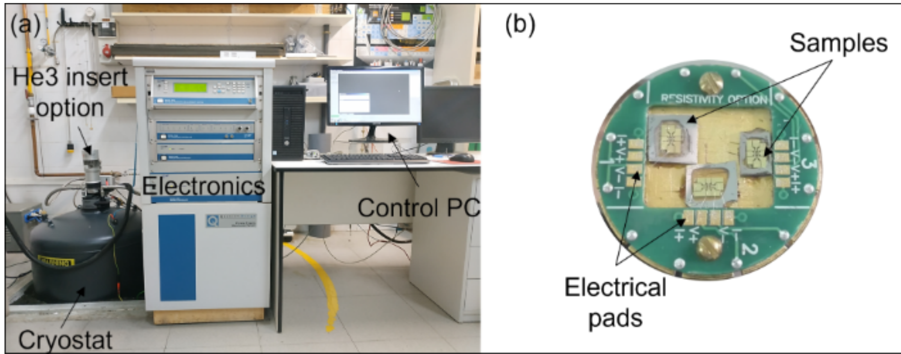

Figure 2.8.: (a) The Physical Properties Measurement System (PPMS) equipped with a 9 T magnet by Quantum Design. (b) Top view of the puck holding three samples, connected to the channels via Al wires. Reprinted from [69].

connections between the instrument and the sample holder, the *puck* (fig. 2.8b). A puck holds up to three samples which are connected to the gold contacts via Al wires. Measurements are typically performed in four-probe configuration, i.e., the sample is biased with a current and a voltage reading is performed and internally converted to a resistance reading using Ohm's law $R = V/I$.
The system is interfaced via the proprietary *MultiVu* software, developed by Quantum Design, allowing one to program nested loops of I, B and T sweeps. Each data point returned by the PPMS is calculated as the average of a predefined number of readings, which the operator sets based on the experimental requirements.
The current source in the system is synchronized to the grid frequency (50 Hz in Spain) and generates a square wave with a frequency of 8.3 Hz (one-sixth of the grid frequency), corresponding to a cycle duration of 120 ms. The current can be set at a resolution of 2.44 nA. It achieves quasi-simultaneous measurement of three samples in parallel by multiplexing the current-sourcing and resistance readout through the three available channels. The system offers two relevant operational modes for resistance measurements: *AC mode* and *DC mode*.

- **AC Mode:** In this mode, resistance measurements are taken during both halves of the square wave cycle (positive and negative, each lasting 60 ms). The system averages these two values across the specified number of cycles to calculate a single data point. This process effectively reduces noise by eliminating internal offsets and minimizing thermoelectric effects within the sample.
- **DC Mode:** Here, measurements are taken during only one half of the square wave cycle, as defined by the user, and averaged across multiple

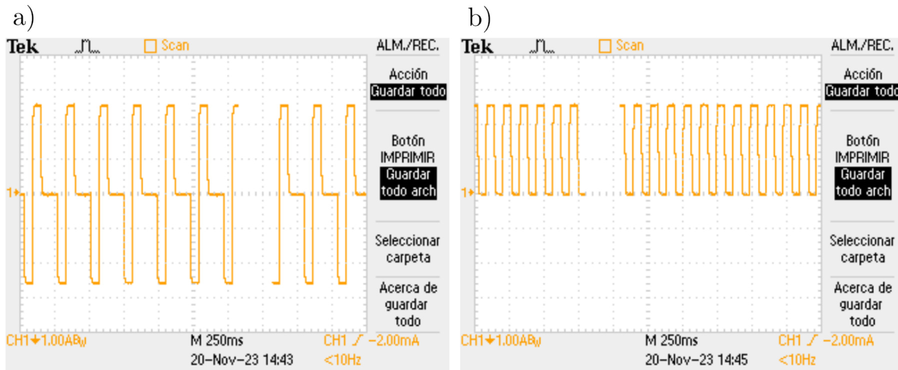

Figure 2.9.: Oscilloscope recordings of the current output of the PPMS in (a) AC mode and (b) DC mode.

readings to produce a data point. While this mode does not offer the same level of noise reduction as AC mode, it preserves information about any asymmetry in the sample's resistance response.

Although AC mode provides superior noise suppression, it assumes that the sample's resistance response is symmetrical with respect to the current's direction. If this condition is not met, the averaging process may distort the data, potentially suppressing real sample features. Therefore, careful consideration is necessary when selecting the appropriate measurement mode to ensure accurate and meaningful results.

2.3.2. Cryogen-Free Measurement System

The Cryogenic-Free Measurement System (CFMS) by *Cryogenic Ltd.* is a versatile research platform similar to the PPMS. It features a cryogenic dewar allowing for magnetotransport experiments at temperatures as low as 1.6 K. It also features a superconducting magnet going up to 9 T at a resolution of 0.18 mT.

In contrast to the PPMS, however, its structure is more modular. The puck offers 20 electric contacts that can be freely connected to instruments via a breakout box. The cryogenic system consists of two distinct helium circuits. The outer circuit is connected to a compressor, liquefying the helium on the spot. The dissipated heat is exchanged with the environment via a heat exchanger and the liquefied helium provides the cooling power for the base temperature, cooling the dewar and the superconducting magnet. The inner circuit, the Variable Temperature Insert (VTI), is cooled by the outer circuit. Gaseous

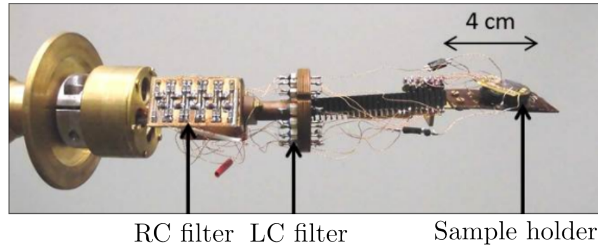

Figure 2.10.: Probe used in the liquid helium dewars. *Photography:* Julian Linek.

helium is circulated and liquefied inside the dewar. It is used to cool down the sample space and can be controlled independently of the outer circuit.
The system comes with two distinct software suites, one to control and monitor the cryostat, and the other one dedicated to set up magnetotransport experiments. All parameters required to run experiments, i.e., the sample temperature, the magnetic field and the bias current, can be set and read via the software, directly at the front panel or via the Virtual Instrument Software Architecture (VISA) interface of the instruments.
As a current source, the Keithley 2450 Source Measure Unit (SMU) is available, allowing to bias the sample with current resolution of 500 fA. Voltage readings are performed by a Keithley 2182A NanoVoltMeter (NVM) at a resolution of up to 1 nV. In chapter 3 we present more details about the flexibility of this design offers to customize and automate experiments run.
A more comprehensive introduction to the Cryogenic-Free Measurement System (CFMS) is given in chapter 3

2.3.3. Systems at the University of Tübingen

The group of Dieter Kölle at the Karl Eberhard University of Tübingen is specialized to the characterization of SQUIDs. They have several systems available dedicated to the characterization of SQUIDs at their disposal. During two research stays in their lab we were able to make use of these systems.

Electronics

In the laboratory great effort has been made to reduce environmental noise in these systems. All electronics, except a single cable to control the setup, is placed inside a steel cage and is powered by a battery. The steel cage shields the setup from high-frequency radiation surrounding us all the time. The battery ensures decoupling from the 50 Hz frequency of the power grid.

The sample holder is equipped with an RC lowpass-filter with a cutoff frequency of 1.7 kHz and an LC filter in the vicinity of the sample and at the same temperature. This allows one to filter thermal noise current I_{th} from the electronics at room temperature. The sample holder is encapsulated in a cup made of mu-metal, further shielding parasitic radiation. Figure 2.10 shows an image of an exemplary probe. All probes are equipped with the same filters.
At the core of the measurement electronics is an *PCI-6014* multifunction I/O device from National Instruments. The card features a 16-bit Analog-to-Digital Converter (ADC) in a range of ± 5 V and an internal gain of (0.5, 1, 10, 100) Together with the pre-amplifier in use a voltage resolution of 0.763 nV is possible. The sampling rate of the PCI is 100 kHz. The current source and the probes are built in-house.
The electronics is controlled by a custom program taylored towards SQUID characterization. It features two independent current sweeps, one for biasing the sample and the other to set the magnetic field via a superconducting coil of known inductance or via a modulation line (see section 4.2.5). During these sweeps, the voltage is continuously measured.
It furthermore features a direct I_{c} measurement routine. After the definition of a voltage threshold V_{th}, the bias current is increased until the sample switches to the normal state, hence the threshold is reached. The program disregards the data collected before and only saves the last bias current before the transition in dependence on the current used to induce a magnetic field.
However, direct control over the magnetic field is not possible. The applied magnetic field has to be calculated from the coil's inductance or normalized by the modulation period which is assumed to be equivalent to the magnetic field required to have a magnetic flux through the loop equal to Φ_0. Furthermore, temperature monitoring or control is not possible in the software and has to be managed externally.

Cryogenic Systems

The group mostly works with Nb SQUIDs that have a critical temperature of 9.2 K [128]. Commonly, the experiments are therefore conducted in liquid helium at 4.2 K, obliterating the need for a cryostat. The probe holding the sample is submerged in a dewar containing the liquid helium in thermal equilibrium. The process is simple and fast and many samples can be characterized in short time.
The facilities also provide a cryostat capable of cooling down samples to 300 mK. Therefore, a probe with closed circuit of ^{3}He is submerged in a bath of ^{4}He, cooling the probe to 4.2 K. At this temperature, the ^{3}He adheres to the acti-

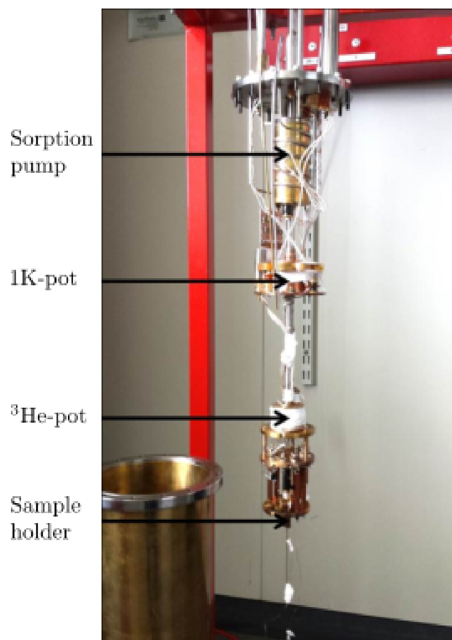

Figure 2.11.: Image of the probe for the cryostat. *Photography:* Julian Linek.

vated charcoal of the sorption pump. By decreasing the pressure in the 1 K-pot, the boiling temperature of the ^{4}He decreases down to the range of 1 K. Heating the charcoal, the ^{3}He degases and condensate in the ^{3}He-pot. Decreasing the charcoal temperature again lowers the pressure and the ^{3}He is readsorbed by the charcoal, cooling the sample space down to 0.3 K. Operation at 1 K to 2 K is possible without the ^{3}He circuit, pumping the 1 K-pot is sufficient. In this probe, the sample space is evacuated to the range of 10^{-7} mbar.
However, the operation is cumbersome compared to the PPMS and CFMS and a cooldown requires two to three days as the entire cryostat has to be heated up and cooled down again to change the sample. Effectively, only one cooldown per week with three samples on the sample holder is possible, drastically limiting the number of experiments that can be conducted, especially on a limited stay in the facilities.

Chapter 3

Cryogen Free Magnet Setup

Contents

3.1. The Cryostat 75
3.1.1. The Primary Circuit 75
3.1.2. The Variable Temperature Insert 76
3.2. Electronics 79
3.3. Operation 81
3.3.1. Preinstalled Interface 81
3.3.2. Development of a Custom Interface 81
3.3.3. User Guide 84
3.4. Testing the System 86
3.4.1. Cooldown 86
3.4.2. Electric Characterization 87
3.4.3. Magnetic Field 89
3.5. Summary 91

3.1. The Cryostat

The Cryogenic-Free Measurement System (CFMS) from Cryogenic Ltd. forms an experimental setup for the characterization of electric and magnetic properties of samples at cryogenic temperatures. It features a 9 T superconducting magnet and can reach a base temperature of approximately 1.6 K. It was delivered to our facilities on June 8, 2021, right in the beginning of this project and amidst the COVID-19 pandemic from the United Kingdom. Due to COVID restrictions, the company could not send a technician to help us and the Spanish vendor had to carry out the installation process.
The CFMS is a self-contained device, which requires no external helium supply. At its core it consists of a cryostat, housing a superconducting NbTi magnet ($B \leq 9\,\mathrm{T}$) and a sample space to measure a specimen at cryogenic temperatures. Further peripherical devices are required to ensure a stable operation of the system. The main components are shown in section 3.1.

3.1.1. The Primary Circuit

The cryostat is cooled by a closed primary helium circuit to a temperature of 3 K to 4 K. Therefore, the helium is liquefied in a compressor located in a separate room next door. The dissipated heat is transferred to water and released into the ambient air by a heat exchanger. The liquid helium is inserted into the cryostat via well-insulated hoses where it evaporates and the gaseous helium is, together with the absorbed heat, returned to the compressor.
The sample is inserted into the cryostat via a vertically mounted probe. Before cooldown, the sample space is evacuated by a secondary scroll pump and charged with 0.1 mbar helium as a contact gas. For sample insertion, the probe is introduced into a load lock, separated from the sample space by a gate valve, and evacuated via an auxiliary pump. Flushing the load lock with helium helps to ensure a contaminant-free sample space.
For thermal insulation of the cryostat to the environment a high quality vacuum ($< 10^{-3}$ mbar) in the vacuum space is required, ensured by a Turbo Molecular Pump (TMP). The purpose of the primary circuit is to provide sufficiently low temperature for the superconducting magnet and the cooling power for a secondary circuit, the Variable Temperature Insert (VTI), to cool down the sample space to a base temperature of $\approx 1.6\,\mathrm{K}$. The VTI consists of a helium dump and an oil-free scroll pump (VTI pump).

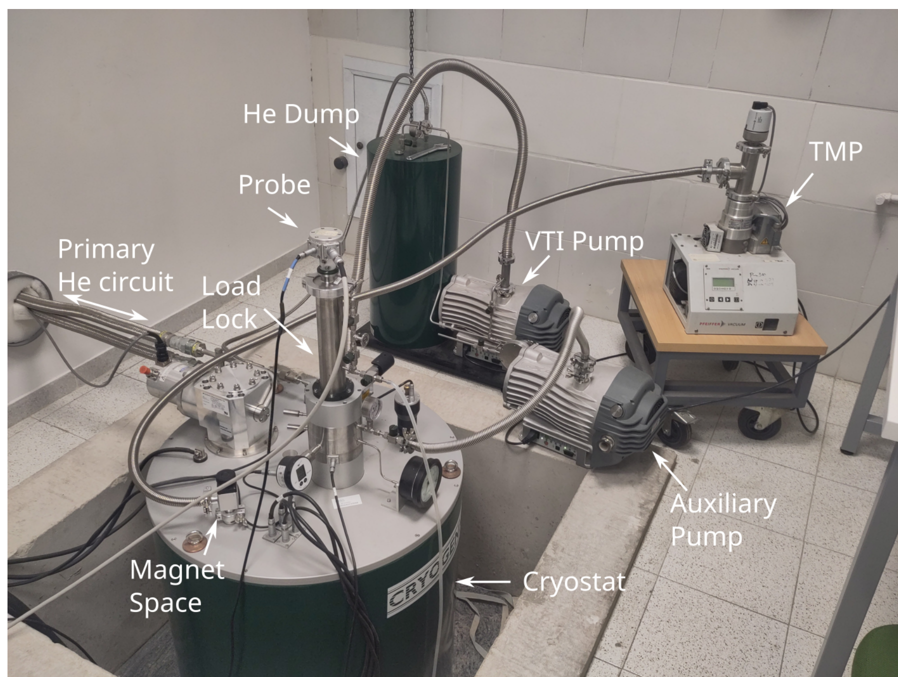

Figure 3.1.: Main components of the CFMS. The cryostat is thermally shielded by a vacuum inside the *Magnet Space*, generated by the *TMP*. The cooling is done in a *Primary He circuit*, connected to a compressor and a water chiller in the room next door. A secondary helium circuit, the VTI, is driven by the *VTI* pump, circulating helium stored in the *He Dump*. The sample is at the lower end of a long *Probe*. Samples are exchanged via a *Load Lock*, evacuated by the *Auxiliary Pump*.

3.1.2. The Variable Temperature Insert

The Variable Temperature Insert (VTI) is a secondary helium circuit in the CFMS used to cool down the sample space to a base temperature of $\approx 1.6\,\mathrm{K}$. The circuit is schematically depicted in fig. 3.2. It is driven by an oil free scroll pump, pumping the helium from the outlet of the VTI into a helium dump. From the dump, the helium enters the the VTI through a charcoal filter at approximately 60 K. Remaining, inavoidable impurities in the helium gas, e.g. N_2 and O_2, condense at these temperatures and are adsorbed by the charcoal, a crucial feature to avoid a blockage of the circuit by freezing of the gases at cryogenic temperatures.
Upon passing through a 40 K and a 4 K stage which are in thermal contact with the primary circuit, the helium condenses in the helium pot. The helium

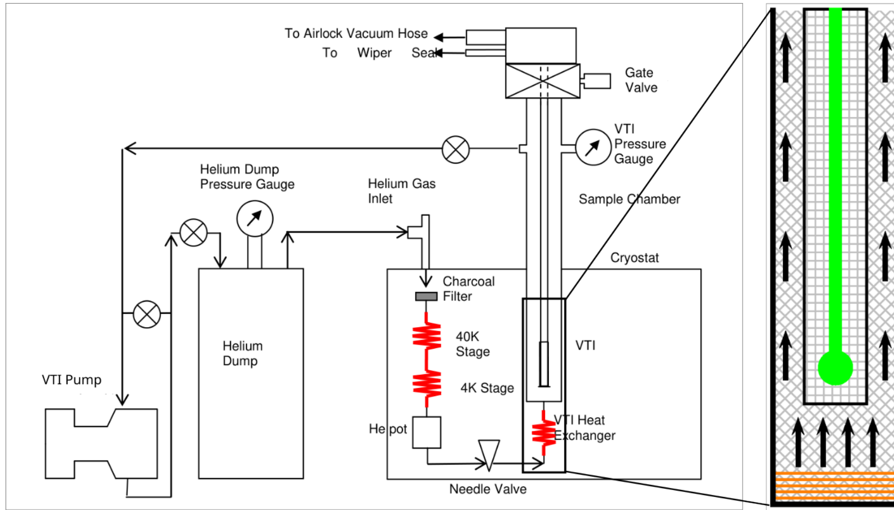

Figure 3.2.: The Variable Temperature Insert (VTI), responsible to cooldown the sample space to a base temperature of ≈ 1.6 K. The inlay represents the sample chamber with diagonal squares indicating flowing helium in the VTI while upright squares represent static helium inside the sample space responsible for thermal contact of the sample to the VTI. Reprinted from [129].

pot is connected to the VTI through an electrically controllable needle valve. Inside the VTI a pressure of 2 mbar to 5 mbar is maintained by the VTI pump. The low pressure in the VTI lowers the boiling temperature of the helium to 1.5 K to 1.6 K, marking the lower physical limit of the temperature.
The base temperature is dependent on the pressure in the VTI which determines the boiling temperature of the helium and the volume flow through the needle valve, determining the heat that can be extracted from the sample space. The volume flow depends on the pressure difference between the helium pot and the VTI and the impedance of the constriction, controllable by the needle valve. In order to adjust the driving pressure, the helium pot temperature can be controlled by an additional thermal element and is adjusted according to the VTI temperature. The needle valve impedance is controlled by controlled heating of a wax element expanding upon heating and thus closing the valve.
Upon passing through the needle valve, the cold helium passes through a heat exchanger used to heat the gas to the desired VTI temperature. Afterwards, it passes by the outer wall of the sample space. The sample is suspended within the sample space and in thermal contact with the VTI via static helium inside the chamber.

The sample temperature is controlled by a second thermal element with less power but higher precision than the VTI heat exchanger. For optimal control of the sample temperature the VTI temperature is set to temperatures just below the desired sample temperature. For temperature stability, the VTI is commonly heated above the physical limit so that the heating element can account for changes in pressure and flow rate.

3.2. Electronics

The control units and electronics for sample characterization are mounted in a rack as depicted in fig. 3.3. The electronics available are:

- **Keithley 2450 SMU**: Source Measure Unit used as a current source.
- **Keithley 2182A NVM**: NanoVolt Meter to measure the voltage.
- **Cryogenics Ltd. SMS Series**: Magnet controller.
- **Lakeshore 350**: Temperature controller used to monitor and control
  - Sample temperature,
  - VTI temperature,
  - Helium pot temperature,
  - Charcoal temperature (monitoring only).
- **Lakeshore 218**: Temperature monitor for various system temperatures.
- A computer to run the control software.

The electronic connection between the SMU, the NVM and the sample is realized by a breakout box, allowing to realize connections to arbitrary contacts. The probe is equipped with 20 lines running to the sample in twisted pairs. For high precision measurements the two directions of a signal should run through the two wires of a pair in order to (partially) cancel out electromagnetic interference.

The connection from the breakout box to the probe is realized by a shielded cable holding the individual signal lines and additional control lines for various probes with additional functionality. The connection between the breakout box and the SMU, the NVM, however, is realized through individual unshielded cables. We identified the unshielded cables as a major source of electronic noise through ElectroMagnetic Interference (EMI) [130].

Therefore, we designed and fabricated, with the help of the Electronic Instrumentation Service of the Research Support Service of the University of Zaragoza, a breakout box using coaxial cables and BNC connectors. Furthermore, we added an additional ground-switch to prevent electrostatic discharge at mounting the sample to the probe. Both breakout boxes are shown in fig. 3.4.

Furthermore, we hooked up an additional *Keithley 2611A* SMU serving as a secondary current or voltage source, e.g. to inject a modulation current in SQUID experiments or apply a gate voltage in gating experiments.

Figure 3.3.: The CFMS rack equipped with the measurement electronics.

a)

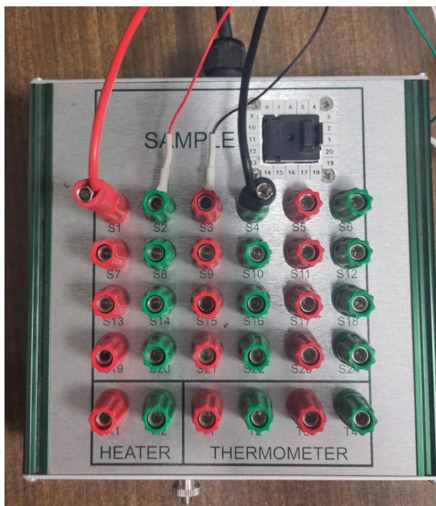

b)

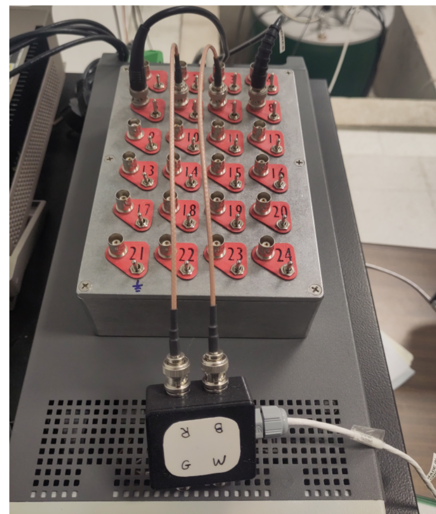

Figure 3.4.: (a) The breakout box used to select the channels connected to the instruments as delivered by Cryogenics Ltd. The cables connecting the box to the instruments are not shielded, making them susceptible to EMI. (b) The custom made breakout box replaces the unshielded cables by coaxial cables connected via BNC. Furthermore, a grounding switch for protecting the sample from electrostatic discharge while mounting and unmouting it to the probe.

3.3. Operation

3.3.1. Preinstalled Interface

The CFMS was shipped with two preinstalled inedpendent runtimes based on LabView.
One of the interfaces is used to monitor and control the cryogenic components of the system, i.e., the VTI. The software basically monitors the VTI pressure and controls the cell temperature of the needle valve, thus adjusting the impedance of the valve. This VTI control interface is displayed in fig. 3.5.
In temperature control mode, the temperature of the cell is kept at a constant value, not changing the impedance. For constant VTI temperature this is usually sufficient. However, when the VTI temperature is changed the differential pressure varies and the needle valve should be adapted accordingly. This is accomplished by the pressure control mode where a Proportional-Integral-Derivative (PID) controller adjusts the cell temperature to maintain a constant pressure in the VTI. However, the latency of the system is high and the controller can only maintain the pressure on average around the target value. Therefore, the VTI temperature is usually set above the physical minimum so that the temperature controller can account for altered helium flow and pressure.
The second interface allows the user to monitor all relevant measurement and sample parameters and set the parameters in real time where applicable. Furthermore, experiments could be designed and run automatically. However, the interface was not fully mature. Bugs in the software required work-arounds, such as the output of the current source was turned off at start of the measurement under certain nested loop configurations and had to be re-activated manually on the front panel of the SMU. Furthermore, the LabView script was delivered as a compiled binary without access to the source, restricting the user to routines considered by the developers.

3.3.2. Development of a Custom Interface

In an early phase of the project, we put forth efforts to understand the response of SQUID devices equipped with a modulation line for compatibility with the laboratories in Tübingen. With the pre-installed interface it was not possible to synchronously sweep an additional current source, prohibiting the measurements of IV-characteristics at altering modulation currents without cumbersome manual adjustment of I_m.

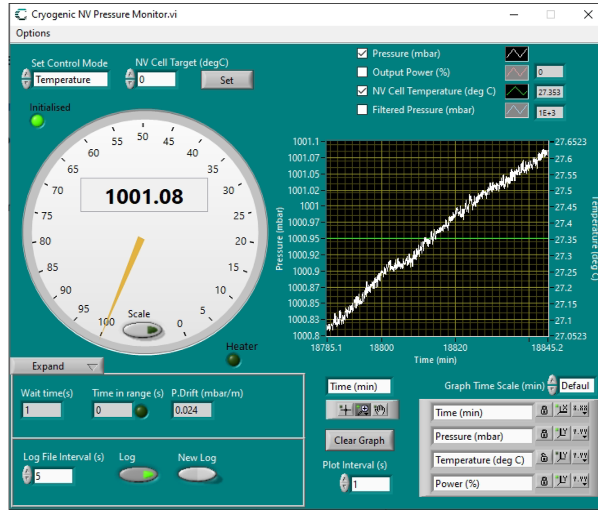

Figure 3.5.: The VTI control interface for the needle valve. The pressure in the VTI is adjusted via a needle valve that can be controlled by varying the temperature of a thermally expanding cell. In temperature control mode the cell temperature is kept constant, in pressure control mode a PID attempts to maintain a stable VTI pressure by adjusting the cell temperature.

Furthermore, a programmable voltage threshold to automatically detect I_c can potentially speed up a measurement tremendously. Upon reaching the voltage threshold, the last current setpoint is saved to the data file, the IV is interrupted and the magnetic field or the modulation current can move to the next setpoint.
To augment the capabilities of the system and to overcome some of the bugs, a custom user interface was developed on the basis of Python. Starting out as dedicated scripts for simple experiments, over time a full-fledged runtime with a Graphical User Interface (GUI) was developed.
The instruments are interfaced via the Virtual Instrument Software Architecture (VISA) [131] Application Programming Interface (API), implemented on all available instruments readily accessible with the `PyVISA` library [132]. The Keithley and Lakeshore instruments are controlled via Standard Commands for Programmable Instruments (SCPI) [131] commands while Cryogenic's SMS magnet controller follows an instrument specific set of commands.
The GUI is based on the Qt framework [133], accessed via bindings provided by the `PyQt6` [134] library. The graphical components are generated in Qt Designer. It consists of a main window shown in fig. 3.6 composed of severalitor widgets displaying and controlling the system:

- **Main Widget**: Plot of the measured data in real time.

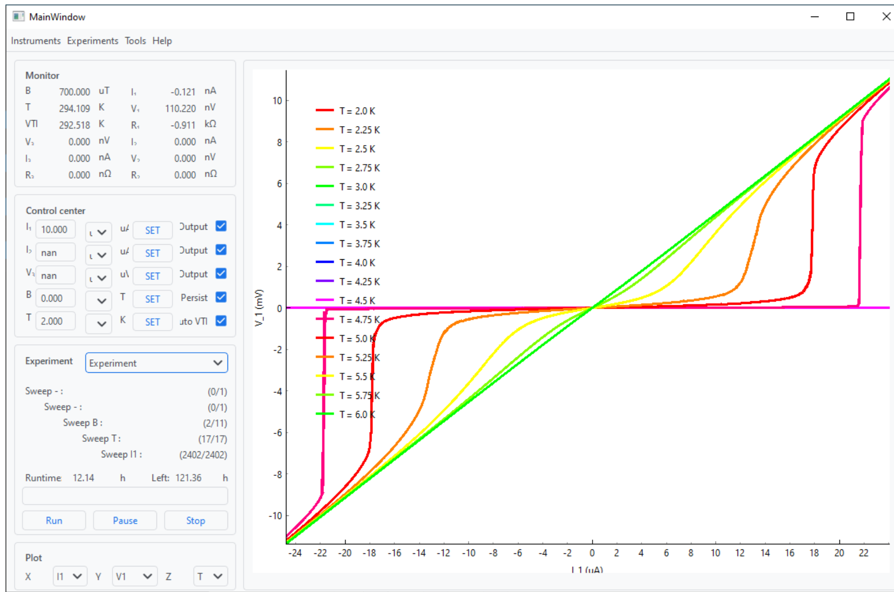

Figure 3.6.: Main window of the custom user interface developed for the CFMS. The main widget shows a plot of the measured data in real time and can be controlled by the *Plot* widget. The *Monitor* widget shows the last reading. In the *control* widget, the settable parameters can be adjusted and the *Experiment* widget allows the selection and control of experiments.

- **Monitor**: Showing the last reading relevant to measurements in real time.
- **Control center**: Controlling setpoints of the settable parameters.
- **Experiment**: Selection and control of the active experiment and display of the current state. The selected experiment is also plotted in the main widget.
- **Plot**: Control over which parameter to display on the axes of the main plot window. The Z setting controls according to which parameter the measurements should be categorized and plotted in different colours.
- **Menu bar**: Access to instrument- and experiment settings.

When launching the program it defaults to the *Monitor* experiment, continuously reading all connected instruments and plotting voltage over time. Custom experiments can be created, loaded and saved from the *Experiments* menu item. Figure 3.7 shows the experiment editor, consisting of the definition of the nested loop configuration (fig. 3.7a) and the definition of the steps within the sweep of an individual parameter (fig. 3.7b).

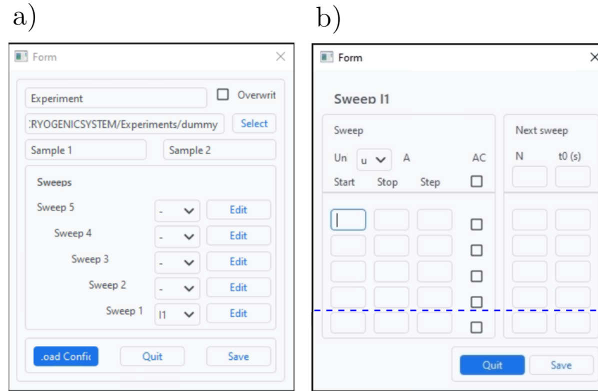

Figure 3.7.: Experiment configuration in the custom interface. (a) Set up the nested loop of various sweeps and the experiment's meta information. The *Name* is used as an identifier in experiment selection. *Path* denotes the directory to save the result at, overwriting or adding a numbered version according to *Overwrite*. (b) Window for setting the sweep itself. Ranges of different start, stop, stepsize and *AC* or DC mode can be configured. The unit of the values can be selected in a drop down menu. *N* and *t0* denote the number of repititions and delay. The menu is cropped at the dashed blue line.

Experiments are identified by a name and an output directory for the data- and config-files is provided. The sample(s) currently measured can be named too. If the *Overwrite* checkmark is selected existing files are overwritten, otherwise a number is added to the end of the name. Five nested loops are provided and the sweep parameter is selected.
For the definition of the individual sweep a prefix to the unit, the start- and stop-values and the stepsize are provided. Optionally, like in the PPMS, AC-mode can be selected and a number of repitions for the next step at each setpoint can be defined. Lastly, a delay before the next step can be provided. In case of the innermost sweep the next step is the voltage reading, otherwise the following sweep.
The code base of the custom user interface for the CFMS is hosted on a GitHub repository. Upon request, we are happy to provide access to the repository.

3.3.3. User Guide

On the host system, we host a wiki of the system written in markdown [135] and compiled via *Read the Docs* [136]. The wiki (see fig. 3.8) consists of a manual on system operation and troubleshooting based on our own experiences, expanding

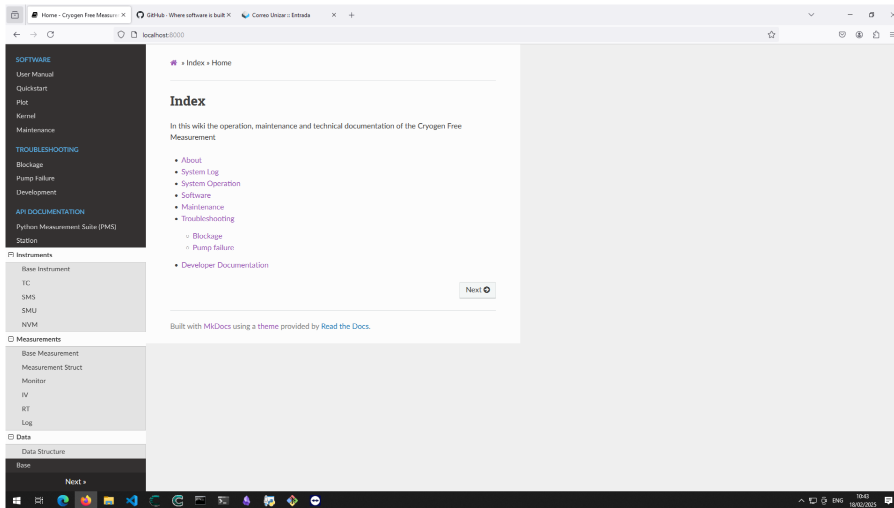

Figure 3.8.: Index page of the wiki of the CFMS. The wiki contains the documentation of the operation, maintenance and troubleshooting of the system as well as a digital labbook and the documentation of usage and code of the custom user interface.

on the documentation provided by Cryogenics Ltd. An operator-maintained log, a digital labbook, is available as well. Furthermore, a manual to the usage of the software and the documentation of the code base can be accessed here.

3.4. Testing the System

3.4.1. Cooldown

Running up the system and cooling it down to base temperature is a time consuming process until all the heat is removed from the system and takes between 1 and 2 days. Figure 3.9a shows the cooldown of the magnet space and the VTI. The VTI pressure and the charcoal temperature are given as a reference as well.

When the system is idle, the temperature of all components are in equilibrium with the environment and the VTI pressure is in equlibrium with the pressure in the helium dump, slightly (~ 50 mbar) above ambient pressure. In a first step, the charcoal and the VTI are heated up to 320 K, the maximum of the temperature controller, and helium is circulated in order to degas the charcoal filter and evaporate potential contaminants from the rest of the system.

In a second step, the needle valve is closed entirely and the VTI is evacuated. Thereafter, the heater of the charcoal is switched off and the outer helium circuit is activated to cooldown the system. The thermal capacity of the magnet is high and dissipation of all the heat requires approximately 18 h. Once the magnet is cold, the needle valve is opened to adjust a VTI pressure of ≈ 15 mbar, initializing the cooldown of the VTI.

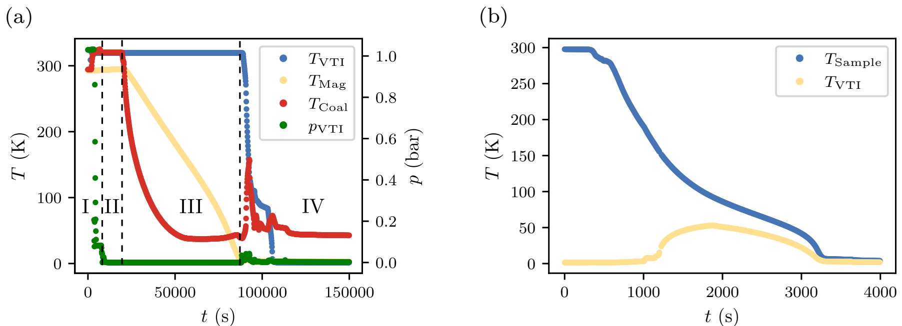

Figure 3.9.: Cooldown of the CFMS. (a) Cooldown of the system from room temperature. (I) At first, the charcoal and the VTI are heated up to 320 K and helium is circulated in the VTI to remove contaminants from the system. (II) In a second step, the VTI is fully evacuated. (III) Upon evacuation, the primary circuit is turned on and the system is cooling down. (IV) As soon as the magnet reaches base temperature, helium is pumped in the VTI, cooling the VTI to base temperature. (b) Insertion of the probe carrying a sample with the system at base temperature. The heat introduced by the sample temporarily increases the VTI temperature.

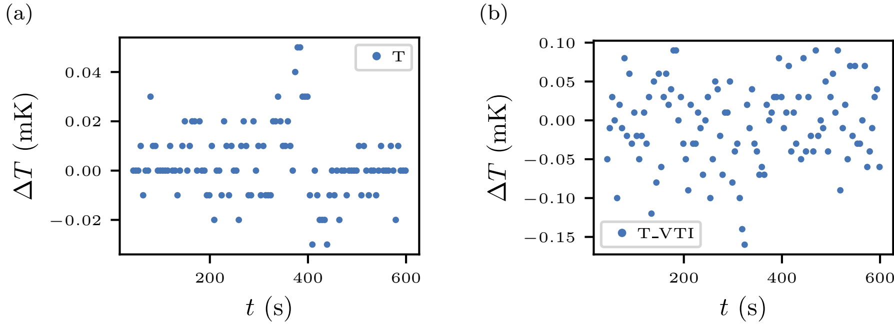

Figure 3.10.: Temperature stability of the CFMS. (a) The sample temperature deviates around the target value (2 K) by ±0.014 mK, (b) the VTI around the target (1.6 K) by ±0.052 mK.

Once the system is at base temperature and stable, inserting a sample mounted on the probe is a fast process. Figure 3.9b shows the sample- and VTI temperature during upon inserting a sample. The probe is lowered in several steps in order to decrease the load on the VTI. The full cooldown takes approximately one hour.
Once the VTI and the sample are in thermal equilibrium, the thermal stability is remarkably high. Figure 3.10 shows the sample- and VTI temperature over 10 min. The standard deviation in this period is ±0.052 mK at the VTI ($T = 1.6$ K). The finer temperature control at the sample achieves a temperature stability of ±0.014 mK at $T = 2$ K.

3.4.2. Electric Characterization

Initial experiments on the electric characterization of long-bridge SQUIDs (section 4.2.1) revealed noise in the transition regime with strongly deviating voltage readings (fig. 3.11a). We had observed similar behavior in samples submerged in a bath of liquid helium at the facilities of our collarborators in Tübingen (see section 5.2.1). In the liquid helium dewar, the behavior was attributed to strong deviations in local temperature due to boiling helium.
In the CFMS, the sample space is filled with helium (≈ 150 mbar) as a contact gas between the VTI and the probe. Figure 3.11b shows the voltage over time at 43 µA, just above the transition while evacuating the sample space. As the pressure in the VTI decreases, the oscillatory behavior is reduced and the voltage stabilizes in the resistive regime.

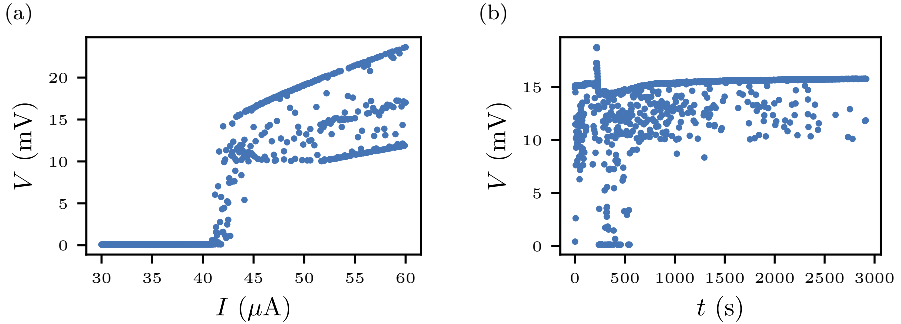

Figure 3.11.: (a) IV characteristics of a SQUID. In the transition range, the voltage exhibits oscillatory behavior which we attribute to sudden, local temperature variations due to condensing and evaporating helium. (b) The voltage of the SQUID in the transition range at 43 µA over time while evacuating the sample space. At lower helium pressure a decrease in the oscillatory behavior is observed.

We attribute the outliers to helium condensing on the chip and boiling off due to the dissipated heat of the SQUID in the resistive regime, in analogy to the behavior observed when measuring directly in a bath of liquefied helium. As the pressure decreases the amount of helium and the boiling point are decreased, resulting in less helium condensing on the sample and reducing the frequency of the effect occuring.

This observation results in a trade off between thermal contact between the sample and the VTI and the stability of the measurement near the transition region from superconducting regime to the normal state.

Nevertheles, at sufficiently low helium pressure, high quality measurements are possible. Figure 3.12 shows the electric properties of a short-constriction SQUID (section 4.2.2) measured during the cooldown presented in section 3.4.1. The measurement was conducted using the custom-made breakout box (fig. 3.4b) where the unshielded cables are replaced with coaxial cables in order to avoid EMI.

The IV characteristic exhibits a sharp transition with a clearly defined critical current at the upsweep. At the downsweep, a pronounced thermal hysteresis (common in constriction-type SQUIDs) is clearly visible and the retrapping occurs in a sharp step as well. These findings hint at a measurement with low noise (section 1.3.3).

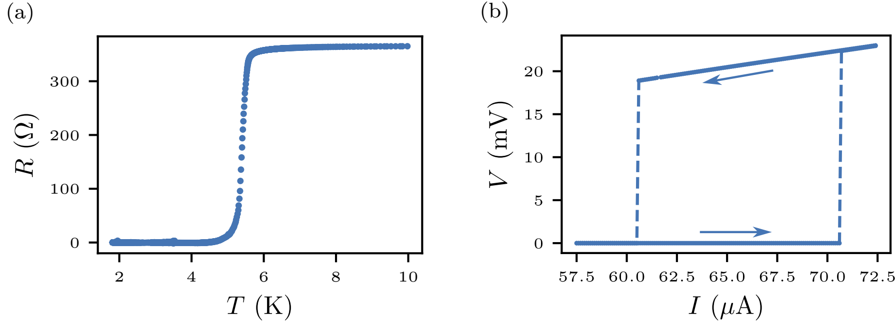

Figure 3.12.: Transport characterization of a short-constriction SQUID in the CFMS after optimization. (a) The resistance over temperature of the sample introduced in the system during the cooldown presented in section 3.4.1. (b) The IV characteristics of the sample at 2 K. A sharp transition and a large thermal hysteresis are observed, in agreement with the expectation of a constriction-type SQUID in a low-noise equipment.

3.4.3. Magnetic Field

The CFMS is equipped with a superconducting NbTi coil and a Superconducting Magnet power Supply (SMS120C) magnetic field controller built by Cryogenics Ltd. The coil has a magnetic field constant of 950.36 G/A and an inductance of 16.56 H [129].
The magnet is equipped with a persistent mode switch. The magnet is shunted by a superconducting contact coupled to a small heater. In normal mode, the heater is switched on, resulting in a resistive shunt. As the magnet is superconducting, the normal conductor acts like an open switch (fig. 3.13b).
If the heater is turned off, however, the shunt is superconducting as well. A superconducting circular current establishes in the magnet and becomes independent of the current source (fig. 3.13c). The resulting magnetic field is not dependent on instabilities in the current source and highly stable[1].
The SMS120C magnet controller is euqipped with a current source allowing for currents of up to ±120 A. The maximum allowed magnetic field of the coil is 9 T, limiting the current to 94.7 A. The Digital-to-Analog Converter (DAC) has 16 bit, presumably one of which is the sign bit. The current resolution therefore is 3.66 mA, corresponding to a magnetic field resolution of 0.348 mT.

[1]In our case, monitoring the stability of the magnetic field is not possible. The magnetic field reading is given by a measurement of the current sourced by the SMS120C. In persistent mode, the current inside the magnet is independent of the source, rendering the reading meaningless.

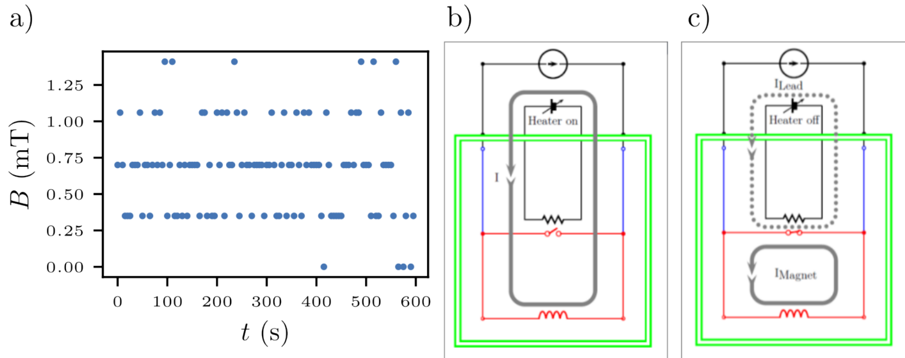

Figure 3.13.: (a) Magnetic field of the CFMS over time at a setpoint of 0 mT. The current source can not be switched off programatically and the magnetic field oscillates around (0.68 ± 0.32) mT with a peak-to-peak distance of 1.4 mT. (b, c) Schematic representation of the persistent mode. A heater is used to switch a shunt of the magnet between superconducting and normal state. The resistive shunt acts like an open switch (a). If the shunt is superconducting (b) the current in the magnet is circulating independently of the current source, resulting in a highly stable magnetic field.

Figure 3.13a shows the magnetic field over time at a setpoint of 0 mT. The output of the current source can not be turned off without cutting power to the power supply. Instead, the magnetic field fluctuates around the second possible setpoint of 0.7 mT. The average is calculated as (0.68 ± 0.32) mT. The peak to peak distance is 1.4 mT.
Unfortunately, this has significant practical implications. As we will see in chapter 5, the expected period in our SQUIDs is around 5 mT. The standard deviation of the magnetic field stability in the CFMS is 6.4 % thereof and the peak-to-peak distance accumulates to 28 %.

3.5. Summary

The CFMS is a cryogenic setup with virtues and drawbacks. The cryogen-free approach is ingenious, making the system self-sufficient and independent of additional facilities. The accessibility of all the electronic instruments via VISA provides a large amount of flexibility and liberty in setting up experiments, not feasible in instruments like the PPMS where the system can only be interfaced via the pre-installed GUI.
However, the liberty also comes at a hefty price, partially due to the COVID pandemic and the lack of professional installation, partially by design. Getting the VTI to run stable took a lot of time and effort and experimentation, also hindered by the documentation that is ambiguous at times and incomplete at others. Other design decissions are not readily understandable, such as the use of unshielded cables connected to ultra-precise electronics.
After all, no experiments conducted in the CFMS are presented in the remainder of this thesis. After initial effort, the oscillatory behavior presented in fig. 3.11a and the limited magnetic field resolution (fig. 3.13a) was observed and the scientific effort was focused on measurements in the PPMS and in the setups of our collaborators in Tübingen.
Nevertheless, the deeper understanding of the system and the development of the custom interface was continuously continued at a lower priority. The relationship between the oscillatory behavior in the transition range and the helium pressure in the sample space, for example, was only found after two years and only near the end of the thesis the breakout box using coaxial cables was ready. For this project, not enough time was left to fully explore the capabilities of the system with the improved noise suppression.
However, the hard limitation for SQUID characterization of this size is the magnetic field resolution. Although the instrument is equipped with a persistent mode switch and a highly stable field can be set, the real value of this field remains unknown within a range of 1.4 mT, corresponding to approximately 30 % of the expected period. Precise characterization of a SQUID modulation in our samples is therefore not feasible and this limitation can only be overcome by the purchase of a more precise current source.

Chapter 4

Ga^{+}-FIB for SQUID Fabrication

Contents

4.1. Deposition of Tungsten-based Nanostructures 95
4.1.1. Conditions on Cantilevers 95
4.1.2. Beam Current 97
4.1.3. Dwell Time 99
4.1.4. Deposition Rate 101
4.2. SQUID-Design Approaches 104
4.2.1. Long Nano-Bridges 104
4.2.2. Short Constrictions 108
4.2.3. SNS-Junctions 110
4.2.4. Deposition on Cantilevers 112
4.2.5. Incorporation of a Modulation line 113
4.3. Summary 116

4.1. Deposition of Tungsten-based Nanostructures

The objective of the project is the functionalization of SPM cantilevers. However, this platform poses additional challenges and can not be fabricated in house but is provided by our collaborator A. Knoll at IBM Zürich. Thus, for an initial understanding of SQUID characteristics based on W-C fabricated by means of FIBID we carry out our first experiments on large, well understood Si/SiO_2 chips.
Initial experiments on SQUIDs fabricated on large Si/SiO_2 chips resulted in functional SQUID devices, shown in detail in section 5.4.1. However, the transfer to cantilevers proved challenging and recipes developed on large chips did not work out of the box on cantilevers.
In this section, we present the common parameters developed in our laboratories for FIBID with Ga^+ ions using the $W(CO)_6$ precursor. At first, in section 4.1.1. we provide a brief overview of the key characteristics the specific cantilever geometry introduces. In section 4.1.2 and section 4.1.3 we outline the development process for the key parameters beam current and dwell time, respectively. In section 4.1.4 we investigate the difference in deposition rate between large chips and cantilevers.

4.1.1. Conditions on Cantilevers

In FIBID, the deposition of the target material strongly depends on the availability of precursor molecules within the beam spot. In section 1.2.2 we introduced the main mechanisms governing the interplay of adsorbtion, desorption and dissociation. In this section we take a look at the key differences between large chips and the cantilevers that we target to deposit the final SQUIDs on.
The geometry of the cantilever introduces a directional dependence near the apex of the tip. On a large chip, diffusive resupply of precursor molecules can occur from an infinite distance in either direction from the beams spot. On a cantilever, however, the lateral region from which diffusion can occur from infinity is limited to an opening angle of 90°, in other directions the reservoir is limited by the edge of the cantilever. These conditions are schematically shown in fig. 4.1a and fig. 4.1b.
The primary availability of precursor gas is governed by the position of the GIS needle. For high reproducibility, it is crucial to operate exactly in the eucentric height and properly adjust the needle with respect to the eucentric height and the optical axis of the microscope.

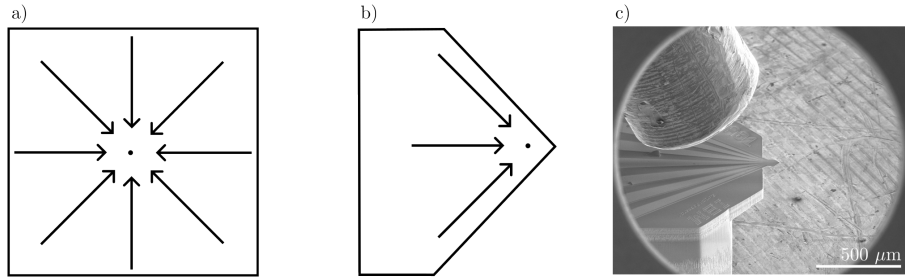

Figure 4.1.: Schematic representation of the diffusion conditions on large chips and cantilevers. (a) On large chips, the gas molecules can diffuse from any direction. (b) On a cantilever, however, the region is limited to a 90° range, with a limited range in other directions, resulting in lowered precursor supply via diffusion. (c) SEM micrograph of a cantilever showing the alignment of the GIS needle. Alignment of the needle with the body of the cantilever leverages the directionality of the precursor flux to enhance precursor supply.

The precursor gas is supplied as a steady flow from the GIS, introducing a directional dependence of the precursor availability. A commonly occuring effect is the *shadow effect* where regions behind an existing protruding structure are depleted of precursor molecules [137]. In order to partially mitigate the limited diffusion and improve precursor supply to the working field we leveraged the directionality of the gas flow from the GIS by aligning the needle with the base of the cantilever (fig. 4.1c).
The resupply of the beam spot with precursor via diffusion on a cantilever is further hindered by a lower temperature of the surface. The diffusion coefficient increases exponentially with the surface temperature of the substrate (eq. (1.19)). The large silicon chips are covered by a 300 nm thick layer of SiO_2. On cantilevers, the oxide layer is only 50 nm thick. While SiO_2 is a thermal insulator with a thermal conductivity of 1.4 W K/m, Si is a good thermal conductor with a conductivity of 149 W K/m.
During FIBID and FEBID, the beam acts as a heat source by transferring the kinetic energy of the charged particles to the substrate within the interaction volume. *Monte Carlo* simulations based on the *binary collision approximation* using the SRIM simulation tool [60] yield an ion range of approximately 60 nm. Hence, the heat source is coupled well to the Si heat sink.
A solution of the heat-diffusion equation in cylindric coordinates (eq. (1.16)) using a Python script based on the Finite Element Method (FEM) reveals an increase of the surface temperature at the beam center of 2.87 K for a 300 nm and 0.98 K for a 50 nm thick layer of SiO_2 on top of Si after 200 ns of irradiation with a beam current of 10 pA. The former is in good agreement with the

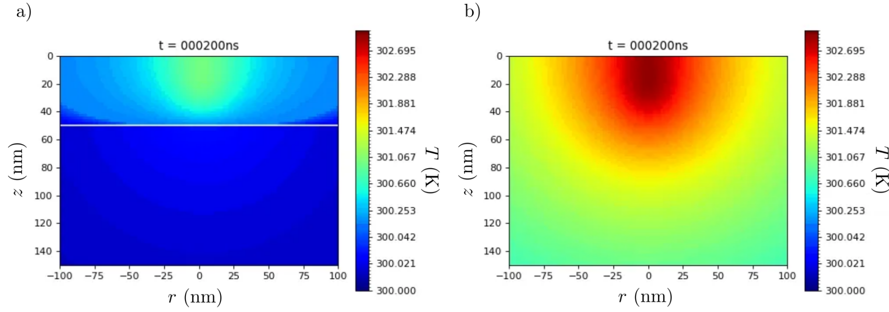

Figure 4.2.: Temperature increase of a Si substrate covered by (a) 50 nm and (b) 300 nm SiO_2 after 200 ns of irradiation with a beam current of 10 pA at an acceleration voltage of 30 kV. Results are obtained by solving the heat diffusion equation numerically with the FEM.

analytical expression in eq. (1.18) for pure SiO_2 which yields a temperature increase of 2.82 K. The simulation details are outlined in section A.1. Figure 4.2 shows the temperature profile around the beam spot in a cross-section of the substrate after 200 ns of irradiation. In fig. 4.3 the temperature development at the surface at the center of the beam is shown.
Unfortunately, literature data on the required parameters — the diffusion coefficient at zero temperature (D_0) and the diffusion activation energy (E_{diff}) are not available. Nevertheless, the temperature increase on the large substrate is ~ 2.9 times higher than on cantilever and an impact on the diffusion coefficient remains plausible.
Due to the smaller region from which diffusion can occur in combination with a potentially lowered diffusion coefficient we attribute the challenges in performing FIBID on cantilevers to lower diffusive precursor supply of the beam spot.

4.1.2. Beam Current

In section 2.1.3 we presented the various substrates used as a foundation for subsequent experiments. The very first samples were carried out on large silicon, prepatterned with OL and EBL. The use of EBL allowed us to trace gold contacts very close to the sample. Therefore, the leads on either side of the sample were very short, minimizing the deposition time. Hence, it was possible to deposit the structures at a beam current of 1.5 pA in a total deposition time of ≈ 3.5 minute.

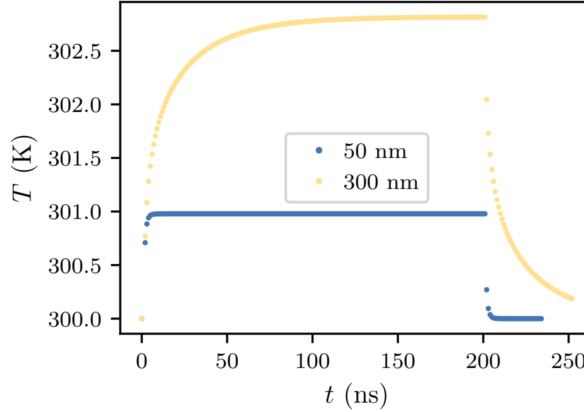

Figure 4.3.: Evolution of the temperature at the center of the beam on the surface of two different Si substrates containing different SiO_2 thickness on top: 50 nm and 300 nm.

The use of EBL, however, introduced a cumbersome, additional step that furthermore would not be possible to implement on SPM cantilevers (section 2.1.4) in the future. Therefore, the second generation of chips was used in the second generation of long-bridge SQUIDs. The longer distance to the gold contacts lead to an increase of deposition time to approximately 1.5 h, an unreasonably high deposition time for prototyping, further complicated by issues with mechanical stability of the process. Drifting of the deposition, likely due to mechanical vibrations in the building or charge in the sample building up slowly, has been observed and plays a more significant role for longer deposition times.
We investigated the use of FIBID-grown platinum to bridge the long distance between the sample and the samples. Platinum, grown from the $(CH_3)_3(CH_3CpPt)$ precursor is a fast growing material available in our system. However, experiments in the sensitive electronics of Tübingen revealed a strong suppression of I_c and a rounding of the IV-characteristics in samples connected via platinum contacts in comparison to contacts of W-C all along.
In Josephson contacts, the rounding of the transition from a discrete step to a broad, smooth transition hints at the presence of noise on the bias current, as discussed in section 1.3.2. FIBID-grown Pt is rich in C. In the standard recipe of our laboratories at a ion acceleration voltage of 30 kV the atomic Pt content is approximately 20 % and the deposit has a resistivity of approximately 800 µΩ cm, making it a poor conductor in comparison to gold (2.2 µΩ cm [138]) and superconducting tungsten, making it a source of Johnson-Nyquist noise

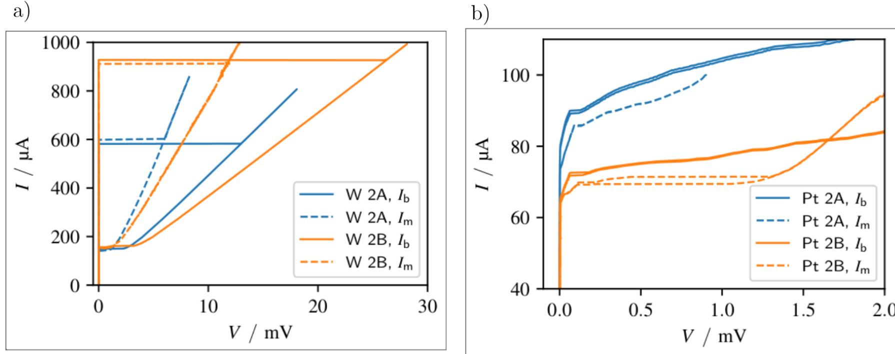

Figure 4.4.: IV characteristics of four similar short-constriction SQUIDs. (a) The two structures, including the long contacts to the prepatterned gold contacts, is grown in a single deposition process of W-C at a beam current of 9.7 µA. The IV characteristics exhibit a sharp, step-like transition indicating a very low influence of noise. (b) The two SQUIDs are made of W-C, deposited with a beam current of 9.7 µA and connected to the gold contacts via a Pt deposit. The IV characteristics exhibit a broad and smooth transition and suppressed critical current, indicating a strong influence of noise in the bias current.

(section 1.3.2). Furthermore, it introduces an additional contact resistance, an additional source of both, flicker and Johnson-Nyquist noise [139].
Therefore, in order to obliterate the requirement for EBL we increased the ion beam current to 9.7 pA to keep the deposition time as low as $\approx$ 15 min in later experiments. Figure 4.4 shows two exemplary samples contacted with Pt and W-C, illustrating the noise introduced by the platinum. The SQUID made entirely from W-C was grown in a single deposition process in order to avoid additional interfaces of subsequently deposited structures, potentially giving rise to contact resistances.

4.1.3. Dwell Time

An increase of the beam current affects the dynamic equilibrium of precursor dissociation and resupply. If the resupply via adsorbtion and diffusion is too low, the deposition will shift towards the precursor limited regime. Upon increasing the beam current from 1.5 pA to 9.7 pA we observed differing deposition results. The higher current results in lower resolution, leading to broader linewidths. Furthermore, the dissociation rate of the precursor increases, moving the deposition conditions more into the precursor limited range. This effect is particularly troublesome on cantilevers, where the precursor resupply via dif-

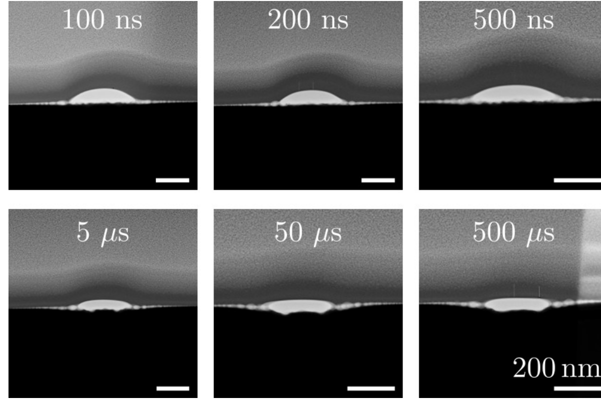

Figure 4.5.: TEM micrographs of a series of W-C deposits at dwell time ranging from 100 ns to 500 µs. The deposits were designed to have a width of 300 nm and a thickness of 50 nm for $\tau_\mathrm{d} = 500\,\mu\mathrm{s}$. With increasing dwell time, the width and the thickness of the both decrease. For a quantitative analysis, see fig. 4.6. The substrate milling for high dwell times is also observed.

fusion is suppressed. At times, the precursor supply was too low to allow for deposition, resulting in effective milling when trying to deposit nanowires in a line-scan-pattern section A.2. To mitigate this issue, we investigated the dwell time and the crossover between deposition regimes in order to remain in the electron limited regime (fig. 1.12a).
Figure 4.5 shows TEM micrographs of a series of 3 µm long and 300 nm wide deposits grown at increasing dwell time on a cantilever with $I_\mathrm{Ion} = 9.7\,\mathrm{pA}$.
Structures grown with $\tau_\mathrm{d} \geq 5\,\mu\mathrm{s}$ result in flattened deposits hinting at being in the diffusion limited regime where the sputter rate through ion milling is competing with the deposition rate of the target material. Deposits with $\tau_\mathrm{d} \leq 500\,\mathrm{ns}$ exhibit the expected droplet shaped deposits as common in the electron limited regime. The targeted height of the deposits was 50 nm, calibrated for a dwell time of 500 µs. In further experiments, we settled for a dwell time of 200 ns as it is well in the electron limited regime and another well known parameter in our group.
The dwell time has implications on the microstructure and chemical composition of the deposit, which in turn affects the conducting properties, e.g., the critical temperature and resistivity [140]. Figure 4.7 shows the cooldown curves of three long-bridge SQUIDs on a chip at $\tau_\mathrm{d} = 500\,\mu\mathrm{s}$ and $\tau_\mathrm{d} = 200\,\mathrm{ns}$. Furthermore, we show a structure deposited at $\tau_\mathrm{d} = 200\,\mathrm{ns}$ on a cantilever. Deposition of a functional long-bridge SQUID device on a cantilever at 500 µs dwell time was not possible. The normal state resistance is normalized to 1, as the different

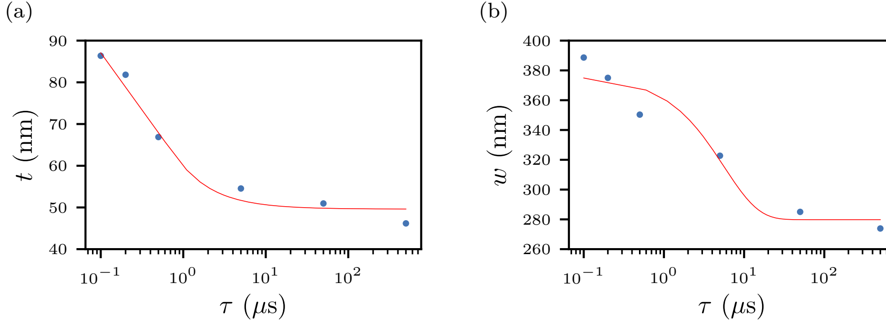

Figure 4.6.: Thickness (a) and width (b) of the deposits as a function of dwell time. The red curve indicates the best fit of an exponential decay. Both, the thickness and the width of the resulting deposits, decrease with increasing dwell time.

deposition rates at the varying parameters potentially alter the cross-sectional area. Therefore, a reliable calculation of the resistivity can not be provided.
The critical temperature of the SQUID deposited at 500 µs dwell time is significantly lower (≈ 1 K) than the critical temperature of the structures grown at 200 ns:

- Substrate, $\tau_\mathrm{d} = 500$ µs: $T_\mathrm{c} = (4.17 \pm 0.08)$ K
- Substrate, $\tau_\mathrm{d} = 200$ ns: $T_\mathrm{c} = (4.94 \pm 0.12)$ K
- Cantilever, $\tau_\mathrm{d} = 200$ ns: $T_\mathrm{c} = (5.07 \pm 0.19)$ K

Furthermore, the transition at 500 µs does not result in full superconductivity but a residual resitance remains. Full superconductivity is only achieved at approximately 2.5 K.
The difference in T_c between chip and cantilever is negligible at $\tau_\mathrm{d} = 200$ ns. However, we observe an earlier onset of the transition and a larger temperature range over which the transition occurs in the SQUID deposited on cantilevers.

4.1.4. Deposition Rate

Another parameter to keep in mind when transferring a recipe developed on large chips to cantilevers is the deposition rate. To quantify the difference, we deposited rectangles of (0.3×3) µm^2 width and length at a distance of 2 µm. We used an ion beam current of 9.7 pA and a dwell time of 200 ns. The experiment was conducted in the same SEM session without breaking the vacuum and short after replacement of the precursor in order to mitigate environmental influences such as different vacuum conditions or aging of the precursor.

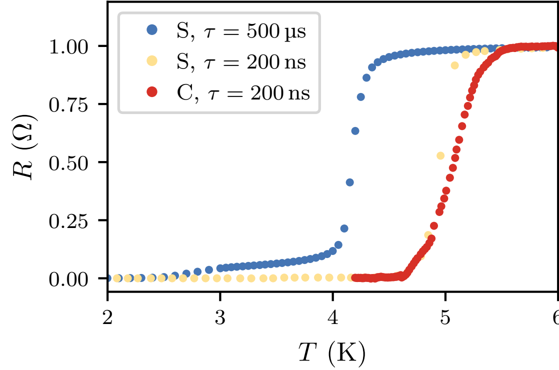

Figure 4.7.: Influence of the dwell time on the critical temperature in long-bridge SQUIDs on chips and cantilever. The structure deposited on a substrate (S) at 500 µs (blue) exhibits a critical temperature of 4.17 K. The structures deposited at 200 ns exhibit a critical temperature of 4.94 K on a substrate (S, yellow) and 5.07 K on a cantilever (C, red).

Figure 4.8 shows the SEM micrographs of the top-view of the deposition rate experiment and the TEM micrographs of the corresponding cross-sections for chips in the left and cantilevers in the right column.
Using *ImageJ2* [141], we measured the thickness in the TEM micrographs. Figure 4.9 shows the effective thickness t in dependence on the nominal thickness t_0 for a large chip and a cantilever in comparison. A linear regression of the data yields $t(t_0) = 3.94 \cdot t_0 + 30.29$ nm on the chip and $t(t_0) = 3.39 \cdot t_0 + 31.87$ nm on the cantilever, resulting in a 16 % faster growth on the chip compared to the cantilever at similar offset.
The TEM analysis confirmed an earlier experiment where we analyzed cross-sections of the same series of deposits in the SEM. In this experiment, the deposition rate on a chip was $t(t_0) = 3.95 \cdot t_0 + 14.89$ nm and $t(t_0) = 2.86 \cdot t_0 + 28.87$ nm on a cantilever. The corresponding data is shown in section A.3.
The deposition rate was estimated several times throughout the course of this project via SEM analysis of cross-sections of a series of rectangles deposited with increasing nominal thickness t_0. This is a necessity as the volume per dose, i.e., the deposition rate, is subject to changes over time as the precursor ages.

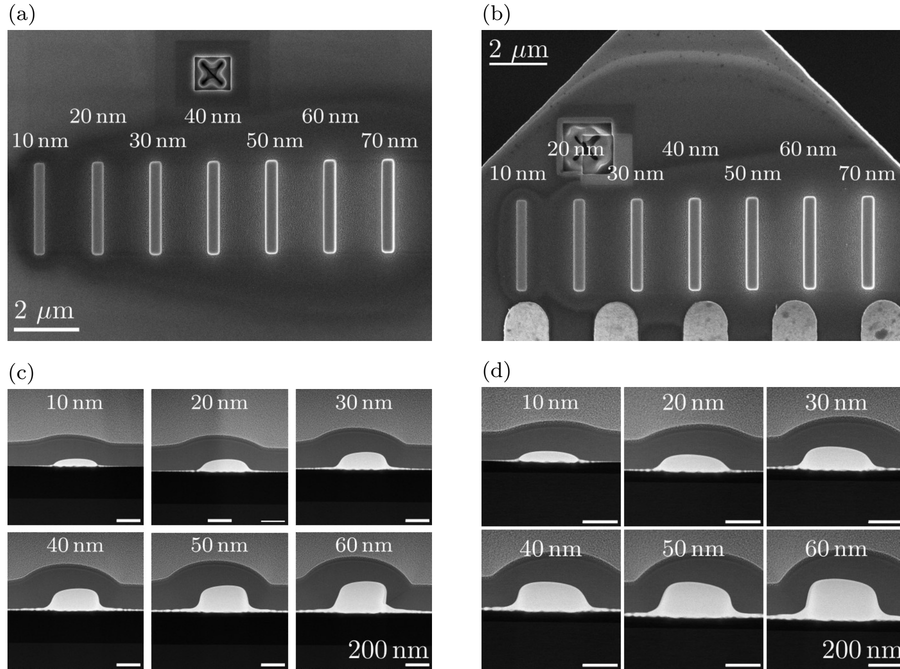

Figure 4.8.: SEM micrographs of a deposition rate experiment on a large chip (a) and a cantilever (b) in top view and corresponding TEM micrographs of a cross-section through the deposits (c, d).

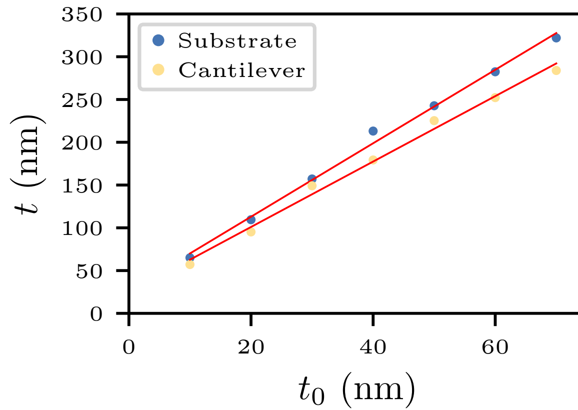

Figure 4.9.: Comparison of the deposition rate of a 300 nm wide and 3 μm long nanostructure on large chips and SPM cantilevers as a function of the nominal thickness. The deposition was performed at 200 ns dwell time and 9.7 pA ion beam current. The red line indicates a linear fit to the data.

4.2. SQUID-Design Approaches

For the fabrication of nano-SQUIDs we developed several approaches. For ease of fabrication, we started out with SQUIDs in which the JJs are constituted by 300 nm long nano-bridges (section 4.2.1). To increase phase coherence inside the constriction we then moved on to constriction-type JJs where we reduced the length down to the resolution limit of our instrument (section 4.2.2). Furthermore, we explored the feasibility of the fabrication of a SQUID based on SNS junctions by a combination of FIBID and FEBID (section 4.2.3).
All approaches have first been developed on large substrates and later on transferred to cantilevers, which we introduce in section 4.2.4. Furthermore, the specific experimental setup at our collaboration partners from the university of Tübingen required the addition of a *modulation line* to couple flux into the SQUID washer, which we lay out in section 4.2.5

4.2.1. Long Nano-Bridges

First Generation

The first approach we pursued was based on 300 nm long nano-bridges serving as JJs. This approach was chosen, as the full structure consists of well-known components put together in a SQUID-like configuration and thus forms a straight-forward approach to fabricate.
The process was carried out on chips prepatterned according to the first approach as displayed in fig. 2.1. In this chip layout, the gold contacts are running all the way to the targeted structure, down to a working area of $(1 \times 1)\,\mu m^2$.
The fabrication process is fully automated to ensure proper alignment of the sequential steps with respect to one another. After flooding the chamber for 20 s with $W(CO)_6$, two 300 nm wide lines are deposited leaving a gap of 900 nm in between to contact the final structure to the prepatterned gold contacts. In a second step, two rectangles of $(200 \times 800)\,nm^2$ are deposited 300 nm apart constituting the main component of the SQUID washer.
As common in FIBID, the deposits are surrounded by undesired material in the close vicinity of the structure, the so-called *halo*. Halo especially plays a role in between structures that are deposited in proximity, such as the pads deposited in the last step. To prevent unintended leaking current, in a third step ion-milling is applied to the region in between the pads after 30 s of evacuating the chamber from $W(CO)_6$. Lastly, the 50 nm wide nanowires are deposited to connect the pads at their outer boundaries. Figure 4.10 schematically shows the steps and fig. 4.11 displays SEM micrographs along the process.

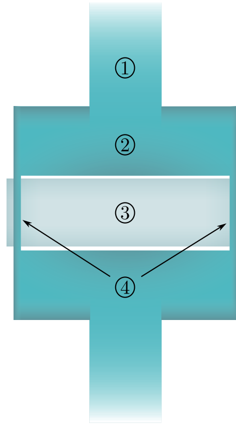

Figure 4.10.: Schematic of the fabrication process of a long-bridge SQUID of 1st generation. In a first step, leads connecting the structure to the gold contacts are patterned (1), followed by the deposition of the main body of the SQUID washer (2). In a third step, the halo inside the SQUID loop is removed via ion milling (3). Lastly, two 50 nm wide nano-wires are deposited to connect the pads (4).

All deposits are grown with a dwell time of $\tau_\mathrm{d} = 500\,\mu\mathrm{s}$ and a final thickness of $t = 50\,\mathrm{nm}$. As the gold contacts are close to the SQUID, there was no need for long W-C contact leads. Therefore, the overall deposition time was about 5 min using the lowest possible current of 1.5 pA, making this a reasonable choice.

Pushing the limit The process described above gave rise to a high reproducibility on chips and was apt for stepwise down-scaling of the inner loop area and overall size of the SQUID washer. Figure 4.12 shows SEM micrographs of SQUIDs with $(300 \times 300)\,\mathrm{nm}^2$, $(200 \times 200)\,\mathrm{nm}^2$ and $(100 \times 100)\,\mathrm{nm}^2$ nominal inner loop area. Therefore, contact pads of 200 nm width are deposited at the end of the 300 nm wide contact leads. The length of each deposit is given by the targeted width of the loop hole plus twice the junction width $l_0 = d_0 + 2 \cdot w_0$ to account for the nominally $w_0 = 50\,\mathrm{nm}$ wide nano-bridges. An overview of the nominal and measured feature sizes is reported in table 4.1.

Second Generation

The use of EBL introduced a cumbersome, additional step that furthermore would not be possible to implement on SPM cantilevers in the future. Therefore, the second generation of chips (section 2.1.3) was used in the second generation of long-bridge SQUIDs. The longer distance to the gold contacts required an increase of the ion beam current to 9.7 pA.

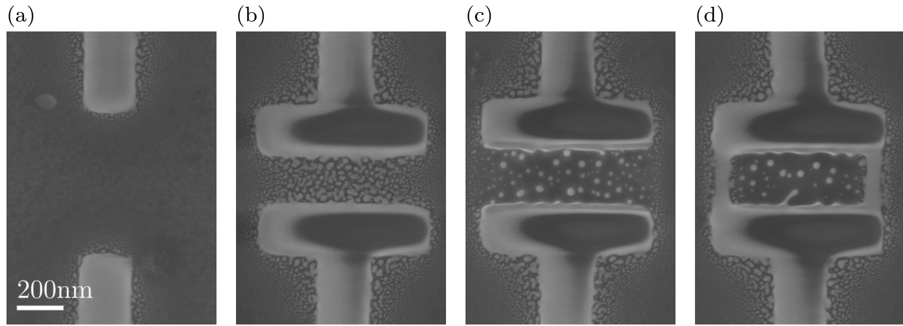

Figure 4.11.: SEM micrographs of the fabrication process of a long-bridge SQUID. (a) In a first step leads connecting the SQUID to the gold contacts are deposited. (b) Thereafter, rectangular pads are deposited forming the main part SQUID washer. (c) In order to remove halo from the hole in the SQUID loop, a brief step of ion milling is employed. (d) Lastly, the pads are connected via 50 nm wide and 300 nm long nano-bridges. The nano-bridges in this case are of 54 nm (left) and 57 nm (right) in width.

Furthermore, in section 4.1.3, we showed that the deposition on cantilevers proved more challenging than on large chips, requiring a reduce of the dwell time from 500 µs to 200 ns, resulting in an increase of the resulting width and height (fig. 4.6).
In combination, these parameters resulted in loss of resolution and each individual component of the structure grew wider than planned and exhibited more *halo*. A SEM micrograph of an exemplary SQUID can be found in fig. A.4. As we intend to fully exploit the physical resolution limit of Ga^+ FIBID in the long

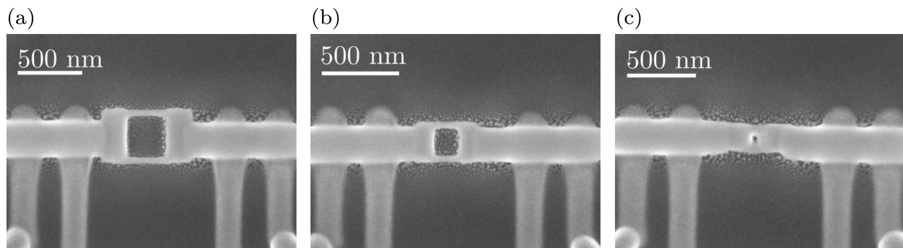

Figure 4.12.: Stepwise reduction of the inner loop area of the SQUID washer starting from a long-bridge SQUID approach. The nominal inner loop area is $(300 \times 300)\,\mathrm{nm}^2$ (a), $(200 \times 200)\,\mathrm{nm}^2$ (b) and $(100 \times 100)\,\mathrm{nm}^2$ (c). For the resulting geometric dimensions, refer to table 4.1.

Table 4.1.: Nominal and measured distances in SQUIDs structures with low inner loop areas. The measured distance directions refer to the SQUID orientation shown in fig. 4.12. When approaching low inner loop areas, the deposition of undesired material (halo) plays an increasing role.

A_0 (nm^2)	d_0 (nm)	l_0 (nm)	$d_\leftrightarrow$ (nm)	$d_\updownarrow$ (nm)	w (nm)
300×300	300	400	297	318	42, 40
200×200	200	300	154	172	36, 35
100×100	100	200	≈ 30	≈ 30	74, 81

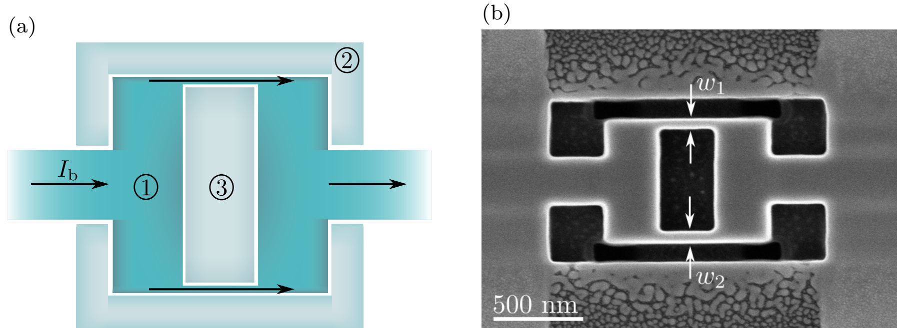

Figure 4.13.: (a) Schematic of the fabrication process of a long-bridge SQUID of second generation. At first, the contacts, the SQUID pads and the nano-bridges are deposited in a single step (1). Secondly, the halo on the outside is removed via ion milling (2), followed by the same cleaning process on the inside of the SQUID loop (3). (b) An exemplary SEM micrograph of a long-bridge SQUID of second generation with a width of $w_1 = 58\,\mathrm{nm}$ for the upper, and $w_2 = 65\,\mathrm{nm}$ for the lower nano-bridge, respectively.

run, we developed a second approach for the fabrication of long-bridge SQUIDs that can also be applied to short-constriction SQUIDs.
In this approach, we make stronger use of ion milling well into the substrate to clearly define the shape of the structure. Furthermore, the first approach required the SQUID to be deposited in several subsequent steps. After one deposit is finished, halo and sputtered material arising from the deposition of the next deposit in line likely redeposits on the already existing structure. Potentially, this results in additional, unintended, SIS or SNS contacts on the interface between adjacent deposits.
To mitigate this risk, the long-bridge SQUIDs of second generation are fully deposited in a single step. In a second step, ion milling is employed to define the outer shape of the SQUID and in a third step the inner loop area is cleaned by ion milling. Figure 4.13a schematically shows this process.
Figure 4.13b shows an SEM micrograph of a SQUID fabricated according to this recipe, fabricated on a cantilever. Under ideal conditions, the minimal junction width we achieved with this approach is $w_1 = 58\,\mathrm{nm}$ and $w_2 = 65\,\mathrm{nm}$.

4.2.2. Short Constrictions

Long-bridge SQUIDs have been chosen as the first approach due to the composition from known components, i.e., a combination of rectangular structures and long nano-bridges. However, long nano-bridges lead to phase slips and thus a multi-valued CPR [142] as laid out in section 1.3.3.
Therefore, after having fabricated initial long-bridge SQUIDs, we turned towards optimization of the magnetic response by minimizing the junction length. We developed two generations of short-constriction SQUIDs which are based on their respective equivalent in the long-bridge approach.

First Generation

The first generation of short-constriction SQUIDs is an adaption of the first generation of long-bridge SQUIDs. Hence, the dwell time employed is 500 µs the ion beam current is 1.5 pA.
The process is sequential, consisting of a total of six steps. At first, the leads connecting the structure to the gold contacts are deposited. Thereafter, 200 nm wide squid banks are deposited 300 nm apart. In a third step, they are connected via 200 nm wide rectangles. After depletion of the vacuum chamber of the precursor gas, the inner loop area is cleaned via ion milling, followed by bisecting the SQUID by cutting a narrow, deep trench via ion milling. In a last step, the bisected SQUID is reconnected by a nano-wire as narrow as possible.

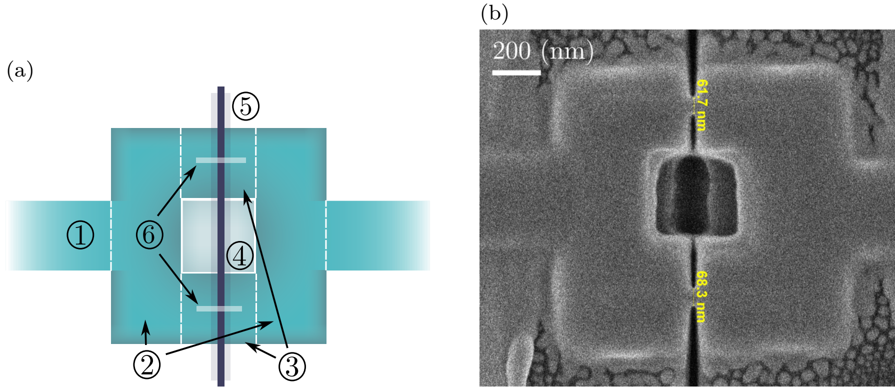

Figure 4.14.: (a) Schematic representation of the fabrication of a first generation short-constriction SQUID. The SQUID washer is fabricated in three subsequent steps (1-3). Thereafter, the region of the inner SQUID loop is cleaned (4) and the structure is bisected (5) via ion milling. In a last step, short nano-wires are deposited to reconnect the two halves of the SQUID (5). (b) a SEM micrograph of an exemplary SQUID with junctions of width (61.7, 68.3) nm and length of (33.6, 36.8) nm.

A schematic representation of the process is shown in fig. 4.14a. This approach was not followed for a long time and optimization could result in higher resolution. Nevertheless, a SQUID with junction widths of (61.7, 68.3) nm and lengths of (33.6, 36.8) nm has been achieved, depicted in fig. 4.14b.

Second Generation

In analogy to the long-bridge approach, the second generation of short-constriction SQUIDs is deposited with a dwell time of 200 ns to ensure transferability to SPM cantilevers.

In a first step, the SQUID washer and the contact leads are deposited in a single writing process. In a second and third step, the outer and afterward the inner halo is removed and the shape of the structure is clearly defined via ion milling. In a fourth step, the ion beam is traced along a single-pixel wide line (line-scan) to cut a trench and bisect the SQUID loop. Lastly, the two halves are reconnected with a nano-wire. The process is schematically illustrated in fig. 4.15a.

Figure 4.15b shows the SEM micrograph of a SQUID with Dayem bridges pushing the limits of our system at hand. The junctions show a width of $w_1 = 40$ nm and $w_2 = 48$ nm, approaching the resolution limit of Ga^+ FIBID. The length of the junctions, i.e., the width of the trench, is measured as $l_1 = 21$ nm and

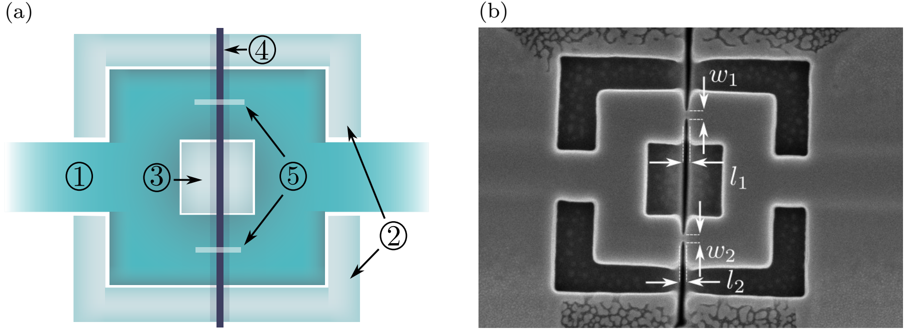

Figure 4.15.: (a) Schematic representation of the fabrication of a second generation short-constriction SQUID. After deposition of the SQUID washer in a single step process (1) the outer (2) and inner (3) outlines of the structure are defined via ion milling. Thereafter, the SQUID is bisected via ion milling (4) and reconnected by depositing a nano-wire (5). (b) SEM micrograph of a Dayem bridge SQUID on a cantilever with junction dimensions at the physical limit of our DualBeam system. The width of the junctions is $w_{1,2} = (40,\ 48)\,\mathrm{nm}$ and the length is $l_{1,2} = (21,\ 22)\,\mathrm{nm}$. SEM micrographs of the single junctions in high magnification can be found in fig. A.5.

$l_2 = 22\,\mathrm{nm}$. A close-up view at high magnification of the junctions is shown in fig. A.5.
We identified this approach as the most promising for the fabrication of W-C SQUIDs by means of Ga$^+$-FIBID. In this particular SQUID, we achieved junctions fulfilling the condition of $l \leq 3.5 \cdot \xi = 21\,\mathrm{nm}$ to maintain phase coherence of the Josephson currents (eq. (1.43)). At the point of writing, the characterization of this particular SQUID is still pending. However, the structure serves as proof of concept that Ga$^+$-FIBID is capable of fabricating high-quality SQUIDs. Further improvement would require techniques with higher resolution, such as ion milling with Ne$^+$ or He$^+$. The improvement possibly achievable with these techniques could also lie in avoiding interfaces between the SQUID washer and the junctions. A possible future experiment could deposit the full SQUID in a single-step process and employ ion milling to cut the trench so that only a narrow junction remains.

4.2.3. SNS-Junctions

Besides various approaches of constriction-type Josephson contacts, we also investigated the fabrication of SQUIDs based on SNS junctions. As outlined in section 1.3.2, SNS-JJs obtain significantly lower thermal hysteresis than c-JJs.

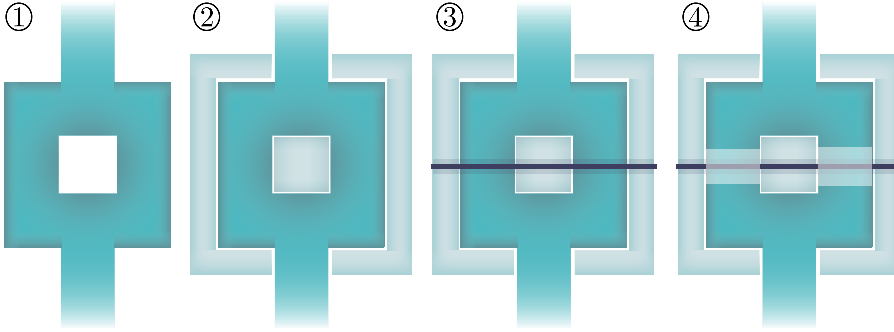

Figure 4.16.: Schematic of the fabrication process of an SNS SQUID. In a first step, the SQUID washer is deposited in a single step process (1). After removal of the precursor gas from the vacuum chamber, first the outer and afterwards the inner bounds of the structure are defined via ion milling (2). Ion milling is then employed to bisect the washer by a narrow trench (3). In a last step, FEBID is used to reconnect the two halves with metallic W-C (4).

In order to fabricate it we employ the differences between W-C fabricated using Ga^+ ions and electrons. As laid out in section 2.2.2, structures resulting from irradiation of the $W(CO)_6$ precursor with electrons exhibit metallic conductivity. As demonstrated by Blom et al. [105], it is possible to create SNS junctions from a heterostructure of superconducting W-C connected with a metallic W-C link.
For the fabrication of SNS-SQUIDs, we use an approach similar to the short-constriction process of second generation as described in section 4.2.2. At first, we deposit the full structure including the contact leads and the 300 nm wide SQUID washer in a single step via Ga^+-FIBID. Thereafter, we clean the halo first around, then, inside the SQUID. In a third step, we bisect the loop via ion milling in line-scan mode. In the final step, we employ FEBID to reconnect the loop with a patch of W-C as wide as the washer itself. A schematic representation of the fabrication process is illustrated in fig. 4.16.
As Blom et al. point out, the conductivity of normal conducting W-C deposited by FEBID increases with both, the electron beam current and the dwell time up to the point where it becomes superconducting. In order to achieve high conductivity but no superconducting behavior, we chose a dwell time of $\tau_\mathrm{d} = 1.4\,\mathrm{ms}$ and a beam current of 10 nA, relying on parameters from Blom et al. [105]
Figure 4.17a shows a SEM micrograph of a SQUID fabricated with the process presented here. The length of the junctions is $l_1 = 31.3\,\mathrm{nm}$ and $l_2 = 33.3\,\mathrm{nm}$ for the upper and lower junctions, respectively. The measurement was performed

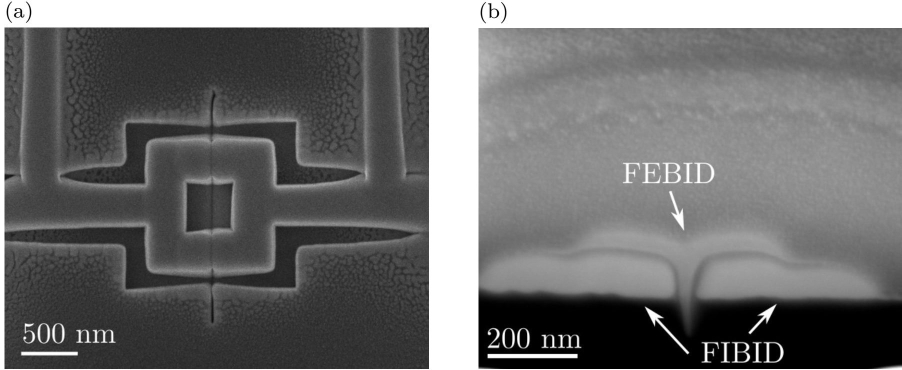

Figure 4.17.: (a) SEM micrograph of an SNS-JJ SQUID. The length of the upper junction is 31.3 nm, the lower junction is 33.3 nm long. The measurement of the junction length is performed on a sem micrograph before the deposition of the junctions (fig. A.6). (b) Cross-sectional view through a SNS junction of an early test structure. We can clearly distinguish the FEBID and FIBID parts through material contrast at the interface.

before the deposition of the metallic W-C forming the junction as displayed in fig. A.6.
Figure 4.17b shows the cross-sectional view through the SNS junction of an early test structure. We notice a clear contrast between the FEBID and FIBID parts through a dark shade on the interface. This could potentially hint at additional Josephson contacts forming at the interfaces and thus diminish functionality of the JJ. However, it allows us to confirm, that the entire trench is filled up with electron-grown W-C instead of growing a suspended bridge.

4.2.4. Deposition on Cantilevers

In section 4.1, we present an analysis of the differences in deposition parameters between large chips and cantilevers. The recipe for first generation long-bridge SQUIDs deposited at $\tau_\mathrm{d} = 500\,\mu\mathrm{s}$ failed on SPM cantilevers. Therefore, subsequent recipes were developed to work on both substrates and can readily be employed to fabricate functional SQUID on either, keeping in mind the different deposition rate and adjusting the nominal height accordingly.
In section 2.1.4 we present cantilevers with two different layouts for the gold contacts. In a first batch, seven leads end roughly 11 µm from the apex of the tip. Most deposition experiments were performed using this platform and in section 5.4 we present functional SQUID-devices. A SEM micrograph of an

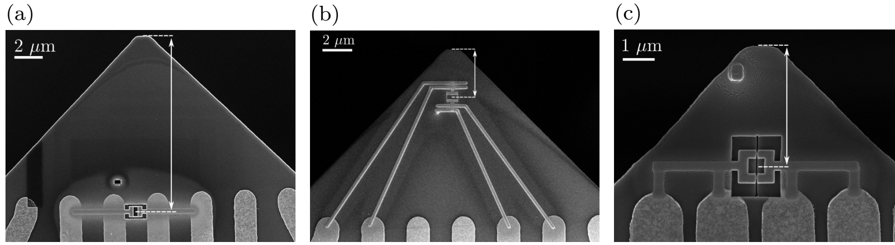

Figure 4.18.: Positioning of SQUIDs on cantilevers. (a) An exemplary SQUID on a cantilever of the first batch. This distance between the center of the loop and the apex is 12.5 µm. (b) An exemplary SQUID on a cantilever of first generation in 3.2 µm distance from the apex, contacted by bridging the distance via FIBID-grown Pt contacts. (c) In a second batch of cantilevers the need for additional contacts was obliterated by running the gold contacts closer to the apex. This distance between the center of the loop and the tip is at 3.8 µm.

exemplary SQUID is shown in fig. 4.18a. The center of the SQUID loop is in 12.5 µm vertical distance from the tip.
For functional SoL devices, the close positioning of the SQUID is crucial to minimize the probe to surface distance and thus increase resolution. For fabrication, however, the geometry poses additional challenges as diffusion of precursor molecules is further limited. Therefore, good calibration of the deposition rate is crucial.
In early experiments we investigated the possibility to deposit the structures right at the apex of the cantilever tip. Therefore, the distance between the gold contacts and the SQUID was at first bridged by FIBID-grown Pt contacts. Figure 4.18b displays a SQUID of first generation positioned in a distance of 3.2 µm from the apex.
The need for additional contacts was obliterated in a second batch of cantilevers where four leads run close up to the tip and end in roughly 4.5 µm distance from the apex. Figure 4.18c shows the successful deposition of a SQUID device on this platform. The center of the SQUID loop is in 4.5 µm vertical distance from the tip of the cantilever. However, at the point of writing, no electric characterization of any SQUID positioned this close to the tip is available yet.

4.2.5. Incorporation of a Modulation line

As laid out in section 2.3.3, our collaboration partners in Tübingen have sophisticated electronics at their disposal. However, they generally don't use an external magnet to couple magnetic flux into the SQUID loop. Instead, they

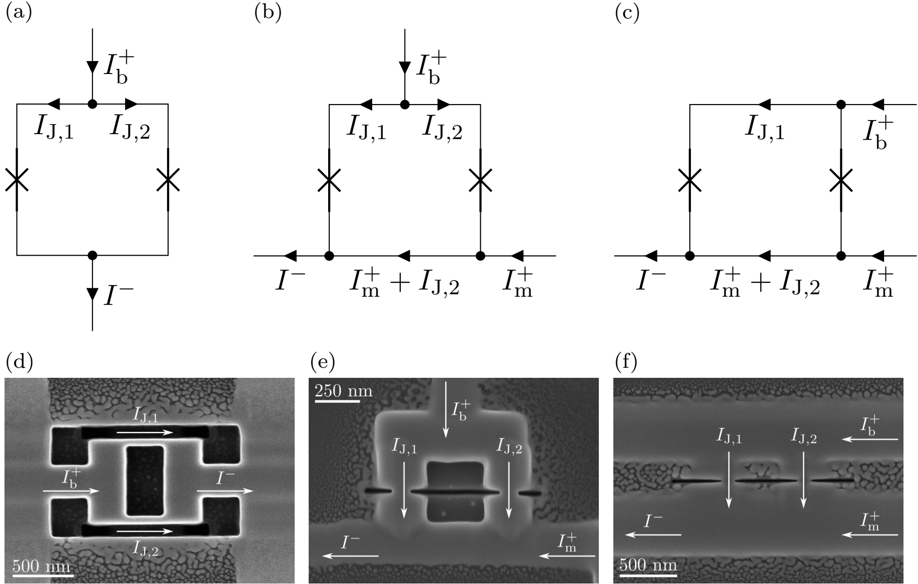

Figure 4.19.: Circuit diagrams of a SQUID without modulation line (a) and with modulation line with asymmetric paths for the Josephson currents (b) and symmetric paths (c) and SEM micrographs of respective examples (d-f).

use a third terminal, the so-called *modulation line* incorporated in the SQUID to pass a modulation current I_m through the structure, which in turn induces magnetic flux coupling directly into the SQUID.
To comply with this restriction, we also incorporated a modulation line into our structures. In first experiments, one pad of the rectangular SQUID structure was extended and connected the source of the modulation current I_m^+ and the combined drain $I^- = I_\mathrm{b}^+ + I_\mathrm{m}^+$ to gold contacts. The source of the bias current I_b^+ was connected perpendicular to the drain.
This approach is straight-forward from the point of view of fabrication. However, the asymmetry has implications on the magnetic properties of the SQUID. In a SQUID with symmetric Josephson contacts, the bias current splits into two equal Josephson currents $I_{\mathrm{J},1} = I_{\mathrm{J},2} = I_\mathrm{b}^+/2$. In a symmetric SQUID design, the two Josephson currents always run in parallel in the same direction and their respective magnetic fields compensate each other inside the SQUID loop. The current path for a symmetric SQUID without modulation line is schematically represented in a circuit diagram in fig. 4.19a and a SEM micrograph of an exemplary SQUID is shown in fig. 4.19d.

In the SQUID layout with modulation line described above, the symmetry is broken and $I_{J,2}$ is flowing in opposite directions on the horizontal paths, as shown in fig. 4.19b. Hence, the magnetic fields induced in these regions point in the same direction, resulting in net flux coupling into the SQUID proportional to the bias current. A SEM micrograph of a corresponding example is shown in fig. 4.19e.
In a reiteration of the design approach for SQUIDs with modulation line, we connected the bias line horizontally to the SQUID as shown in fig. 4.19c and fig. 4.19f. In this case, the Josephson currents always flow in the same direction, recovering the compensation of their magnetic fields and thus resulting in zero net flux inside the SQUID loop.
In practice, the parallel structures in close proximity result in halo and influence the growth of one another. Therefore, we extended the upper horizontal structure to the left to ensure symmetric growth of the vertical components. Furthermore, we used ion milling in between the parallel lines to avoid unintended contact between the leads through the halo.

4.3. Summary

In this chapter, we present the way towards the development of functional SQUID devices directly written on SPM cantilevers via Ga^+ Focused Ion Beam Induced Processing (FIBIP), i.e., a combination of FIBID and ion milling.
We have explored various procedures for the fabrication of W-C SQUIDs via FIBIP based on three types of JJs, i.e., long-nanobridges, short-constrictions and SNS heterostructures. The requirement by our collaborators from Tübingen of a modulation line was readily met by minor modifications of the recipe thanks to the high versatility of FIBIP.
All recipes were at first developed for large chips, using a dwell time of 500 µs at a beam current of 1.5 pA. However, to ensure a stable deposition process, the low current required an additional step of EBL to ensure a reasonably high yield. The EBL process was not an option on SPM cantilevers of first generation, and the beam current was increased to 9.7 pA to maintain a high yield.
Furthermore, the transfer of the process to SPM cantilevers proved challenging. Near the tip of the cantilevers, the precursor supply is limited due to the limited opening angle from which the molecules can diffuse towards the beam spot. To ensure deposition in the electron-limited regime, we had to reduce the dwell time to 200 ns.
The reduction of the dwell time, in turn, has implications on the resolution of the deposition, requiring the development of a more sophisticated, second generation SQUID design. Furthermore, we noticed an increase of the critical temperature in samples deposited at 200 ns compared to their 500 µs counterpart.
In this chapter, we demonstrated, that Ga^+ FIBID of W-C is capable to fabricate SQUIDs structures. It is feasible to fabricate junctions short enough to fulfill the condition for phase coherence, albeit the short coherence length in W-C.

Chapter 5

SQUID Characterization

Contents

5.1. Long Nano-Bridge SQUIDs 119
5.1.1. Fabrication 119
5.1.2. Electrical Properties 120
5.1.3. Magnetic Properties 121
5.2. Short Constriction Junctions 126
5.2.1. First Generation 126
5.2.2. Second Generation 131
5.3. SNS Contacts 138
5.3.1. Fabrication 138
5.3.2. Electrical Properties 138
5.4. SQUID on Lever 141
5.4.1. Long-bridge SoL 141
5.4.2. Short-Constriction SoL 148
5.5. Summary 154

5.1. Long Nano-Bridge SQUIDs

5.1.1. Fabrication

The first attempt on W-C SQUID fabrication by means of Ga^{+} FIBID was a long-bridge SQUID of 1st generation as described in section 4.2.1 with an ion beam current $I_{\mathrm{Ion}} = 1.5\,\mathrm{pA}$ and a dwell time $\tau_{\mathrm{d}} = 500\,\mathrm{\mu s}$. The two SQUIDs were fabricated on the same chip and characterized in parallel in the PPMS. SEM micrographs of the two SQUIDs are shown in fig. 5.1.
The gold contacts on the pre-patterned substrates were extended via EBL, terminating in contacts spaced 1.2 µm apart. Additionally, we patterned gold contacts 900 nm apart for potential future experiments aimed at tuning I_{c} of either junction via gating [143, 144]. This approach was intended to compensate for the asymmetry typically observed between the two parallel JJs in a SQUID. The proximity of the gold gates at the junctions necessitated an additional ion milling step after device deposition to prevent any current leakage through halo. However, the process was not automated and the alignment for the milling step proved imprecise, resulting in partial milling of the device. Deviation in the alignment resulted in one highly symmetric SQUID, referred to as sample A, with a junction width of $w = (39,\ 43)\,\mathrm{nm}$ for the left and right junction, respectively.
The second device, sample B, exhibits asymmetry with junction widths of $w = (33,\ 66)\,\mathrm{nm}$ for the left and right junctions, respectively.

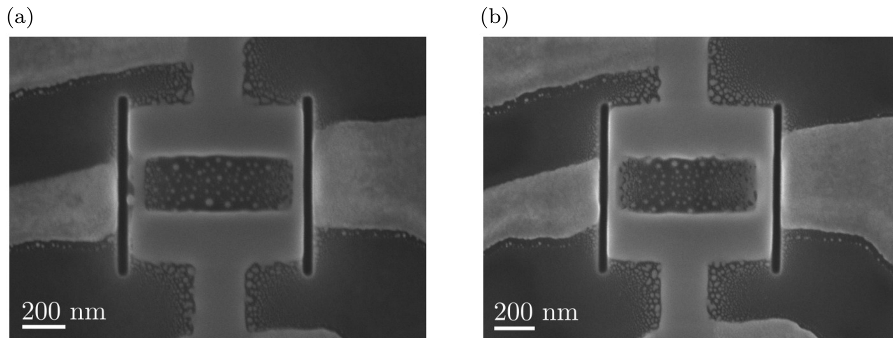

Figure 5.1.: SEM micrographs of the first-generation long-bridge SQUIDs. (a) Sample A with the left junction measuring 39 nm in width and the right junction 43 nm, hence very symmetric junctions. (b) Sample B with the left junction of 33 nm and the right junction of 66 nm in width, being asymmetric.

5.1.2. Electrical Properties

In the measurements presented below, each data-point is measured by taking 25 consecutive resistance readings at the same current set-point in AC-mode. Thus, the PPMS reports the mean and the standard deviation of the 25 resistance readings at positive bias currents and the 25 readings at negative currents.
Upon cooling down the cryostat, the SQUIDs were biased with $I_\mathrm{b} = 0.2\,\mu\mathrm{A}$. The temperature dependence of the resistance at low temperatures is shown in fig. 5.2a. The structures exhibit a very similar normal-state resistance of $R_\mathrm{N,A} = (497.7 \pm 4.5)\,\Omega$ and $R_\mathrm{N,B} = (493.6 \pm 2.9)\,\Omega$, obtained by calculating the mean of the measured values for the resistance in the range $5\,\mathrm{K} \leq T \leq 10\,\mathrm{K}$.
The samples exhibit a major transition at $T_{\mathrm{c},A} = 4.29\,\mathrm{K}$, $T_{\mathrm{c},B} = 4.17\,\mathrm{K}$, followed by a region of gradually decreasing resistance down to full superconductivity. This region is not characterized by a sudden transition and therefore cannot be modelled by a Gaussian distribution in $\mathrm{d}R/\mathrm{d}T$. Full superconductivity is achieved at 2.6 K, where the resistance drops below a threshold of $R_\mathrm{th} = 0.01 \cdot R_\mathrm{N} = 4.98\,\Omega$ in sample A. In sample B, the threshold $R_\mathrm{th} = 4.94\,\Omega$ is reached at 2.5 K.
We attribute the low transition to full superconductivity to the long bridges, which carry a larger current density due to the low cross-sectional area compared to the rest of the structure. However, a local imaging technique of the superconducting state would shed more light on this point.
At the base temperature of 2 K the structures are fully superconducting. Upon cooldown, we measured IV characteristics (fig. 5.2b) at 0 mT in AC mode with 25 readings per data-point on either current flank. The current is swept upwards from 0 µA to 15 µA and downwards from 15 µA to 0 µA.
The curves both exhibit several broad and rounded transitions without hysteresis, indicating a strong influence of electronic noise on the injected bias current, resulting in a high effective temperature (section 1.3.2). To determine I_c, a superposition of several Gaussian distributions was fitted to the derivative of the resistance over the current $\mathrm{d}R/\mathrm{d}I$.
The first transition is observed at $I_{\mathrm{c}_1}^\mathrm{A} = (8.513 \pm 0.004)\,\mu\mathrm{A}$ and $I_{\mathrm{c}_1}^\mathrm{B} = (7.980 \pm 0.004)\,\mu\mathrm{A}$. At higher currents, two additional transitions can be observed. However, in sample A, the fitting routine can only resolve a single broad transition at $I_{\mathrm{c}_2}^\mathrm{A} = (11.61 \pm 0.02)\,\mu\mathrm{A}$. In sample B, the distinct transitions can be resolved by the fitting routine: $I_{\mathrm{c}_2}^\mathrm{B} = (10.65 \pm 0.02)\,\mu\mathrm{A}$, $I_{\mathrm{c}_3}^\mathrm{B} = (11.71 \pm 0.03)\,\mu\mathrm{A}$.
By filtering the data of sample A with a rolling average over three data points applied three times, the broad second transition splits into two convoluted Gaussian distributions. However, these are too narrow to be reliably resolved.

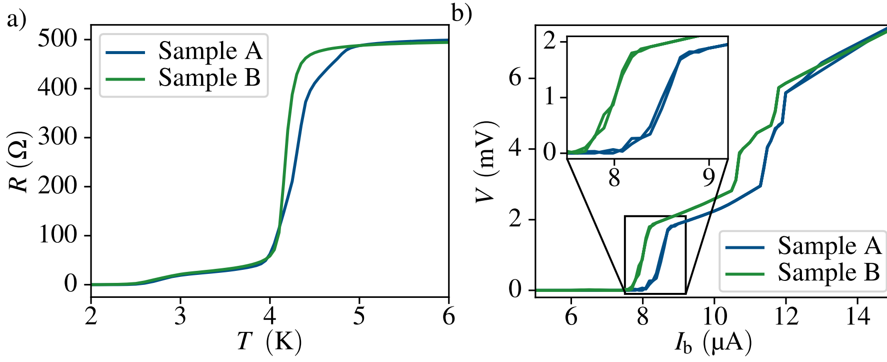

Figure 5.2.: Electric properties of long-bridge SQUIDs. (a) Temperature dependence of the resistance at low temperatures, showing the transition to superconductivity. (b) IV characteristics measured at 0 mT in AC mode at the base temperature of 2 K. Reprinted from [98].

5.1.3. Magnetic Properties

To characterize the response of the SQUID to a varying magnetic field, we measured full IV characteristics from 0 µA to 15 µA in AC mode at a reading count of 25 at magnetic fields ranging from −15 mT to 15 mT.

While I_c can be readily extracted from the curves by modelling the derivative $\mathrm{d}R/\mathrm{d}I$ as a superposition of Gaussian peaks, filtering increases the stability of the fit and thus the quality of the extracted $I_c(B)$ curve and the properties derived therefrom. However, it is a trade-off with the transfer coefficient in the voltage modulation. In this case, we figured that filtering the data with a rolling average over seven data points yields good results for both metrics. The results presented in the following are based on this filter.

Figures 5.3a and 5.3b illustrate the modulation of I_c, normalized by I_0, as a function of the magnetic flux threading the SQUID loop, in units of Φ_0. The modulation exhibits the sawtooth-shape typical for SQUIDs with high inductance L and screening parameter β_L. The red curve indicates the fitting of the sawtooth-model introduced in eq. (1.53).

The model yields a period of $\delta B_A = (6.39 \pm 0.02)$ mT and $\delta B_B = (5.67 \pm 0.03)$ mT.

Due to flux quantization within the SQUID loop, the period of the modulation corresponds to a change of flux threading the SQUID of Φ_0. Using the relation of flux and magnetic field (eq. (1.49)), we obtain an effective area of $A_{\mathrm{eff,A}} = (0.3238 \pm 0.0008)\,\mu\mathrm{m}^2$ and $A_{\mathrm{eff,B}} = (0.3647 \pm 0.0017)\,\mu\mathrm{m}^2$, which agrees well the geometric dimension of the SQUIDs.

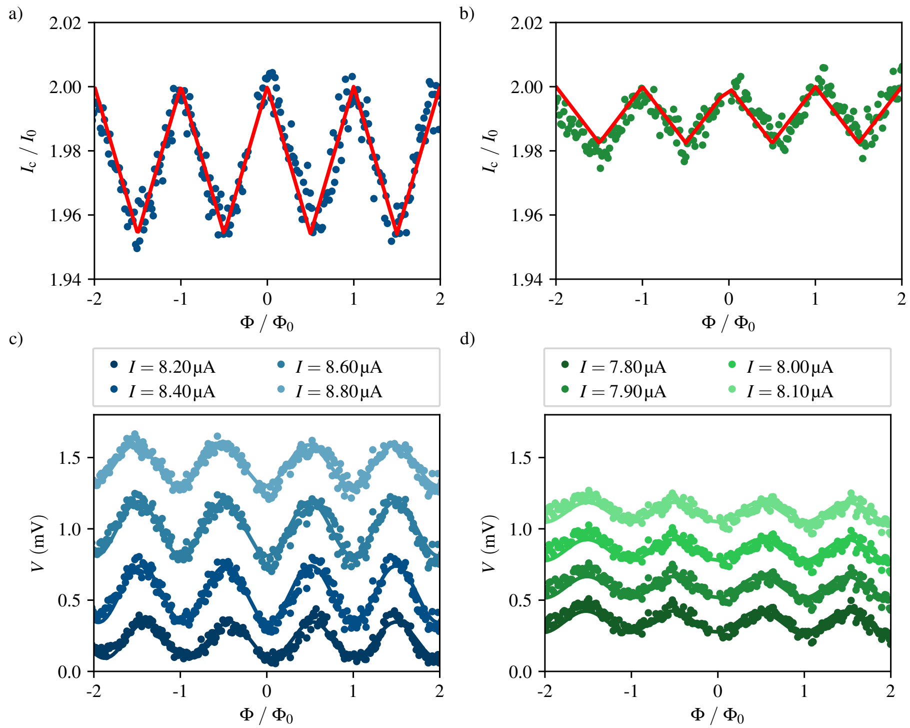

Figure 5.3.: Magnetic properties of long-bridge SQUIDs around I_{c_1} at 2 K. (a, b) The modulation of the critical current I_c normalized by I_0, as a function of the magnetic flux through the SQUID loop, in units of Φ_0. (c, d) Selected voltage vs. flux curves at constant bias currents, exhibiting sinusoidal modulation. Reprinted from [98].

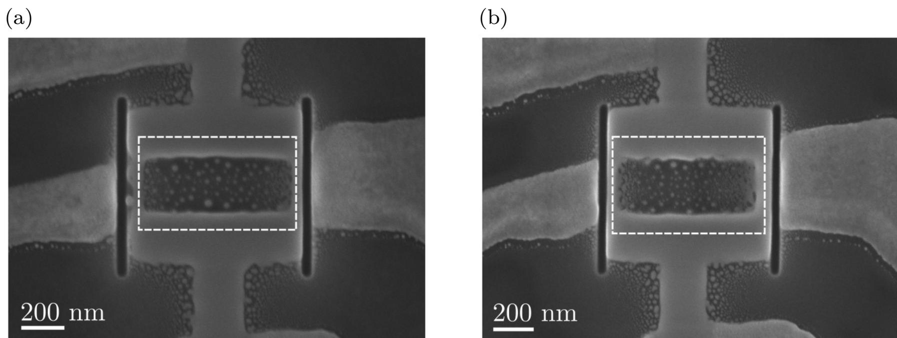

Figure 5.4.: SEM micrographs of the long-bridge (a) sample A and (b) sample B with the dashed line indicating the effective area obtained from the analysis of the critical current modulation.

The geometric inner loop area is $A_{\mathrm{geom,i}} \approx 0.175\,\mu\mathrm{m}^2$, the outer geometry is $A_{\mathrm{geom,o}} \approx 0.566\,\mu\mathrm{m}^2$. Due to flux focusing, the effective area is generally larger than the geometric inner loop but cannot exceed the outer geometric bounds. A schematic representation of the effective area is presented in fig. 5.4 for both long-bridge SQUIDs.

Additionally, the sawtooth model provides an inductance of the SQUIDs of $L_{\mathrm{A}} = (10.4 \pm 0.4)\,\mathrm{nH}$ and $L_{\mathrm{B}} = (29.2 \pm 1.4)\,\mathrm{nH}$, resulting in a screening factor (eq. (1.50)) of $\beta_{\mathrm{L,A}} = 43.5 \pm 1.5$ and $\beta_{\mathrm{L,B}} = 114 \pm 6$, and a modulation depth of 2.3 % and 0.9 % in sample A and B, respectively.

In the design of nanoSQUIDs, generally a modulation depth of 50 %, corresponding to $\beta_{\mathrm{L}} = 1$, is targeted. The inductance of nanoSQUIDs reported in literature is generally in the pH range [83]. For instance, recent works on constriction-type SQUIDs consisting of Nb report estimated values of $L = 40\,\mathrm{pH}$ to $150\,\mathrm{pH}$ with screening factors close to 1 [96, 145]. Nevertheless, Arpaia et al. [146] show, that YBCO SQUIDs with high screening factors ($\beta_{\mathrm{L}} = 18$ to 24) can achieve spectral densities of flux noise below $1\,\mu\Phi_0/\sqrt{\mathrm{Hz}}$, comparable to the state of the art.

We attribute the high inductance observed in our SQUIDs to a high kinetic inductance within the long nano-bridges, further amplified by the large London penetration depth of W-C. Therefore, a reduction of the length of the constriction junction is crucial.

Additionally, the electronic noise coupling into the bias current, responsible for the broad transitions, potentially suppresses the intrinsic critical current of the structures. Therefore, the I_{c} modulation could be suppressed as well and we have reasons to believe that characterization of the SQUIDs in noise-free conditions could reveal the true potential of the SQUIDs.

Figures 5.3c and 5.3d show selected voltage curves as a function of flux at constant bias currents, extracted from the first transition, exhibiting a sinusoidal modulation.

Figure 5.5 presents the results obtained by modelling the $V(B)$ curves with a sinusoidal model for all available bias currents. The fit converges well for bias currents in the vicinity of the first transition.

The period of the sinusoidal modulation in $V(B)$ results in a period that corresponds well with the period of the I_{c}-modulation. In sample A, we obtain a period of $\delta B_{\mathrm{A}} = (6.17 \pm 0.19)\,\mathrm{mT}$, averaged over the range $7.6\,\mu\mathrm{A} \leq I_{\mathrm{b}} \leq 9.1\,\mu\mathrm{A}$. In sample B, the period is $\delta B_{\mathrm{B}} = (5.71 \pm 0.10)\,\mathrm{mT}$, in the range $7.6\,\mu\mathrm{A} \leq I_{\mathrm{b}} \leq 8.5\,\mu\mathrm{A}$. The period of the sinusoidal modulation in $V(B)$ correspond to an effective area of $A_{\mathrm{eff,A}} = (0.335 \pm 0.010)\,\mu\mathrm{m}^2$ and $A_{\mathrm{eff,B}} = (0.361 \pm 0.006)\,\mu\mathrm{m}^2$, which aligns well with the results obtained from the I_{c} modulation, thus confirming the validity of the model.

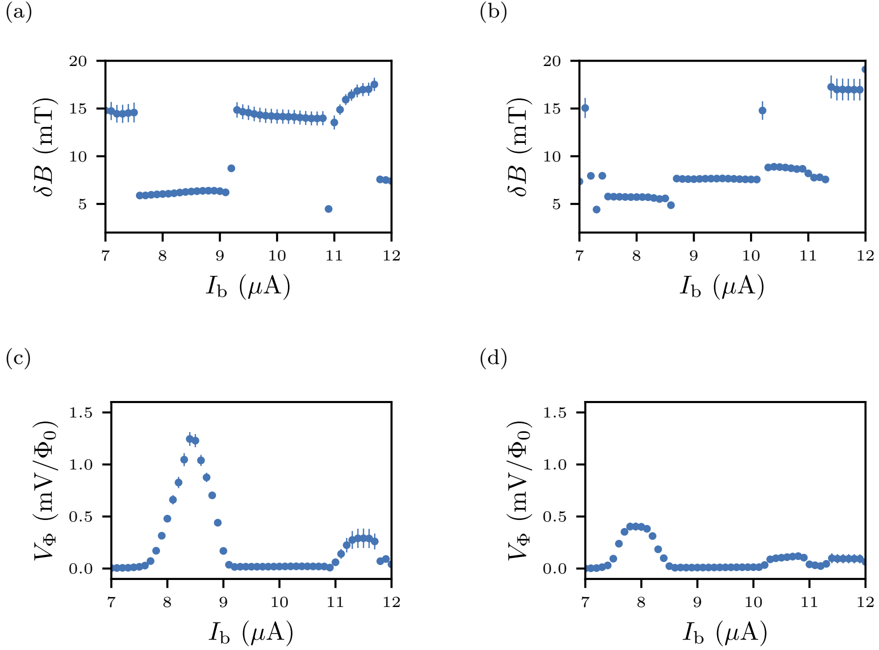

Figure 5.5.: Meta analysis of the $V(B)$ curves at constant I_b for a large range of bias currents. (a, b) The period obtained from fitting the voltage modulation to a sinusoidal model in sample A (a) and sample B (b). (c, d) The transfer coefficient of sample A (c) and sample B (d). Both metrics show the fit converging well in the vicinity of the first transition.

Using eq. (1.56), the transfer coefficient is calculated at each bias current. We observe finite voltage responses within either of the transitions, with the first transition being the most significant. The maximum transfer coefficient is obtained at 8.5 µA as $V_{\Phi\mathrm{A}} = (1300 \pm 30)\,\mu\mathrm{V}/\Phi_0$ in sample A and at 7.9 µA as $V_{\Phi\mathrm{B}} = (473 \pm 26)\,\mu\mathrm{V}/\Phi_0$ in sample B (figs. 5.5c and 5.5d).
Similar to the modulation of I_c, the asymmetry of the junctions in sample B is also reflected in the voltage modulation with the transfer coefficient being significantly lower than in sample A.
The transfer coefficient is comparably large compared to constriction-type nano-SQUIDs based on crystalline Nb, where recent works report values in the range of $40\,\mu\mathrm{V}/\Phi_0$ to $200\,\mu\mathrm{V}/\Phi_0$ [96, 145]. The YBCO SQUIDs reported by Arpaia et al. exhibit transfer coefficients of $1.5\,\mathrm{mV}/\Phi_0$ to $3.6\,\mathrm{mV}/\Phi_0$ [146].
Therefore, we conclude that the samples presented in this section represent promising candidates for the use as flux-to-voltage transducers and hence being

used in SoL devices. The low modulation depth of I_c due to a high, mostly kinetic, inductance, is compensated by a large voltage modulation. Although experiments on the flux noise of our SQUIDs have not been conducted, similar YBCO-SQUIDs are reported to exhibit flux noise below $1\,\mu\Phi_0/\sqrt{\mathrm{Hz}}$.

5.2. Short Constriction Junctions

5.2.1. First Generation

Fabrication

To overcome the limitations of long nano-bridges, we aimed to minimize the length of the constrictions. The SQUIDs presented here are fabricated using the first generation recipe described in section 4.2.2. Additionally, they were characterized in the laboratory of our collaborators in Tübingen, which necessitated the inclusion of a modulation line (section 4.2.5).
We present two SQUIDs with an inner loop area of $(125 \times 185)\,\mathrm{nm}^2$ (sample A: fig. 5.6a) and $(315 \times 335)\,\mathrm{nm}^2$ (sample B: fig. 5.6b)
In this initial attempt, we achieved short junction lengths of approximately 30 nm for sample A and approximately 25 nm for sample B. The lengths of the junction are slightly above 21 nm, the criterion for transport maintaining phase coherence (eq. (1.43)). However, the junction widths are relatively large, with (60 and 90) nm for the left and the right junction in sample A and 100 nm for both junctions in sample B. These widths can be substantially reduced in further experiments as demonstrated in section 4.2.2.
We did not employ EBL to define the gold leads down to a small working field. Therefore, we used an ion beam current of 9.7 pA to keep the deposition time reasonably short and the process sufficiently stable. The structures are grown with a dwell time $\tau_\mathrm{d} = 500\,\mathrm{\mu s}$.

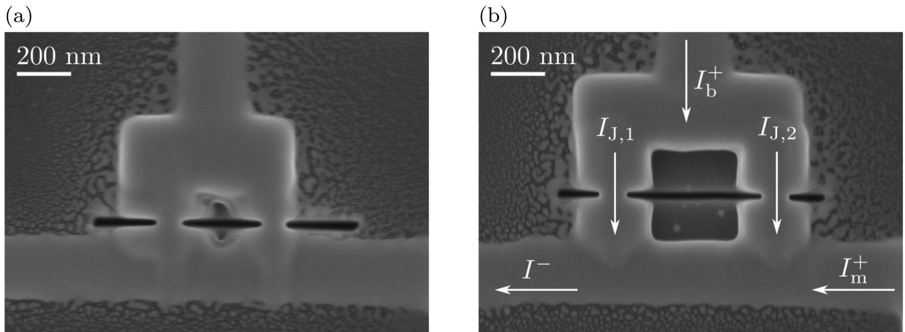

Figure 5.6.: SEM micrographs of short-constriction SQUIDs with modulation lines. (a) For sample A, the inner loop area is $(125 \times 185)\,\mathrm{nm}^2$, with a junction length of approximately 30 nm and widths of (60 and 90) nm for left and right junctions, respectively. (b) For sample B, the inner loop area is $(315 \times 335)\,\mathrm{nm}^2$, with a junction length of approximately 25 nm and a junction width of 100 nm in both junctions.

Electrical Properties

The instruments available in Tübingen are highly optimized for the suppression of electronic and environmental noise. However, the temperature control is highly limited, and a superconducting coil is not available. As a result, we did not directly assess the critical temperature of the structures and measured IV characteristics at several discrete temperatures.
Figure 5.7a and fig. 5.7b show the IV characteristic of each sample at 2 K. Both curves exhibit two distinct, sharp transitions and a large hysteresis. In superconducting structures with a constriction, generally a large thermal hysteresis is expected as the high current density within the constriction results in a high dissipation of heat in the normal conducting regime.
The normal state resistance at 2 K is with $R_{\mathrm{N},A} = (292.28 \pm 0.03)\,\Omega$ and $R_{\mathrm{N},B} = (273.78 \pm 0.39)\,\Omega$, approximately 40 % lower than in the long-bridge SQUIDs presented in section 5.1. This is likely partly due to the shorter constriction lengths, but also due to their increased width. The critical currents, obtained by a voltage threshold, are measured at $I_\mathrm{c}^A = (11.32,\ 12.60)\,\mu\mathrm{A}$ $I_\mathrm{c}^B = (11.04,\ 12.24)\,\mu\mathrm{A}$, approximately 30 % higher than in the long-bridge SQUIDs.
In fig. 5.7c and fig. 5.7d we show the IV characteristics at various temperatures. With increasing temperature, both the critical current and the hysteresis decrease, while the transition becomes broader and rounder, supporting the claim that the effective temperature in the PPMS is increased due to extrinsic noise coupling into the bias current.

Magnetic properties

The readout of I_c in the instrument is automatic, i.e., the current source ramps up the bias current until a threshold voltage V_th is reached. The last current below V_th is then saved to a datafile as I_c. For $I_\mathrm{c}(B)$ measurements, the modulation current is thereafter incremented and the bias current reset to repeat the readout.
Coupling flux into the SQUID via the modulation line comes at a high cost, however. The range in which the magnetic field can be modulated is limited by I_c of the modulation line. Measurements are only possible for opposite modulation and bias currents as the drain runs a total current of

$$I^{-} = I_\mathrm{b} + I_\mathrm{m}. \tag{5.1}$$

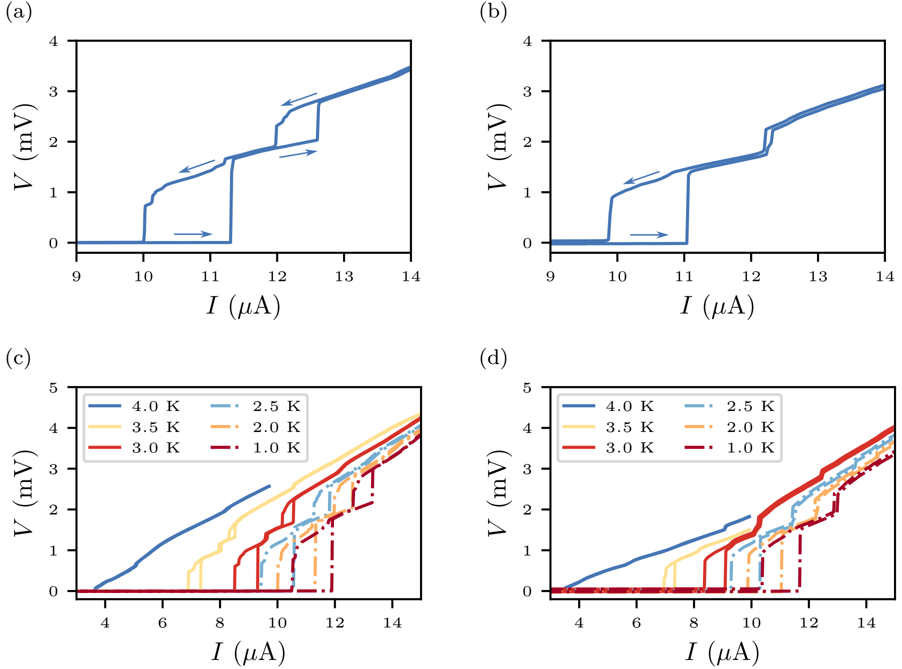

Figure 5.7.: IV characteristics of short-constriction SQUIDs with modulation lines. (a, b) IV characteristics at 2 K of sample A (a) and sample B (b). The curves exhibit sharp transitions and a large hysteresis. The arrows indicate the sweep direction. (c, d) IV characteristics at various temperatures of sample A (c) and sample B (d). Increasing temperature results in a broadening of the transitions and a decrease in the hysteresis.

In fig. 5.8, we present the dependence of I_c on I_m at 2 K. Here, we observe a lobe in I_c that we attribute to the upper part of the standard SQUID modulation for SQUIDs with moderate β_L (fig. 1.20).
Although the critical current is clearly modulating, the modulation line cannot be tuned high enough to couple a full flux quantum into the SQUID. Therefore, we can not experimentally retrieve the relation between the modulation current and magnetic flux coupled into the SQUID.
However, we can estimate a lower bound for the modulation depth and thus an upper limit for the screening factor (eq. (1.52)) and the SQUID inductance (eq. (1.50)) from the minimal and the maximal value of I_c.
The results of these estimations are shown in table 5.1. The modulation depth is roughly 20 % for both SQUIDs, which results in an upper limit for the screening

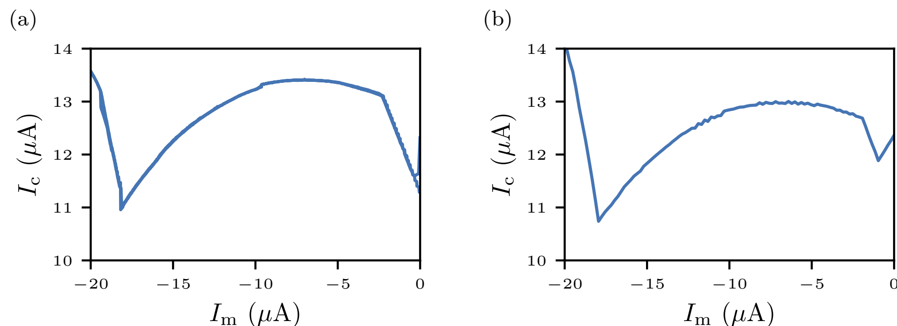

Figure 5.8.: The critical current in dependence of the modulation current of short-constriction SQUIDs at 2 K, (a) corresponds to Sample A and (b) to sample B. The modulation current is used to couple magnetic flux into the SQUID washers. The limited range is due to the current running on the modulation line, constitued of the modulation and the bias current, exceeding the critical current of the modulation line.

Table 5.1.: Results of an estimation of the minimal depth of the I_c modulation induced by a modulation current at 2 K. Thereof, an upper limit of the screening factor and the SQUID inductance is estimated.

	Sample A	Sample B
I_{max} (µA)	13.42	13.00
I_{min} (µA)	11.06	10.74
β_L	5.69	5.75
L (pH)	875.9	912.9

factor as low as 5.69 in sample A and 5.75 in sample B. The corresponding inductance is below 875 pH for sample A and 912 pH for sample B.
A comparison between the two samples is hardly possible. The values reported form an upper bound for the inductance and the screening factor, limited by the modulation line, which is the same in both samples. From geometric considerations we would expect sample A to exhibit a lower inductance due to the lower loop area and therefore a higher modulation depth.
The screening factor is in the same order of magnitude as the target value ($\beta_L = 1$) and as it is an upper limit, the real value is likely to come even closer to this target. Nevertheless, the upper limit is already outperforming some YBCO SQUIDs [146] and approaching values reported on Nb SQUIDs [96, 145]. The same holds for the inductance.

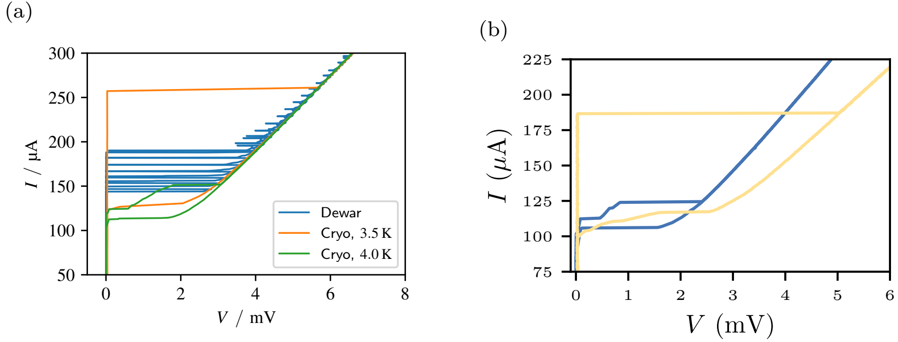

Figure 5.9.: (a) IV characteristics of the same sample measured in liquid helium and the vacuum of the cryostat. Presumably the boiling of liquid helium in the resistive state sufficiently cools down the sample and allows it to relax to the superconducting state. (b) IV characteristics of two similar samples measured at 4.2 K. One sample exhibits strong influence of noise whereas the other operates in the low-noise regime.

In comparison to the long-bridge SQUIDs presented in section 5.1, we observe an improvement of the SQUID performance by one order of magnitude. The underlying cause for this improvement is twofold. On the one hand, the junction length is reduced by one order of magnitude, approaching the limit for phase coherence within the junctions. On the other hand, the electronics used for the experiments are highly optimized to reduce extrinsic noise, visible in the quality of the individual IV characteristics (fig. 5.7).

Experimental Conditions

Unfortunately, electric characterization of our samples was not feasible in the liquid helium dewars. While superconductivity was generally achieved, when measuring IV characteristics the voltage turned out to be very unstable in the transition region jumping from the superconducting to the normal state and back. Experiments in the cryostat on the same sample in the vacuum of the cryostat do not exhibit this behavior (fig. 5.9a). We attribute this behavior to the spontaneous boiling of the liquid helium on the resistively heated sample, temporarily reducing the temperature and allowing the sample to relax to the superconducting state.

Furthermore, the vicinity to the critical temperature makes the sample susceptible to noise. Figure 5.9b shows the IV characteristics of two similar samples consecutively fabricated after the same recipe on the same chip and in the same cooldown at 4.2 K. Minute difference in the material properties apparently have a huge influence on the noise factor. Sample A displays multiple transitions

while sample B exhibits a clear transition in a single step as expected for low noise measurements. To stabilize the sample behavior we generally conduct experiments at 2 K.

5.2.2. Second Generation

The sample presented in this section was fabricated and characterized in close collaboration with a new member of our group at that time, Amaia Saénz. The design of sample and experiment are from the author of this work. The optimization and actual fabrication was conducted by Amaia Saénz. The characterization was conducted jointly and thereafter characterized independently. Amaia's meticulous approach and commitment in the optimization and fabrication process resulted in a high-quality sample with astonishingly symmetric junctions and are gratefully acknowledged here.

Fabrication

The sample does not fully match the classification of fabrication processes presented in section 4.2. It rather forms an intermediate step between the first and the second generation. It was fabricated at a dwell time of 200 ns at a beam current of 9.7 pA. However, it lacks the cleaning step to define the shape of the SQUID more precisely.

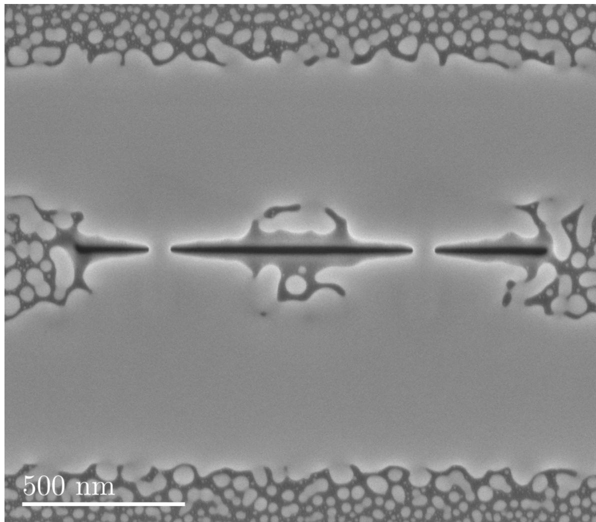

Figure 5.10.: SEM micrograph of a short-constriction SQUID of first generation. The junctions are highly symmetric with a width of 65 nm an a length of (30, 34) nm.

As can be seen in the SEM micgrograph of this SQUID shown in fig. 5.10, the junctions are highly symmetric with a width off 65 nm and a deviation below the accuracy of manual measurements in ImageJ. The length of the junctions is (30, 34) nm.
Furthermore, the sample disposes of a modulation line (see section 4.2.5) for potential later characterization in the facilities of our collaborators in Tübingen. The corresponding SEM micrograph is shown in fig. 5.10.

Electrical Properties

Upon cooldown, the sample was biased at a current of 1 µA. The cooldown curve is shown in fig. 5.11. It exhibits a clear transition at a critical temperature of $T_c = (4.54 \pm 0.08)$ K. The normal state resistance before transition is $R_N = (485 \pm 1)\,\Omega$.
Figure 5.12 shows IV characteristics at 2 K and 0 mT. They were measured in DC mode taking five individual readings with $N = 1$ at each current set point. In figs. 5.12a and 5.12b, the results are shown for negative and positive currents. For negative currents, two distinct transitions are visible, hinting at two different regions of the sample transiting independently.
In a broad transition range the voltage readings are either superconducting or in normal state, no readings fall in between the transition. We notice, that within the transition range, the density of resistive readings increases with bias current. The resistance of the partially superconducting regime is $(261.5 \pm 1.5)\,\Omega$. On the positive current flank, an additional step arises with a resistance of $(133.1 \pm 1.8)\,\Omega$.
The horizontal lines in figs. 5.12a and 5.12b indicate the threshold voltages $V_{th} = 5.5$ mV and 11 mV, yielding critical currents of $I^-_{c_1} = -25.37$ µA and $I^-_{c_2} = -33.68$ µA on the negative, and $I^+_{c_1} = 25.08$ µA and $I^+_{c_2} = 30.68$ µA on the positive side.
We attribute the oscillatory behavior, i.e., the discrete jumping between superconducting and normal state to the measurement design of the PPMS. The sample is biased by a pulsed current injection (section 2.3.1). In between two distinct resistance (voltage) readings, the current is switched off. This delay allows the superconductor to relax from resistive to superconducting. Triggering the transition from the superconductive to the normal state is a statistical process due to the high electric noise of the system.
Using statistical methods, the broad, smooth transitions as observed in the long-bridge SQUIDs presented in section 5.1 measured at a reading count of 25 in AC mode can be recovered. The decision to measure with a reading count of 1 instead of 25 is reasoned in the appendix B.2.1

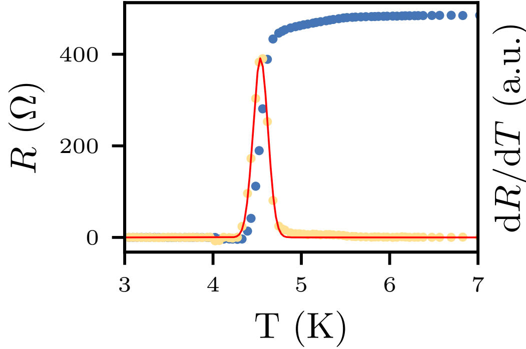

Figure 5.11.: Cooldown curve of a short-constriction SQUID of second generation. A single, clear transition is visible at $T_c = (4.54 \pm 0.08)\,\mathrm{K}$. The normal state resistance of the sample is $R_N = (485 \pm 1)\,\Omega$.

Figures 5.12c and 5.12d shows the IV characteristics after averaging the five individual readings and filtering the data with a rolling average over five points, applied three times. The derivative $\mathrm{d}R/\mathrm{d}I$ exhibits distinct peaks that can be modelled as a superposition of Gaussian curves. The best fit of the derivative yields critical currents of $I^-_{c_1} = (-26.216 \pm 0.002)\,\mu\mathrm{A}$ and $I^-_{c_2} = (-35.526 \pm 0.002)\,\mu\mathrm{A}$ for negative currents and $I^+_{c_1} = 25.368\,\mu\mathrm{A}$, $I^+_{c_2} = (31.516 \pm 0.003)\,\mu\mathrm{A}$ and $I^+_{c_3} = (34.317 \pm 0.001)\,\mu\mathrm{A}$ for positive currents.
The critical current is increased by a factor of approximately 3 compared to the long-bridge SQUIDs of first generation and a factor of approximately 2.5 to the short-constriction SQUIDs of first generation. We attribute this to the higher tungsten content in the W-C due to the lower dwell time used in deposition.

Magnetic Properties

The magnetic field response of the SQUID was probed at 2 K by sweeping the field in a range of $-25\,\mathrm{mT} \leq B \leq 25\,\mathrm{mT}$ while measuring IV characteristics at each setpoint. IV characteristics were measured as described above with five independent readings at each current setpoint in DC mode.
In order to extract I_c, we analyzed the curves with a voltage threshold and the fit of $\mathrm{d}R/\mathrm{d}I$ as described above. With neither approach a modulation of I_c could be found. The extracted critical current in dependence on the magnetic field with either method is shown in the appendix B.2.2.

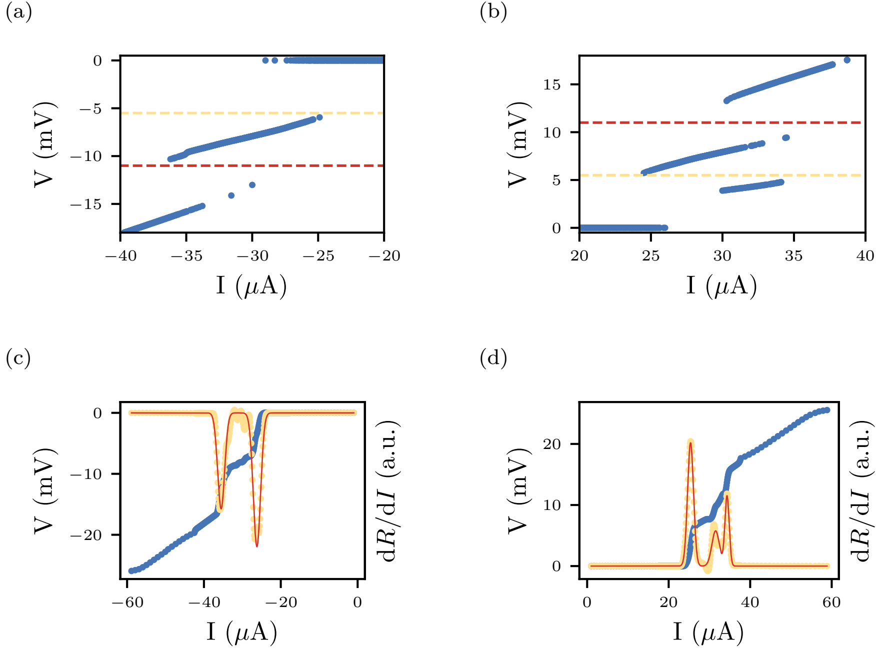

Figure 5.12.: IV characteristics of a short-constriction SQUID on a large substrate. (a) The negative and (b) positive current flanks of the IV characteristic. Each current setpoint consists of five independent datapoints with a reading count of 1. The horizontal lines indicate the voltage thresholds used to extract I_c. (c) Negative and (d) positive current flanks of the sample after averaging the individual datapoints and applying a rolling average filter over the two adjacent neighbors, applied three times. The yellow datapoints represents the derivative of the derivative dR/dI and the red curve the best fit to a superposition of Gaussian distributions.

To investigate the voltage modulation in dependence on the magnetic field, we selected datapoints from a specific transition. Therefore, we used the voltage thresholds indicated as horizontal lines in figs. 5.12a and 5.12b. In the intermediate region, that is for voltages in the range of 5.5 mV to 11 mV, we observe a strong magnetoresistive contribution, resulting in a hyperbolic magnetic field dependence. An exemplary $V(B)$ curve for an exemplary negative and a positive current is shown in figs. 5.13a and 5.13b. The red curve indicates the fit of a parabolic function.
After subtraction of the magnetoresisitive contribution and calculation of the five independent curves, a faint modulation is visible. Figures 5.13c and 5.13d show select currents on both sides after subtraction of the background. They

are shifted in y-direction for clarity. The red curves indicate the corresponding sinusoidal fit.

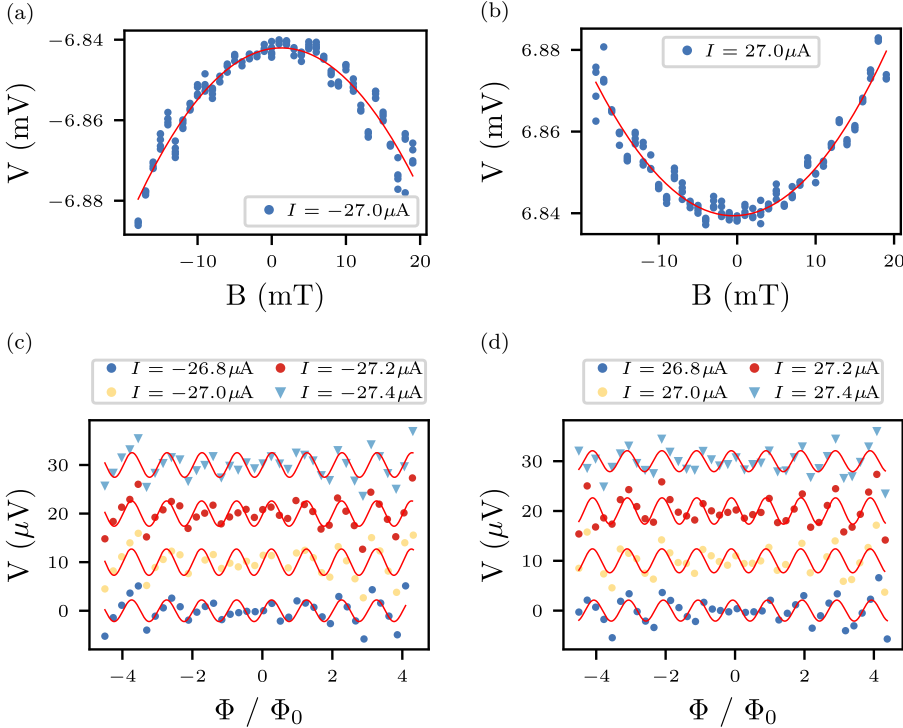

Figure 5.13.: Voltage modulation of a first generation short constriction SQUID. (a, b) Voltage in dependence of the magnetic field of a selected curve for negative (a) and positive (b) currents. For each current setpoint five voltage readings were measured. A magnetoresistive contribution is visible. The red curve indicates the best fit to a parabolic function. (c, d) Voltage modulation in dependence on the flux in units of Φ_0 after subtraction of the parabolic background and after averaging the five datapoints for negative (c) and positive (d) currents. The red curves indicate the sinusoidal fit of the voltage modulation. The data is shifted by 10 µV for clarity.

Figure 5.14 presents the parameters obtained after fitting $V(B)$ curves at constant bias to sinusoidal functions. The sine yields a modulation period of $\delta B^- = (4.21 \pm 0.05)\,\mathrm{mT}$ and $\delta B^+ = (4.20 \pm 0.06)\,\mathrm{mT}$ in a bias current range from 27 µA to 29 µA. The positive and negative current flanks are thus in good correspondence and the weighted mean is $\delta B = (4.21 \pm 0.04)\,\mathrm{mT}$. The given period corresponds to an effective area of $(0.488\,599 \pm 0.000\,005)\,\mu\mathrm{m}^2$. The effective area is indicated in fig. 5.15.

Combining the period with the amplitude of the resulting best fit we obtain maximal transfer coefficients of ${V_\Phi}^- = (17.78 \pm 3.06)\,\mu\text{V}/\Phi_0$ at $-27.3\,\mu\text{A}$ and ${V_\Phi}^+ = (16.66 \pm 3.38)\,\mu\text{V}/\Phi_0$ at $27.2\,\mu\text{A}$. The results once again are remarkably similar for the positive and negative side, hinting at a highly symmetric behavior, likely due to the highly symmetric junctions.

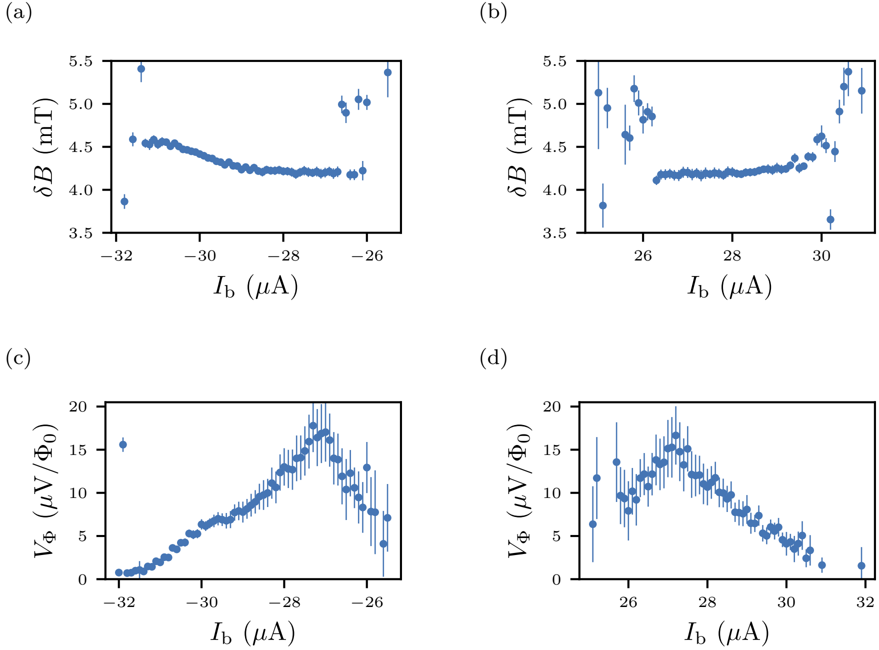

Figure 5.14.: Fit parameters of the sinusoidal fit of $V(B)$ curves at constant bias current. (a, b) The period of the sinusoidal fit for negative (a) and positive (b) bias currents. A stable modulation is observed for currents of $27\,\mu\text{A} \leq |I_\text{b}| \leq 29\,\mu\text{A}$. (c, d) The transfer coefficient of the voltage modulation. Two maxima are observed at $-27.3\,\mu\text{A}$ and $27.2\,\mu\text{A}$.

The voltage modulation is highly suppressed compared to the first-generation long-bridge SQUIDs by almost two orders of magnitude and the I_c modulation vanished entirely. Nevertheless, the structure forms a functional SQUID device. The higher critical current requires the current source to operate in a higher output range, resulting in lower current resolution and a higher noise current amplitude (section B.2.1).
Furthermore, the dwell time is significantly reduced compared to the first-generation, resulting in a different chemical and compositional structure, e.g., higher tungsten content. While the increased I_c is likely a result thereof, it

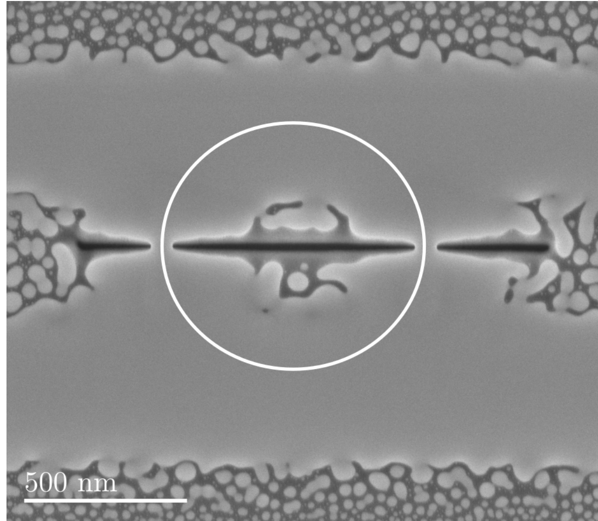

Figure 5.15.: SEM micrograph of the short-constriction SQUID of second generation presented in this section. The white circle indicates the effective area, matching the geometry very well.

remains an open question whether it also directly influences the SQUID properties.
However, we lean towards the experimental setup being responsible for the decreased critical current and voltage modulation. Dwell times in the range of hundreds of ns are common in literature [108, 117, 147, 148] and fascinating properties such as long-range vortex transport [149] have been observed. Further experiments of these structures using optimized, low-noise electronics could help settle this question.

5.3. SNS Contacts

5.3.1. Fabrication

In this section, we present a SQUID with SNS junctions serving as Josephson contacts. The sample was fabricated following the procedure presented in section 4.2.3. Hence, it is a SQUID of second generation fabricated with a dwell time of 200 ns and the beam current of 9.7 pA. The deposition of the metallic junction was carried out at an electron beam of 10 nA and a dwell time of 1.4 ms.
In fig. 5.16a the sample is shown before the deposition of the metallic junction via FEBID, in fig. 5.16b the full SQUID is shown. The junction length in this sample is highly symmetric with 40 nm for either junction.

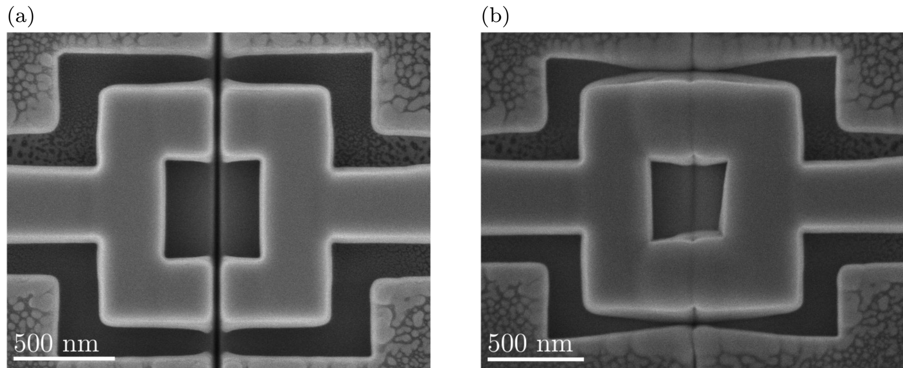

Figure 5.16.: SEM micrographs of an SNS SQUID before (a) and after (b) the deposition of the metallic W-C. Both junctions have a length of 40 nm.

5.3.2. Electrical Properties

During cooldown, the sample was biased with a current of 1 µA. The temperature dependence of the resistance at low temperatures is displayed in fig. 5.17a. We observe a normal state resistance $R_{\mathrm{N}} = (155.63 \pm 0.16)\,\Omega$ and a superconducting phase transition at $T_{\mathrm{c}} = (4.45 \pm 0.07)\,\mathrm{K}$.
However, the structure is turning only partially superconducting. A constant residual resistance of $R_{\mathrm{res}} = (24.04 \pm 0.32)\,\Omega$, i.e., 15 % of R_{N}, remains down to the base temperature of the PPMS at 2 K.

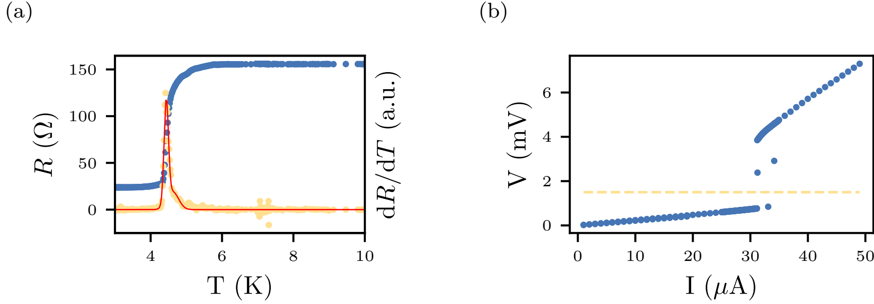

Figure 5.17.: Electric properties of long-bridge SQUIDs. (a) Temperature dependence of the resistance at low temperatures, showing the transition to superconductivity. A residual resistance of 24 Ω remains down to the base temperature of 2 K. (b) IV characteristics measured at 0 mT in DC mode at the base temperature of 2 K.

The IV-characteristic at 2 K, shown in fig. 5.2b, exhibits a single, sharp transition at $I_c = (31.185 \pm 0.001)$ µA. The sharp transition allows for a very well converging fit with remarkably low error. This sharp transition hints at a lower susceptibility of the SNS contact to electronic noise in comparison to constrictions.

The normal-state resistance is low compared to the constriction-type SQUIDs of first generation (sections 5.1.2 and 5.2.1) and the critical current is approximately three times larger. We attribute this to the large cross-sectional area of the junction in combination with the higher tungsten content of the structures fabricated at $\tau_d = 200$ ns.

As a consequence of the only partially achieved superconductivity, we were not able to measure modulation of I_c or V in upon varying flux coupled into the SQUID.

However, the junctions are of 40 nm length, approximately twice the limit to achieve coherent transport accross a weak link (eq. (1.43)). In section 4.2.3 we demonstrated the fabrication of junctions with a length of 30 nm, coming closer to coherent transport. Furthermore, Blom et al. reported functional single JJs with a residual resistance of 3 % to 10 % [105]. As the comparably high electronic noise inside the PPMS decreases the phase coherence in the highly sensitive SQUID structures, we have justified reason to believe that the repetition of the experiment in an optimized setup has the potential to result in a functional SQUID device.

Due to promising results in long-bridge (section 5.1) and short-constriction (section 5.2) SQUIDs and limited resources, we did not investigate this approach

any further. Nevertheless, we remain optimistic that future experiments are worth pursuing this approach.

5.4. SQUID on Lever

In this section we present the results of the electric and magnetic characterization of both, a long-bridge (section 5.4.1) and a short-constriction (section 5.4.2) SQUID fabricated at the apex of an SPM cantilever. The cantilevers were provided by Armin Knoll et al. from IBM Zürich.
The fabrication process of the devices follow the routine we developed and presented in section 4.2. As detailed in section 4.2, the dwell time had to be reduced compared to initial experiments on large substrates to $\tau_\mathrm{d} = 200\,\mathrm{ns}$.
As in previous experiments, we began with an initial characterization of the fundamental superconducting properties, namely, the critical temperature T_c and the critical current I_c at $B = 0\,\mathrm{mT}$.
In a separate cooldown two weeks later, the SQUID properties are assessed by a measurement of the IV characteristics of the SQUID at varying magnetic field set points. At each set point, we consecutively measured five independent IV curves in DC mode for both positive and the negative bias currents I_b at a reading count of 1.
The experiments commenced at a high positive field of $B = 75\,\mathrm{mT}$ sweeping towards $B = 0\,\mathrm{mT}$. However, the experiments were interrupted due to equipment maintenance at $B = 45\,\mathrm{mT}$, preventing the assessment of the low field region. Subsequent attempts to continue the experiment using a similar instrument were unsuccessful due to higher electric noise. All experiments are conducted at $T = 2\,\mathrm{K}$.

5.4.1. Long-bridge SoL

Fabrication

Figure 5.18 displays SEM micrographs of the SQUID presented in this subsection. The sample resembles a long-bridge SQUID of second generation as described in section 4.2.1 under consideration of the specifics to SPM cantilevers as laid out in section 4.1.1.
The inner loop area of the structure is $A_\mathrm{i} = (280\times615)\,\mathrm{nm}^2$ and the outer area of the washer is $A_\mathrm{o} = (930 \times 775)\,\mathrm{nm}^2$, well comparable the long-bridge SQUIDs of first generation presented in section 5.1. The nano-bridges are of width $w_{1,2} = (81,\ 75)\,\mathrm{nm}$, approximately double the width of the first generation SQUIDs. Although narrower bridges have been fabricated (section 4.2.1), no electrical characterization of these are available to the point of writing.

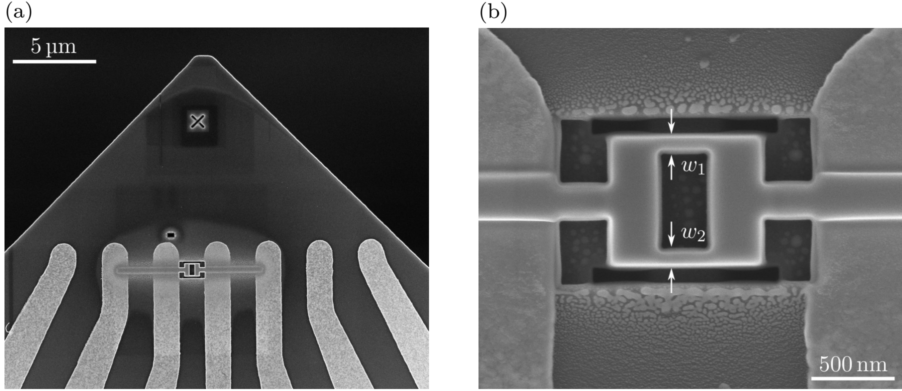

Figure 5.18.: SEM Micrographs of a long-bridge SQUID on a cantilever. The SQUID obtained a width of the nano-bridges of $w_{1,2} = (81,\ 75)\,\mathrm{nm}$, an inner loop area of $A_\mathrm{i} = (280 \times 615)\,\mathrm{nm}^2$ and an outer area of $A_\mathrm{o} = (930 \times 775)\,\mathrm{nm}^2$. (a) General view of the SQUID fabricated on a SPM cantilever and (b) magnified view.

Initial Characterization

Upon cooldown, the SQUID was biased by a current $I_\mathrm{b} = 1\,\mathrm{\mu A}$ and the resistance was measured in dependence of the temperature, as shown in fig. 5.19a. We observe a normal state resistance of $R_\mathrm{N} = (129.49 \pm 0.15)\,\Omega$, obtained by calculating the mean of the resistance measured in the range $6.0\,\mathrm{K} \leq T \leq 10.0\,\mathrm{K}$. The normal state resistance is only 26 % of the resistance of the long-bridge SQUIDs of first generation, likely due to the increased tungsten content of the W-C fabricated at $\tau_\mathrm{d} = 200\,\mathrm{ns}$ and the increased width of the junctions.
Modelling $\mathrm{d}R/\mathrm{d}T$ yields best results for the superposition of two Gaussian functions, one major peak with a small shoulder to the right side. The center of the distributions is interpreted as the critical temperatures $T_{\mathrm{c}_1} = (4.41 \pm 0.16)\,\mathrm{K}$ and $T_{\mathrm{c}_2} = (4.78 \pm 0.27)\,\mathrm{K}$. Unlike in the first-generation SQUIDs, after the transition full superconductivity is achieved.
Figure 5.19b shows a single IV-characteristic of the SQUID at $B = 0\,\mathrm{mT}$ and $T = 2\,\mathrm{K}$. The measurement was conducted in DC-mode and with a reading count of 1.
Similar to other experiments on second-generation SQUIDs (sections 5.2.2 and 5.4.2) we observe discrete jumps between $V = (0\,\mathrm{V},\ V_\mathrm{N})$ in the transition range. In this case, the transition range is large, and the derivative does not yield conclusive results with reasonably applied filtering. Defining a voltage threshold $V_\mathrm{th} = 0.1\,\mathrm{mV}$ yields a first transition at $I_{\mathrm{c}_1} = 24.38\,\mathrm{\mu A}$. A second transition is found at $I_{\mathrm{c}_2} = 24.99\,\mathrm{\mu A}$ with a voltage threshold of $V_\mathrm{th} = 2.1\,\mathrm{mV}$.

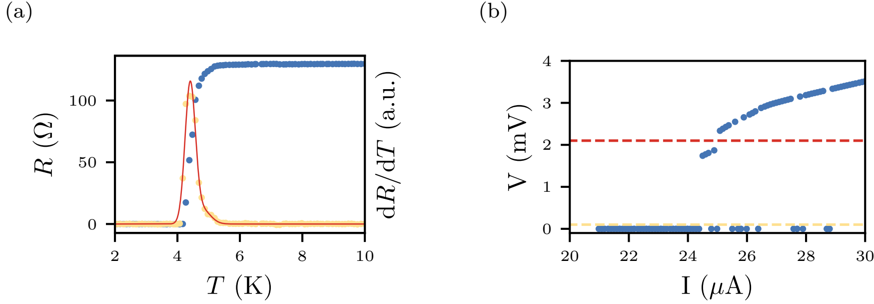

Figure 5.19.: Initial characterization of the superconducting properties of a long-bridge SQUID measured at $B = 0\,\mathrm{mT}$. (a) $R(T)$ measured with $I = 1\,\mu\mathrm{A}$. The yellow data points show the numerical derivative $\mathrm{d}R/\mathrm{d}T$, normalized to fit the plot. The red curve shows the result of a fit modelling the data as a superposition of several Gaussian curves. (b) $V(I)$ at $T = 2\,\mathrm{K}$. The horizontal lines indicate the voltage threshold used to obtain an estimate of I_c.

IV-Characteristics at High Fields

Figure 5.20 shows the IV-characteristics of the SQUID at $B = 50\,\mathrm{mT}$ after averaging and three times applying a rolling mean filter over the next adjacent datapoints, the derivative $\mathrm{d}R/\mathrm{d}I$ and the corresponding fit of the data by superimposed Gaussian functions. Remarkably, the critical current, although at higher magnetic field, is increased in comparison to the initial characterization carried out in another cooldown two weeks in advance.
In the expected transition region between $20\,\mu\mathrm{A} \leq I \leq 35\,\mu\mathrm{A}$, the step size between two current set points is $\delta I = 0.1\,\mu\mathrm{A}$. At current set points outside this range, the step size is $\delta I = 0.5\,\mu\mathrm{A}$.
Remarkably, the SQUID exhibits strong asymmetric behavior with respect to positive and negative currents biasing the system with I_c^- being way lower than I_c^+. For negative currents (fig. 5.20a), the analysis yields two transitions $I_{\mathrm{c}_1}^- = (-28.20 \pm 0.13)\,\mu\mathrm{A}$ and $I_{\mathrm{c}_2}^- = (-29.20 \pm 0.27)\,\mu\mathrm{A}$.
On the positive current flank (fig. 5.20b), the transition region is spreading into the region of the measurement with current steps of $\delta I = 0.5\,\mu\mathrm{A}$. As a result, small features in the transition can not be resolved and $\mathrm{d}R/\mathrm{d}I$ exhibits large jumps that the model of a Gaussian function can not fully approximate. Thus, quantitative analysis is mostly prohibited, and we will mainly focus on negative currents in the following. The fit for the positive current flank reports a critical current $I_\mathrm{c}^+ = (34.84 \pm 0.86)\,\mu\mathrm{A}$.

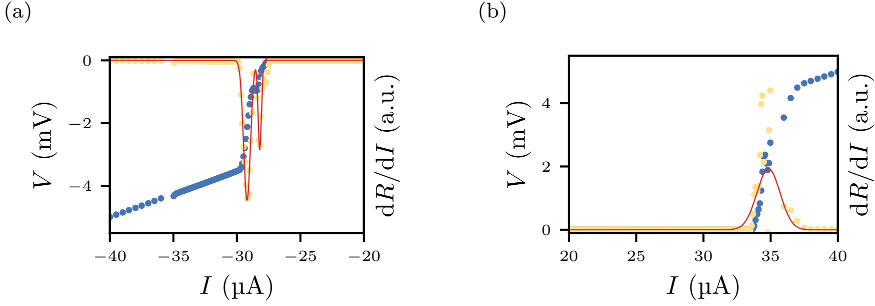

Figure 5.20.: IV-characteristics of a long-bridge SQUID on a cantilever at 50 mT for negative (a) and positive (b) currents. Each data point is the mean of five data points from independently measured $V(I)$ curves. The data is furthermore smoothed by three times averaging each data point with its adjacent points. The yellow data points show the numerical derivative $\mathrm{d}R/\mathrm{d}I$, normalized to fit the plot. The red curve shows the result of a fit modelling the data as a superposition of several Gaussian curves.

Magnetic Properties

Figure B.5 shows the magnetic field dependence of the first transition I_{c_1}. Over the range measured no modulation is observed on either current side. On the negative current flank a strong variation of I_c is observed for $B \lesssim -60\,\mathrm{mT}$. For $B \gtrsim 60\,\mathrm{mT}$ I_c is more stable and suitable for analysis of the voltage modulation. Thus, in the following we consider the magnetic field range $62.5\,\mathrm{mT} \leq B \leq 75\,\mathrm{mT}$.

In order to analyze the magnetic field dependence of the voltage we extract curves of constant current from the smoothed data of the analysis of $I_\mathrm{c}(B)$. In fig. 5.21 we present an exemplary curve of the voltage modulation at $I = \pm 34\,\mu\mathrm{A}$, i.e., beyond the last transition.

For positive currents, no modulation is observed. For negative currents, however, a sinusoidal modulation on top of a parabolic background is visible. The background is attributed to a magneto-resistive contribution at increasing magnetic field.

Figures 5.21c and 5.21d shows $V(\Phi)$ after subtraction of the magneto-resistive contribution. Each curve is shifted by $1\,\mu\mathrm{V}$ for clarity. The red curve indicates the fit of the sinusoidal modulation.

While the positive side does not exhibit a clear modulation and the fit does not converge well, the negative side shows a sinusoidal modulation of the voltage for currents $I \leq -34\,\mu\mathrm{A}$. The amplitude of the modulation is decreasing the higher the distance of I_b from I_c.

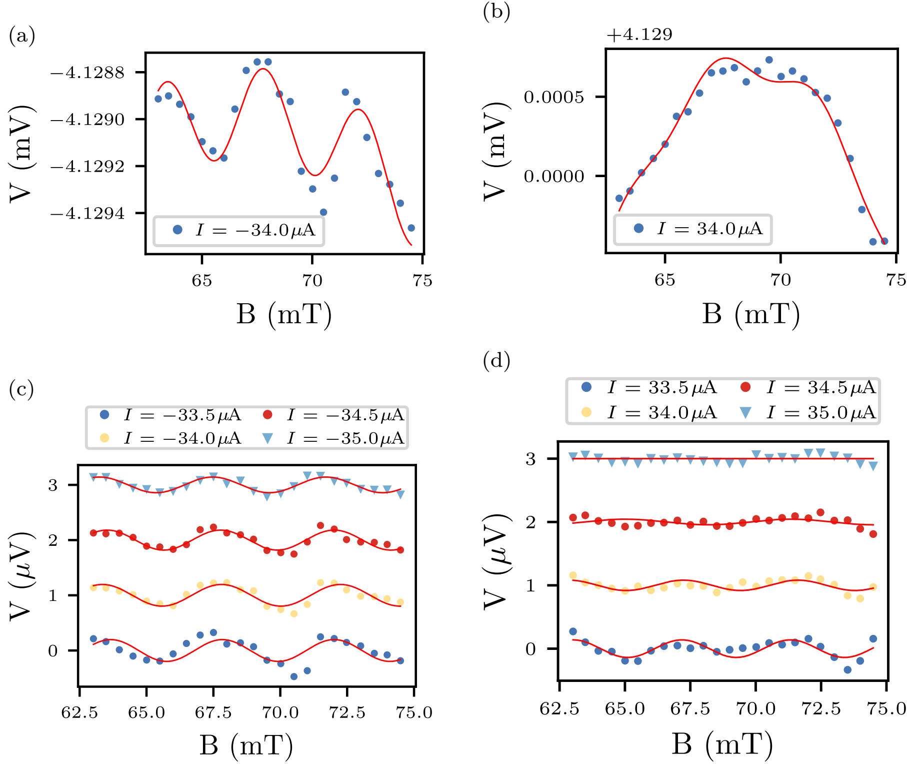

Figure 5.21.: (a, b) Voltage modulation of a long-bridge SQUID on a cantilever for $I = \pm 34\,\mu\text{A}$. The curve is obtained by extracting data points at constant current set point from the smoothed IV-characteristic. The red curve indicates a fit modelling the data as a sinusoidal function superimposed by a parabolic background. (c, d) Voltage modulation of a long-bridge SQUID on a cantilever for currents with a stable modulation period. The curve is obtained by extracting data points at constant current set point from the smoothed IV-characteristic. The red curve indicates a fit modelling the data as a sinusoidal function after subtraction of the parabolic, magneto-resistive contribution. The curves are shifted by 1 µV for clarity.

Figure 5.22 shows the quantitative analysis of the period of the modulation δB and the transfer coefficient V_Φ.
Averaging values in the current range $-35\,\mu\text{A} \leq I_\text{b} \leq -34\,\mu\text{A}$ yields a period of $\delta B = (4.33 \pm 0.15)\,\text{mT}$ and a transfer coefficient of $V_\Phi = (1.15 \pm 0.15)\,\mu\text{V}/\Phi_0$ on the negative side. For positive currents in the range $33\,\mu\text{A} < I_\text{b} \leq 33.5\,\mu\text{A}$ we obtain a period of $\delta B = (4.06 \pm 0.22)\,\text{mT}$ and a transfer coefficient of $V_\Phi = (0.93 \pm 0.40)\,\mu\text{V}/\Phi_0$.
The modulation on the negative side is faint but clearly visible. On the positive side, however, the fit results have a large error and little confidence. The

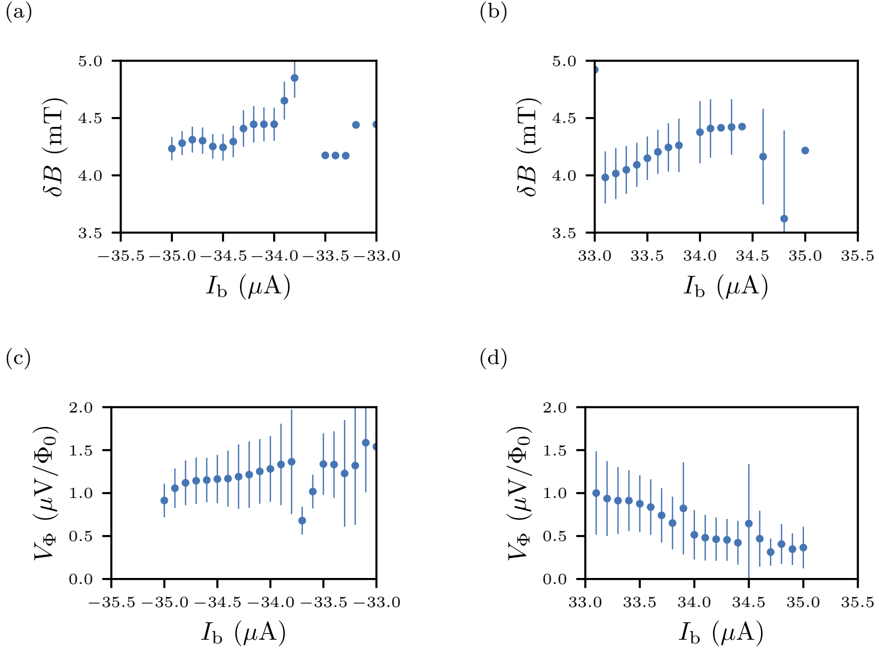

Figure 5.22.: (a, b) Period of a long-bridge SQUID on a cantilever for negative and positive currents above I_c of the last transition. (c, d) Transfer coefficient for the same currents.

analysis on the positive side is hindered by the slightly higher I_c, moving parts of the transition into the region of lower current resolution. Judging by the negative side, we assume that the SQUID is functional. Nevertheless, the voltage modulation is decreased by three orders of magnitude compared to the first-generation long-bridge SQUID presented in section 5.1 and one order of magnitude compared to the second-generation short-constriction SQUIDs, presented in section 5.2.2.

The comparably low quality stems from a combination of the two disadvantages discussed in the respective sections:

- Long-bridge SQUIDs are expected to exhibit higher kinetic inductance and don't allow for phase coherence across the long nanobridge.
- Second-generation samples have a higher critical current, resulting in experimental challenges in the PPMS.

The effective area according to eq. (1.49) is $A_{\mathrm{eff}} = 0.472\,\mathrm{\mu m}^2$ on the negative side and $A_{\mathrm{eff}} = 0.478\,\mathrm{\mu m}^2$ on the positive side. Figure 5.23 shows a SEM micrograph of the SQUID with a white rectangle indicating the effective area.

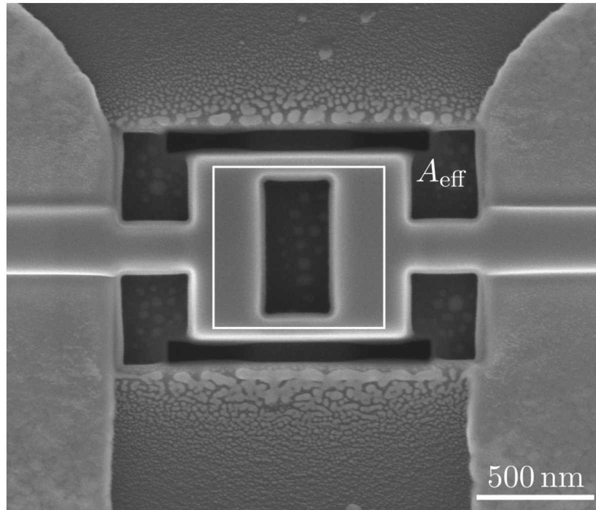

Figure 5.23.: SEM micrograph of a long-bridge SQUID on a cantilever. The white rectangle indicates the effective area.

5.4.2. Short-Constriction SoL

Fabrication

The fabrication process of short-constriction SQUIDs is described in detail in section 4.2.2 under consideration of the specifics for cantilevers as outlined in section 4.2.4.
In this section, the SQUID as shown in fig. 5.24, obtained a junction length and width of $l_{1,2} = (40,\ 55)\,\mathrm{nm}$ and $w_{1,2} = (113,\ 97)\,\mathrm{nm}$. The inner loop area is $A_i = (442 \times 418)\,\mathrm{nm}^2$ and the outer boundaries of the washer are $A_o = (1020 \times 1004)\,\mathrm{nm}^2$.

Initial Characterization

Figure 5.25 displays the initial characterization of the short-constriction SQUID on cantilever. The normal-state resistance of the device is $R_\mathrm{N} = (71.19 \pm 0.12)\,\Omega$.
In the cooldown curve we observe one major transition and one less pronounced transition at $T_{\mathrm{c}\,1} = (4.52 \pm 0.25)\,\mathrm{K}$ and $T_{\mathrm{c}\,2} = (5.24 \pm 0.12)\,\mathrm{K}$.
The IV-characteristics at $B = 0\,\mathrm{mT}$ and $T = 2\,\mathrm{K}$ shows a narrow transition range with one major transition at $I_{\mathrm{c}_1} = 43.48\,\mu\mathrm{A}$ and two smaller ones at $I_{\mathrm{c}_2} = 47.68\,\mu\mathrm{A}$ and $I_{\mathrm{c}_3} = 48.10\,\mu\mathrm{A}$. The transition is remarkably clean with a single discrete step, the back and forth switching between super- and normal-conducting phases is not observed at all.

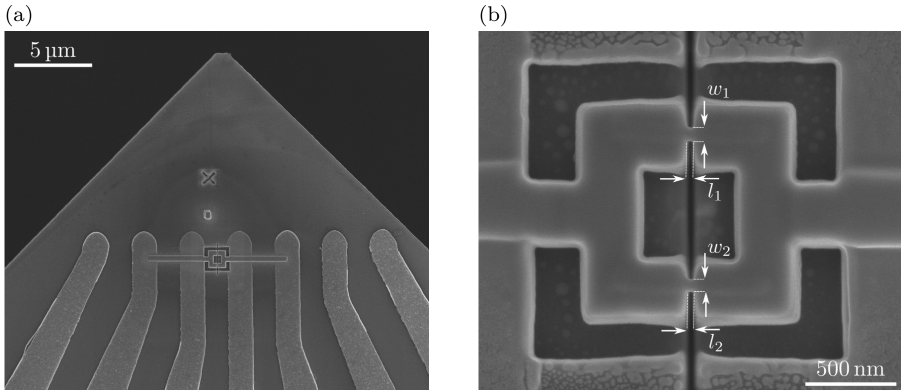

Figure 5.24.: SEM Micrographs of a short-constriction SQUID on a cantilever. The SQUID obtained a width of the constrictions of $w_{1,2} = (113,\ 97)\,\mathrm{nm}$ and a length of $l_{1,2} = (40,\ 55)\,\mathrm{nm}$. The inner loop area is $A_\mathrm{i} = (442 \times 418)\,\mathrm{nm}^2$ and an outer area of the washer $A_\mathrm{o} = (1020 \times 1004)\,\mathrm{nm}^2$.

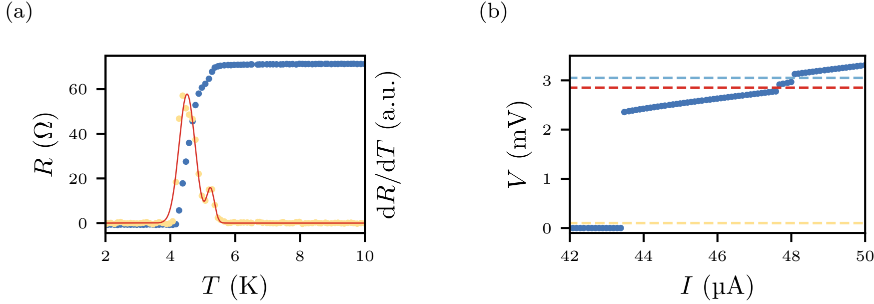

Figure 5.25.: Initial characterization of the superconducting properties of a short-constriction SQUID measured at $B = 0\,\mathrm{mT}$. (a) $R(T)$ measured with $I = 1\,\mu\mathrm{A}$. The yellow data points show the numerical derivative $\mathrm{d}R/\mathrm{d}T$, normalized to fit the plot. The red curve shows the result of a fit modelling the data as a superposition of several Gaussian curves. (b) $V(I)$ at $T = 2\,\mathrm{K}$. The horizontal lines indicate the voltage threshold used to obtain an estimate of I_c.

The step size between adjacent current set points is $\delta I = 0.1\,\mu\mathrm{A}$ for currents $I_\mathrm{b} \leq 50\,\mu\mathrm{A}$. For currents $I_\mathrm{b} > 50\,\mu\mathrm{A}$ the current source switches to a new range, resulting in a lower step size of $\delta I \geq 0.3\,\mu\mathrm{A}$ and higher electronic noise, prohibiting the quantitative analysis of higher currents.

IV-Characteristics at High Fields

In the IV characteristics at higher magnetic field, the discrete transition between superconducting and normal phase reappears. Therefore, we show the IV characteristics at $50\,\mathrm{mT}$ after averaging the individual readings and filtering the data with a moving average for three times in fig. 5.26. The negative side is best modelled by a superposition of three Gaussian functions. On the positive side, the main transition splits into two convoluted transitions resulting in a broader transition range and generally a more difficult analysis. At $B = 50\,\mathrm{mT}$ this approach yields

- $I^-_{\mathrm{c}_1} = (-43.18 \pm 0.16)\,\mu\mathrm{A}$,
- $I^-_{\mathrm{c}_2} = (-46.95 \pm 0.31)\,\mu\mathrm{A}$ and
- $I^-_{\mathrm{c}_3} = (-48.01 \pm 0.19)\,\mu\mathrm{A}$

on the negative side and

- $I^+_{\mathrm{c}_1} = (42.99 \pm 0.13)\,\mu\mathrm{A}$,
- $I^+_{\mathrm{c}_2} = (43.41 \pm 0.31)\,\mu\mathrm{A}$,
- $I^+_{\mathrm{c}_3} = (47.04 \pm 0.24)\,\mu\mathrm{A}$ and

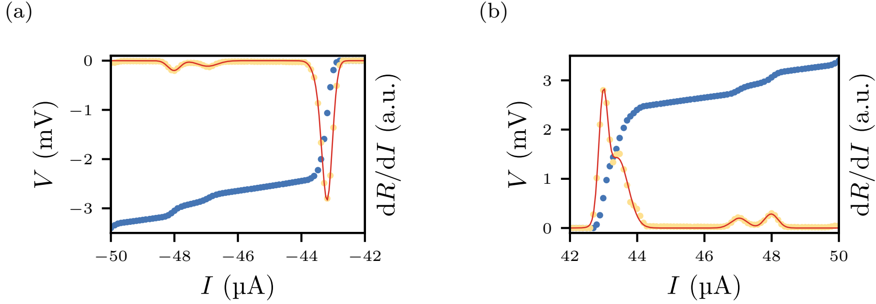

Figure 5.26.: IV-characteristics of a short-constriction SQUID on a cantilever at 50 mT for negative (a) and positive (b) currents. Each data point is the mean of five data points from independently measured $V(I)$ curves. The data is furthermore smoothed by three times averaging each data point with its adjacent points. The yellow data points show the numerical derivative $\mathrm{d}R/\mathrm{d}I$, normalized to fit the plot. The red curve shows the result of a fit modelling the data as a superposition of several Gaussian curves.

- $I_{c4}^{+} = (47.99 \pm 0.20)\,\mu\mathrm{A}$

on the positive side. The aging effect observed in the long-bridge SoL (section 5.4.1) is not observed in this sample.

Magnetic Properties

The analysis of the Figure B.6 shows the critical current of the first transition. We could not find a conclusive modulation of I_c in either of the transitions. However, the critical current is stable for negative currents and mostly stable on the positive current flank.

A conclusive voltage modulation can be found at currents above the last transition $I_b \gtrsim 48.5\,\mu\mathrm{A}$. In fig. 5.27 we present a selected curve of the voltage in dependence of the magnetic field at a constant current $I_b = 50\,\mu\mathrm{A}$. The red curve resembles the fit of a sinusoidal function on top of a parabolic background. In figs. 5.27c and 5.27d we present several curves after subtraction of the magneto-resistive contribution, shifted by $5\,\mu\mathrm{V}$ for clarity.

The meta-analysis of the fit results reveals that the period and the transfer coefficient (section 5.4.2) can be reliably determined in a current range $48.5\,\mu\mathrm{A} \leq |I_b| \leq 50\,\mu\mathrm{A}$. For currents below $48.5\,\mu\mathrm{A}$ the influence of the second upmost transition prohibits a conclusive analysis. For currents above $50\,\mu\mathrm{A}$ the switch of the current range of the source injects too much noise for a conclusive analysis.

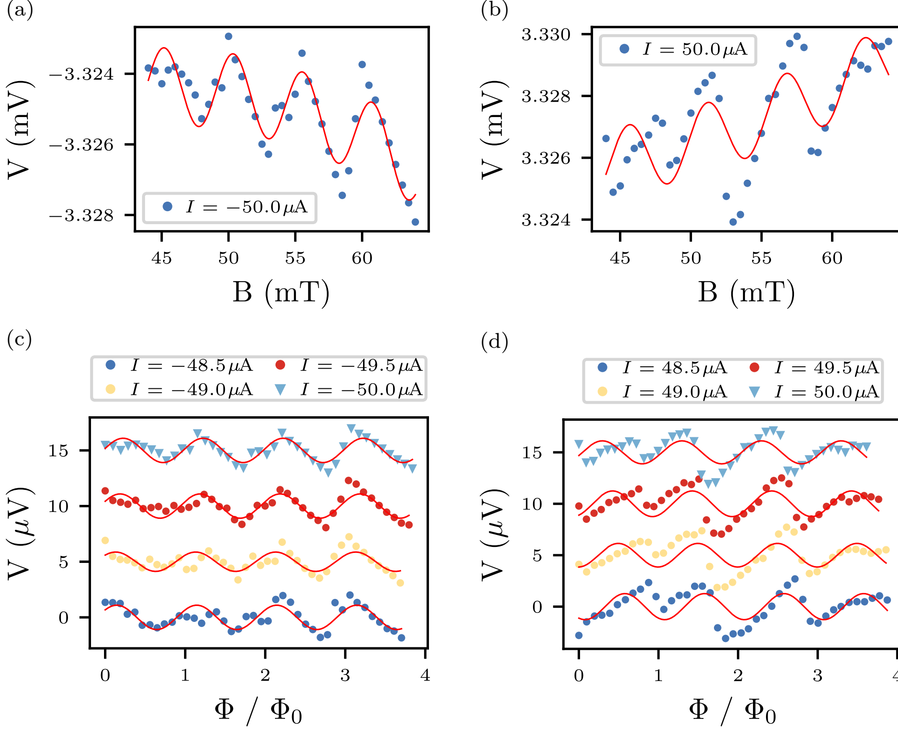

Figure 5.27.: (a, b) Voltage modulation of a short-constriction SQUID on a cantilever for $I = \pm 50\,\mu\text{A}$. The curve is obtained by extracting data points at constant current set point from the smoothed IV-characteristic. The red curve indicates a fit modelling the data as a sinusoidal function superimposed by a parabolic background. (c, d) Voltage modulation of a short-constriction SQUID on a cantilever. The curve is obtained by extracting data points at constant current set point from the smoothed IV-characteristic. The red curve indicates a fit modelling the data as a sinusoidal function after subtraction of the parabolic, magneto-resistive contribution. The curves are shifted by $5\,\mu\text{V}$ for clarity.

Averaging the period and the transfer coefficient in the given current range yields a period $\delta B = (5.15 \pm 0.34)\,\text{mT}$ on the negative and $\delta B = (5.22 \pm 0.22)\,\text{mT}$ on the positive side. The transfer coefficient is given by $V_\Phi = (5.93 \pm 1.66)\,\mu\text{V}/\Phi_0$ for negative and $V_\Phi = (7.42 \pm 2.59)\,\mu\text{V}/\Phi_0$ for positive currents. The positive and negative current flanks are well comparable.
The effective area obtained from the period is $A_{\text{eff}} = (0.391 \text{ and } 0.406)\,\mu\text{m}^2$ for the negative and the positive side. Figure 5.29 shows a SEM micrograph of the SQUID with the white line indicating the effective area.

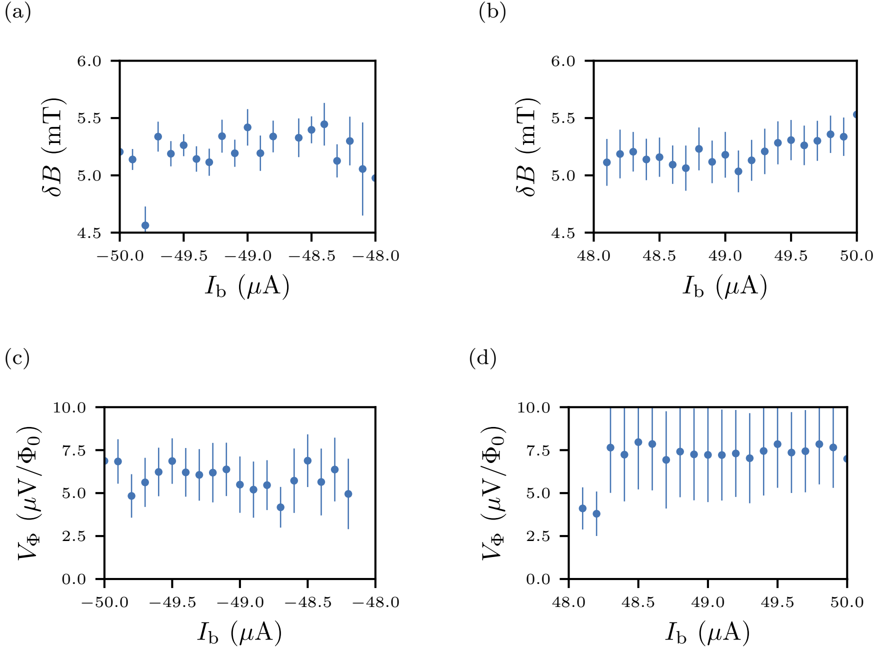

Figure 5.28.: (a, b) Period of a short-constriction SQUID on a cantilever for negative and positive currents above I_c of the last transition. (c, d) Transfer coefficient for the same currents.

Although the error to the fit is fairly large, the modulation is clearly visible. Compared to the long-bridge SoL, the modulation depth is increased by a factor of five. The shorter constriction clearly helped increasing the quality of the SQUID device.

The transfer coefficient of the short-constriction SQUID of second generation fabricated on a large substrate is three times larger than for the SoL. However, the data is hard to compare as the investigated magnetic field range differs a lot. Similar to the SQUID on a substrate, a magnetoresistive background is observed.

Both SoL presented here were of an early batch. In section 4.2.4 we have presented samples after the refinement of the deposition process in which we have obtained junction widths of $w \gtrsim 40\,\mathrm{nm}$ and lengths of $l \gtrsim 20\,\mathrm{nm}$. As the junction dimensions play a crucial role in SQUID performance, we expect further experiments on optimized samples to yield better results.

The available ranges of the current source prohibited the analysis of higher bias currents. Furthermore, the analysis of the low field range is missing due to the

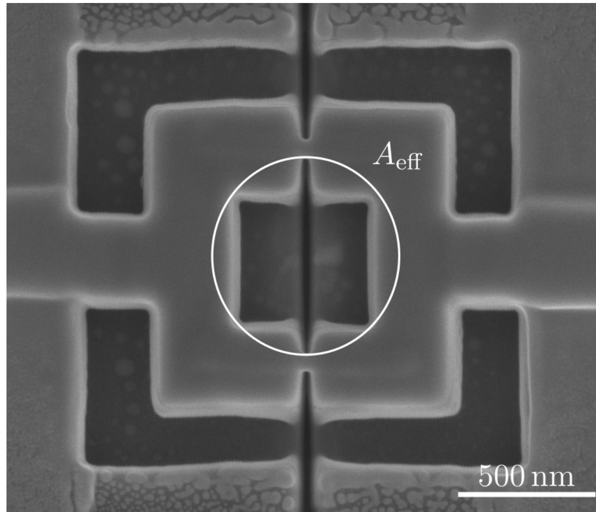

Figure 5.29.: SEM micrograph of a short-constriction SQUID on a cantilever. The white circle indicates the effective area.

maintenance of the equipment. We suggest repeating the experiment in the low field region.
The transfer coefficient determined in the experiment presented here is low in comparison to high performance SQUIDs found in literature [96, 145, 146]. However, the high electronic noise of our equipment suppresses the coherence of the superconducting phase in our SQUIDs. The analysis of a short-constriction SoL in a low-noise environment, e.g., in the lab of our collaboration partners in Tübingen or Basel, would provide more comprehensive insight in the quality of our approach.

5.5. Summary

On the path towards a functional SQUID on Lever (SoL) grown in a bottom-up, single-step Focused Ion Beam Deposition (FIBID) process several SQUIDs designs on both, large substrates and prepatterned cantilevers have been characterized and their electrical and magnetic properties assessed.
The first generation of SQUIDs was fabricated on large substrates. The deposition process was carried out with a dwell time of 500 µs. In section 5.1 and section 5.2.1 two SQUIDs based on long-bridge Josephson Junction (JJ) and two SQUIDs based on short-constriction JJs were presented.
The long-bridge SQUIDs were characterized in our laboratory's PPMS (section 2.3.1) system. They exhibit both, critical current and voltage modulation. While the critical current modulation is comparably low (1 % to 2 %) and the screening factor is comparably high ($\gtrsim 44$), the voltage modulation of up to $1300\,\mu V/\Phi_0$ is comparable to existing SQUIDs device in literature [96, 145, 146]. The approach was chosen due to fabricational simplicity, as the structure was composed from well understood components, i.e., broad pads and narrow nanowires.
The quality of the SQUID properties in these structures is mostly limited by the long nanobridges of approximately 300 nm length, introducing a large kinetic inductance ($L_{\mathrm{tot}} = L_{\mathrm{geom}} + L_{\mathrm{kin}} \gtrsim 10\,\mathrm{nH}$) and hindering phase-coherent transport. To overcome these limitations, the constriction length was reduced as far as possible. The junction length in the SQUIDs presented in section 5.2.1 was decreased by one order of magnitude down to 25 nm to 30 nm.
The structures were characterized in the laboratories of our collaboration partners in Tübingen in experimental setups optimized for low-noise measurements (section 2.3.3). The combination of the low-noise setup and the reduction of the junction length resulted in an upper limit for the screening factor of $\lesssim 5.7$, approaching the target value of 1 and an upper limit of the total inductance of $\lesssim 900\,\mathrm{pH}$. The reported values forms an upper limit due to experimental restrictions introduced by the modulation line.
In a second generation of SQUID design approaches the dwell time was decreased to 200 ns, necessitated by the specific growth conditions on cantilevers. Experiments of a short-constriction and an SNS-JJ SQUID on large substrates (sections 5.2.2 and 5.3) were presented as well as long-bridge and short-constriction SoLs (sections 5.4.1 and 5.4.2).
The characterization of all of these samples was carried out in the PPMS. In general, the increased tungsten content in the deposits due to the higher dwell time resulted in higher critical temperatures and critical currents in the

second-generation SQUIDs. Furthermore, the IV characteristics exhibited discrete jumps from the superconducting to the normal state and back within a broad current range, an experimental challenge formerly unknown. The best explanation we can provide for this is the high sensitivity of SQUIDs to current-noise, obtaining a higher noise amplitude at higher bias currents. In a statistical process, the total current consisting of current setpoint and a temporal noise current causes transition to the normal state. The PPMS injects current in a pulsed way, giving the superconducting structure the chance to relax to the superconducting state while the current source is turned off.
Due to the oscillatory behavior in the transition region, the critical current can not be determined with sufficient precision to observe modulation in the critical current. Nevertheless, voltage modulations can be extracted. The short-constriction SQUID of second generation presented in section 5.2.2 exhibits a transfer coefficient of approximately $17\,\mu V/\Phi_0$. This is two orders of magnitude lower than the values observed in the long-bridge SQUID of first generation (section 5.1). We can not conclusively say whether the reduced transfer coefficient is a direct consequence of the different dwell time or an indirect artefact from a higher noise level at higher critical currents. Further experiments in low-noise systems are required to solve this riddle.
The SNS SQUID on a large substrate (section 5.3) does not exhibit voltage modulation. Nevertheless, we remain optimistic that it is worthwhile to pursue the approach further. The same arguments about the noise level in the PPMS hold for this experiment. Furthermore, later experiments have shown that a reduction of the junction length from 40 nm in this sample to 20 nm are feasible, increasing phase coherence across the junction.
Finally, we fabricated and characterized long-bridge and short-constriction SQUIDs on levers provided by Armin Knoll et al. from IBM Zürich (section 5.4). The long-bridge SoL exhibited faint a voltage modulation with a transfer coefficient of approximately $1\,\mu V/\Phi_0$. It comes to no surprise that the short-constriction SoL outperforms the long-bridge counterpart by a factor of six to seven, i.e., a transfer coefficient of $6\,\mu V/\Phi_0$ and $7\,\mu V/\Phi_0$ for negative and positive currents, respectively.
The short-constriction SoL marks the first proof of concept of a functional SQUID device grown in a single-step, bottom-up FIBID process on a commercial SPM cantilever. Admitedly, compared to other SoL and SoT devices, the performance of the SQUID is rather low. However, in our laboratories we did not have electronics at hand optimized for the characterization of highly sensitive SQUID devices. Experiments conducted in the laboratory of the Eberhard Karls University of Tübingen (section 2.3.3) suggest, that the results obtained in our facilities are limited by the equipment rather than the internal device

characterisitcs. Further experiments with low-noise instruments are required to conclusively tell whether FIBID grown SoL devices on the basis of W-C are able to compete with traditional materials or not.

Chapter 6

Conclusions and Outlook

Contents

6.1. Cryogen Free Magnet System 159
6.2. Ga^+-FIBID for SQUID Nanofabrication 160
6.3. SQUID Characterization 162

This thesis was embedded in the FIBSuperProbes initiative, forming a consortium of researchers from the CSIC-University of Zaragoza, the Eberhard Karls University of Tübingen, and the University of Basel. The researchers joined their efforts to explore the capabilities of FIB processing in order to functionalize SPM probes provided by *IBM Zürich* with superconducting sensors, extending the capabilities of SPM (see section 1.4).
Therefore, various approaches were pursued. While our collaborators were mostly focused on top-down approaches, i.e., FIB milling of a superconducting thin film, our group in the CSIC-University of Zaragoza focused on a bottom-up approach. Ga^+-FIBID with the $W(CO)_6$ precursor was employed in order to deposit SQUID sensors on the basis of W-C in a direct-write process.
The ambitious goals of the project required working at the physical limitations of Ga^+-FIBID with simultaneous high demands regarding the electronic characterization. The following sections summarize how these challenges were met, finally resulting in the first functional SoL fabricated in a direct-write process via Ga^+-FIBID and provide an overview of potential future work building on the foundation laid in this thesis.

6.1. Cryogen Free Magnet System

In the early months of the thesis, on June 8, 2020, the Cryogenic-Free Measurement System (CFMS) was delivered to our facilities. Chapter 3 outlines the functionality of the cryogenic and electronic components of the system in detail and how the system was customized to meet our demands.
Initially, the use of the system was hindered by the COVID-19 pandemic. Due to travel restriction, the technician of the british manufacturer (Cryogenics Ltd.) could not travel to Spain and the installation was done by us and the spanish vendor through which it was purchased.
Upon installation, the CFMS was extensively tested and improved to meet our needs. Once the cryogenic components were well understood and running stable, the temperature stability down to 2 K was found remarkably high with a standard deviation of ± 0.014 mK.
The electronic instruments shipped with the system, a Keithley 2450 SMU and a Keithley 2182A NVM offer high precision and accuracy for sourcing current and reading voltage. However, their potential could not be fully exploited due to EMI coupling into the unshielded cables connecting the instruments to a breakout box. The quality of the transport characterization of samples could be greatly improved by replacing the breakout box with a custom built breakout

box using BNC connectors and coaxial cables to the point where a clear thermal hysteresis opening up in ideal conditions.
The software suite shipped with the system was replaced by a custom interface allowing to connect additional instruments. We connected an additional Keithley 2611A SMU, allowing to source a second current or a voltage. The integration of the instrument into the custom interface allows for the additional signal to be sweeped synchronously to the measurement routine of the experiment. The experiment design is further flexibilized by custom routines like the direct readout of I_c upon reaching a voltage threshold.
Unfortunately, the final shortcoming of the system, the low magnetic field resolution (peak-to-peak distance: 1.4 mT) could not be overcome. Given the typical modulation period of our SQUIDs of typically ~ 5 mT, the uncertainty of the magnetic field setpoint in persistent mode is too high for reliable measurements of I_c or voltage modulations.
Therefore, the system was not used for results presented in this thesis. Nevertheless, our facilities benefit from the efforts put into the development of the system. The custom breakout box greatly improves the noise characteristics of the system and the additional SMU allows for a broad range of experiments. On the basis of the existing software, the hurdle towards adding further instruments or providing additional routines not accounted for yet is reduced. To make the system fit for SQUID characterization, the only possibility we see is the purchase of a higher resolution magnetic field controller. Cryogenics Ltd. offers a version of the SMS120C featuring a 20 bit DAC, offering a theoretical resolution of 0.02 mT.

6.2. Ga^+-FIBID for SQUID Nanofabrication

In chapter 4 we layed out the path towards the fabrication of W-C-SoL by means of Ga^+-FIBID. Two interdependent challenges had to be met: the exploration of a fabrication routine of nanoSQUIDs on well understood large substrates and the transfer of the process to SPM cantilevers, meeting the differing deposition conditions.
The deposition routines can be categorized in two generations. Initial experiments were conducted with an ion beam current of 1.5 pA and a dwell time of 500 µs. However, the low beam current required an additional step of EBL to prepattern the substrate in order to keep the deposition time reasonably low,

limiting throughput. In order to increase throughput, the beam current was increased to 9.7 pA, yielding reasonably comparable results on large substrates. Furthermore, after troubles in the transfer of the deposition process to cantilevers, a systematic study in a TEM on the influence of the dwell time on the deposition regime was conducted on cantilevers. In order to prevent a crossover from the electron-limited regime to a diffusion limit we decreased the dwell time to 200 ns. At 200 ns dwell time and 9.7 pA beam current, further TEM analyses of deposits grown with different nominal thickness, i.e., deposition time, showed a 16 % higher deposition rate on substrates than on cantilevers, which we attribute to the decreased diffusion on cantilevers.
The cantilevers differ from large substrates by their geometry and composition. On cantilevers, we work near the apex of the tip, limiting the region from which diffusion can occur unrestricted to an opening angle of 90° while on substrates the diffusion is unhindered in all directions. Furthermore, the Si body of cantilever is covered by 50 nm of thermally grown SiO_2 while on large substrates the oxide layer is 300 nm thick. The low thermal conductivity of SiO_2 results in a stronger temperature increase upon irradiation with an ion beam on substrates (2.8 K) compared to cantilevers (1 K) under standard conditions. Potentially, this further hinders diffusion as the diffusion coefficient increases exponentially with temperature.
Regarding the SQUID design, several approaches have been followed. For fabricational simplicity, at first we fabricated long-bridge nanoSQUIDs. The SQUID washer nominally consisted of 800 nm wide banks connected via 300 nm long, 50 nm wide nanowires, yielding a nominal inner loop area of $A_0 = (300 \times 700)\,\mathrm{nm}^2$. In the first generation process, junction widths of down to (54, 57) nm were achieved, in second generation routines (58, 65) nm. Experiments on structures with decreasing inner loop area reveal that downsizing is straight forward down to nominal $A_0 = (200 \times 200)\,\mathrm{nm}^2$. Below, the deposition of halo results in a broadening of the structures.
In order to increase the phase coherence and decrease the kinetic inductance of the junctions, and thus the overall SQUID performance, the constriction length was reduced to fabricate short-constriction SQUIDs with a nominal inner loop area of $(300 \times 300)\,\mathrm{nm}^2$. With the first generation approach, the length was reduced down to (33, 36) nm and the width to (62, 68) nm. Using the second generation recipe, upon optimization, a width of (40, 48) nm and a length of down to (21, 22) nm was achieved, approaching the condition for phase coherence $l \leq 3.5\xi = 21\,\mathrm{nm}$.
The experiments on cantilevers were mostly conducted on cantilevers of the first batch where the gold contacts end 12.5 µm from the apex of the tip. Using Pt deposits as additional contacts, the distance to the apex could be reduced to

3.8 µm. However, Pt contacts have a strong impact on the noise characteristics. On cantilevers of the second batch, a SQUID was fabricated with a distance of 4.5 µm from the apex of the tip.
The challenges in SQUID- and SoL fabrication directly affected the performance of the resulting devices. At the same time, the results in characterization affected the design decissions for fabrication in a continuous process of refinement. In the following, we will summarize the results in characterization of SQUIDs fabricated along the processes summarized here. We see, that the length of the constriction-type junctions plays a crucial role for the SQUID performance. The shortest constrictions fabricated in the course of this work are 20 nm long, close to the physical limit of Ga^+-FIB. The use of lighter elements for FIB such as He or Ne could help to further decrease the length of the junctions and improve the SQUID performance.
Furthermore, the choice of 9.7 pA beam current was mostly due to the long process time when depositing at 1.5 pA. On the second batch of cantilevers the gold contacts run much closer to the apex of the tip (4 µm), obliterating the need for the deposition of long contacts with FIBID. On cantilevers of the second batch, the current could therefore be decreased, resulting in higher resolution and potentially reducing the negative influence of suppressed diffusion on cantilevers.

6.3. SQUID Characterization

This thesis has explored the development and characterization of SQUIDs fabricated via FIBID on both large substrates and prepatterned SPM cantilevers. The experimental challenges and the path towards the development of fabricational routines was summarized above. At the core of the work is the characterization of the magnetotransport properties of the SQUIDs, presented in chapter 5.
The first-generation SQUIDs were developed for the fabrication on large substrates with a dwell time of 500 µs. The first two functional devices, based on long-bridge Josephson Junction (JJ), exhibited voltage modulation comparable to literature values, with a transfer coefficient reaching $1300\,\mu V/\Phi_0$. However, the long nanobridges (300 nm) introduced significant kinetic inductance and exceeded the criterion for phase coherent transport by one order of magnitude. Therefore, the modulation depth of the critical current was strongly suppressed, reaching values of up to 2 %, a high screening factor of 44, and a high inductance of ~ 10 nH.

Reducing the junction length to 25 nm to 30 nm improved performance, with measurements in low-noise environments yielding a reduced screening factor ($\lesssim 5.7$) and lower total inductance ($\lesssim 900$ pH). In these experiments, the use of a modulation current instead of an external magnet in order to couple flux into the SQUID only allowed for an estimation of an upper limit of the given parameters. The experiment presented here gives justified reason to believe that the high noise level in the PPMS, used for the other experiments presented, suppresses the full potential of our SQUIDs.
In the second-generation SQUIDs, the dwell time was reduced to 200 ns to accommodate the growth conditions on cantilevers. This adjustment resulted in increased tungsten content and improved critical temperatures and currents. However, voltage measurements in the PPMS revealed discrete jumps between the superconducting and normal states, attributed to current noise and the current injection in form of a square wave, given by the internal working principle of the PPMS. The oscillatory behavior prevented the determination of I_c with sufficient confidence.
The short-constriction SQUID of second generation presented here exhibits a transfer coefficient of 17 µV/Φ_0, two orders of magnitude below the transfer coefficient of the long-bridge SQUIDs of first generation, raising questions about the impact of deposition parameters on performance. Further experiments in optimized low-noise conditions are required to clarify these effects. The SNS SQUID, fabricated according to the second generation recipe on a large substrate, did not exhibit voltage modulation. Nevertheless, subsequent work suggested that reducing junction length to 20 nm is feasible. Thereby, the coupling of the superconducting banks via the proximity effect is increased, potentially allowing to achieve full superconducting behavior, which was not observed in the SNS device.
Additionally, SQUIDs were successfully fabricated on commercial cantilevers, with short-constriction designs achieving a transfer coefficient six to seven times higher than their long-bridge counterparts. These results mark the first demonstration of SQUID devices grown via a single-step, bottom-up FIBID process on SPM cantilevers.
While the overall performance of these SQUIDs remains below that of conventional SoL devices, measurements in the facilities of our collaborators in Tübingen indicate that experimental constraints in the PPMS, rather than intrinsic device limitations, were the primary bottleneck. Nevertheless, the setup in Tübingen does not make use of an external magnet but relies on a modulation line, coming with its own set of challenges. Therefore, we suggest the characterization of promising SQUID devices in noise-free environments using an external magnet to couple flux into the SQUID loop. At the point of writing,

such experiments are underway in the facilities of our other collaborators at the university of Basel.
This thesis has demonstrated the feasibility of FIBID for SQUID fabrication and provided insights into the interplay between fabrication parameters and device performance. The integration of SQUIDs onto SPM cantilevers represents a significant step toward their application in scanning probe techniques, laying the groundwork for further advancements in this field.

Chapter 7

Conclusiones y Perspectivas

Contents

7.1. Sistema Criogénico Libre de Helio 167
7.2. FIBID con Ga^+ para Nanofabricación de SQUIDs 168
7.3. Caracterización de SQUIDs 170

Esta tesis se enmarca en la iniciativa FIBSuperProbes, un consorcio de investigadores de la Universidad de Zaragoza-CSIC, la Universidad Eberhard Karls de Tubinga y la Universidad de Basilea. Los investigadores unieron esfuerzos para explorar las capacidades del procesamiento mediante Focused Ion Beam (FIB) con el fin de funcionalizar sondas de Scanning Probe Microscopy (SPM), proporcionadas por IBM, con sensores superconductores, ampliando así las capacidades de la microscopía de sonda de barrido (véase sección 1.4).
Para ello, se exploraron diversos enfoques. Mientras que nuestros colaboradores se centraron principalmente en enfoques de fabricación descendente (top-down), es decir, el fresado FIB de una película delgada superconductora, nuestro grupo en la Universidad de Zaragoza-CSIC se enfocó en un enfoque ascendente (bottom-up). Se empleó la deposición inducida por haz de iones focalizado (Focused Ion Beam Induced Deposition, FIBID) con un precursor de hexacarbonilo de tungsteno ($W(CO)_6$) para depositar sensores SQUID basados en carburo de tungsteno (WC) mediante un proceso de escritura directa.
Los ambiciosos objetivos del proyecto exigieron trabajar en los límites físicos del Ga^+-FIBID, con altos requerimientos en cuanto a caracterización electrónica. En las siguientes secciones se resume cómo se abordaron estos desafíos, logrando finalmente la fabricación del primer SQUID-on-Lever (SoL) funcional mediante un proceso de escritura directa con Ga^+-FIBID, y se presenta una visión general del trabajo futuro potencial basado en los fundamentos establecidos en esta tesis.

7.1. Sistema Criogénico Libre de Helio

En los primeros meses de la tesis, el 8 de junio de 2020, se recibió en nuestras instalaciones el sistema criogénico libre de helio (Cryogen-Free Magnet System, CFMS). En el capítulo 3 se detalla la funcionalidad de los componentes criogénicos y electrónicos del sistema, así como las modificaciones realizadas para adaptarlo a nuestras necesidades.
Inicialmente, la instalación del sistema se vio dificultada por la pandemia de COVID-19. Debido a las restricciones de viaje, el técnico del fabricante británico (Cryogenics Ltd.) no pudo desplazarse a España, por lo que la instalación fue realizada por nuestro equipo con la asistencia del proveedor español.
Tras su instalación, el sistema fue sometido a pruebas exhaustivas y mejoras. Una vez que se comprendieron y estabilizaron los componentes criogénicos, se encontró que la estabilidad térmica a temperaturas de hasta 2 K era notablemente alta, con una desviación estándar de ± 0.014 mK.

Los instrumentos electrónicos proporcionados con el sistema, un Keithley 2450 SMU y un Keithley 2182A NVM, ofrecen alta precisión en la generación de corriente y la medición de voltaje. Sin embargo, su potencial no pudo aprovecharse plenamente debido a la interferencia electromagnética (EMI) en los cables sin blindaje que los conectaban a una caja de distribución. La calidad de la caracterización eléctrica podría mejorarse significativamente sustituyendo esta caja por una personalizada con conectores BNC y cables coaxiales, reduciendo el ruido hasta lograr una clara histéresis térmica en condiciones ideales.
El software original del sistema fue reemplazado por una interfaz personalizada que permite la conexión de instrumentos adicionales. Se integró un Keithley 2611A SMU adicional, permitiendo la generación de una segunda corriente o voltaje. Esta integración permite realizar barridos sincronizados con la rutina de medición del experimento y facilita nuevas estrategias de diseño experimental.
Desafortunadamente, la baja resolución del campo magnético del sistema (distancia peak-to-peak: 1.4 mT) no pudo mejorarse. Dado que los SQUIDs típicamente presentan un período de modulación de ~ 5 mT, la incertidumbre del campo magnético en modo persistente es demasiado alta para medidas fiables de la corriente crítica (I_c) o de la modulación de voltaje.
Por esta razón, el sistema no fue utilizado para los resultados presentados en esta tesis. No obstante, las mejoras realizadas benefician nuestras instalaciones. La caja de distribución personalizada mejora las características de ruido del sistema, y el SMU adicional permite una mayor variedad de experimentos. La interfaz personalizada facilita la incorporación de nuevos instrumentos y la implementación de nuevas rutinas. Para hacer que el sistema sea adecuado para la caracterización de SQUIDs, la única solución viable que vemos es la adquisición de un controlador de campo magnético de mayor resolución. Cryogenics Ltd. ofrece una versión del sistema con un convertidor digital-analógico (DAC) de 20 bits, con una resolución teórica de 0.02 mT.

7.2. FIBID con Ga^+ para Nanofabricación de SQUIDs

En el capítulo 4 se describió el proceso de fabricación de WC-SoL mediante Ga^+-FIBID. Se abordaron dos desafíos interdependientes: la exploración de una rutina de fabricación de nanoSQUIDs en sustratos grandes bien caracterizados y la transferencia de este proceso a micropalancas de SPM, adaptándose a las distintas condiciones de deposición.

Las rutinas de deposición pueden clasificarse en dos generaciones. Los experimentos iniciales se realizaron con una corriente de haz de iones de 1.5 pA y un tiempo de residencia de 500 µs. Sin embargo, la baja corriente del haz requería un paso adicional de litografía por haz de electrones (Electron Beam Lithography, EBL) para prepatronar el sustrato y mantener el tiempo de deposición en niveles razonables, lo que limitaba el rendimiento. Para aumentarlo, la corriente del haz se incrementó a 9.7 pA, logrando resultados razonablemente comparables en sustratos grandes.

Además, tras encontrar dificultades en la transferencia del proceso de deposición a micropalancas, se realizó un estudio sistemático mediante microscopía electrónica de transmisión (Transmission Electron Microscopy, TEM) sobre la influencia del tiempo de residencia en el régimen de deposición. Para evitar la transición del régimen limitado por electrones a un régimen de difusión, se redujo el tiempo de residencia a 200 ns. A este tiempo de residencia y con una corriente de haz de 9.7 pA, nuevos análisis TEM de depósitos con distintos espesores nominales (es decir, diferentes tiempos de deposición) mostraron una tasa de deposición un 16 % mayor en sustratos que en micropalancas, lo que atribuimos a la disminución de la difusión en estos últimos.

Las micropalancas difieren de los sustratos grandes en su geometría y composición. En las micropalancas, se trabaja cerca del ápice de la punta, limitando la región de difusión a un ángulo de apertura de 90°, mientras que en los sustratos la difusión es libre en todas las direcciones. Además, el cuerpo de Si de la micropalanca está recubierto con 50 nm de SiO_2 crecido térmicamente, mientras que en los sustratos grandes la capa de óxido tiene 300 nm de espesor. La baja conductividad térmica del SiO_2 provoca un mayor aumento de temperatura tras la irradiación con el haz de iones en los sustratos (2.8 K) en comparación con las micropalancas (1 K) en condiciones estándar. Esto podría dificultar aún más la difusión, ya que el coeficiente de difusión aumenta exponencialmente con la temperatura.

En cuanto al diseño de los SQUIDs, se siguieron varias estrategias. Inicialmente, por simplicidad en la fabricación, se produjeron nanoSQUIDs de puente largo. El cuerpo del SQUID consistía nominalmente en rectángulos de 800 nm de ancho conectados mediante nanohilos de 300 nm de largo y 50 nm de ancho, lo que daba como resultado un área de bucle interno nominal de $A_0 = (300 \times 700)\,\mathrm{nm}^2$. En la primera generación, se lograron anchuras de unión de hasta (54, 57) nm, mientras que en la segunda generación las uniones tenían anchuras de (58, 65) nm. Experimentos con estructuras de área de bucle decreciente revelaron que la reducción de tamaño es viable hasta un área nominal de $A_0 = (200 \times 200)\,\mathrm{nm}^2$, ya que por debajo de este valor la deposición de halo ensancha las estructuras.

Para aumentar la coherencia de fase y reducir la inductancia cinética de las uniones, mejorando así el rendimiento general del SQUID, se redujo la longitud de las constricciones, fabricando nanoSQUIDs de constricción corta con un área nominal de bucle interno de $(300 \times 300)\,\mathrm{nm}^2$. Con la primera generación, la longitud se redujo a (33, 36) nm y la anchura a (62, 68) nm. Usando la receta de la segunda generación, tras la optimización, se logró una anchura de (40, 48) nm y una longitud de hasta (21, 22) nm, acercándose a la condición de coherencia de fase $l \leq 3.5\xi = 21\,\mathrm{nm}$.
Los experimentos en micropalancas se realizaron principalmente en la primera tanda de dispositivos, en la que los contactos de oro terminaban a 12.5 µm del ápice de la punta. Utilizando depósitos de Pt como contactos adicionales, la distancia al ápice pudo reducirse a 3.8 µm. Sin embargo, los contactos de Pt tienen un fuerte impacto en las características de ruido. En la segunda tanda de micropalancas, se fabricó un SQUID con una distancia al ápice 4.5 µm.
Los desafíos en la fabricación de SQUIDs y SoL afectaron directamente al rendimiento de los dispositivos obtenidos. Al mismo tiempo, los resultados de caracterización influyeron en las decisiones de diseño en un proceso continuo de refinamiento. A continuación, resumiremos los resultados de la caracterización de los SQUIDs fabricados con los procesos descritos. Se observa que la longitud de las uniones tipo constricción desempeña un papel crucial en el rendimiento del SQUID. Las constricciones más cortas fabricadas en este trabajo tienen una longitud de 20 nm, cercana al límite físico del Ga^+-FIB. El uso de elementos más ligeros en FIB, como He o Ne, podría permitir una reducción adicional de la longitud de las uniones y mejorar el rendimiento del SQUID.
Además, la elección de una corriente de haz de 9.7 pA se debió principalmente al largo tiempo de proceso al depositar con 1.5 pA. En la segunda tanda de micropalancas, los contactos de oro se extienden mucho más cerca del ápice de la punta (4 µm), eliminando la necesidad de depositar contactos largos mediante FIBID. En estas micropalancas, la corriente podría reducirse, lo que resultaría en una mayor resolución y posiblemente reduciría la influencia negativa de la difusión limitada en las micropalancas.

7.3. Caracterización de SQUIDs

Esta tesis ha explorado el desarrollo y la caracterización de SQUIDs fabricados mediante FIBID tanto en sustratos grandes como en micorpalancas de SPM prepatronados. Los desafíos experimentales y el camino hacia el desarrollo de rutinas de fabricación se han resumido anteriormente. En el núcleo del trabajo

se encuentra la caracterización de las propiedades de magnetotransporte de los SQUIDs, presentada en el capítulo 5.

Los SQUIDs de primera generación fueron desarrollados para su fabricación en sustratos grandes, con un tiempo de residencia del haz de 500 µs. Los dos primeros dispositivos funcionales, basados en uniones Josephson de puente largo, exhibieron una modulación de voltaje comparable a los valores reportados en la literatura, con un coeficiente de transferencia de hasta 1300 µV/Φ_0. Sin embargo, los nanopuentes largos (300 nm) introdujeron una inductancia cinética significativa y superaron el criterio para el transporte de fase coherente en un orden de magnitud. Como resultado, la profundidad de modulación de la corriente crítica (I_c) se vio fuertemente suprimida, alcanzando valores de hasta un 2 %, con un alto factor de apantallamiento de 44 y una elevada inductancia de aproximadamente $\sim$ 10 nH.

Reducir la longitud de la unión a un rango de 25 nm to 30 nm mejoró el rendimiento, obteniéndose medidas en entornos de bajo ruido que mostraron un factor de apantallamiento reducido ($\lesssim 5.7$) y una menor inductancia total ($\lesssim 900$ pH). En estos experimentos, el uso de una corriente de modulación en lugar de un imán externo para acoplar flujo en el SQUID solo permitió estimar un límite superior de los parámetros analizados. Los resultados presentados aquí sugieren que el alto nivel de ruido en el PPMS, utilizado en otros experimentos de la tesis, suprime el rendimiento completo de nuestros SQUIDs.

En los SQUIDs de segunda generación, el tiempo de residencia del haz se redujo a 200 ns para adaptarse a las condiciones de crecimiento en las micropalancas. Este ajuste resultó en un mayor contenido de tungsteno y en una mejora de las temperaturas y corrientes críticas. Sin embargo, las medidas de voltaje en el PPMS revelaron saltos discretos entre los estados superconductor y normal, atribuidos al ruido de la corriente y a la inyección de corriente en forma de onda cuadrada, inherente al principio de funcionamiento del PPMS. Este comportamiento oscilatorio impidió la determinación de I_c con la suficiente fiabilidad.

El SQUID de constricción corta de segunda generación presentado aquí exhibe un coeficiente de transferencia de 17 µV/Φ_0, dos órdenes de magnitud por debajo del coeficiente de transferencia de los SQUIDs de puente largo de primera generación, lo que plantea interrogantes sobre el impacto de los parámetros de deposición en el rendimiento. Se requieren experimentos adicionales en condiciones optimizadas de bajo ruido para aclarar estos efectos. El SQUID tipo SNS, fabricado siguiendo la receta de segunda generación en un sustrato grande, no mostró modulación de voltaje. Sin embargo, trabajos posteriores sugieren que reducir la longitud de la unión a 20 nm es factible. Esto incrementaría el acoplamiento de los bancos superconductores mediante el efecto de proximidad,

lo que potencialmente permitiría alcanzar un comportamiento completamente superconductor, aún no observado en el dispositivo SNS.
Además, se lograron fabricar con éxito SQUIDs en micropalancas comerciales, donde los diseños de constricción corta alcanzaron un coeficiente de transferencia entre seis y siete veces mayor que sus contrapartes de puente largo. Estos resultados representan la primera demostración de dispositivos SQUID fabricados mediante un proceso FIBID de un solo paso y de abajo hacia arriba en micropalancas de SPM.
Si bien el rendimiento general de estos SQUIDs sigue siendo inferior al de los dispositivos SoL convencionales, las medidas realizadas en las instalaciones de nuestros colaboradores en Tubinga indican que las limitaciones experimentales en el PPMS, más que las limitaciones intrínsecas del dispositivo, fueron el principal obstáculo. No obstante, el sistema de Tubinga no emplea un imán externo, sino que depende de una línea de modulación, lo que introduce sus propios desafíos. Por lo tanto, sugerimos la caracterización de los dispositivos SQUID más prometedores en entornos libres de ruido utilizando un imán externo para acoplar flujo en el lazo del SQUID. Al momento de redactar esta tesis, tales experimentos están en curso en las instalaciones de nuestros colaboradores en la Universidad de Basilea.
Esta tesis ha demostrado la viabilidad del uso de FIBID para la fabricación de SQUIDs y ha proporcionado información sobre la interacción entre los parámetros de fabricación y el rendimiento del dispositivo. La integración de SQUIDs en micropalancas de SPM representa un paso significativo hacia su aplicación en técnicas de microscopía de sonda de barrido, sentando las bases para futuros avances en este campo.

Acronyms

$W(CO)_6$	Tungsten Hexacarbonyl
W-C	Amorphous to nano-crystalline matrix of Tungsten and Carbon
ABF	Annular Bright Field
ADC	Analog-to-Digital Converter
AFM	Atomic Force Microscopy
API	Application Programming Interface
BCS	Bardeen-Cooper-Schrieffer
BSE	Back Scattered Electron
c-JJ	Constriction-type Josephson Junction
CCS	Cleaning Cross Section
CFMS	Cryogenic-Free Measurement System
CPR	Current Phase Relation
DAC	Digital-to-Analog Converter
DC	Direct Current
EBL	Electron Beam Lithography
EDXS	Energy Dispersive X-Ray Spectroscopy
EMI	ElectroMagnetic Interference
ESA	Excited Surface Atom
ETD	Everhart-Thornley-Detector
EUV	Extreme UltraViolet
FEBID	Focused Electron Beam Deposition
FEM	Finite Element Method
FEV	Field Evaporation
FIB	Focused Ion Beam

FIBID	Focused Ion Beam Deposition
FIBIP	Focused Ion Beam Induced Processing
FWHM	Full Width Half Maximum
GB	Grain Boundary
GFIS	Gas Field Ion Source
GIS	Gas Injection System
GL	Ginzburg-Landau
GUI	Graphical User Interface
HAADF	High-Angle Annular Dark Field
JJ	Josephson Junction
KPFM	Kelvin Probe Force Microscopy
LMAIS	Liquid Metal Alloy Ion Source
LMIS	Liquid Metal Ion Source
LPCVD	Low Pressure Chemical Vapor Deposition
MFM	Magnetic Force Microscopy
NIL	NanoImprint Lithography
NSOM	Near-field Scanning Optical Microscopy
NVM	NanoVoltMeter
OL	Optical Lithography
PE	Primary Electron
PID	Proportional-Integral-Derivative
PLD	Pulsed Laser Deposition
PPMS	Physical Properties Measurement System
PR	Photo Resist
PSF	Point Spread Function
RCS	Regular Cross Section
RCSJ	Resistively Capacitively Shunted Junction
RF	Radio Frequency
SA	Sputtered Atom

SCPI	Standard Commands for Programmable Instruments
SE	Secondary Electron
SEM	Scanning Electron Microscopy
SI	Secondary Ion
SIS	Superconducting-Insulating-Superconducting
SMS120C	Superconducting Magnet power Supply
SMU	Source Measure Unit
SNS	Superconducting-Normal-Superconducting
SoL	SQUID on Lever
SoT	SQUID on Tip
SPL	Scanning Probe Lithography
SPM	Scanning Probe Microscopy
SQUID	Superconducting Quantum Interference Device
SRIM	Stopping and Range of Ions in Matter
SSM	Scanning SQUID Microscopy
STEM	Scanning Transmission Electron Microscopy
STM	Scanning Tunneling Microscope
TEM	Transmission Electron Microscopy
TLD	Through-the-Lens Detector
TMP	Turbo Molecular Pump
UV	UltraViolet
VISA	Virtual Instrument Software Architecture
VTI	Variable Temperature Insert
YBCO	$YBa_2Cu_3O_7{-}x$

Symbols

A	Area
A_0	Nominal Inner Loop Area
A_{eff}	Effecitve Area
A_{geom}	Geometric Area
$\boldsymbol{A}$	Magnetic Vector Potential
N_{A}	Avogadro's Constant
B	Magnetic Field Density
B_{c}	Critical Magnetic Field of a Superconducting Structure
β_{c}	Stewart-McCumber Parameter
β_{L}	Screening Parameter
C	Capacitance
c	Speed of Light
D	Diffusion Coefficient
d	Distance between two Objects
d_0	Nominal Distance between two Deposit
δB	Period of a modulation upon variation of the magnetic field.
δ	Phase Difference
δ_r	Spatial Resolution
δI	Current step size
d_z	Vertical distance
E	Energy
e	Euler's constant
E_0	Primary Electron or Ion Energy
e_0	Elementary Charge
E_{des}	Desorption Energy

E_{diff}	Diffusion Energy
E_{kin}	Kinetic Energy
η	Factor of Energy Dissipated to the Vacuum via Particles and Radiation
F	Force
f	Distribution Function
Γ	Noise Parameter
γ_{D}	Deposition Yield
γ_{ESA}	Excited Surface Atom Yield
γ_{S}	Sputter Yield
γ_{SE}	Secondary Electron Yield
H	Magnetic Field Strength
h	Planck Constant
$\hbar$	Reduced Planck Constant
H_{S}	Heat Source
I	Current
I_0	Maximal critical current of a single JJ
I_{B}	Electron or Ion Beam Current
I_{b}	Bias Current
I_{c}	Critical Current of a Superconducting Structure
I_{c}^{+}	Critical Current of a Superconducting Structure for positive currents
I_{c}^{-}	Critical Current of a Superconducting Structure for negative currents
I_{el}	Electron Beam Current
I_{Ion}	Ion Beam Current
I_{J}	Josephson Current
I_{loop}	Circular Loop Current
I_{m}	Modulation Current
I_{N}	Current Noise
I_{r}	Return Critical Current
I_{th}	Thermal Noise Current
J	Precursor Flux
J_{c}	Critical Current Density
$\boldsymbol{J}_{\mathrm{s}}$	Density of a Supercurrent

κ	Thermal Diffusivty
k_{B}	Boltzman's Constant
L	Inductance
l	Length
l_0	Nominal Length of the Deposit
λ	Wavelength
λ_{L}	London Penetration Depth
L_{F}	Fluctuation Threshold Inductance
$\boldsymbol{m}$	Magnetic Dipole Moment
m	Mass of an Object
m^*	Effective Mass of a Particle
M_{mol}	Molar Mass
μ	Coefficient of Friction
μ_0	Magnetic Vacuum Permeability
NA	Numerical Aperture
n_{p}	Number of Adsorbed Precursor Molecules per Surface Unit
n_{p_0}	Number of Available Adsorbation Sites per Surface Unit
n_{s}	Density of Superconducting Electrons
ω_{c}	Characteristic Frequency
ω_{J}	Josephson Frequency
Φ	Magnetic Flux
φ	Phase of a Wave Function
Φ_0	Magnetic Flux Quantum
ψ_{s}	Superconducting Wave Function
q	Charge of a Particle
R	Resistance
r	Radial Distance
R_{D}	Vertical Deposition Rate
ρ_{diff}	Diffusion Length
ρ_{mol}	Molar Density

$\widetilde{\rho}$	Diffusion Length Ratio
R_{I}	Radius of the Interaction Volume
R_{N}	Normal State Resistance
R_{S}	Vertical Sputter Rate
R_{th}	Threshold Resistance
$\boldsymbol{r}$	Spatial Vector
s	Sticking Probability
σ	Interaction Cross Section
σ_{N}	Standard Deviation of the Normal Distribution
S_{Φ}	Spectral Density of Flux Noise
S_{V}	Spectral Density of Voltage Noise
T	Temperature
t	Thickness of a Deposit
t_0	Nominal Thickness of the Deposit
τ_{d}	Dwell Time
τ_{eff}	Effective Residence Time
τ_{r}	Residence Time
$\widetilde{\tau}$	Residence Time Ratio
T_{c}	Critical Temperature of a Superconducting Structure
t	Time
U	Potential
V_{a}	Electron or Ion Acceleration Voltage
V_{el}	Electron Acceleration Voltage
V_{Ion}	Ion Acceleration Voltage
U_{J}	Tilted Washboard Potential
V	Voltage
V_{c}	Characteristic Voltage
V_{N}	Normal State Voltage
V_{p}	Volume of a Decomposed Precursor Molecule
V_{Φ}	Transfer Coefficient
V_{th}	Threshold Voltage
w	Width
w_0	Nominal Width of the Deposit

x	x-Coordinate
ξ	Superconducting Coherence Length
ξ_{N}	Coherence Length of a Normal Conductor
y	y-Coordinate
z	z-Coordinate

Publications

Throughout the development of the project the following publications were published:

1. Sigloch, F., Sangiao, S., Orús, P. & Teresa, J. M. de. Direct-Write of Tungsten-Carbide nanoSQUIDs Based on Focused Ion Beam Induced Deposition. *Nanoscale Advances* **4,** 4628–4634 (2022).
2. Orús, P., Sigloch, F., Sangiao, S. & De Teresa, J. M. Superconducting Materials and Devices Grown by Focused Ion and Electron Beam Induced Deposition. *Nanomaterials* **12,** 1367 (2022).

Furthermore, the collaborative efforts of our group resulted in active contribution to the following publications:

1. Orús, P., Sigloch, F., Sangiao, S. & De Teresa, J. M. Cryo-Focused Ion Beam-Induced Deposition of Tungsten–Carbon Nanostructures Using a Thermoelectric Plate. *Applied Sciences* **11,** 10123 (2021).
2. Orús, P., Sigloch, F., Sangiao, S. & De Teresa, J. M. Superconducting W-C Nanopillars Fabricated by Ga+ Focused Ion Beam Induced Deposition. *Journal of Solid State Chemistry* **315,** 123476 (2022).
3. Orús, P., Sigloch, F., Sangiao, S. & De Teresa, J. M. Low-Resistivity, High-Resolution W-C Electrical Contacts Fabricated by Direct-Write Focused Electron Beam Induced Deposition. *Open Research Europe* **2,** 102 (2022).

Bibliography

1. Hartridge, H. Visual Acuity and the Resolving Power of the Eye. *The Journal of Physiology* **57,** 52–67 (1922).
2. *The Origins of the Telescope* (ed Van Helden, A.) *History of Science and Scholarship in the Netherlands* **v. 12.** 368 pp. (KNAW Press, Amsterdam, 2010).
3. Helden, A. V. The Invention of the Telescope. *Transactions of the American Philosophical Society* **67,** 1 (1977).
4. Feynman, R. P. There's Plenty of Room at the Bottom: An Invitation to Enter a New Field of Physics. *Resonance* **16,** 890–905 (2011).
5. Binnig, G. & Rohrer, H. Scanning Tunneling Microscopy. *IBM Journal of Research and Development* **44,** 279–293 (2000).
6. Wong, J. K. *et al.* Will Nanotechnology Bring New Hope for Gene Delivery? *Trends in Biotechnology* **35,** 434–451 (2017).
7. Airy, G. B. On the Diffraction of an Object-glass with Circular Aperture. *Transactions of the Cambridge Philosophical Society* **5,** 283 (1835).
8. Rayleigh. XXXI. *Investigations in Optics, with Special Reference to the Spectroscope. The London, Edinburgh, and Dublin Philosophical Magazine and Journal of Science* **8,** 261–274 (1879).
9. Heintzmann, R. & Ficz, G. Breaking the Resolution Limit in Light Microscopy. *Briefings in Functional Genomics and Proteomics* **5,** 289–301 (2006).
10. Malsch, F. Erzeugung stark vergrößerter Röntgen-Schattenbilder. *Die Naturwissenschaften* **27,** 854–855 (1939).
11. Horowitz, P. & Howell, J. A. A Scanning X-Ray Microscope Using Synchrotron Radiation. *Science* **178,** 608–611 (1972).
12. Jacobsen, C. *X-Ray Microscopy* (Cambridge University Press, Cambridge, UK, 2020).
13. Knoll, M. & Ruska, E. Das Elektronenmikroskop. *Zeitschrift für Physik* **78,** 318–339 (1932).

14. Von Ardenne, M. & Beischer, D. Untersuchung von Metalloxyd-Rauchen Mit Dem Universal-Elektronenmikroskop. *Zeitschrift für Elektrochemie und angewandte physikalische Chemie* **46,** 270–277 (1940).

15. Reimer, L. & Kohl, H. *Transmission Electron Microscopy: Physics of Image Formation* 5. ed. *Springer Series in Optical Sciences* **36.** 587 pp. (Springer, New York, NY, 2008).

16. Binnig, G., Rohrer, H., Gerber, Ch. & Weibel, E. Tunneling through a Controllable Vacuum Gap. *Applied Physics Letters* **40,** 178–180 (1982).

17. Salapaka, S. M. & Salapaka, M. V. Scanning Probe Microscopy. *IEEE Control Systems* **28,** 65–83 (2008).

18. Klemperer, O. E. & Barnett, M. E. *Electron Optics* Third ed., first paperback ed. 506 pp. (Cambridge Univ. Press, Cambridge, 2010).

19. Egerton, R. *Physical Principles of Electron Microscopy* (Springer International Publishing, Cham, 2016).

20. *Handbook of Charged Particle Optics* 2nd ed (ed Orloff, J.) (CRC Press / Taylor & Francis, Boca Raton, 2009).

21. Hlawacek, G., Veligura, V., Van Gastel, R. & Poelsema, B. Helium Ion Microscopy. *Journal of Vacuum Science & Technology B, Nanotechnology and Microelectronics: Materials, Processing, Measurement, and Phenomena* **32,** 020801 (2014).

22. Utke, I., Hoffmann, P. & Melngailis, J. Gas-Assisted Focused Electron Beam and Ion Beam Processing and Fabrication. *Journal of Vacuum Science & Technology B: Microelectronics and Nanometer Structures Processing, Measurement, and Phenomena* **26,** 1197–1276 (2008).

23. Shukuri, S., Wade, Y., Tamura, M., Umemura, K. & Ishitani, T. Precise Measurement of a Focused Ion Beam Profile. *Journal of The Electrochemical Society* **134,** 1536–1540 (1987).

24. Callegari, V. & Nellen, P. M. Spontaneous Growth of Uniformly Distributed In Nanodots and InI_3 Nanowires on InP Induced by a Focused Ion Beam. *physica status solidi (a)* **204,** 1665–1671 (2007).

25. Röhr, J. A. Electron Transport in Solution Processed Antimony Sulphide Thin Films Made from a Xanthate Precursor (2014).

26. Reimer, L. *Scanning Electron Microscopy: Physics of Image Formation and Microanalysis* 2nd completely rev. and updated ed. *Springer Series in Optical Sciences* **45** (Springer, Berlin Heidelberg New York, 1998).

27. Li, L., Mao, L. & Yang, J. A Review of Principles, Analytical Methods, and Applications of SEM-EDS in Cementitious Materials Characterization. *Advanced Materials Technologies,* 2401175 (2024).

28. *Nanofabrication: Nanolithography Techniques and Their Applications* (ed Teresa, J. M. de) 1 p. (IOP Publishing, Bristol, 2020).

29. Giannuzzi, L. A. & Stevie, F. A. *Introduction to Focused Ion Beams: Instrumentation, Theory, Techniques, and Practice* (Springer, New York, 2005).

30. Everhart, T. E. & Thornley, R. F. M. Wide-Band Detector for Micro-Microampere Low-Energy Electron Currents. *Journal of Scientific Instruments* **37,** 246–248 (1960).

31. Binnig, G., Quate, C. F. & Gerber, Ch. Atomic Force Microscope. *Physical Review Letters* **56,** 930–933 (1986).

32. Binnig, G., Gerber, C., Stoll, E., Albrecht, T. R. & Quate, C. F. Atomic Resolution with Atomic Force Microscope. *Europhysics Letters (EPL)* **3,** 1281–1286 (1987).

33. Martin, Y. & Wickramasinghe, H. K. Magnetic Imaging by ‘‘Force Microscopy’’ with 1000 Å Resolution. *Applied Physics Letters* **50,** 1455–1457 (1987).

34. Hartmann, U. MAGNETIC FORCE MICROSCOPY. *Annual Review of Materials Science* **29,** 53–87 (1999).

35. Kazakova, O. *et al.* Frontiers of Magnetic Force Microscopy. *Journal of Applied Physics* **125,** 060901 (2019).

36. Belova, L. M., Hellwig, O., Dobisz, E. & Dan Dahlberg, E. Rapid Preparation of Electron Beam Induced Deposition Co Magnetic Force Microscopy Tips with 10 Nm Spatial Resolution. *Review of Scientific Instruments* **83,** 093711 (2012).

37. Koblischka, M., Hartmann, U. & Sulzbach, T. Improving the Lateral Resolution of the MFM Technique to the Range. *Journal of Magnetism and Magnetic Materials* **272–276,** 2138–2140 (2004).

38. Pablo-Navarro, J., Sangiao, S., Magén, C. & De Teresa, J. M. Magnetic Functionalization of Scanning Probes by Focused Electron Beam Induced Deposition Technology. *Magnetochemistry* **7,** 140 (2021).

39. Christensen, D. V. *et al.* 2024 Roadmap on Magnetic Microscopy Techniques and Their Applications in Materials Science. *Journal of Physics: Materials* **7,** 032501 (2024).

40. Lam, S. K. H. & Tilbrook, D. L. Development of a Niobium Nanosuperconducting Quantum Interference Device for the Detection of Small Spin Populations. *Applied Physics Letters* **82,** 1078–1080 (2003).

41. Zhou, H. *et al.* Scanning SQUID-on-tip Microscope in a Top-Loading Cryogen-Free Dilution Refrigerator. *Review of Scientific Instruments* **94,** 053706 (2023).

42. Finkler, A. *et al.* Self-Aligned Nanoscale SQUID on a Tip. *Nano Letters* **10,** 1046–1049 (2010).

43. Anahory, Y. *et al.* SQUID-on-tip with Single-Electron Spin Sensitivity for High-Field and Ultra-Low Temperature Nanomagnetic Imaging. *Nanoscale* **12,** 3174–3182 (2020).

44. Finkler, A. *et al.* Scanning Superconducting Quantum Interference Device on a Tip for Magnetic Imaging of Nanoscale Phenomena. *Review of Scientific Instruments* **83,** 073702 (2012).

45. Nonnenmacher, M., O'Boyle, M. P. & Wickramasinghe, H. K. Kelvin Probe Force Microscopy. *Applied Physics Letters* **58,** 2921–2923 (1991).

46. Ma, X. *et al.* 6 Nm Super-Resolution Optical Transmission and Scattering Spectroscopic Imaging of Carbon Nanotubes Using a Nanometer-Scale White Light Source. *Nature Communications* **12,** 6868 (2021).

47. Caplan, J., Niethammer, M., Taylor, R. M. & Czymmek, K. J. The Power of Correlative Microscopy: Multi-Modal, Multi-Scale, Multi-Dimensional. *Current Opinion in Structural Biology* **21,** 686–693 (2011).

48. Novotna, V. *et al.* AFM-in-SEM as a Tool for Comprehensive Sample Surface Analysis. *Microscopy Today* **28,** 38–46 (2020).

49. Eigler, D. M. & Schweizer, E. K. Positioning Single Atoms with a Scanning Tunnelling Microscope. *Nature* **344,** 524–526 (1990).

50. Crommie, M. F., Lutz, C. P. & Eigler, D. M. Confinement of Electrons to Quantum Corrals on a Metal Surface. *Science* **262,** 218–220 (1993).

51. (director IBM) *A Boy And His Atom: The World's Smallest Movie* 2013.

52. Hutcheson, G. D. *Moore's Law, Lithography, and How Optics Drive the Semiconductor Industry* in *Extreme Ultraviolet (EUV) Lithography IX* Extreme Ultraviolet (EUV) Lithography IX (eds Felix, N. M. & Goldberg, K. A.) (SPIE, San Jose, United States, 2018), 501.

53. ASML. *EUV Lithography Systems* 2024.

54. Hu, W. (, Sarveswaran, K., Lieberman, M. & Bernstein, G. H. Sub-10 Nm Electron Beam Lithography Using Cold Development of Poly(Methylmeth-Acrylate). *Journal of Vacuum Science & Technology B: Microelectronics and Nanometer Structures Processing, Measurement, and Phenomena* **22,** 1711–1716 (2004).

55. Ichimura, T., Ren, Y. & Kruit, P. A Large Current Scanning Electron Microscope with MEMS-based Multi-Beam Optics. *Microelectronic Engineering* **113,** 109–113 (2014).

56. Chou, S. Y., Krauss, P. R., Zhang, W., Guo, L. & Zhuang, L. Sub-10 Nm Imprint Lithography and Applications. *Journal of Vacuum Science & Technology B: Microelectronics and Nanometer Structures Processing, Measurement, and Phenomena* **15,** 2897–2904 (1997).

57. Chou, S. Y., Krauss, P. R. & Renstrom, P. J. Imprint of Sub-25 Nm Vias and Trenches in Polymers. *Applied Physics Letters* **67,** 3114–3116 (1995).

58. Preiß, E. I. *et al.* Applicability of Focused Ion Beam (FIB) Milling with Gallium, Neon, and Xenon to the Fracture Toughness Characterization of Gold Thin Films. *Journal of Materials Research* **36,** 2505–2514 (2021).

59. Bischoff, L., Mazarov, P., Bruchhaus, L. & Gierak, J. Liquid Metal Alloy Ion Sources—An Alternative for Focussed Ion Beam Technology. *Applied Physics Reviews* **3,** 021101 (2016).

60. Ziegler, J. F., Ziegler, M. & Biersack, J. SRIM – The Stopping and Range of Ions in Matter (2010). *Nuclear Instruments and Methods in Physics Research Section B: Beam Interactions with Materials and Atoms* **268,** 1818–1823 (2010).

61. Lipp, S. *et al.* A Comparison of Focused Ion Beam and Electron Beam Induced Deposition Processes. *Microelectronics Reliability* **36,** 1779–1782 (1996).

62. Fowlkes, J. D., Randolph, S. J. & Rack, P. D. Growth and Simulation of High-Aspect Ratio Nanopillars by Primary and Secondary Electron-Induced Deposition. *Journal of Vacuum Science & Technology B: Microelectronics and Nanometer Structures Processing, Measurement, and Phenomena* **23,** 2825–2832 (2005).

63. Ishitani, I. & Kaga, H. Calculation of Local Temperature Rise in Focused-Ion-Beam Sample Preparation. *Journal of Electron Microscopy,* 331–336 (1995).

64. Sushko, G. B., Solov'yov, I. A. & Solov'yov, A. V. Molecular Dynamics for Irradiation Driven Chemistry: Application to the FEBID Process*. *The European Physical Journal D* **70,** 217 (2016).
65. De Vera, P., Verkhovtsev, A., Sushko, G. & Solov'yov, A. V. Reactive Molecular Dynamics Simulations of Organometallic Compound W(CO)6 Fragmentation, *The European Physical Journal D* **73,** 215 (2019).
66. De Vera, P. *et al.* Multiscale Simulation of the Focused Electron Beam Induced Deposition Process. *Scientific Reports* **10,** 20827 (2020).
67. Prosvetov, A., Verkhovtsev, A. V., Sushko, G. & Solov'yov, A. V. Atomistic Modeling of Thermal Effects in Focused Electron Beam-Induced Deposition of Me$$_2$$Au(Tfac). *The European Physical Journal D* **77,** 15 (2023).
68. Garcia, R., Knoll, A. W. & Riedo, E. Advanced Scanning Probe Lithography. *Nature Nanotechnology* **9,** 577–587 (2014).
69. Gracia Abad, R. *Lithography and Electric Transport in Bi2Se3-based Devices for Quantum Technologies* PhD thesis (CSIC-Universidad de Zaragoza, Zaragoza, 2023).
70. Van Delft, D. & Kes, P. The Discovery of Superconductivity. *Physics Today* **63,** 38–43 (2010).
71. Van Delft, D. Little Cup of Helium, Big Science. *Physics Today* **61,** 36–42 (2008).
72. Tinkham, M. *Introduction to Superconductivity* 2. ed. 454 pp. (McGraw-Hill, New York, 1996).
73. *Superconductivity* 2. ed (ed Poole, C. P.) 646 pp. (Academic, Oxford, 2007).
74. De Gennes, P. G. *Superconductivity of Metals and Alloys* 1st ed. (CRC Press, 2018).
75. Likharev, K. K. Superconducting Weak Links. *Reviews of Modern Physics* **51,** 101–159 (1979).
76. Meissner, W. & Ochsenfeld, R. Ein neuer Effekt bei Eintritt der Supraleitfähigkeit. *Die Naturwissenschaften* **21,** 787–788 (1933).
77. London, F. & London, H. The Electromagnetic Equations of the Supraconductor. *Proceedings of the Royal Society of London. Series A - Mathematical and Physical Sciences* **149,** 71–88 (1935).

78. Orús Calvet, P. *Nanofabrication of Metallic and Superconducting Tungsten-Carbon Nanostructures Using Focused Ion Beams* (Universidad de Zaragoza, Zaragoza, 2020).

79. Bardeen, J., Cooper, L. N. & Schrieffer, J. R. Theory of Superconductivity. *Physical Review* **108,** 1175–1204 (1957).

80. Fetter, A. L. & Hohenberg, P. C. in Parks, R. *Superconductivity* (ed Parks, R. D.) 1st ed., 817–923 (Routledge, 2018).

81. Gor'Kov, L. P. Microscopic Derivation of the Ginzburg-Landau Equations in the Theory of Superconductivity. *Sov. Phys. JETP* **9,** 1364–1367 (1959).

82. Josephson, B. Possible New Effects in Superconductive Tunnelling. *Physics Letters* **1,** 251–253 (1962).

83. Clarke, J. & Braginski, A. I. *The SQUID Handbook* (Wiley-VCH, Weinheim, 2004).

84. Courtois, H., Meschke, M., Peltonen, J. T. & Pekola, J. P. Origin of Hysteresis in a Proximity Josephson Junction. *Physical Review Letters* **101,** 067002 (2008).

85. José Martínez-Pérez, M. & Koelle, D. NanoSQUIDs: Basics & Recent Advances. *Physical Sciences Reviews* **2** (2017).

86. Clarke, J. in *SQUID Sensors: Fundamentals, Fabrication and Applications* (ed Weinstock, H.) 1–62 (Springer Netherlands, Dordrecht, 1996).

87. Ketchen, M. B., Kopley, T. & Ling, H. Miniature SQUID Susceptometer. *Applied Physics Letters* **44,** 1008–1010 (1984).

88. Gardner, B. W. *et al.* Scanning Superconducting Quantum Interference Device Susceptometry. *Review of Scientific Instruments* **72,** 2361–2364 (2001).

89. HYPRES, Inc. *HYPRES - The Digital Superconductor Company* 2024.

90. Drung, D. *et al.* Thin-Film Microsusceptometer With Integrated Nanoloop. *IEEE Transactions on Applied Superconductivity* **24,** 1–6 (2014).

91. Schmelz, M. *et al.* Investigation of All Niobium Nano-SQUIDs Based on Sub-Micrometer Cross-Type Josephson Junctions. *Superconductor Science and Technology* **28,** 015004 (2015).

92. Anders, S. *et al.* Sub-Micrometer-Sized, Cross-Type Nb–AlOx–Nb Tunnel Junctions with Low Parasitic Capacitance. *Superconductor Science and Technology* **22,** 064012 (2009).

93. Wölbing, R. *et al.* Nb Nano Superconducting Quantum Interference Devices with High Spin Sensitivity for Operation in Magnetic Fields up to 0.5 T. *Applied Physics Letters* **102,** 192601 (2013).

94. Martínez-Pérez, M. J. *et al.* Three-Axis Vector Nano Superconducting Quantum Interference Device. *ACS Nano* **10,** 8308–8315 (2016).

95. Hasselbach, K., Veauvy, C. & Mailly, D. MicroSQUID Magnetometry and Magnetic Imaging. *Physica C: Superconductivity* **332,** 140–147 (2000).

96. Troeman, A. G. P. *et al.* NanoSQUIDs Based on Niobium Constrictions. *Nano Letters* **7,** 2152–2156 (2007).

97. Hao, L. *et al.* Measurement and Noise Performance of Nano-Superconduct-Ing-Quantum-Interference Devices Fabricated by Focused Ion Beam. *Applied Physics Letters* **92,** 192507 (2008).

98. Sigloch, F., Sangiao, S., Orús, P. & Teresa, J. M. de. Direct-Write of Tungsten-Carbide nanoSQUIDs Based on Focused Ion Beam Induced Deposition. *Nanoscale Advances* **4,** 4628–4634 (2022).

99. Wyss, M. *et al.* Magnetic, Thermal, and Topographic Imaging with a Nanometer-Scale SQUID-On-Lever Scanning Probe. *Physical Review Applied* **17,** 034002 (2022).

100. Ruffieux, S. *et al.* The Role of Kinetic Inductance on the Performance of YBCO SQUID Magnetometers. *Superconductor Science and Technology* **33,** 025007 (2020).

101. FIBSuperProbes Project. *FIBSuperProbes: Advancing Scanning Probe Microscopy with Superconducting Sensors* 2024.

102. Vasyukov, D. *et al.* A Scanning Superconducting Quantum Interference Device with Single Electron Spin Sensitivity. *Nature Nanotechnology* **8,** 639–644 (2013).

103. Müller, B. *et al.* Josephson Junctions and SQUIDs Created by Focused Helium-Ion-Beam Irradiation of Y Ba 2 Cu 3 O 7. *Physical Review Applied* **11,** 044082 (2019).

104. Córdoba, R., Ibarra, A., Mailly, D. & De Teresa, J. M. Vertical Growth of Superconducting Crystalline Hollow Nanowires by He+ Focused Ion Beam Induced Deposition. *Nano Letters* **18,** 1379–1386 (2018).

105. Blom, T. J. *et al.* Direct-Write Printing of Josephson Junctions in a Scanning Electron Microscope. *ACS Nano* **15,** 322–329 (2021).

106. KLayout. *KLayout - Layout Viewer and Editor* version 0.26.11. 2021.

107. DeltaMask. *Photomask Manufacturing* 2023.

108. Orús, P., Fomin, V. M., De Teresa, J. M. & Córdoba, R. Critical Current Modulation Induced by an Electric Field in Superconducting Tungsten-Carbon Nanowires. *Scientific Reports* **11,** 17698 (2021).

109. IBM Zürich. *IBM Research Zürich* 2023.

110. Vettiger, P. *et al.* The "Millipede" - Nanotechnology Entering Data Storage. *IEEE Transactions on Nanotechnology* **1,** 39–55 (2002).

111. Alcock, C. B., Itkin, V. P. & and, M. K. H. Vapour Pressure Equations for the Metallic Elements: 298–2500K. *Canadian Metallurgical Quarterly* **23,** 309–313 (1984).

112. Sadki, E. S., Ooi, S. & Hirata, K. Focused-Ion-Beam-Induced Deposition of Superconducting Nanowires. *Applied Physics Letters* **85,** 6206–6208 (2004).

113. Gibson, J. W. & Hein, R. A. Superconductivity of Tungsten. *Physical Review Letters* **12,** 688–690 (1964).

114. Kondo, S. Superconducting Characteristics and the Thermal Stability of Tungsten-Based Amorphous Thin Films. *Journal of Materials Research* **7,** 853–860 (1992).

115. Sadki, E., Ooi, S. & Hirata, K. Focused Ion Beam Induced Deposition of Superconducting Thin Films. *Physica C: Superconductivity and its Applications* **426–431,** 1547–1551 (2005).

116. Luxmoore, I. *et al.* Low Temperature Electrical Characterisation of Tungsten Nano-Wires Fabricated by Electron and Ion Beam Induced Chemical Vapour Deposition. *Thin Solid Films* **515,** 6791–6797 (2007).

117. Spoddig, D. *et al.* Transport Properties and Growth Parameters of PdC and WC Nanowires Prepared in a Dual-Beam Microscope. *Nanotechnology* **18,** 495202 (2007).

118. Li, W., Fenton, J. C. & Warburton, P. A. Focused-Ion-Beam Direct-Writing of Ultra-Thin Superconducting Tungsten Composite Films. *IEEE Transactions on Applied Superconductivity* **19,** 2819–2822 (2009).

119. Córdoba, R. *et al.* Magnetic Field-Induced Dissipation-Free State in Superconducting Nanostructures. *Nature Communications* **4,** 1437 (2013).

120. Li, W., Fenton, J. C., Wang, Y., McComb, D. W. & Warburton, P. A. Tunability of the Superconductivity of Tungsten Films Grown by Focused-Ion-Beam Direct Writing. *Journal of Applied Physics* **104,** 093913 (2008).

121. Córdoba, R. in *Functional Nanostructures Fabricated by Focused Electron/Ion Beam Induced Deposition* (ed Córdoba Castillo, R.) 95–132 (Springer International Publishing, Cham, 2014).

122. Dai, J. *et al.* Superconductivity in Tungsten-Carbide Nanowires Deposited from the Mixtures of W(CO)6 and C14H10. *Japanese Journal of Applied Physics* **52,** 075001 (7R 2013).

123. Sun, Y. *et al.* Voltage-Current Properties of Superconducting Amorphous Tungsten Nanostrips. *Scientific Reports* **3,** 2307 (2013).

124. Guillamón, I. *et al.* Direct Observation of Melting in a Two-Dimensional Superconducting Vortex Lattice. *Nature Physics* **5,** 651–655 (2009).

125. Huth, M., Klingenberger, D., Grimm, C., Porrati, F. & Sachser, R. Conductance Regimes of W-based Granular Metals Prepared by Electron Beam Induced Deposition. *New Journal of Physics* **11,** 033032 (2009).

126. Sengupta, S. *et al.* Superconducting Nanowires by Electron-Beam-Induced Deposition. *Applied Physics Letters* **106,** 042601 (2015).

127. Zhakina, E. *et al. Vortex Motion in Reconfigurable Three-Dimensional Superconducting Nanoarchitectures* version 1. `https://arxiv.org/abs/2404.12151` (2025). Pre-published.

128. Berger, L. I. & Roberts, B. W. Properties of Superconductors. *CRC Handbook of Chemistry and Physics,* 12–60 (1997).

129. Cryogenic Ltd. *Cryogen Free Magnet System User Manual* 2016.

130. Ott, H. W. *Noise Reduction Techniques in Electronic Systems* 2nd ed. 426 pp. (Wiley, New York, 1988).

131. IVI Foundation. *VISA* 2024.

132. PyVISA Development Team. *PyVISA* 2024.

133. The Qt Company. *Qt6* 2025.

134. Riverbank Computing Limited. *PyQt6* 2024.

135. Gruber, John. *Markdown* 2004.

136. Read the Docs, Inc. *Read the Docs* 2022.

137. Fang, C. & Xing, Y. Investigation of the Shadow Effect in Focused Ion Beam Induced Deposition. *Nanomaterials* **12,** 905 (2022).

138. Lide, D. R. *CRC Handbook of Chemistry and Physics: 2008-2009 a Ready-Reference Book of Chemical and Physical Data* 89th ed (CRC press, Boca Raton, 2008).

139. Wang, C., Zou, L. & Feng, Y. *Analysis of the Effect of Contact Resistance on the Output Accuracy of Standard Signal Generating Circuits* in *2024 3rd International Symposium on Semiconductor and Electronic Technology (ISSET)* 2024 3rd International Symposium on Semiconductor and Electronic Technology (ISSET) (IEEE, Xi'an, China, 2024), 352–356.

140. Winhold, M., Weirich, P. M., Schwalb, C. H. & Huth, M. Identifying the Crossover between Growth Regimes via In-Situ Conductance Measurements in Focused Electron Beam Induced Deposition. *Nanofabrication* **1** (2014).

141. Rueden, C. T. *et al.* ImageJ2: ImageJ for the next Generation of Scientific Image Data. *BMC Bioinformatics* **18,** 529 (2017).

142. Trabaldo, E. *et al.* Transport and Noise Properties of YBCO Nanowire Based nanoSQUIDs. *Superconductor Science and Technology* **32,** 073001 (2019).

143. Paolucci, F., De Simoni, G., Strambini, E., Solinas, P. & Giazotto, F. Ultra-Efficient Superconducting Dayem Bridge Field-Effect Transistor. *Nano Letters* **18,** 4195–4199 (2018).

144. Orús, P., Córdoba, R. & De Teresa, J. M. in *Nanofabrication* (ed De Teresa, J. M.) 5-1-5–58 (IOP Publishing, 2020).

145. Rodrigo, R., Faley, M. & Dunin-Borkowski, R. NanoSQUIDs Based on Nb Nanobridges. *Journal of Physics: Conference Series* **1559,** 012011 (2020).

146. Arpaia, R. *et al.* Improved Noise Performance of Ultrathin YBCO Dayem Bridge nanoSQUIDs. *Superconductor Science and Technology* **30,** 014008 (2017).

147. Langfischer, H., Basnar, B., Hutter, H. & Bertagnolli, E. Evolution of Tungsten Film Deposition Induced by Focused Ion Beam. *Journal of Vacuum Science & Technology A: Vacuum, Surfaces, and Films* **20,** 1408–1415 (2002).

148. Fu, Y., Bryan, N. K. A. & Shing, O. N. Characterization of Focused Ion Beam Induced Deposition Process and Parameters Calibration. *Sensors and Actuators A: Physical* **88,** 58–66 (2001).

149. Córdoba, R. *et al.* Long-Range Vortex Transfer in Superconducting Nano-Wires. *Scientific Reports* **9,** 12386 (2019).

Appendices

Appendix A

Ga^+ FIBID for SQUID Fabrication

A.1. Thermal Diffusion

Finite Element Method (FEM) was employed to estimate the heating of the surface under irradiation with an ion beam of 10 pA at an acceleration voltage of 30 kV.
The system is parametrized in cylindrical coordinates and the rotation symmetry is exploited to reduce the three dimensional problem to two dimensions. The continuous diffusion equation (eq. (1.16)) is discretely solved by

$$\begin{aligned} T^{n+1}(r,z) = T^n(r,z) + \Delta t \cdot \alpha \Big[& \frac{T(r+\Delta r,z) - 2T(r,z) + T(r-\Delta r,z)}{\Delta r^2} \\ & + \frac{1}{r}\frac{T(r+\Delta r,z) - T(r-\Delta r,z)}{2\Delta r} \\ & + \frac{T(r,z+\Delta z) - 2T(r,z) + T(r,z-\Delta z)}{\Delta z^2} \\ & \Big] + Q^n(r,z) \cdot \Delta t \ . \end{aligned} \tag{A.1}$$

Spatial discretization is achieved by subdividing a cylindrical volume with radius $R = 2048\,\text{nm}$ and a depth of $Z = 1024\,\text{nm}$ into a grid of voxels with $\Delta r = 2\,\text{nm}$ and $\Delta z = 2\,\text{nm}$.

The power $V_\mathrm{a} \cdot I_\mathrm{B}$ of the heat source of the beam is modelled to be dissipated in a gaussian distribution:

$$P\left(\boldsymbol{r},\boldsymbol{z}\right) = \frac{V_\mathrm{a} \cdot I_\mathrm{B}}{\left(2\cdot\pi\right)^{3/2}\sigma_r^2\sigma_z}\exp\left(-\frac{\left(\boldsymbol{r}-\boldsymbol{r}_0\right)^2}{2\sigma_r^2}-\frac{\left(\boldsymbol{z}-\boldsymbol{z}_0\right)^2}{2\sigma_z^2}\right) \tag{A.2}$$

where $(\boldsymbol{r}_0,\ \boldsymbol{z}_0 = (0\,\mathrm{nm},\ 25\,\mathrm{nm}))$ denote the center of the beam and $\sigma_r = 12\,\mathrm{nm}$ and $\sigma_z = 15\,\mathrm{nm}$ are the standard deviation of the gaussian distribution, obtained from SRIM simulations. The material specific heat source term in the heat diffusion equation is

$$Q\left(\boldsymbol{r},\boldsymbol{z}\right) = \frac{P\left(\boldsymbol{r},\boldsymbol{z}\right)}{\rho c_p}\ , \tag{A.3}$$

where ρ is the density of the material and c_p the specific heat capacity of the voxel's material.
The surface of the substrate is treated by a Neuman boundary condition with constant heat flow $\Delta T/\Delta z = 0$. The bottom and outer borders of the system are treated as a Dirichlet boundary condition, forming an infinite heat sink with constant temperature $T = 300\,\mathrm{K}$. In the interface between SiO_2 and Si a Neuman boundary condition of constant heat flux under consideration of the thermal contact resistance is applied.

A.2. Dwell Time

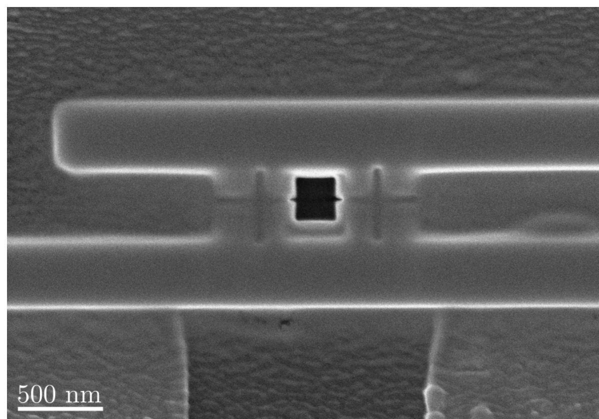

Figure A.1.: Failed deposition process of an SoL. The SQUID was deposited at a dwell time of 500 µs and a current of 9.7 µA. The resupply with precursor molecules was too low at the deposition step of the nanobridges, resulting in effective milling.

A.3. Deposition Rate

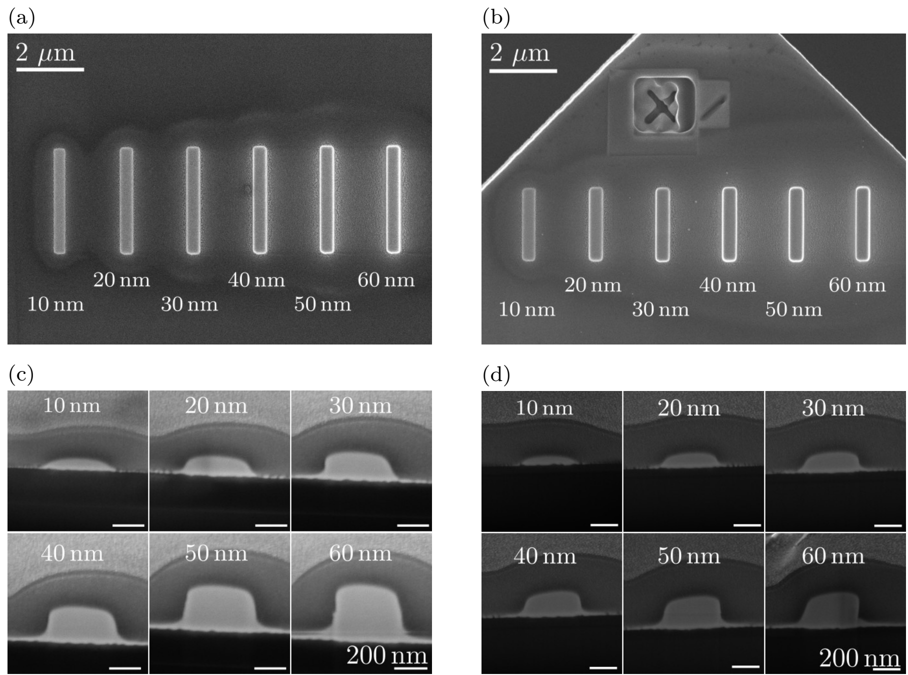

Figure A.2.: SEM micrographs of a deposition rate experiment on a large chip (a) and a cantilever (b) in top view and corresponding SEM micrographs of a cross-section through the deposits (c, d).

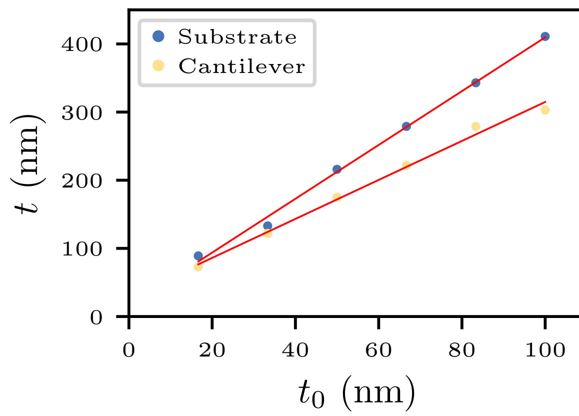

Figure A.3.: Comparison of the deposition rate of a 300 nm wide long nanostructure on large chips and SPM cantilevers. The deposition was performed at 200 ns dwell time and 9.7 pA ion beam current. The red line indicates a linear fit to the data.

A.4. SQUID

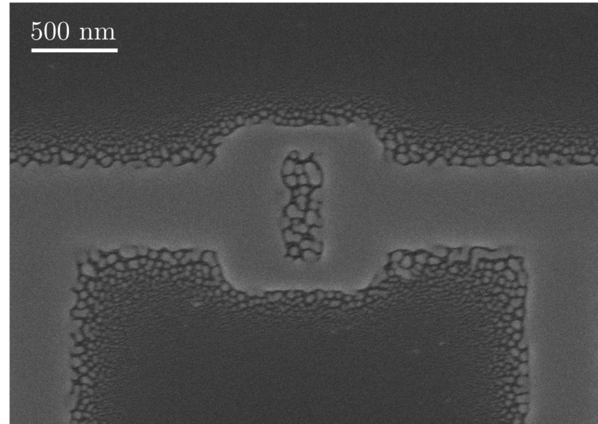

Figure A.4.: SEM micrograph of a long-bridge SQUID deposited following the procedure of the first generation (section 4.2.1) on a cantilever with $I_{\mathrm{Ion}} = 9.7\,\mathrm{nA}$ and $\tau_{\mathrm{d}} = 200\,\mathrm{ns}$. The upper junction obtained a width of 134 nm, the lower junction 149 nm. The broadening of all structures lead us to employ ion milling to sharply define the SQUID structure in the recipe of second generation long-bridge SQUIDs.

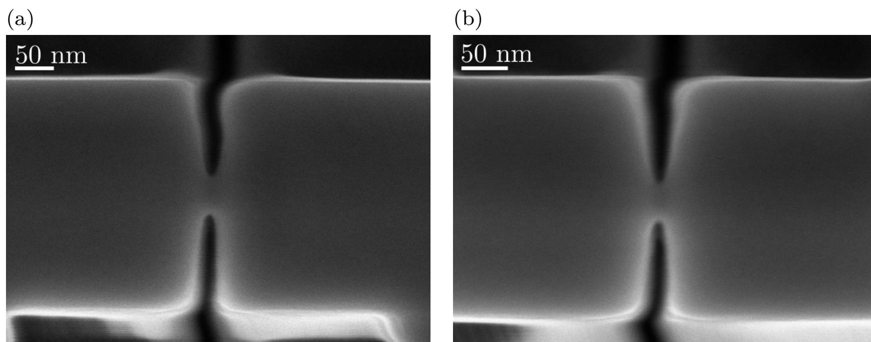

Figure A.5.: High magnification SEM micrographs of the upper- (a) and the lower junction (b) of the short-constriction SQUID shown in fig. 4.15b.

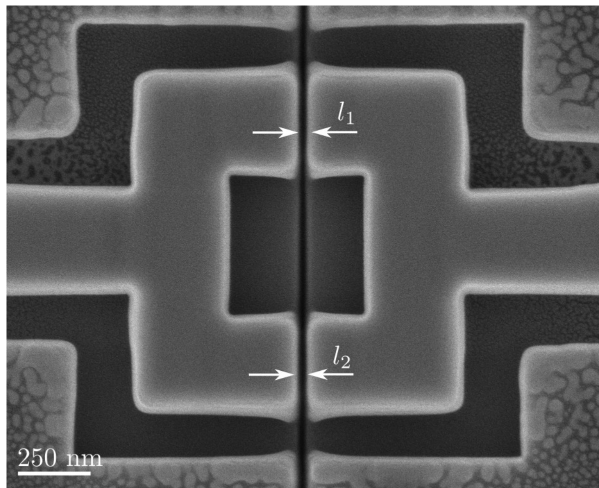

Figure A.6.: SEM micrograph of the SNS-SQUID presented in fig. 4.17a before deposition of the metallic W-C used to precisely measure the length of the junction.

Appendix B

SQUID Characterization

B.1. Long Nano-Bridge SQUIDs

B.1.1. The Cooldown Curve

In section 5.1 we presented the analysis of the cooldown curve modeled with a single transition which gives a good estimate of the critical temperature. Interestingly, sample A exhibits additional features inside the transition and is best modelled by a superposition of four Gaussian functions. The transition onsets at roughly 4.4 K, followed by the main transition at 4.2 K.

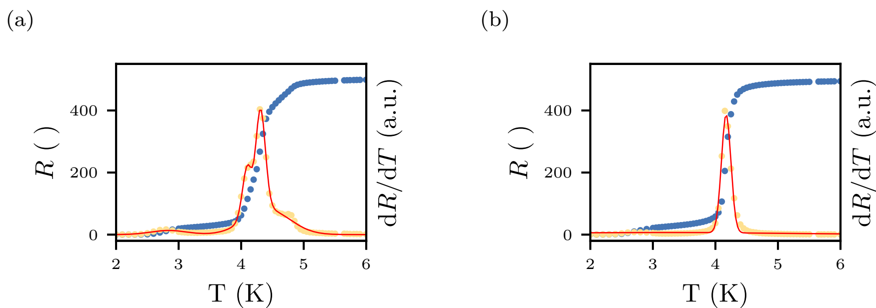

Figure B.1.: Cooldown curves of the long-bridges SQUIDs presented ((a) sample A, (b) sample B) with a model composited by a superposition of multiple Gaussian distributions. The model is capable of resolving the convoluted peaks in sample A.

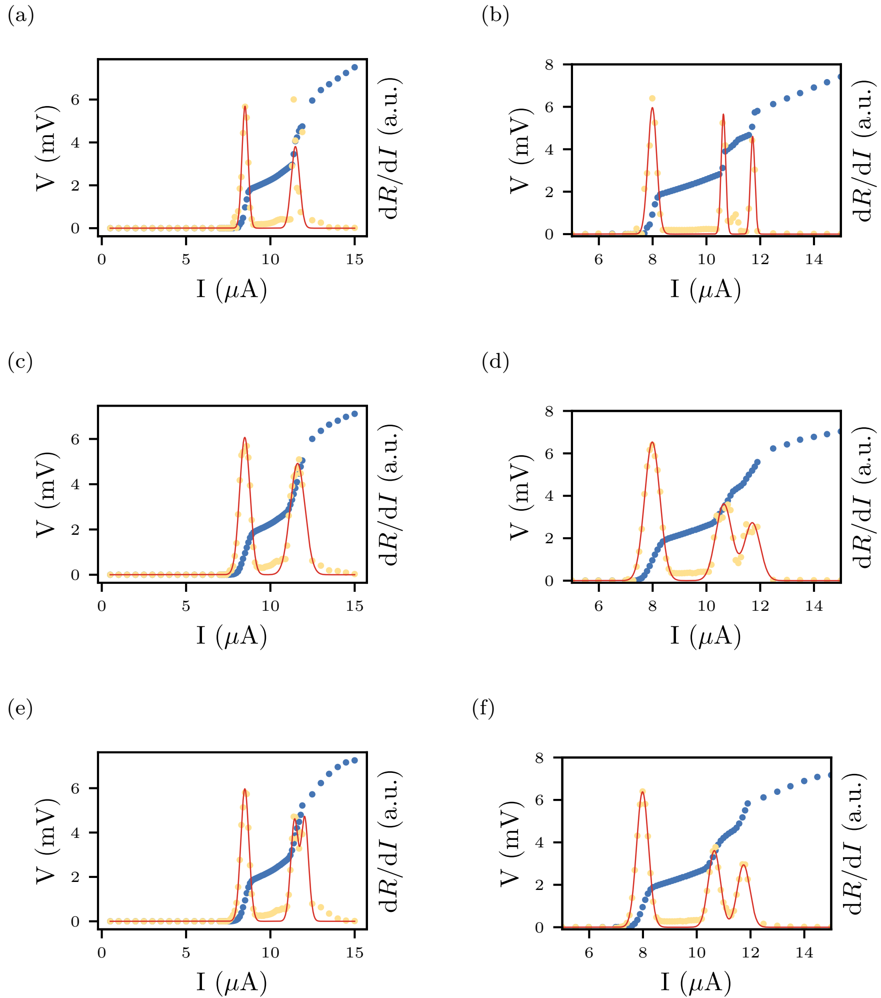

Figure B.2.: IV characteristics of sample A (left column) and sample B (right column), analyzed without a filter (a, b), after applying a rolling average filter over seven datapoints (c, d), and after three times applying a rolling average filter over three datapoints (e, f). The filter using seven datapoints provides a good trade-off for the magnitude of the I_c and the V modulation. The three times three filter reveals that the upper transition of sample A is a convolution of two individual transitions.

The main transition exhibits a convolution of two transitions that are very similar in value but can be resolved. Below the main transition we observe a region where the resistance constantly decays down to 2.8 K, below which the structure reaches full superconductivity. The critical temperatures reported by the fitting function are

$$T_{\mathrm{c,A,1}} = (2.843 \pm 0.289)\,\mathrm{K}\ , \tag{B.1}$$

$$T_{\mathrm{c,A,2}} = (4.211 \pm 0.091)\,\mathrm{K}\ , \tag{B.2}$$

$$T_{\mathrm{c,A,3}} = (4.211 \pm 0.091)\,\mathrm{K}\ , \tag{B.3}$$

$$T_{\mathrm{c,A,4}} = (4.417 \pm 0.360)\,\mathrm{K}\ . \tag{B.4}$$

B.2. Short-Constriction SQUIDs

B.2.1. The Influence of the Reading Count

With the introduction of the recipe of second generation SQUIDs ($\tau_\mathrm{d} = 200\,\mathrm{ns}$) we were facing new challenges regarding electrical characterization in the PPMS. While in initial experiments with SQUIDs of first generation ($\tau_\mathrm{d} = 500\,\mu\mathrm{s}$) a reading count of 25 resulted in a broad, smooth transition, the samples' response to increasing currents significantly changed.
The transition region became more irregular with consecutive readings deviating significantly. Experiments with a reading count of 1 revealed that the there was actually two discrete states that the resistance (voltage) readings were jumping between in a irregular way. Experiments at a reading count of 10 show datapoints in discrete steps of $1/10{\cdot}\Delta R$. Figure B.3 shows the IV characteristics of a short-constriction SQUID of second generation measured at reading counts of 1, 10 and 25.
As the PPMS is turning the current source off in between consecutive readings (section 2.3.1) and at higher reading counts is internally calculating the average over all independent readings, we suspect the individual readings to be either R_i or R_{i+1} with no actual readings in between.

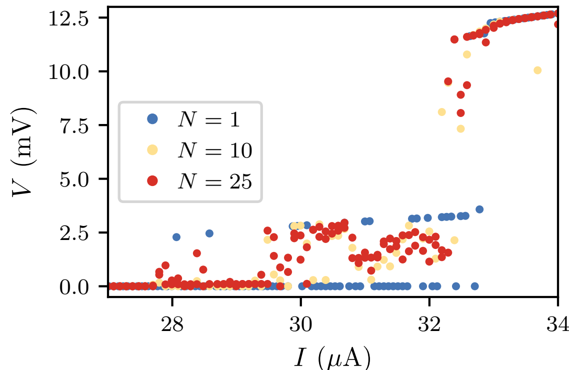

Figure B.3.: IV of a short-constriction SQUID of second generation at 1, 10, 25 readings

Our best explanation for this behavior is that the superconducting phase of a given region, likely the junctions, is very susceptible to perturbations via noise current amplitudes. It is a statistical process whether turning on the current source the superconducting phase collapses or not and therefore whether the

reading is fully resistive or fully superconducting. Resetting the current source in between readings allows the superconductor to relax.
This behavior was not observed in initial experiments with SQUIDs of first generation where the transition was always smooth. Further investigation is required to figure out why this behavior arises with the SQUIDs of second generation. The differences coming to mind are:

- different magnetic properties due to changes of the chemical composition and the microstructure of the deposit and
- higher noise amplitude due to a generally higher critical current, requiring the current source to operate in a higher output range.

As a consequence, we decided to conduct following experiments with a reading count of 1 to preserve as much information as possible. For more statistical data, we were taking multiple individual readings at each current setpoint. Therefore, we could mostly reproduce the internal mechanisms of the PPMS while maintaining the raw data.

B.2.2. Modulation of I_c

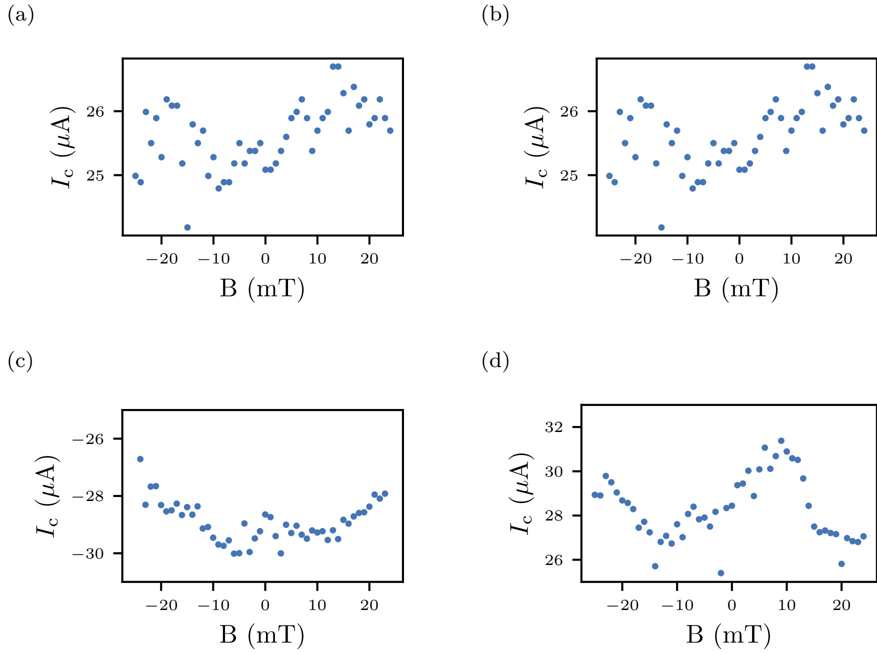

Figure B.4.: Field dependence of I_c^+ (a) and I_c^- (b) of the first transition for a short-constriction SQUID on a cantilever, obtained by a voltage threshold (a, b) and modelling $\mathrm{d}R/\mathrm{d}I$ with a superposition of multiple Gaussian curves (c, d).

B.3. SQUID on Lever

B.3.1. Long-Bridge SoL

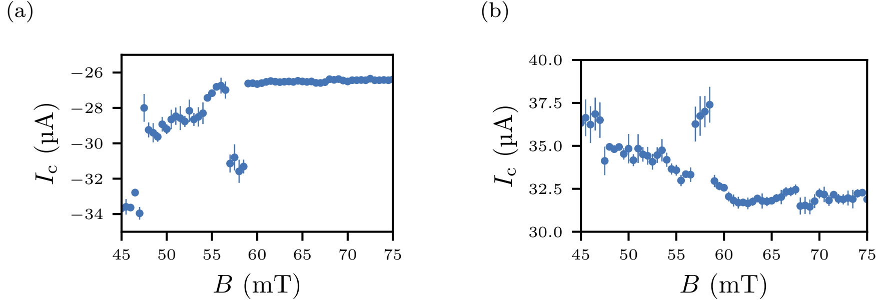

Figure B.5.: Field dependence of I_c^+ (a) and I_c^- (b) of the first transition for a long-bridge SQUID on a cantilever, obtained by modelling $\mathrm{d}R/\mathrm{d}I$ with a superposition of multiple Gaussian curves.

B.3.2. Short-Constriction SoL

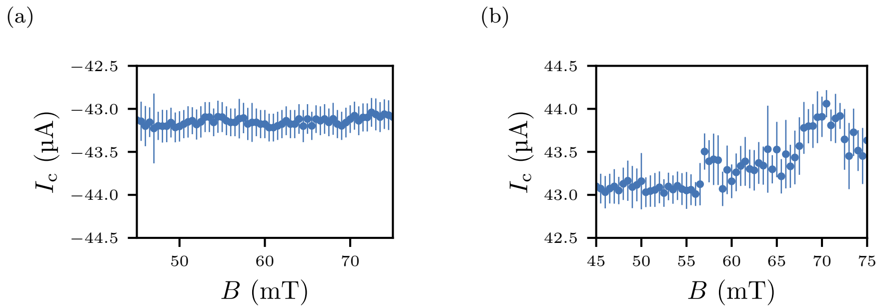

Figure B.6.: Field dependence of I_c^+ (a) and I_c^- (b) of the first transition for a long-bridge SQUID on a cantilever, obtained by modelling $\mathrm{d}R/\mathrm{d}I$ with a superposition of multiple Gaussian curves.